An experimental investigation of drop impact phenomena with complex fluids on heated and soft surfaces

Thesis submitted in accordance with the requirements of
the University of Liverpool for the degree of Doctor in Philosophy
by

Simeng Chen

Supervisor: Dr. Volfango Bertola

August 2017

Abstract

The present thesis is the result of a four year experimental research, which aims at studying the impact of non-Newtonian droplets (i.e., droplets of complex fluids such as polymer solutions) on heated surfaces (i.e., surfaces with a temperature above the Leidenfrost point) and soft surfaces (i.e., surfaces that undergo temporary or permanent deformations upon drop impact) through high-speed imaging.

In the first year we focused on the Leidenfrost drop impact of different model fluids with matching flow curves. We demonstrate that the total kinetic energy carried by low-viscosity Newtonian drops during retraction is partly transformed into rotational kinetic energy rather than dissipated (published on *Physical Review E*, 2016). In the second year we extended the Leidenfrost drop impact experiment to viscoplastic fluids. The results show that the main contribution to drop rebound is due to surface forces rather than the elasticity of vapour cushion (published on *Soft Matter*, 2016). A systematic investigation on the impact of viscoplastic drops onto viscoplastic substrates was carried out in the third year. It is shown that the yield stress magnitude of drop/substrate strongly affects the final shape of the impacting drop (published on *Soft Matter*, 2017). The fourth year was devoted to the drop impact on spherical elastic surfaces. The dynamic contact angle measured using a novel digital image processing scheme is found to be significantly affected by the impact parameters and a quantitative estimation of the deformation energy is proposed (published on *Physics of Fluids*, 2017).

KEY WORDS: Drop impact, high-speed imaging, complex fluids, soft surfaces.

Declaration

I do hereby declare that this thesis was composed entirely by myself and that the work described within is my own, except where explicitly stated otherwise.

August 2017

Acknowledgement

Time flies. I still remember the first day when I said hello and introduced myself to everyone in the fluid group as if it was yesterday. Without you guys, I would not have had the fantastic four years in Liverpool.

I would like to thank Dr. Volfango Bertola first, not only for his continuous support and encouragement as a mentor in my academic career, but also for his kindness and humbleness as a sincere friend I have met in my life. After many years, I would still memorise all the long time scientific discussions and numerous 'group meetings' with him.

I am very grateful to meet Oguzhan Der. He is such a nice friend that I would treasure our friendship for the rest of my life. I sincerely wish him a good luck with his PhD study. Special thanks go to Hesam Maleki for plenty of interesting conversations and funny jokes. I would like to thank my roommates: Haonan Xu, Chaofan Wen and Yue Zhang for having thousands of hot pot parties together.

Undoubtedly I would like to express my sincere gratitude to my parents. This work would never have been done without your endless support and selfless love.

I am so lucky to meet my girlfriend, Xiaoli Xu, in the last year of my PhD. No words can express my gratitude to her pure and enduring love. Her smile will always encourage me to face whatever challenges the life may offer.

Publications

Peer-reviewed Journals

Chen, S. and Bertola, V., 2017. Drop impact on spherical soft surfaces. *Physics of Fluids*, 29(8), p.082106.

Chen, S. and Bertola, V., 2017. Morphology of viscoplastic drop impact on viscoplastic surfaces. *Soft Matter*, 13(4), pp.711-719.

Chen, S. and Bertola, V., 2016. Jumps, somersaults, and symmetry breaking in Leidenfrost drops. *Physical Review E*, 94(2), p.021102.

Chen, S. and Bertola, V., 2016. The impact of viscoplastic drops on a heated surface in the Leidenfrost regime. *Soft Matter*, 12(36), pp.7624-7631.

Conference Proceedings

Chen, S. and Bertola, V., 2016. Viscoplastic Leidenfrost Drops. *Proc. 27th Annual European Conference on Liquid Atomization and Spray Systems, 4-7 Sept. Brighton, UK.*

Chen, S. and Bertola, V., 2015. Morphology of drop impact on a viscoplastic gel. *Proc. 13th Triennial International Conference on Liquid Atomization and Spray Systems, 23-27 Aug. Tainan, Taiwan.*

Chen, S. and Bertola, V., 2014. On the energy dissipation in Leidenfrost drop impacts: Newtonian vs. non-Newtonian fluids. *Proc. 26th Annual European Conference on Liquid Atomization and Spray Systems, 8-10 Sept. Bremen, Germany.*

List of Figures

List of Tables

Contents

Chapter 1

Introduction

Drop impact dynamics on solid surfaces is a classical subject of interfacial hydrodynamics. So far, most of the studies are restricted within Newtonian fluids and isothermal solid surfaces. Although the drop impact characteristics of some non-Newtonian fluids such as shear-thinning and yield-stress fluids on solid surfaces have been experimentally investigated using different model fluids, there is very little research contribution which characterises the drop impact morphology of non-Newtonian fluids and the drop impact behaviours on heated and soft surfaces. However these situations are relevant to various applications, such as spray cooling, 3D ink-jet printing, and manufacture processes of food, pharmaceutical and cosmetic industries. Thus the experimental investigation of these cases is of both scientific and practical importance.

1.1 Research background and motivation

1.1.1 Leidenfrost drops

When a liquid droplet impacts on a high-temperature surface, one may observe bouncing back of the droplet off the surface due to the creation of a thin vapour film between the drop and surface upon impact. This phenomenon is known as "dynamic Leidenfrost phenomenon" [24, 130, 151], and is encountered in various industrial applications including spray cooling, fire suffocation [83] and spray quenching [11] (as shown in Figure 1.1). So far research efforts to understand

the Leidenfrost phenomenon were mainly focused on Newtonian fluids such as water [13, 117]. However, there is a growing interest in non-Newtonian drops because of their role in food, cosmetics, and biopharmaceutical industries, among others. Thus a better understanding of Leidenfrost drop impact behaviours of both Newtonian and non-Newtonian fluids and the physical mechanisms behind them is necessary to improve such industrial processes.

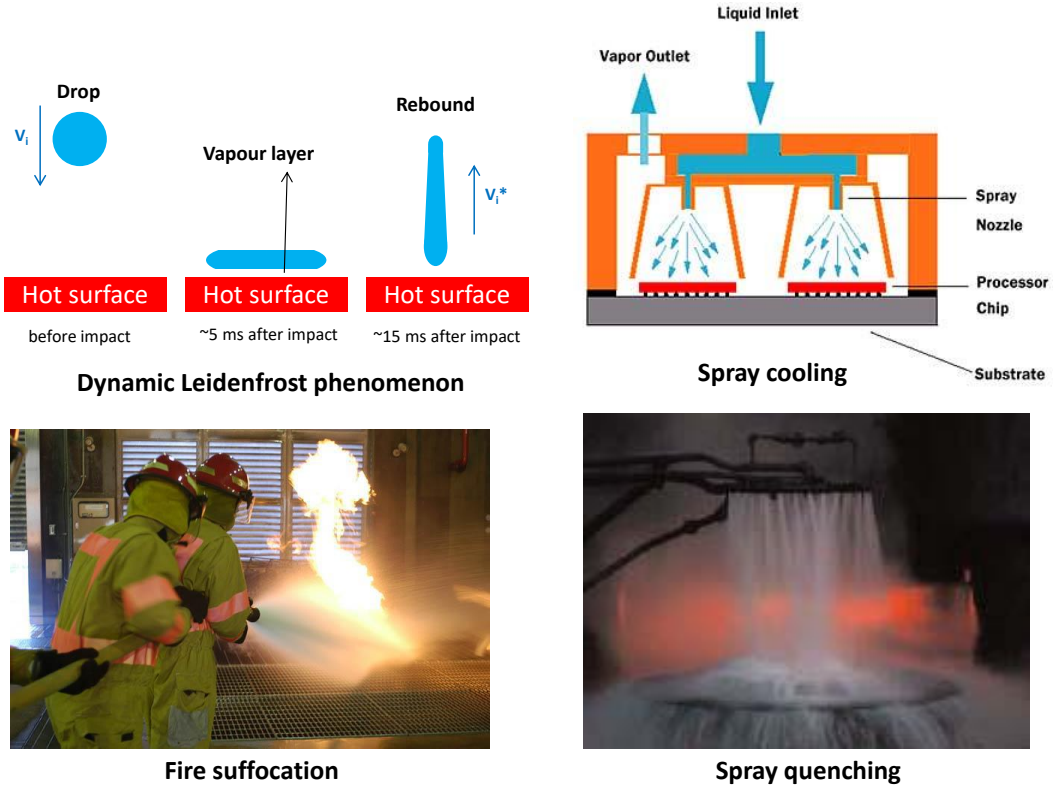

Figure 1.1: Dynamic Leidenfrost phenomenon and its industrial applications.

Effect of polymer additives on maximum bouncing height

In recent studies on Leidenfrost drops of dilute polymer solutions, quantitative measurements (such as the maximum diameter, maximum bouncing height and retraction velocity etc.) which characterise the impact morphologies are obtained for both Newtonian drops (water) and viscoelastic drops (PEO) through high-speed imaging [17, 30]. The polymer additives are found to slightly reduce the maximum spreading diameter and retraction velocity of the impacting drop [17].

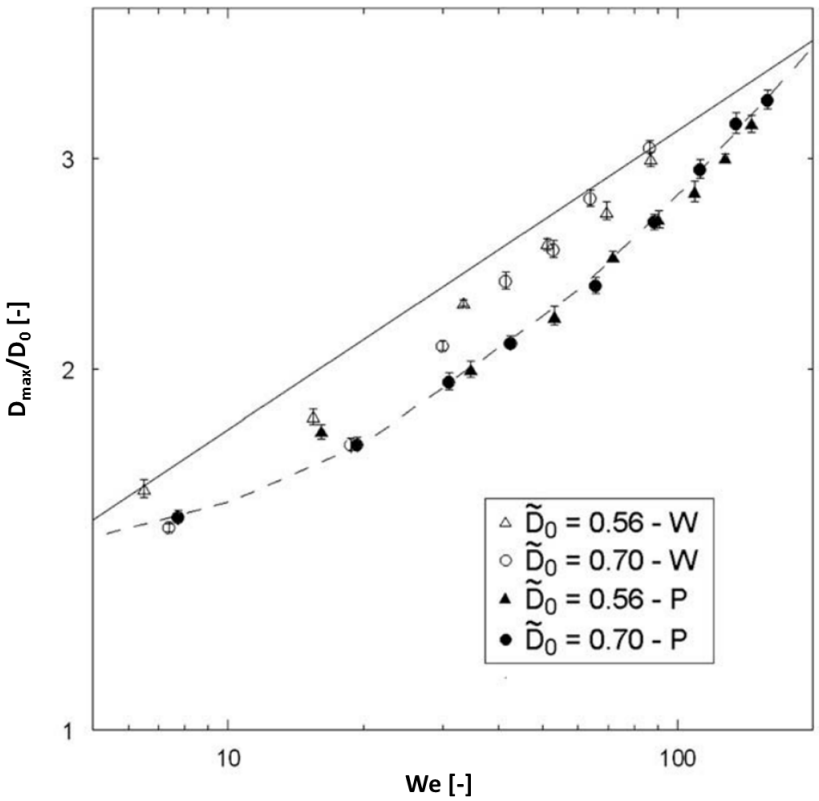

Figure 1.2: Normalised maximum spreading diameter of water drops (open symbols) and polymer solution drops (filled symbols) as a function of Weber numbers with a surface temperature T = 400^{o}C. The equilibrium drop diameter is normalised with respect to the capillary length ($l_c = \sqrt{\sigma/(\rho g)}$): $\tilde{D}_0 = D_0/(2l_c)$. Solid and dashed lines represent the scaling laws $D_\mathrm{m}/D_0 \sim \mathrm{We}^{1/4}$ and $D_\mathrm{m}/D_0 \sim \mathrm{We}^{1/2}$ respectively. (Adapted from [17])

Figure 1.2 compares the normalised maximum spreading diameter of water drops (open symbols) to that of polymer solution (PEO, 200 ppm) drops (filled symbols) at different Weber numbers, in which it can be clearly observed that polymer additives cause a slight reduction of the maximum spreading diameter. Surprisingly the maximum bouncing height of the impacting drops is observed to increase significantly by adding very small amount of polymer additives as shown by Figure 1.3 [17, 30]. This effect has been explained in terms of the reduction of energy dissipation caused by polymer additives during the drop retraction and rebound, resulting in higher mechanical energy available for bouncing (see Section 2.6.2 for details). However this proposal is questionable since it only qualitatively com-

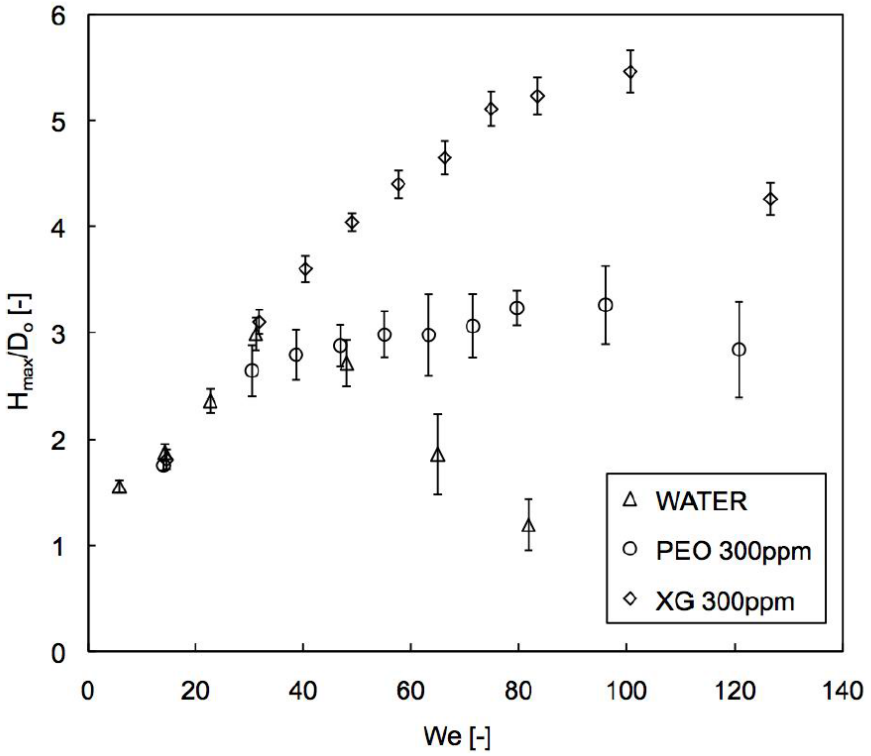

Figure 1.3: Maximum bouncing height of water and polymer solution drops as a function of the impact Weber number. The data for PEO polymer solution (polyethylene oxide, 300 ppm) drops and XG polymer solution (xanthan gum, 300 ppm) drops are represented by circles and diamonds respectively; triangle symbols denote the data for water drops. (Adapted from [30])

pares the energy dissipations between Newtonian and non-Newtonian drops based on various assumptions. Further systematic investigations of the effect of rheology on the impact morphology are needed to understand the energy distribution during the impact process.

Rebound mechanisms in Leidenfrost drops

The reflection of impacting drops is a distinct feature of the drop impacts in the Leidenfrost regime. In principle, the rebound of Leidenfrost drops results from the combination of two independent mechanisms: (i) the rapid release of the surface energy stored during inertial spreading, and (ii) the elasticity of the compressible vapour film between the drop and the surface [133]. The former mechanism is

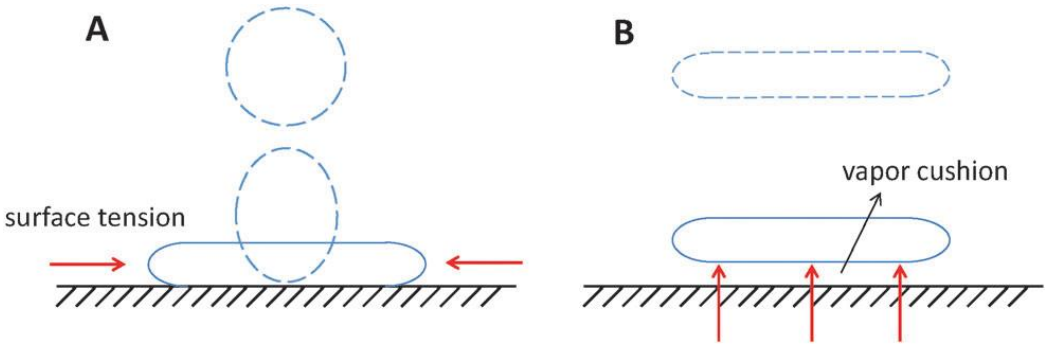

Figure 1.4: Rebound mechanisms of a drop impinging on a hot surface in the Leidenfrost regime: (A) surface tension; (B) vapour cushion.

also responsible for drop rebound on non-heated, hydrophobic surfaces (where no vapour film exists) [114, 135]. After impact the drop first spreads radially and then forms a liquid lamella at the end of spreading after impact on a hot surface. The curvature of the free surface at the rim is very large, which provides strong surface tension forces pointing radially to the centre of the lamella, therefore a retraction phase follows the initial spreading. In terms of energy transformation, the excess surface energy stored during spreading is converted into kinetic energy as the drop retracts, and propels the drop off the surface, as illustrated in Figure 1.4A. In several Leidenfrost drop models, rebound is described using only the surface energy approach, while the elasticity of the vapour layer is not considered explicitly. The only effect of the vapour layer is to introduce a slip boundary condition at the liquid-solid interface. The good agreement between numerical results and experimental data indicates that Leidenfrost drop rebounds can be explained by the surface tension mechanism alone [72, 96].

However, some authors suggest that the rebound is also due to the formation of a high-pressure vapour layer between the liquid and solid surface during impact. The high-pressure vapour layer is working as an elastic cushion which provides

forces opposite to the impact velocity. The upward forces cause a change in the momentum of the impinging drop leading to its reflection, as shown schematically in Figure 1.4B. In the so-called disk model [133], rebound is driven by the cushion mechanism, in which the shape dynamics of the liquid drop is not considered (i.e., radius and thickness of the liquid disk are constant).

So far, no systematic investigations on the contributions of surface tension and elasticity of the vapour layer to the rebound behaviours of Leidenfrost drops have been reported in literature. The special properties of a yield-stress fluid enable one to examine the two reflection mechanisms by conducting Leidenfrost drop impacts using viscoplastic drops with different magnitudes of yield stress.

1.1.2 Effect of yield stress in capillary flows

Capillary flows describe the type of flows where the capillary forces dominate. They are often associated with a flow characteristic length which is comparable or smaller than the capillary length. Examples of the capillary flows are shown in Figure 1.5, including the dynamics/oscillations of free-fall or deposited drops, the capillary breakup of liquid jets, the drop impacts and the flows in capillaries/microchannels.

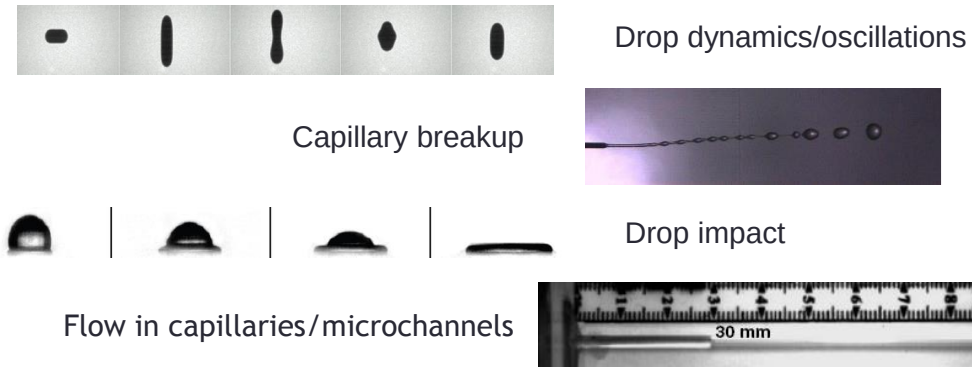

Figure 1.5: Examples of capillary flows.

In simple cases, such as Newtonian fluids, the capillary flow is usually char-

acterised by a dimensionless number called capillary number:

$$Ca = \frac{\mu V}{\sigma}, \tag{1.1}$$

where V represents the characteristic velocity, μ is the dynamic viscosity of the fluid, and σ is the surface tension between the two fluid phases. It expresses the competition between viscous forces and surface forces on the interface between a gas and a liquid, or between two immiscible liquids. If the capillary number is sufficiently low (a rule of thumb: $Ca \leq 10^{-5}$), e.g., the flow in porous media [59], the flow is dominated by capillary forces. However for high Ca number the capillary forces are negligible compared to the viscous forces. Here the capillary flows of viscoplastic (or yield-stress) fluids are considered. In particular, the attention is paid on the capillary flows where the yield stress is comparable with the Laplace pressure. In such cases the capillary number is no longer favourable to describe the flow behaviours due to the uncertainty of the apparent viscosities. Ideally the flow behaviours could be characterised by a single dimensionless number referred as the 'Bingham-Capillary' number [16] which is the product of Bingham number ($Bm = (\tau_0 D_0)/(\mu V)$) and capillary number:

$$\widehat{B} = Bm \times Ca = \frac{\tau_0 D_0}{\sigma}, \tag{1.2}$$

where τ_0 denotes the yield stress of the viscoplastic fluid. The Bingham-Capillary number expresses the relative effect of the yield stress to the Laplace pressure. At low Bingham-Capillary numbers ($\widehat{B} < 1$), the action of capillarity is able to overcome the yield point of the fluid thus the fluid flows. However in case of high Bingham-Capillary numbers ($\widehat{B} \geq 1$), the capillary forces fail to deform the fluid hence the flow stops. However, so far there are two defects with this dimensionless number. Firstly, the surface tension of viscoplastic fluids is ill-defined. It is difficult to isolate the effect of yield stress when measuring the surface tension of viscoplastic fluids using conventional techniques. Secondly, the measured value of yield stress from rheometers is only a single component of the

stress tensor. Thus the yield stress in three-dimensional flows (e.g., drop impact) might be different from the value found in rheometric tests.

1.1.3 3D ink-jet printing

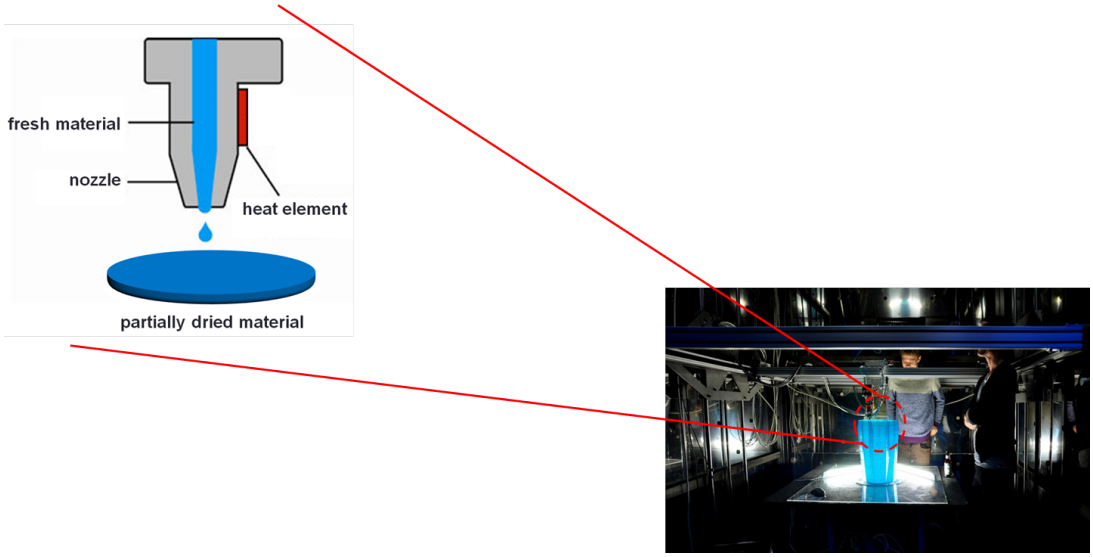

Figure 1.6: Manufacturing process of 3D inkejet printing.

3D inkjet printing is a non-contact, data-driven, low-cost, high-speed, additive, and automated, eco-friendly technique. Its exploitation can rapidly shorten product development, significantly reduce the production cost of many devices, and it has been shown to enable a reduced time-to-market. When used as a rapid manufacturing technology, 3D inkjet printing enables the fabrication of products layer by layer, which makes it possible to manufacture customised products in small series without having to use expensive tools.

The manufacturing process of 3D inkjet printing involves the formation of yield-stress drops from the printing head and their interaction with the target surfaces. The target surfaces are not solid, non-deformable materials, but can be better described as soft solids, which undergo local deformations upon drop impact. The response to deformations of these materials ranges from pure elastic response to permanent plastic deformation, which can be either instantaneous or time-dependent. This affects the drop impact dynamics hence the characteristics

of the final product.

The inkjet manufacturing process (as shown in Figure 1.6), where a layer of fresh material is deposited on a partially dried or cured layer of the same material, is modelled by the impact experiments of viscoplastic drops on viscoplastic surfaces characterised by different magnitudes of yield stress. So far, no systematic studies about these systems have been reported in the open literature to date, including their basic phenomenological characterisation.

1.1.4 Effect of geometrical shapes of target surfaces

The geometrical shapes of target surfaces may not always be planar in many industrial applications. For example, drop impact on curved surfaces of cylinders in horizontal-tube falling film evaporators, in the manufacturing of digital displays consisting of numerous polymer light-emitting diodes, or drops of polymer liquid impact on rectangular microcavities [106]. However, most of the studies on the effect of geometrical shapes of target surfaces are constricted in rigid (i.e. non-deformable) surfaces. In some cases, the compliance of the surface also play an important role in the drop dynamics, such as the 3D inkjet printing where the surface of partially cured material could be convex (see Section 1.1.3). Thus, a better understanding of the effect of arbitrary shape of the surface, soft surface in particular, on the dynamics of impacting drops is necessary. To date, the research work focusing on the coupled effect of surface curvature and surface compliance on drop impact dynamics is very limited in literature.

1.2 Aims and objectives

The objective of the present work is to get a deeper insight on the dynamic behaviours of the impact of non-Newtonian droplets on heated and soft surfaces by conducting experiments using different combinations of model fluids and model surfaces, and to investigate the effect of different factors (such as impact kinetic

energy, rheology, substrate softness, geometric shape of the surface etc.) on the drop impact morphology by comparing the experimental results of different combinations. More specifically, the present research targets the following objectives:

1. The first objective of the investigation on Leidenfrost drops is to get a deeper insight on the energy distribution in the Leidenfrost drop impact process, and to investigate the effect of different factors (such as viscosity, shearthinning or viscoelastic behaviour, and flow structure) on the energy distribution by comparing the Leidenfrost drop impact experimental results of three fluids (water solutions of glycerol, xanthan gum and polyacrylamide, respectively) with similar rheology (see Figure 1.7 for the strategy of model fluids preparation and Section 3.4.1 for measured flow curves).

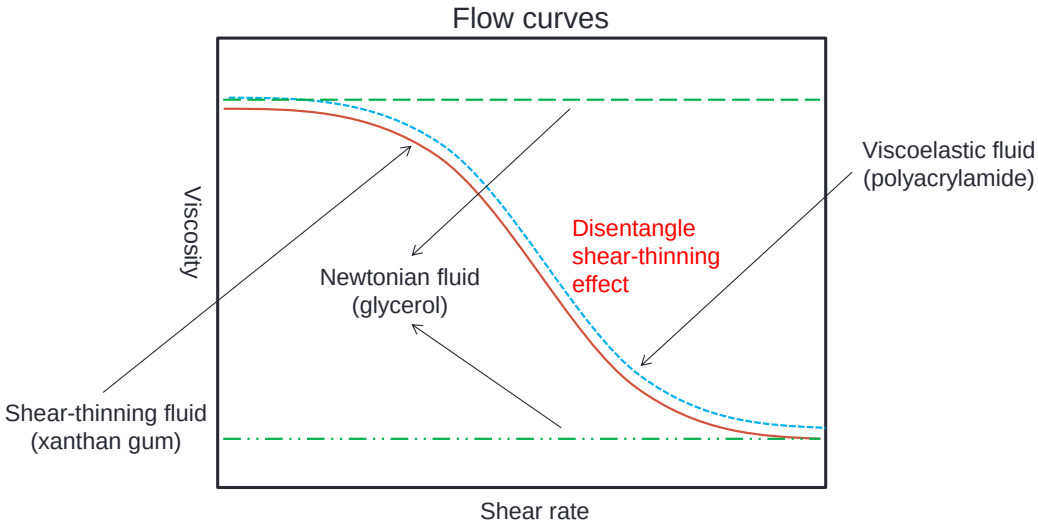

Figure 1.7: Model fluids with similar rheology.

2. The second objective of the investigation on Leidenfrost drops is to examine the two reflection mechanisms (Section 1.1.1) by conducting Leidenfrost drop impacts using viscoplastic drops with different magnitudes of yield stress, and to characterise the impact morphology using a single dimensionless number called the Bingham-Capillary number, which compares the yield stress with the Laplace pressure. Through the comparisons of the maximum bouncing height of yield-

stress drops with different BinghamCapillary numbers at the same impact Weber number, the contribution of the elastic vapor cushion to the reflection can be evaluated.

3. The objective of the investigation on the impact of viscoplastic drops on viscoplastic surfaces is to construct a map showing the final profiles of the impacting drops for different combinations of drops and substrates with different magnitudes of yield stresses at different Weber numbers, and to compare the experimental data of the temporal crater evolution with the prediction of one of the existing models on crater evolution through a different definition of the Reynolds number. In particular, the effect of various impact parameters on the volume of final shape, which is an important indicator of surface roughness in inkjet printing manufacturing process, is to be extensively investigated.

4. The investigation of drop impact on spherical soft surfaces aims at systematically studying the effect of various impact parameters, such as substrate softness, surface curvature, Weber number etc., on the drop dynamics. In particular, the dynamic contact angle is to be measured using a novel digital image-processing scheme based on a goniometric mask (see Section 2.11 for details), which does not require edge fitting. In addition, a theoretical analysis on the quantitative estimation of substrate deformation energy is to be carried out.

Chapter 2

Literature Review

2.1 Drop impact on solid surfaces

Drop impact has been a classic research subject since Worthington [156] firstly studied the morphology of drop impacts of different fluids on a horizontal plate in 1876. It has a variety of applications in industry such as the delivery of agrochemicals [10] and pharmaceuticals [56], spray coating, ink-jet printing [60], fire suffocation [83] and the fabrication of micro-lenses [21]. High-speed drop impacts on solid walls can cause severe erosion (e.g., in steam turbines). In spray coating, the interaction between droplets and the bare or partially coated surfaces can significantly affect the coating quality (e.g., roughness and/or bubble entrainment). In agriculture, knowledge of the impact behaviour of pesticide droplets on foliage (such as rebound or splashing) enables a reduction of the quantities of pesticides used per unit area. Furthermore, pesticides falling off the foliage due to rebound or splashing can pollute soil. The morphology of drops impacting on a surface can vary significantly with the properties of the fluid, and of the substrate, as well as those of the fluid medium where drops travel before impact. The simplest case which has been studied extensively in the literature is the drop impact on a homo-thermal solid surface, however there is a growing interest in other cases, e.g., drop impact on heated surface, drop impact on deformable surfaces etc.

2.1.1 Dimensionless numbers

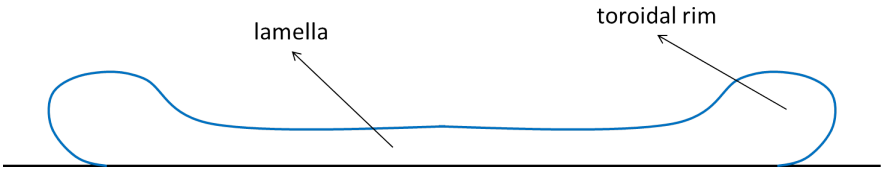

Figure 2.1: Schematic of a spreading drop.

Due to inertial forces, drops will spread after the initial impact with a surface and will form a thin disk called a lamella surrounded by a toroidal rim at the end of the inertial expansion stage as shown schematically by Figure 2.1. During this process, the kinetic energy of the drop will be converted into surface energy through the increase of the drop surface area. Thus drop impacts can be characterized by the competition between inertial force and capillary force. This competition is described by a dimensionless Weber number,

$$We = \frac{\rho v_i^2 D_0}{\sigma}, \tag{2.1}$$

where ρ is the fluid density, σ is the surface tension of the fluid, v_i denotes the normal component of the impact velocity with respect to the surface, and D_0 represents the equilibrium drop diameter before impact. However the We number alone can not completely describe drop impact since it does not take energy dissipation into account. For drops of highly viscous fluids, most of the kinetic energy of the drop may dissipate during impact rather than convert into surface energy. The Reynolds number can be introduced to account for viscous effects,

$$Re = \frac{\rho v_i D_0}{\mu}, \tag{2.2}$$

where μ denotes the dynamic viscosity of the fluid. Another option is the introduction of Ohnesorge number,

$$Oh = \frac{\sqrt{We}}{Re} = \frac{\mu}{\sqrt{\rho \sigma D_0}}, \tag{2.3}$$

which relates the viscous forces to inertial and capillary forces. A retraction phase may occur after the spreading, especially for drop impacts on hydrophobic surfaces. At the beginning of retracting, the impacting droplet is static. As a result the retraction is driven by the surface forces which minimize the free surface of the drop and resisted by viscous forces. This can be expressed as the Capillary number,

$$Ca = \frac{\mu v_{ret}}{\sigma}, \tag{2.4}$$

where v_{ret} represents the retraction velocity of the liquid lamella. The Ohnesorge number statically describes the properties of the fluid and the characteristic length whilst the Capillary number contains dynamic information of the flow due to the introduction of the velocity term.

2.1.2 Spreading behaviours

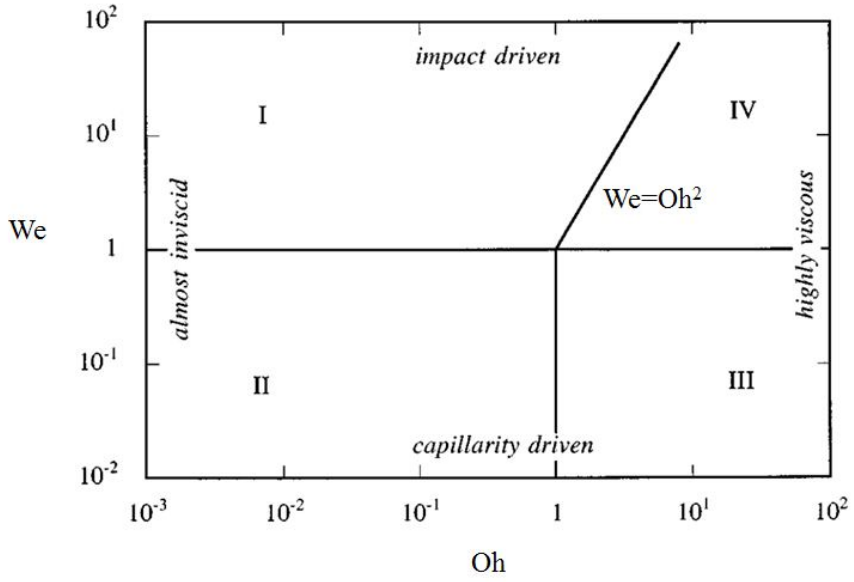

Figure 2.2: The four spreading regions in the (We, Oh) plane. (adapted from [143])

The spreading behaviour is mainly characterized by the We number and the Oh number. The Weber number scales the driving force for the spreading process of a droplet. At high Weber number the droplet is more likely to expand radially

due to large kinetic energy during the inertial spreading stage. On the contrary the Ohnesorge number scales the resisting force which counters the spreading process. At high Ohnesorge number large viscous forces are able to resist the radial expansion of the droplet. The spreading characteristics of a liquid droplet can be divided into four asymptotic regions on the We and Oh plane, as shown in Figure 2.2.

Region I (inviscid impact-driven). The spreading is primarily driven by dynamic pressure. The characteristic time scale of the inertial spreading is very short. Viscous effects are negligible during the initial stage of spreading, however damp the subsequent oscillations in next stage.

Region II (inviscid capillarity-driven). The spreading is mainly driven by the capillary forces at the contact line and the impact velocity effects are negligible. Spreading is followed by interfacial oscillations with the a time scale of the same order as the spreading.

Region III (highly viscous capillarity-driven). The spreading is driven by capillary forces and resisted by viscous forces. Impact velocity has negligible effects. The inertial oscillations are overdamped by high viscosity.

Region IV (highly viscous impact-driven). The spreading is driven by inertial forces and resisted by viscous forces. Capillarity has negligible effects. The oscillations are absent as in Region III.

2.1.3 Wettability of the surface

Depending on the properties of materials and dynamic parameters, the impact may result in different outcomes, such as deposition, splashes and rebound *etc.* One of the important factors is the wettability. Wettability describes the ability of a drop to spread on the solid surface and is characterised by the static contact angle at the contact line. The contact angle is determined by the balance between adhesive and cohesive forces. In other words, it is the result of the minimization

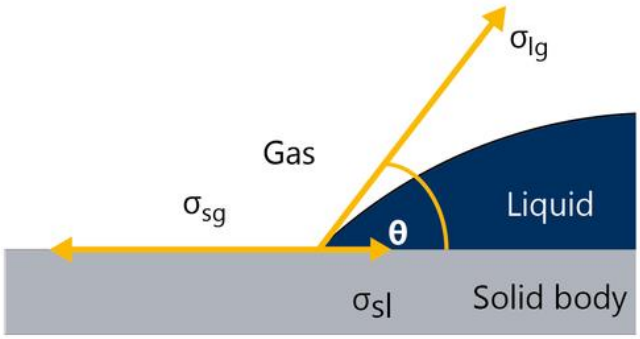

Figure 2.3: Schematic of a static drop on the solid surface showing the surface tensions at the contact line.

of surface energies between three phases: liquid, gas and solid. This is expressed by the well-known Young's equation, as shown in Figure 2.3:

$$\sigma_{sg} - \sigma_{sl} - \sigma_{lg}\cos\theta = 0, \tag{2.5}$$

which correlates the surface tensions (σ_{sg}: solid & gas, σ_{sl}: solid & liquid, σ_{lg}: liquid & gas) between the three phases. Conventionally a system with a static contact angle below 90° is described as wetting and it becomes non-wetting if the contact angle is over 90°. The two scenarios are schematically compared in Figure 2.4.

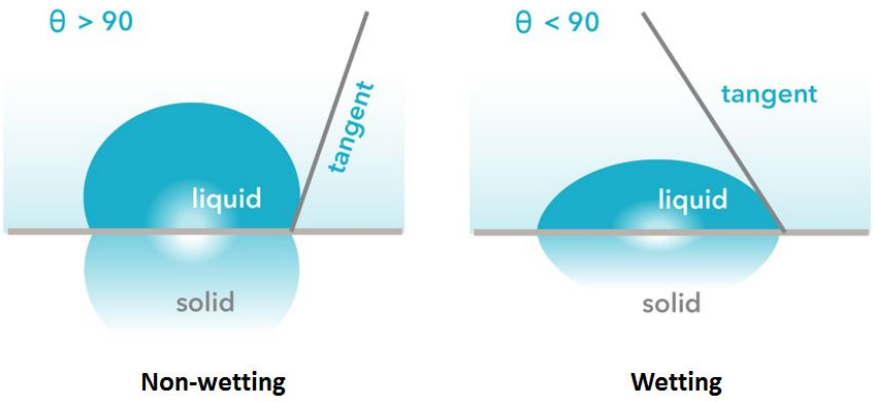

Figure 2.4: Non-wetting and wetting systems.

When the droplet is moving on the solid surface, one can define the dynamic

contact angles, namely the advancing contact angle in the spreading stage and the receding contact angle in the recoiling stage. Advancing and receding contact angles provide the maximum and minimum static contact angles a droplet can have on the solid surface. The difference between them is called the contact angle hysteresis. Contact angle hysteresis arises from the chemical and structural heterogeneity of the surface, solution impurities absorbing on the surface, or rearrangement of the surface by the solvent [74, 115]. Dynamic contact angles and contact angle hysteresis have attracted intensive research interests because of its relevance to the rapid development of hydrophobic and self-cleaning surfaces [35, 66]. Generally there are two methods to measure the dynamic contact angles: changing the volume of the droplet or tilting the surface. Schematic of the volume changing method is shown in Figure 2.5(a). The advancing contact angle is measured by recording the gradually growing droplet (increasing volume) through the injection of liquid from a needle, while the receding contact angle is measured by decreasing the volume. Figure 2.5(b) demonstrates the principle of tilting surface method. The drop is firstly deposited on a horizontal surface and then the surface is gradually tilted. The advancing contact angle is measured at the front three-phase interface just before the moment that the droplet begins to move; the receding contact angle is measured at the back three-phase interface at the same moment.

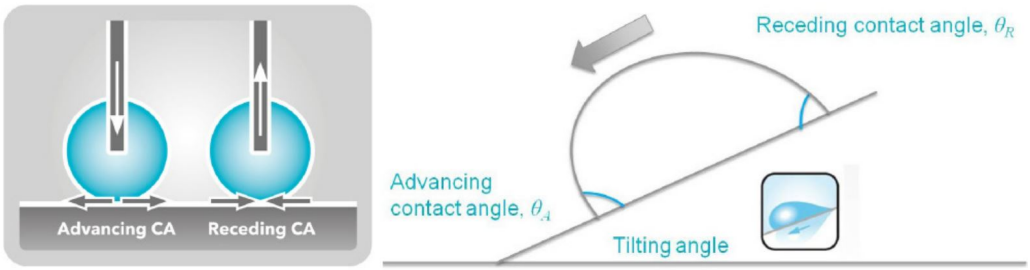

Figure 2.5: Measurement methods of dynamic contact angles: (a)volume changing; (b)tilting surface.

2.1.4 Prediction models of spreading behaviours

Scaling laws

There are a number of empirical, semi-empirical and theoretical models to predict the maximum spreading diameter, D_{m} (or minimum height, h_{m}) reached by the liquid lamella at the end of spreading. Early development of the prediction models considers the algebraic relationships between maximum spreading factor (i.e., normalised maximum spreading diameter with respect to equilibrium drop diameter), $\beta_{\mathrm{m}} = D_{\mathrm{m}}/D_0$ (or minimum height factor, $\xi_{\mathrm{m}} = h_{\mathrm{m}}/D_0$) and a single dimensionless number (e.g., We, Re). These models are commonly referred to as 'scaling law' models. Since the complex flow physics is not considered in these models, their predictive capabilities are limited.

In a theoretical study, Bejan and Gobin presented a model of geometry generation during molten droplet impact based on the constructal law of maximisation of flow access [9]. The maximum spreading factor is proposed as:

$$\beta_{\mathrm{m}} \sim 2\mathrm{Re}^{\frac{1}{2}}. \tag{2.6}$$

Clanet et al. experimentally investigated the drop impact of low-viscosity fluid on super-hydrophobic surface [48]. Resulting from the effective acceleration experienced by the drop during impact, the scaling law is given as:

$$\beta_{\mathrm{m}} \sim \mathrm{We}^{\frac{1}{4}}. \tag{2.7}$$

This model is also observed to be valid when predicting the spreading behaviours on partially wetted surface as long as drop liquids of low-viscosity are used. In the same study, it is proposed that, for a viscous drop, the spreading is expected to be limited by the effect of viscosity, which yields a scaling law as:

$$\beta_{\mathrm{m}} \sim \mathrm{Re}^{\frac{1}{5}}, \tag{2.8}$$

with a corresponding height scale of

$$\xi_{\mathrm{m}} \sim \frac{1}{\mathrm{Re}^{\frac{2}{5}}}. \tag{2.9}$$

Furthermore, Attane et al. suggested that since the $\mathrm{We}^{\frac{1}{4}}$ scaling law works well for the drop fluids with low Ohnesorge numbers, this scaling law should be modified to [3]:

$$\beta_{\mathrm{m}} \sim \mathrm{We}^{\frac{1}{6}} \tag{2.10}$$

at higher Ohnesorge numbers, with a corresponding minimum height factor:

$$\xi_{\mathrm{m}} \sim \frac{1}{\mathrm{We}^{\frac{1}{3}}}. \tag{2.11}$$

Energy balance models

In literature, the method that has been most frequently utilized in order to predict the maximum spreading factor of an impact drop is the energy balance approach. The energy balance equation of an impact drop can be expressed as:

$$\frac{\mathrm{d}}{\mathrm{dt}}(E_{\mathrm{k}} + E_{\mathrm{g}} + E_{\mathrm{s}}) + \dot{W} = 0, \tag{2.12}$$

where E_{k} denotes the kinetic energy carried by the drop, E_{g} is the gravity potential energy, E_{s} is the surface energy, $\dot{W}$ is the rate of total energy loss during drop impact, including viscous dissipation and the energy transmitted to the substrate due to deformation. However, in most of the studies, the energy absorbed by the substrate is often neglected and only the viscous dissipation is considered for the energy loss rate. The viscous dissipation is the most difficult quantity to estimate precisely due to the limited information about the velocity profiles and secondary flows inside the drop. Another difficult quantity to estimate accurately is the surface energy, because the precise calculation of the surface energy at the end of spreading is greatly determined by the accuracy of shape approximation of the spreading drop. Ford and Furmidge proposed an approximation of cylindrical shape of the drop at maximum spreading, which leads to an expression of surface energy as [68]:

$$E_{\mathrm{s}} = \frac{\pi}{4} D_{\mathrm{m}}^2 \sigma (1 - \cos\theta_{\mathrm{a}}), \tag{2.13}$$

where θ_a represents the advancing contact angle. Equation 2.13 can be rewritten using the static contact angle θ_s as [114]:

$$E_s = \sigma[\frac{\pi}{4}D_m^2(1-\cos\theta_s) + \frac{2}{3}\pi\frac{D_0^3}{D_m}]. \tag{2.14}$$

However some authors suggested that the drop shape could be approximated by a spherical cap [8, 131], resulting in an equation of surface energy,

$$E_s = \frac{\pi}{3}D_0^2\sigma[\xi_m^{-1} + 2\xi_m^2 - (\xi_m^{-1} - \xi_m^2)\cos\theta_s] \tag{2.15}$$

as a function of the minimum height factor ξ_m.

Bechtel et al. utilized Lagrangian methods with an assumed flow field and a truncated sphere model to derive a second-order differential equation for the drop height as a function of time [8]. The reduced first-order system from the second-order differential equation is given in dimensionless form as:

$$\begin{aligned} \dot{\xi} &= y, \\ \dot{y} &= -\frac{C(\xi)y^2 + D(\xi)y + E(\xi)}{2A(\xi)}, \end{aligned} \tag{2.16}$$

where a dot represents differentiation with respect to the dimensionless time, $t^* = t(\rho D_0^3/\sigma)^{-1/2}$, $A(\xi)$ expresses the kinetic energy of the drop. The functions $C(\xi)$, $D(\xi)$ and $E(\xi)$ are defined, respectively, by

$$\begin{aligned} C(\xi) = &(\frac{13\xi^4}{36} + \frac{11\xi}{72} + \frac{\xi^{-2}}{72})(\frac{1}{3} + \frac{2\xi^3}{3})^2(\frac{\xi}{3} + \frac{\xi^4}{6})^{-2} \\ &+ (\frac{13\xi^5}{90} + \frac{11\xi^2}{72} + \frac{\xi^{-1}}{36})(\frac{1}{3} + \frac{2\xi^3}{3}) \\ &\times [2\xi^2(\frac{\xi}{3} + \frac{\xi^4}{6}) - (\frac{1}{3} + \frac{2\xi^3}{3})^2](\frac{\xi}{3} + \frac{\xi^4}{6})^{-3}, \end{aligned} \tag{2.17}$$

$$D(\xi) = VIS(\xi^4 - 2\xi + \xi^{-2})(\frac{1}{3} + \frac{2\xi^3}{3})^2(\frac{\xi}{3} + \frac{\xi^4}{6})^{-2}, \tag{2.18}$$

$$E(\xi) = 2[4\xi - \xi^{-2} - ST(2\xi + \xi^{-2})], \tag{2.19}$$

in which VIS and ST are introduced dimensionless viscosity and surface tension parameters respectively:

$$VIS = \frac{\sqrt{\pi}}{12}\mathrm{Oh}^{1/2}, \tag{2.20}$$

$$ST = -\cos\theta_s. \tag{2.21}$$

The initial conditions for Equations 2.16 are provided by

$$\begin{aligned} \xi|_{t^*=0} &= 1, \\ y|_{t^*=0} &= -\mathrm{We}^{1/2}. \end{aligned} \tag{2.22}$$

The system (Equations 2.16 - 2.21) was rewritten by Attane et al. in a more concise way [3]:

$$\begin{aligned} &\frac{1}{12}\frac{\mathrm{d}}{\mathrm{d}t^*}[(\frac{1+2\xi^3}{2\xi+\xi^4})^2(\frac{\xi^{-1}}{9}+\frac{11\xi^2}{18}+\frac{26\xi^5}{45})(\frac{\mathrm{d}\xi}{\mathrm{d}t^*})^2] \\ &+\frac{\mathrm{d}}{\mathrm{d}t^*}[\frac{1}{3}(\xi^{-1}+2\xi^2-(\xi^{-1}-\xi^2)\cos\theta_s)] \\ &+\frac{\Lambda}{18}\mathrm{Oh}[\frac{(\xi^3-1)^2(1+2\xi^3)^2}{\xi^4(2+\xi^3)^2}](\frac{\mathrm{d}\xi}{\mathrm{d}t^*})^2 = 0, \end{aligned} \tag{2.23}$$

where

$$\Lambda = \sqrt{\pi}\mathrm{Oh}^{-1/2}. \tag{2.24}$$

However, in the same study it was pointed out the expression for Λ in Equation 2.24 was incorrectly derived due to a sing error in Equation 2.17 and a more precise empirical expression was proposed as [3]:

$$\Lambda = 23\mathrm{Oh}^{-1/2}. \tag{2.25}$$

Equating the kinetic and surface energies at the impact moment of the drop to the sum of the kinetic energy, surface energy and viscous dissipation energy at the end of the spreading phase (i.e., maximum spreading), Chandra and Avedisian derived an energy balance equation based on the approximation of a cylindrical shape of the drop at maximum spreading [44]:

$$\frac{3}{2}\frac{\mathrm{We}}{\mathrm{Re}}\beta_m^4 + (1-\cos_a)\beta_m^2 - (\frac{1}{3}\mathrm{We}+4) \approx 0. \tag{2.26}$$

The expression of total viscous dissipation energy, W during spreading was proposed as:

$$W = \int_0^{t_c}\int_V \phi \mathrm{d}V\mathrm{d}t \approx \phi V t_c, \tag{2.27}$$

where ϕ is defined as the dissipation function, given by

$$\phi = \mu(\frac{\partial v_i}{\partial x_j} + \frac{\partial v_j}{\partial x_i})\frac{\partial v_i}{\partial x_j} \approx \mu(\frac{U}{h})^2 \tag{2.28}$$

and U is the impact velocity, h is the height of the lamella. t_c in Equation 2.27 is approximated by assuming it to be the time taken for drop height h to decrease from the maximum value D_0 to zero:

$$t_c = \frac{D_0}{U}. \tag{2.29}$$

Under the assumption of a cylindrical shape of the drop at end of spreading, the volume V can be written as:

$$V = \frac{1}{4}\pi D_m^2 h. \tag{2.30}$$

Combining Equations 2.27 - 2.30, the viscous dissipation energy W can be estimated as:

$$W = \frac{1}{4}\pi\mu(\frac{U}{h})D_0 D_m^2. \tag{2.31}$$

In a following experimental and numerical investigation by Pasandideh-Fard et al. [123], the energy balance model proposed by Chandra and Avedisian (Equation 2.26) was observed to overpredict the values of D_m up to 40% for low-viscosity droplets. It was suggested that the poor performance of this model is due to the incorrect estimate of the value of characteristic length (h) in the viscous dissipation term (Equation 2.28). Instead of the lamella height h, the boundary layer thickness δ is proposed as the characteristic length (L), and the viscous dissipation function (ϕ) can be rewritten by

$$\phi \approx \mu(\frac{U}{L})^2 = \mu(\frac{U}{\delta})^2. \tag{2.32}$$

Under the assumption of an axisymmetric stagnation flow inside the impacting droplet, an analytical expression for the boundary layer thickness (δ) in Equation 2.32 is obtained:

$$\delta = 2\frac{D_0}{\sqrt{\mathrm{Re}}}. \tag{2.33}$$

Using the approach described above, a simple expression of the maximum spreading factor is derived:

$$\beta_{\mathrm{m}} = \sqrt{\frac{\mathrm{We} + 12}{3(1 - \cos\theta_{\mathrm{a}}) + 4(\mathrm{We}/\sqrt{\mathrm{Re}})}}. \tag{2.34}$$

Based on the energy balance model by Chandra and Avedisian [44], Mao et al. developed a more broadly applicable model through a number of modifications [114]. First, instead of the dynamic advancing contact angle (θ_{a}), the static contact angle (θ_{s}) was used to estimate the surface energy of the droplet disk at maximum spreading due to its unique relationship with the surface tensions (Equation 2.14). Second, it was pointed out that, for highly viscous liquids, the boundary layer thickness δ obtained from the analytical solution of a stagnation-point flow is actually larger than the height of the droplet disk: $\delta > h$. Thus it was suggested that the boundary layer thickness δ should be defined separately for low-viscosity ($\delta < h$) and high-viscosity regimes ($\delta > h$), and a theoretical viscous dissipation model was proposed for two regimes. A general viscous dissipation model was obtained empirically by fitting the experimental data of both low-viscosity and high-viscosity liquids to a model structure, which led to a general maximum spreading model:

$$[\frac{1}{4}(1 - \cos\theta_{\mathrm{s}}) + 0.2\frac{\mathrm{We}^{0.83}}{\mathrm{Re}^{0.33}}]\beta_{\mathrm{m}}^3 - (\frac{\mathrm{We}}{12} + 1)\beta_{\mathrm{m}} + \frac{2}{3} = 0. \tag{2.35}$$

2.1.5 Outcomes of drop impacts on solid surfaces

Based on the morphologies of drop impacts on solid surfaces, the impact outcomes can be divided into six different categories as shown in Figure 2.6 [136]. A detailed description of the distinguishing features of each outcome is given below.

Deposition. The drop stays attached to the solid surface during the entire impacting process without any types of breakup.

Prompt splash. Prompt splash is only observed when drops are impacting on rough surfaces. It is characterised by the generation of numerous droplets at

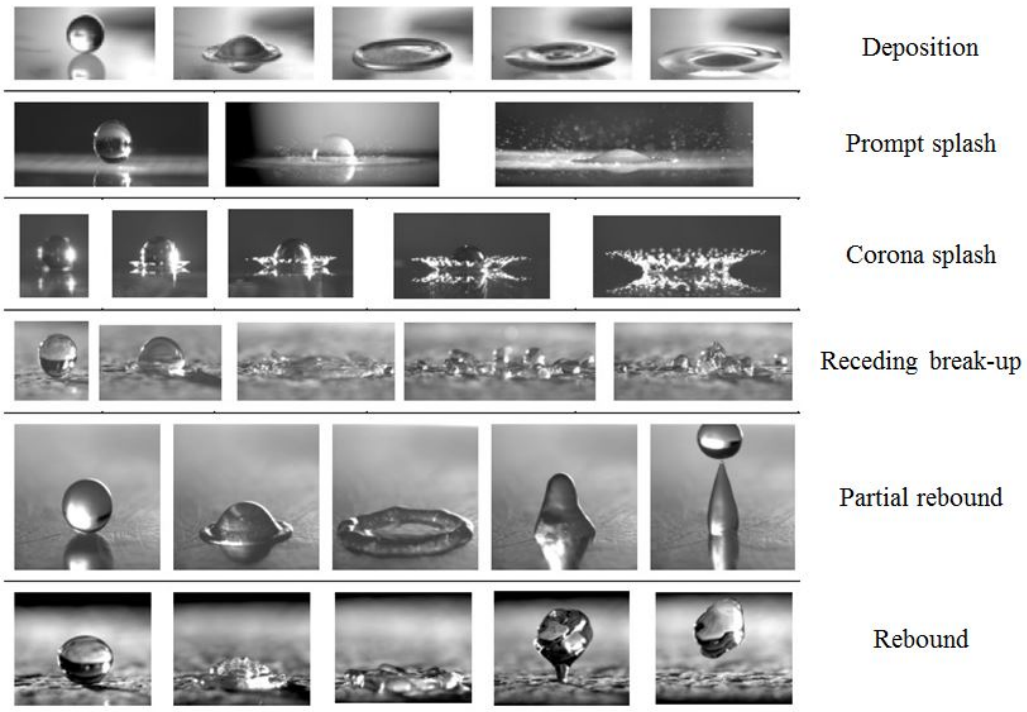

Figure 2.6: Six different outcomes of impact drops. (adapted from [136])

the moving contact line during early spreading and is obviously affected by the surface structure.

Corona splash. Corona splash is characterised by a liquid corona detached from the solid surface with droplets formed around the rim. Despite the fact that corona splash often occurs in drop impacts on liquid films, it can also be observed on solid surfaces. This happens in a later stage of impact process and is well investigated in literatures [160].

Receding breakup. The receding breakup is completely a wetting phenomenon. After the spreading drop reaches its maximum diameter, it starts to recoil as the dynamic contact decreases. Some smaller droplets are left behind if the dynamic contact angle decrease to the limiting value of zero [33].

Partial rebound. The rebound behaviour of drops impacting on solid surface mainly depends on two parameters: the impact Weber number (i.e., ratio of kinetic energy to surface energy) and the receding contact angle (i.e., wettability of the surface). A receding phase may follow the maximum spreading provided

both parameters are sufficiently high. If the receding contact angle is not very high, the drop may break up into two (or more than two) droplets, with one (or more than one) bouncing off the surface and another attaching the surface. This is referred as partial rebound.

Rebound. As described in the *partial rebound* section, if the receding contact angle is high enough, the entire drop may be observed to bounce off the surface.

2.2 Drop impact on heated surfaces

The present research work focuses on the experimental investigation of drop impact phenomena, where either the drop, or the surface or both, are made of complex fluids or materials, which exhibit non-linear mechanical behaviour. These include: drop impact on viscoplastic surface, drop impact on elastic surface and drop impact on heated surface, where drops are separated from the surface by a thin vapour film, which is known as the Leidenfrost phenomenon. Drop impacts on heated surface in the Leidenfrost regime can be regarded as a model experiment without wetting effects due to the creation of a thin elastic vapour film which acts like a 'cushion' between the drop and the surface upon impact.

2.2.1 Impact morphology

The collision of droplets with hot surfaces is observed everywhere in our daily lives as well as in various industrial applications, including spray cooling [37], fuel injection in combustion engines [116], fire suppression [83, 113] and spray quenching [11]. When a droplet makes contact with a surface which is heated far above the boiling point of the liquid. The liquid at the contact point is rapidly heated above the saturation temperature and the temperature of the solid surface drops sharply [144]. Boiling only occurs at the liquid/surface interface due to high local temperature since the temperature profile in the liquid decreases dramatically away from the interface. There are two kinds of bubble nucleation

in boiling: heterogeneous nucleation and homogeneous nucleation [4, 34]. If the liquid temperature is below the superheat limit, the heterogeneous boiling mechanism dominates, in which the bubbles are generated at pre-existing nuclei such as cavities, defects etc. on the solid surface [34]. Homogeneous nucleation occurs when temperature is above the limit of superheat, where nuclei are spontaneously generated in the liquid due to molecular density fluctuations associated with rapid phase change from liquid to vapour [34]. If the liquid is heated abruptly up to the limit of superheat, both heterogeneous nucleation and homogeneous nucleation happen, which leads to the nucleation of numerous vapour bubbles. These rapidly generated bubbles grow and coalesce to form a very thin vapour film between the liquid and the solid surface. In conclusion, the morphology of the droplet is strongly affected by these boiling phenomena which depend on the temperature of the solid surface. Besides the influence of surface temperature, the morphology of drop impacts on heated surfaces is also affected by other impact parameters such as Weber, Reynolds numbers etc., which has been discussed in Section 2.1.1.

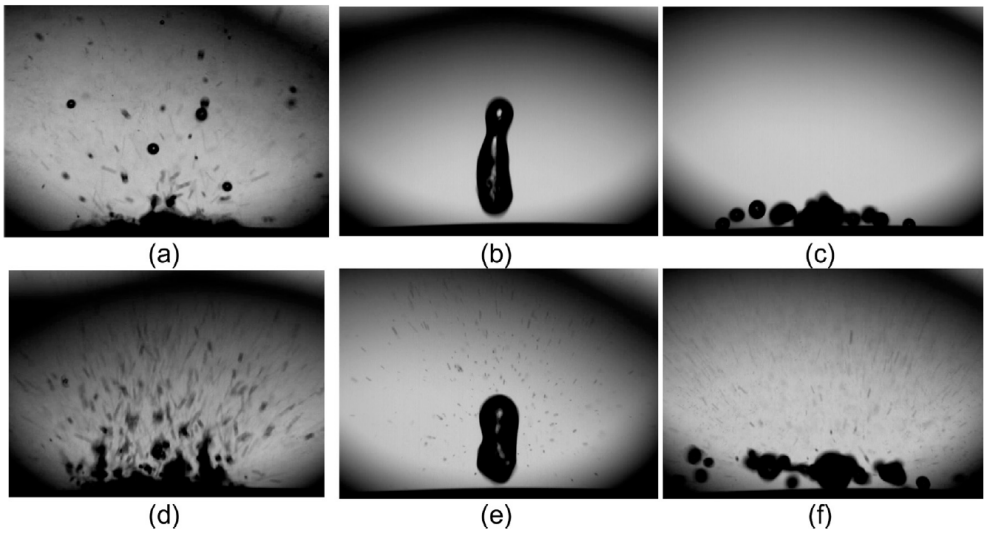

Figure 2.7: Different impact outcomes on heated surfaces: (a, d), secondary atomization; (b), rebound; (c), breakup/splashing; (e), rebound with secondary atomization; (f), splashing with secondary atomization (adapted from [19]).

Figure 2.7 shows different possible types of impact outcomes of a single droplet

on heated surfaces, including secondary atomization (numerous small droplets burst out from the liquid surface); rebound (entire drop bounces off the heated surface); rebound with secondary atomization; breakup/splashing (entire drop breaks up into small droplets); splashing with secondary atomization.

2.2.2 Impact regimes

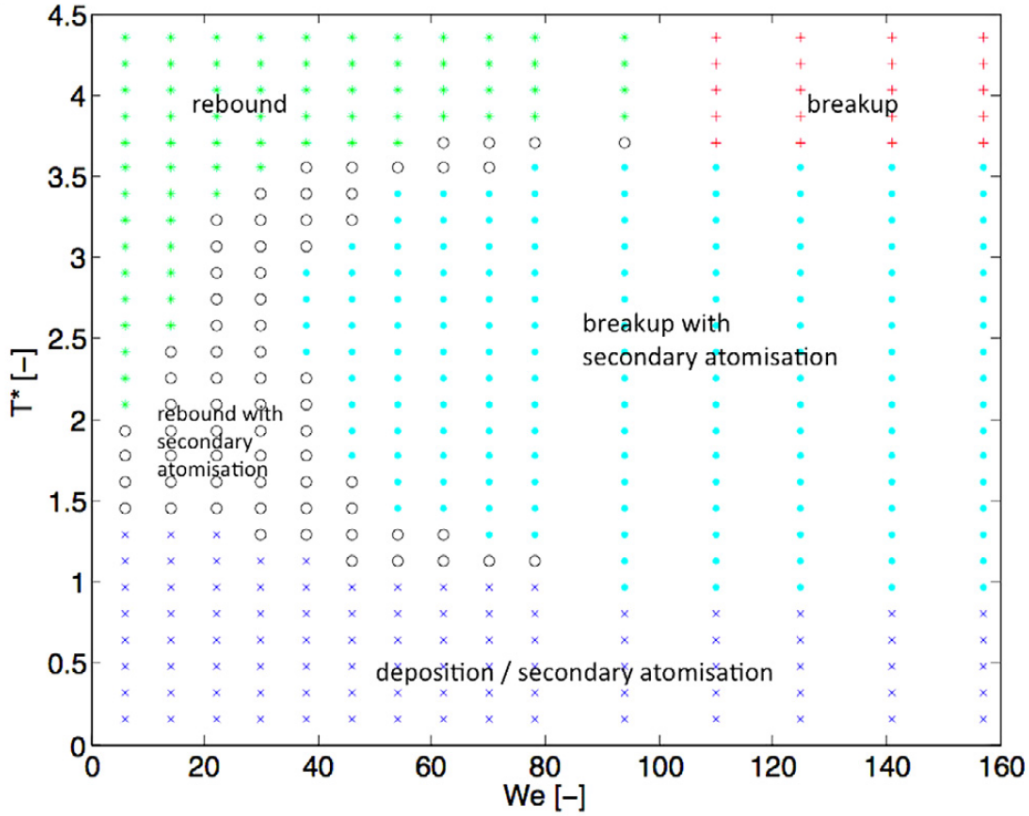

Figure 2.8: Impact regimes of drop impacts on heated surfaces (adapted from [19]).

Temperature of the solid surface, impact velocity and fluid properties of the droplet play important roles in the morphology of drop impacts on hot surfaces. Surface temperature affect the local boiling phenomena of the liquid. High surface temperature enables fast bubble generations and evaporation at the interface between liquid and solid surface. If the evaporation rate is high enough a stable thin vapour film can be formed, which separates the liquid from the solid surface and reduces heat transfer rate. The formation of a stable vapour film is essential

to the dynamic Leidenfrost phenomenon, which will be discussed in later sections. The impact velocity indicates the kinetic energy carried by the droplet before impact. The breakup of the impacting drop is the result of the competition between kinetic energy and surface energy, which can be expressed as the impact Weber number. Smaller satellite droplets are generated when the local dynamic pressure is over the Laplace pressure at the liquid/gas interface. Therefore a map with surface temperature and Weber number as variables can be created to characterised the behaviours of impacting drops on heated surfaces in different regimes.

Figure 2.8 displays an example of the drop impact regimes as a function of the Weber number and the dimensionless wall temperature (T^*) [19]. The dimensionless wall temperature is defined as:

$$T^* = \frac{T_S - T_{sat}}{T_L - T_{sat}}, \tag{2.36}$$

where T_S denotes the wall temperature, T_{sat} the saturation temperature, and T_L represents the Leidenfrost temperature of a sessile drop on polished aluminium. If the Weber number is beyond a critical threshold, the capillary forces and viscous effects can no longer maintain the integrity of the drop so that it breaks up into smaller droplets (breakup/splashing). The increase of the wall temperature will lower the critical Weber number for splashing since the drop receives more energy and becomes more unstable during the impact process [133].

For intermediate values of the wall temperature and of the Weber number (as shown by the filled blue circles and open black circles in Figure 2.8), one can observe secondary droplets bursting from the drop surface [119, 151], which is often referred as secondary atomisation. The size of the droplets can be very small compared to the major drop.

For high wall temperatures and low Weber numbers (as indicated by the filled green circles in Figure 2.8), bouncing back of the droplet off the surface occurs due

to the creation of a continuous vapour film between the drop and surface upon impact [151]. This phenomenon is known as 'dynamic Leidenfrost phenomenon' [101]. The impact morphology of Leidenfrost drops is relatively simple: upon impact, the drop spreads over the vapour film in a short time (about 5 ms); after maximum spreading, it will recoil under the action of surface forces, to minimize the surface energy, and eventually bounce off the surface if there is sufficient kinetic energy at the end of the recoil. Bouncing Leidenfrost drop impact experiment represents a unique model system to investigate the effect of fluid properties on the impact behaviour without the influence of drop-surface interactions due to the existence of the vapour film. Whilst there is extensive literature on Newtonian Leidenfrost drops [14, 50, 73, 81, 124, 133, 151, 152, 158], the number of studies about non-Newtonian drops in the Leidenfrost regime is very limited [17, 18, 30].

Other examples of maps of impact regimes based on wall temperature and impact Weber number can also be found in previous studies [5, 99]. The principles are similar and they are all essentially qualitative. The impact regimes are approximately defined and no analytical criteria for transition boundaries are available. Recently more precise criteria for transitions between different regimes have been achieved by utilizing K-number and effective wall temperature [42]. If the wall temperature is lower than the Leidenfrost temperature, droplets partially make contact with the solid surface due to an unstable vapour film. In order to take the local cooling of the wall surface by the droplets into account, the wall temperature is replaced by the effective contact temperature, which has been proposed to characterise the secondary atomization of impacting droplets [51]:

$$T_{eff} = \frac{\varepsilon_w T_w + \varepsilon_l T_l}{\varepsilon_w + \varepsilon_l}, \tag{2.37}$$

where T_w and T_l denote the wall temperature and droplet temperature before impact respectively. $\varepsilon_w = \sqrt{k_w \rho_w C_{p,w}}$ and $\varepsilon_l = \sqrt{k_l \rho_l C_{p,l}}$ correspond to the thermal

effusivities of the materials of solid wall and drop liquid. Equation 2.37 originates from the conservation of the heat flux at the interface between the droplet and the wall when neglecting any thermal contact resistance [140]. Instead of impact Weber number, the dimensionless number $K = WeOh^{-2/5} = We^{4/5}Re^{2/5}$, which has been used successfully to describe the transition between from deposition to splashing regimes for drop impacts on thin liquid films [49], has been adopted as the threshold for splashing to account for viscous effects. Based on these two parameters, an example of the $T^* - K$ diagram clearly describing three regimes (deposition, rebound and splashing) is shown in Figure 2.9. Note here the effective wall temperature is nondimensionalised ($T^* = (T_{eff} - T_b)/(T_{Leid} - T_b)$) by the difference between the boiling temperature, T_b and Leidenfrost temperature, T_{Leid}.

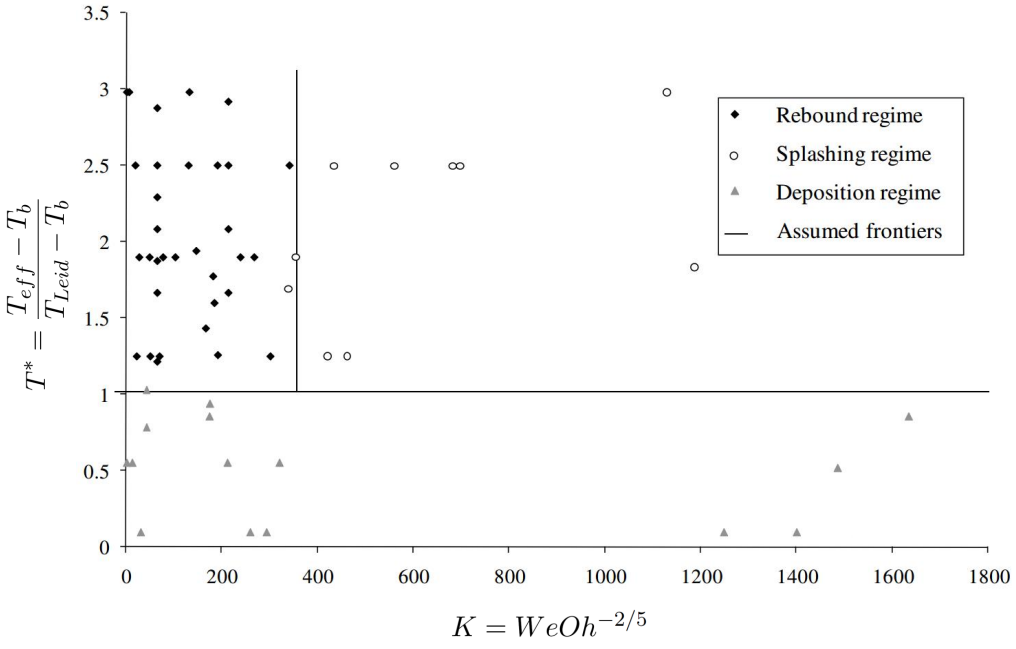

Figure 2.9: Example of impact regimes in $T^* - K$ diagram. (adapted from [42])

In addition, experimental investigations have shown that dry impact (Leidenfrost regime) may occur at a temperature much lower than the Leidenfrost

temperature which has long been taken as the criterion to classify impact regimes due to the squeeze film effect [152]. Besides, contrary to the constant value of the boiling temperature which only depends on the properties of the liquid, it has been shown the surface roughness is able to decrease the Leidenfrost temperature due to the increased number of nuclei for local boiling [12]. If the drop is moving towards the wall with very high momentum, the vapour film needs to be thicker to avoid the direct contact between liquid and solid surface, which causes an increase of the Leidenfrost temperature [133]. In short, the pursuit for more accurate mapping of impact regimes is a never-ending task.

2.2.3 Disk model for Leidenfrost drops

Rein proposed a 'disk model' which accounts for the contribution of elasticity of the vapour film to the rebound behaviours of Leidenfrost drops [133]. In this model, the reflection of an impacting drop from a heated surface is compared to the scenario of the bouncing back of an elastic plate impinging on a solid wall. In the case of an elastic plate impacting on a wall, the physical mechanism for the reflection is based on the deformation of the elastic plate, which stores a part of the kinetic energy as elastic energy during impact. In the next stage, the elastic energy is released and converted back to the kinetic energy as the deformed plate recovers its original shape, which leads to the bounce back of the impinging plate. The deformation of the plate is resulted from the high pressure of the vapour film formed between the plate and the wall, which provides upward forces to the plate and finally causes the reversal of the momentum.

In order to simplify the modelling of the physics, Rein made a number of assumptions on which the disk model is based [133]. Here some important assumptions are listed below.

• The radius and thickness of the disk are constant, thus the hydrodynamics of the drop is not considered.

• The entire drop liquid is at the saturation temperature, so the heat transfer inside the drop is not considered.

• The evaporation rate and the heat transfer between the drop and the wall surface are considered to be spatially uniform (i.e., do not change in the radial direction).

• A one-dimensional, inviscid and incompressible flow is assumed for the radial flow of the vapour in the gap between the drop and the surface.

Radius of the disk

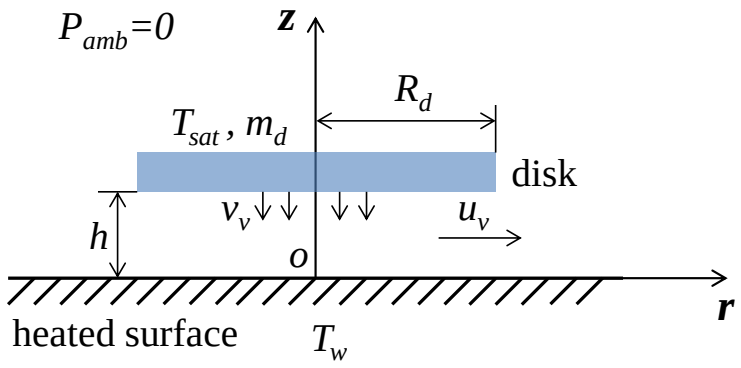

Figure 2.10: Schematic of the disk model.

The schematic of the disk model is shown in Figure 2.10. The radius of the disk is derived from an energy balance approach which takes into account the kinetic energy, the surface energy and also the energy loss during impact. The energy loss is obtained by subtracting the kinetic energy after reflection from the kinetic energy before impact:

$$E_{loss} = E_{\mathrm{k}}^{i} - E_{\mathrm{k}}^{r}, \tag{2.38}$$

where $E_{\mathrm{k}}^{i} = 4\pi/3R_0^3\rho v_i^2/2$ and $E_{\mathrm{k}}^{r} = 4\pi/3R_0^3\rho v_r^2/2$, and v_i and v_r are the impact velocity and reflection velocity respectively. The disk radius is taken from the radius reached by the liquid lamella at maximum spreading: $R_d = D_{\mathrm{m}}/2$, and it is assumed that the kinetic energy at the end of spreading is zero. For the sake

of simplicity, the energy loss is assumed to happen only in the spreading stage of the whole impact process. Consequently, considering the moment before impact and the moment at maximum spreading, an energy balance equation is given by:

$$E_{\mathrm{k}}^{i} + E_{\mathrm{s}}^{i} - E_{loss} = E_{\mathrm{s}}^{d}, \tag{2.39}$$

where $E_{\mathrm{s}}^{i} = 4\pi R_0^2\sigma$ represents the surface energy of the impacting drop and $E_{\mathrm{s}}^{d} = 2\pi R_d^2\sigma$ denotes the surface energy of the disk. A parameter called the reflection ratio is defined as the ratio of the reflection velocity to the impact velocity:

$$\alpha = v_r/v_i. \tag{2.40}$$

Combing Equations 2.38, 2.39, 2.40 and the definition of Weber number $We = \rho u_i^2 2R_0/\sigma$, the normalized disk radius with respect to the equilibrium drop radius can be solved as:

$$\frac{R_d}{R_0} = \sqrt{\frac{\alpha^2}{6}We + 2}. \tag{2.41}$$

In the disk model, the value of α is approximated by 0.5 based on the experimental results from [2].

2.3 Drop impact onto liquid surfaces (deep pools)

Early investigations on the drop impacts on liquid surfaces are mainly limited to simple Newtonian fluids [62, 108, 138], such as water, ethanol and glycerol solutions etc. Some researchers have investigated the effect of the depth of the liquid pool (close or smaller than the drop diameter) on the splashing behaviours of impact droplets [107]. However in most cases the liquid pool is assumed to be deep, which means the thickness of the liquid layer does not affect the impact process of drops. Although in some papers the depth of the liquid pool may not be explicitly mentioned, it is clear from the context that a deep liquid layer has been considered. In the present study, the drop impacts onto liquid pools have been extended to a special type of non-Newtonian fluids called visoplastic (or yield-stress) fluid.

2.3.1 Impact morphology

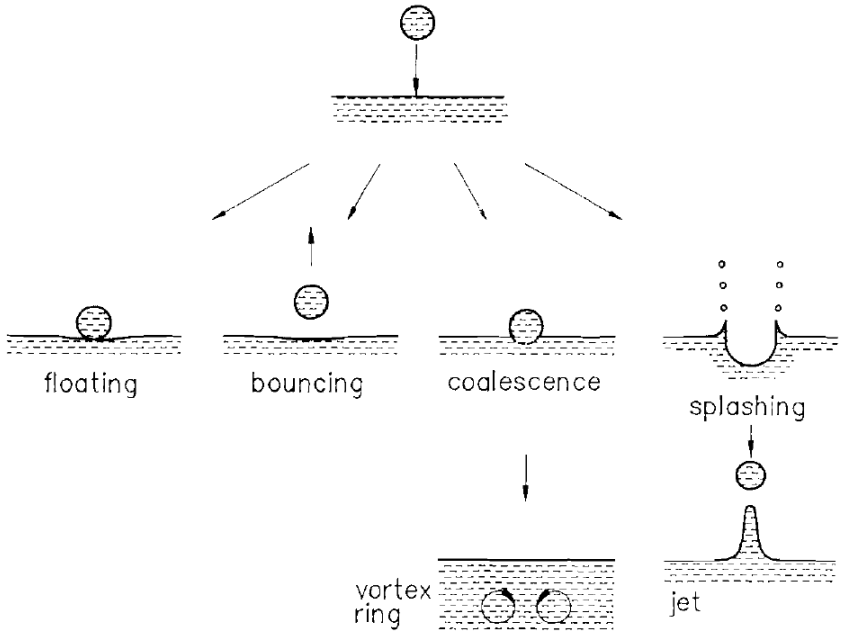

Figure 2.11: Outcomes of drop impacts onto deep pools. (adapted from [131])

The outcomes of the collisions of droplets with liquid pools can be classified as floating, bouncing, coalescence and splashing. The schematic of all the scenarios is shown in Figure 2.11. Sometimes the drops may be observed to float or bounce off the liquid surface. The drops can stay on the surface for several seconds and finally merge with the liquid pool. It has been shown that the cleanliness of the liquid surface is crucial to produce such floating behaviours [134]. However sometimes the drops disappear quickly when they make contact with the liquid surface without any floating or bouncing. If the impact Weber number is low ($We \sim 1$), the liquid surface is only slightly perturbed, with the formation of small crater, and no secondary droplets are generated during the entire impact process. This phenomenon is usually referred to as 'coalescence'; it is often followed by the formation of vortex rings which travel downwards below the surface. If the Weber

number is sufficiently high ($We > 60$), the surface experiences a large deformation as a crater with a radius which can be an order of magnitude larger than the drop radius is formed. A cylindrical liquid sheet rises at the circumference of the crater, which is usually referred to as 'crown formation' in literatures. After the crater and liquid sheet collapse, a central jet (Worthington jet) may be formed at the centre of the crater. The generation of the central jet has been suggested as the criterion for splashing by some authors [138]. Sometimes secondary droplets are ejected from the rim of the crown and/or from the central jet.

2.3.2 Criteria of splashing

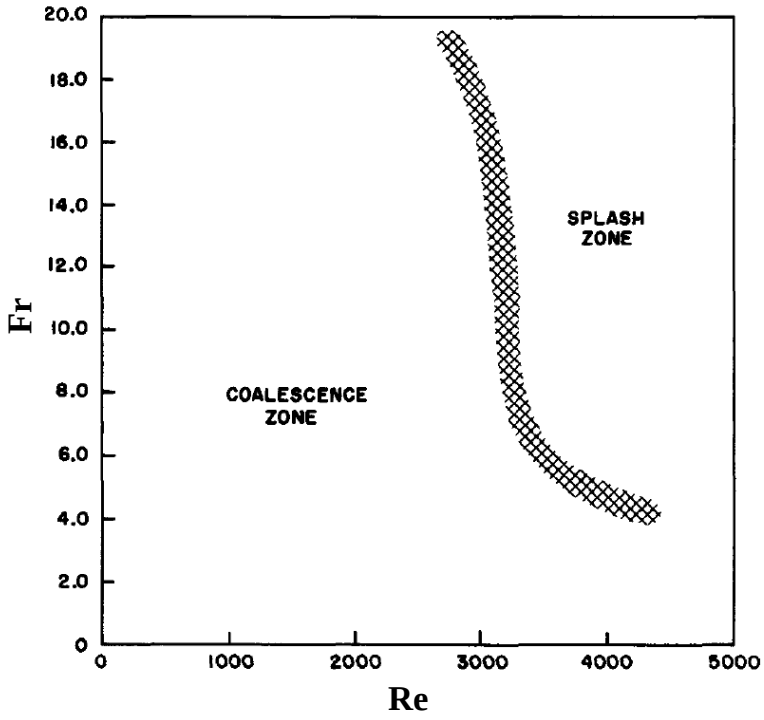

Figure 2.12: Different impact zones based on the combination of Froude number and Reynolds number. (adapted from [138])

The transition from coalescence to splashing in drop impacts onto deep pools has attracted the interest of many researchers. Besides the dimensionless numbers mentioned in Section 2.1.1, another important dimensionless number which

has been used frequently to characterised the impact behaviours is the Froude number:

$$Fr = \frac{v_i}{\sqrt{gD_0}}, \tag{2.42}$$

where g denotes the gravitational acceleration. It compares the inertial forces with the external forces, namely gravity. Gravity must be taken into account because of its influence on the crater formation, crown formation and central jet during the impact process. In early experimental investigations, the combination of Froude number and Reynolds number has been used to characterise the transition from coalescence to splashing [138]. The map showing different impact regimes (coalescence and splashing) based on these two numbers is plotted in Figure 2.12, from which it is clear that the transition boundary between coalescence and splashing regimes is not sharp but rather defines a region where either impact outcome may occur. In a previous numerical investigation, it has been found that splashing can occur in the coalescence zone [86, 87]. However, some authors point out this surprising behaviour is observed when surface tension is neglected in the numerical simulations [41]. For this reason, the Weber number could also play a role in the splashing criterion. In a following experimental study on the splashing limit, a single dimensionless number (Weber number) was found to characterise the splashing behaviour successfully [92]. The Weber number can be defined as the ratio of two time scales ($We = \lambda_s/\lambda_c$): a characteristic time scale of surface tension effects, $\lambda_s = \sqrt{\rho D_0^3/\sigma}$ and a convective time scale, $\lambda_c = D_0/v_i$. (Note: normally the Weber number takes the form of the square of this ratio in literatures: $We = (\lambda_s/\lambda_c)^2$.) If $\lambda_c \gg \lambda_s$, which means the convective time scale is much longer than the time scale of surface tension effects, the surface tension can easily deform the drop into a vortex ring without splashing. On the contrary when $\lambda_s \gg \lambda_c$, the convective time scale is so short that the surface tension is not able to deform the drop. Then splashing occurs. Drop impact experiments onto liquid pools have been conducted using water and mercury (with a surface

tension value one order of magnitude greater than water) to validate the proposed criterion for slashing in terms of Weber number [92]. It was found that the critical Weber number for splashing is almost independent of the Froude number: $We_{crt} = v_i\sqrt{\rho D_0/\sigma} \cong 8$, as shown in Figure 2.13. (Note: in the more common form of We it should be $We_{crt} = \rho D_0 v_i^2/\sigma \cong 64$.) However, viscosity effects are not taken into account if one uses only the Weber number to characterise the splashing behaviours. Moreover, it was shown that splashing is more likely to happen at low kinematic viscosities, and coalescence occurs when the kinematic viscosity is high [149]. As a result, the critical Weber number can be a function of the Reynolds number.

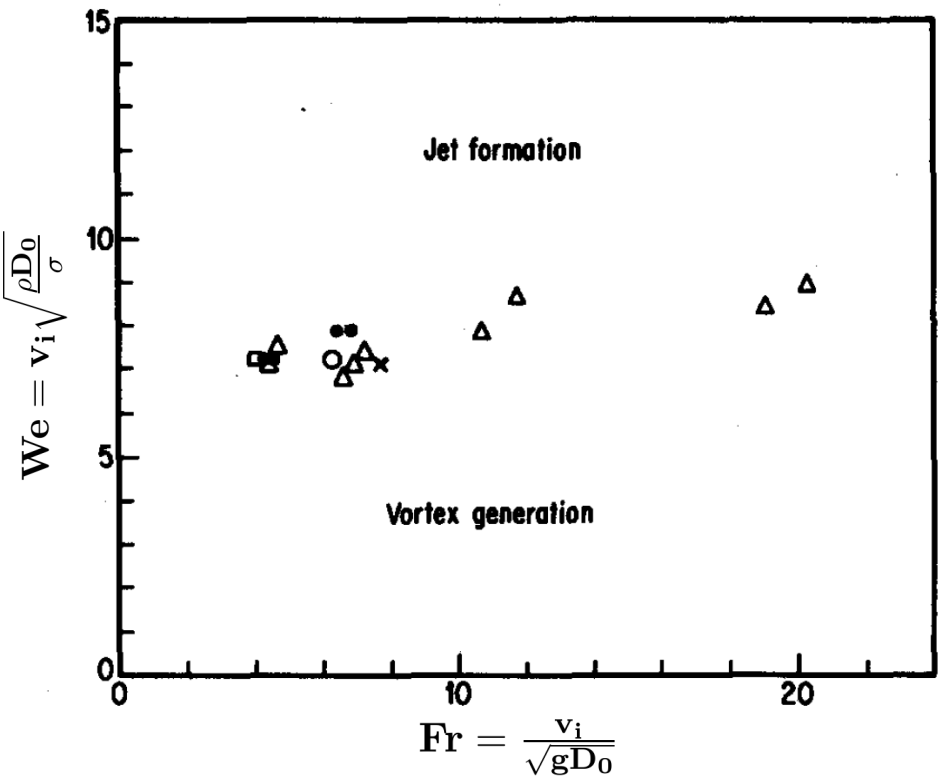

Figure 2.13: Critical Weber number for splashing as a function of Froude number. (adapted from [92])

2.3.3 Crater formation model

The interactions between impacting drops and liquid layers are related to various engineering applications, including secondary atomization by collision with a wall, spray deposition, coating, and spray cooling. In these applications, the crater formation by drop impact plays an important role because of its relation to several basic impacting outcomes (e.g., maximum spreading, penetration depth, splashing behaviour etc.). The underwater noise of rain generated by crater formation during drop impact enables the detection and characterization of rain over the oceans by remote acoustic sensors [128]. An experimental study on the impact of a water drop onto a water surface using high-speed imaging shows that the crater formation and impact drop behaviour depend on both the Weber and the Froude numbers [102]. The impact of a drop on liquid surface (water & aqueous glycerol solution) has been studied experimentally and theoretically in the region of fully developed splashing [65]. A theoretical model for the crater evolution is presented and it is found that the maximum crater radius and the crater collapse time depend both on the Froude number and on the (dimensionless) capillary length.

More recently, an experimental and theoretical investigation on the crater formed by impact of a single drop onto a semi-infinite target of the same liquid led to a theoretical model which is able to predict the temporal variation of the crater depth for various impact parameters [29]. Basically, the whole process of crater evolution is divided into two phases, illustrated in Figure 2.14 (note the dimensionless time $\lambda = v_i t/D_0$, is used here). During the first stage ($\lambda < \lambda^*$), the material interface between the drop and the substrate is not visible and the penetration velocity of the crater is found to be $0.44v_i$, which is derived from a modified quasistationary model of the initial drop penetration. Thus, the dimensionless crater depth, Δ, grows linearly with respect to the dimensionless time: $\Delta = 0.44\lambda$. During the second phase ($\lambda > \lambda^*$), the shape of the crater can be

well approximated by the shape of the drop/target interface due to a very thin residual liquid layer of the drop material on the crater surface. The evolution of the crater is obtained from the balance of stresses at the crater interface, accounting for inertia, gravity, and surface tension. In the present work, this model is adapted to viscoplastic fluids and compared with experimental results.

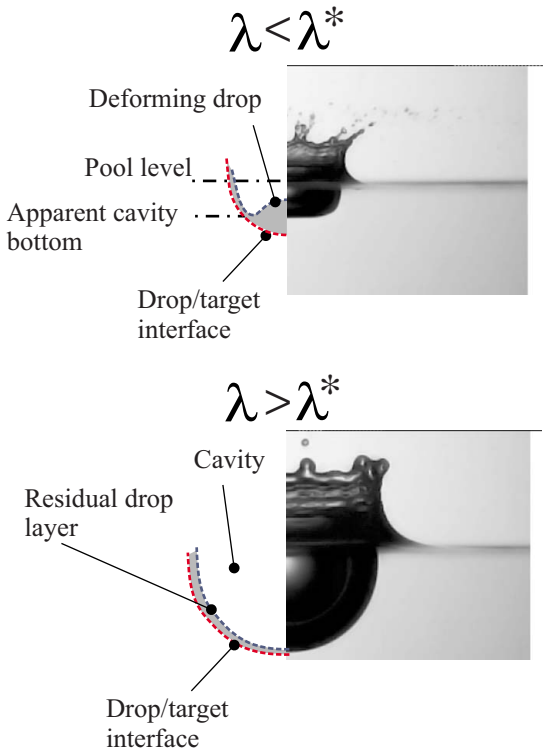

Figure 2.14: Two phases of crater evolution. (Adapted from [29])

2.4 Drop impact on flexible surfaces

The role of the compliance of flexible substrates is important to understand since it is involved in various application such as the delivery of pesticides on leaves [142] and the spray cooling of flexible surfaces. Also it is suggested that the use of a compliant coating on some materials could reduce the damage of erosion processes caused by drop impacts [67]. One of the most important effect of the substrate flexibility is the partial absorption of kinetic energy of the impacting drop by the substrate, which may influence the outcome of drop impact (e.g.,

splashing, rebound).

2.4.1 Elastic surfaces

Wetting ridge

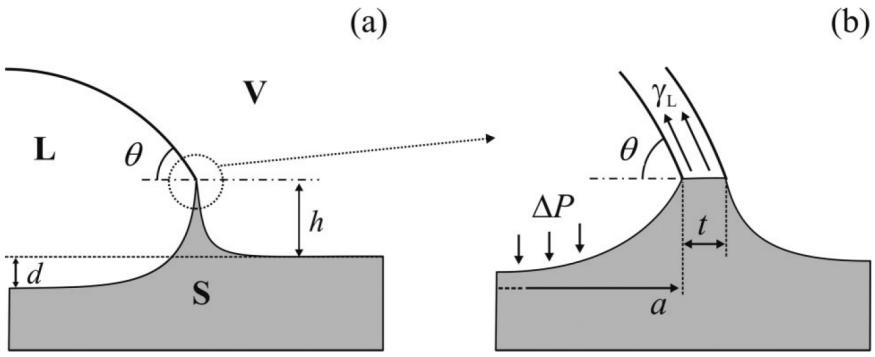

Figure 2.15: Schematic of the formation of wetting ridge at the TPCL: (a) L, S and V represent the liquid, solid and gas phases respectively. θ is the equilibrium contact angle and h the height of the ridge; (b) Magnified schematic of the contact point at the TPCL. (Adapted from [127])

The majority of the early research works on the role of the substrate compliance in drop impact considers an elastic substrate. It has been shown that the surface tension component of the drop liquid perpendicular to the surface of elastic substrate can significantly influence the wetting behaviours at the three-phase contact line (TPCL) [63, 94, 126, 127, 147]. This is to due to the formation of a 'wetting ridge' at the TPCL (see Figure 2.15). The scale of this ridge ranges from tens of nanometers to several micrometers. A more recent study reports that the formation of 'wetting ridge' associated with the viscoelastic nature of the substrate is able to slow the motion of the TPCL, which is referred as the 'visoelastic braking' effect [45].

Influence on impact outcomes

Compared to rigid surface, elastic surface allows much higher transformation rate of kinetic energy of the drop to the elastic energy of the substrate due to the deformation of the surface. This could considerably reduce the inertial forces

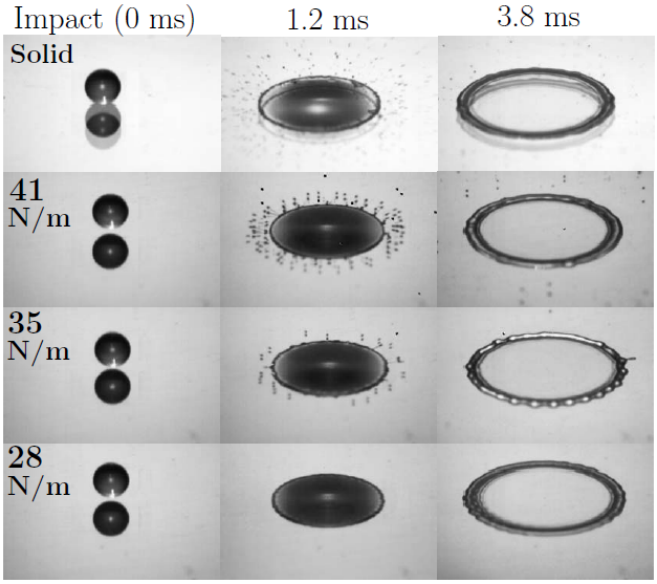

Figure 2.16: Images of drop impact (D_0 = 2.02 mm, v_i = 2.5 m/s) on membranes with different tensions. (Adapted from [125])

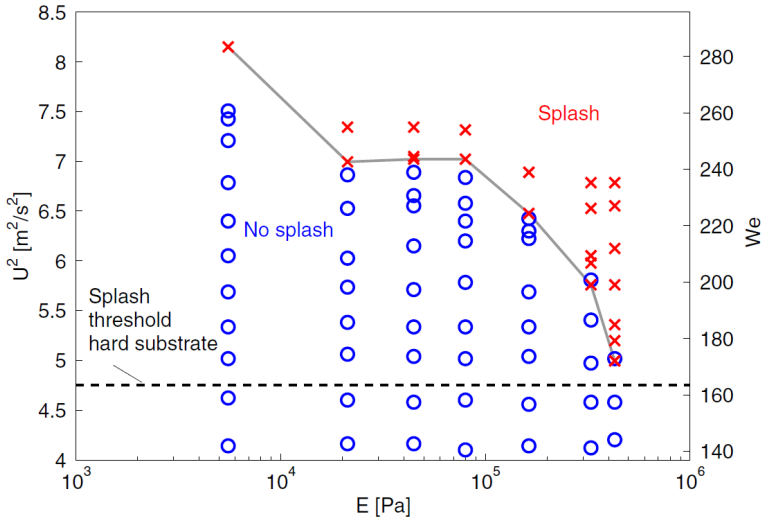

Figure 2.17: Splashing behaviour as a function of Young's modulus and Weber number. (Adapted from [91])

of the drop and lead to completely different impact outcome. It is found that the tension in the elastic membrane could strongly affect the splashing behaviour and reducing this tension is able to suppress the splashing (as shown by Figure 2.16) [125]. The effect of substrate stiffness on the splashing threshold has been experimentally investigated in [91] by imaging ethanol drops impacting on silicone gels of different Young's moduli. The splashing behaviour as a function of Young's

modulus and Weber number is displayed in Figure 2.17, from which it is observed that the splashing threshold decreases and approaches the limit of rigid substrate threshold as the Young's modulus increases.

The substrate flexibility is also found to enhance the superhydrophobicity of the surface [150, 154], resulting in less contact time for the rebound of the impacting drop.

2.4.2 Other types of flexible surfaces

Besides the investigations on solid elastic surfaces, Gart et al. consider a cantilever system [75], where it is found that the hydrophobicity of the surface can reduce the torque experienced by the bending beam. While most of the existing literature has a focus on PDMS or other hydrophobic substrates, some is limited to an elastic or viscoelastic surface, there are some interesting experiments on wetting on soft hydrophilic substrates [95].

2.5 Non-Newtonian fluids

Newtonian fluids represent the simplest type of all the fluids in terms of the reactions when subjected to external forces. The constitutive equation exhibits a linear relationship between the stress tensor and the strain rate tensor:

$$\mathbf{T} = -p\mathbf{I} + 2\mu\mathbf{D}, \tag{2.43}$$

where $\mathbf{T}$ and $\mathbf{D}$ denote the stress tensor and strain rate tensor respectively, $\mathbf{I}$ the identity matrix as shown below,

$$\mathbf{T} = \begin{bmatrix} \tau_{xx} & \tau_{xt} & \tau_{xz} \\ \tau_{xy} & \tau_{yy} & \tau_{yz} \\ \tau_{xz} & \tau_{yz} & \tau_{zz} \end{bmatrix}, \qquad \mathbf{I} = \begin{bmatrix} 1 & 0 & 0 \\ 0 & 1 & 0 \\ 0 & 0 & 1 \end{bmatrix},$$

$$\mathbf{D} = \frac{1}{2}\begin{bmatrix} 2\frac{\partial u}{\partial x} & (\frac{\partial u}{\partial y} + \frac{\partial v}{\partial x}) & (\frac{\partial u}{\partial z} + \frac{\partial w}{\partial x}) \\ (\frac{\partial v}{\partial x} + \frac{\partial u}{\partial y}) & 2\frac{\partial v}{\partial y} & (\frac{\partial v}{\partial z} + \frac{\partial w}{\partial y}) \\ (\frac{\partial w}{\partial x} + \frac{\partial u}{\partial z}) & (\frac{\partial w}{\partial y} + \frac{\partial v}{\partial z}) & 2\frac{\partial w}{\partial z} \end{bmatrix},$$

p the local pressure, and μ the dynamic viscosity. From the expression of the constitutive equation, the two most important features of Newtonian fluids can be derived: the constant viscosity and zero normal stress differences (i.e., isotropic pressure).

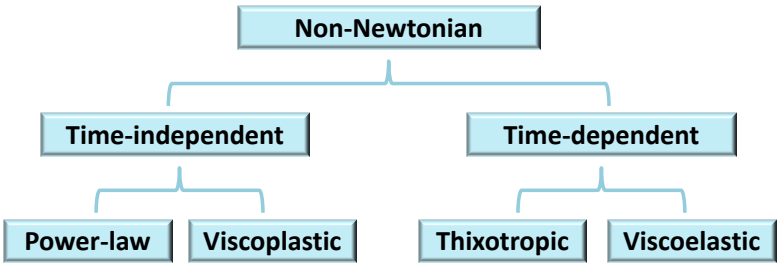

Figure 2.18: Classification of non-Newtonian fluids.

The relationship between the stress tensor and strain rate tensor for non-Newtonian fluids is non-linear. The stress may not be only the function of strain rate but also the spatial position $\mathbf{x}$ and sometimes the time t, which means the flow history also plays a role:

$$\mathbf{T} = f(\mathbf{D}, \mathbf{x}, t). \tag{2.44}$$

As a result, the viscosity of a non-Newtonian fluid is no longer a constant, and it can be expressed as a function of the strain rate: $\mu = \mu(\mathbf{D})$. However it should be noted that in some cases the function $f(\mathbf{D}, \mathbf{x}, t)$ in Equation 2.44 can be linearised depending on certain flow conditions and the non-Newtonian behaviours may not be explicitly revealed. Thus the Newtonian or non-Newtonian natures are the properties of the flow, rather than the properties of the fluid. In general, non-Newtonian fluids can be classified into two groups (see Figure 2.18): 'time-independent', where normally viscosity is a monomial function of the shear rate, and 'time-dependent', where the apparent viscosity varies in time (thixotropic) or viscoelastic behaviours occur.

In nature, almost all the fluids exhibit non-Newtonian behaviours, e.g., crude oil, lavas, clays etc. Also the liquids used industrial process (such as the food and cosmetics industries) are non-Newtonian fluids and their non-Newtonian behaviours are of great importance if one aims to improve the efficiency of manufacturing processes in these industries. Several common types of non-Newtonian fluids and constitutive models will be introduced in this section.

2.5.1 Power-law fluids

The power-law model (also called the Ostwald-de Waele model) is perhaps the best known and simplest non-Newtonian model. It expresses the shear stress, τ as a power-law function of the shear rate, $\dot{\gamma}$:

$$\tau = K\dot{\gamma}^n, \tag{2.45}$$

where K is referred to as the consistency with the units of Pa·s^n, and n is the flow index (also called power-law index). If Equation 2.45 is rewritten in the form of common linear relationship between shear stress and shear rate ($\tau = \mu(\dot{\gamma}) \cdot \dot{\gamma}$) one can obtain the so-called 'apparent viscosity':

$$\mu = K\dot{\gamma}^{n-1}, \tag{2.46}$$

Depending on the value of n, these fluids exhibit different behaviours : $n < 1$, shear-thinning; $n = 1$, Newtonian; $n > 1$, shear-thickening. A schematic of the typical flow curves for different power-law fluids is shown in Figure 2.19.

The biggest drawback of the power-law model is that it is only valid for a certain range of shear rate. For instance, in the case of shear-thinning fluids ($n < 1$), if the shear rate gets infinitely low ($\dot{\gamma} \to 0$), the apparent viscosity will be infinitely high ($\mu = K\dot{\gamma}^{n-1} \to \infty$), which is not physical. In order to overcome such limitations, the power-law model has been extended to various more complex models featuring additional parameters as described in the following.

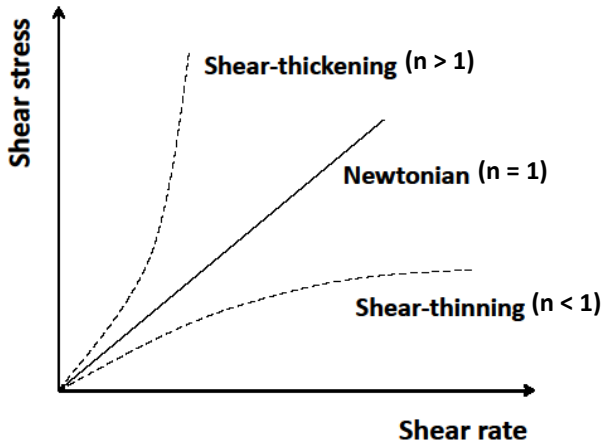

Figure 2.19: Flow behaviours of power-law fluids.

Shear-thinning fluids

Since viscometers became available to investigate the influence of shear rate on viscosity, most common non-Newtonian fluids (such as dispersions and polymer solutions) were found to exhibit 'shear-thinning' effect (i.e., the viscosity decreases with the increase of the shear rate). For shear-thinning fluids, the general flow curve (the variation of viscosity with shear rate) is shown in Figure 2.20.

Contrary to the singular property at low shear rates in the power-law model, the viscosities of real shear-thinning fluids in the limit of very low shear rate are constant (called 'zero-shear-rate viscosity') as indicted in Figure 2.20. When the shear rate becomes considerably large, the viscosity reaches another constant value (called 'infinite-shear-rate viscosity'), which is lower than the previous constant. The constitutive equations which predict the shape of the flow curve in Figure 2.20 need at least four parameters. Cross [54] proposed such an equation in 1965,

$$\frac{\mu - \mu_\infty}{\mu_0 - \mu_\infty} = \frac{1}{1 + (K\dot{\gamma})^m}, \tag{2.47}$$

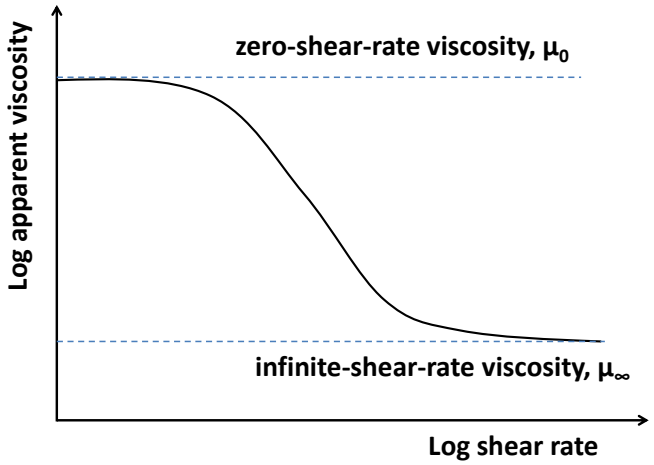

Figure 2.20: Flow curve of typical shear-thinning fluids.

where μ_0 and μ_∞ refer to the zero-shear-rate viscosity and the infinite-shear-rate viscosity respectively. K is a constant parameter with the dimension of time and m is a dimensionless parameter representing the degree of shear-thinning in the middle region of the general flow curve.

We can obtain some other simpler and widely used models by making approximations to the Cross model. For instance, if $\mu \ll \mu_0$ and $\mu \gg \mu_\infty$, the Cross model reduces to

$$\mu = \frac{\mu_0}{(K\dot{\gamma})^m}, \tag{2.48}$$

which can be rewritten as

$$\mu = K_2\dot{\gamma}^{n-1}. \tag{2.49}$$

Equation (2.49) is the power-law model mentioned previously.

If $\mu \ll \mu_0$ and η_∞ is not negligible, Equation (2.47) reduces to

$$\mu = \mu_\infty + \frac{\mu_0}{(K\dot{\gamma})^m}, \tag{2.50}$$

which can be further rewritten as

$$\mu = \mu_\infty + K_2\dot{\gamma}^{n-1}. \tag{2.51}$$

This is called the Sisko model [145]. If n is set to zero in Sisko model, we have

$$\mu = \mu_\infty + \frac{K_2}{\dot{\gamma}}, \tag{2.52}$$

which, with a change of parameters can be rewritten as

$$\tau = \tau_0 + \mu_p \dot{\gamma}, \tag{2.53}$$

where τ_0 is called the yield stress and μ_p the plastic viscosity. Equation (2.53) is called the Bingham model [25]. The fluids with a constitutive equation of Bingham model are called yield-stress or viscoplastic fluids, which will be discussed in Section 2.5.2.

A popular modification of the original Cross model was made by Carreau [39],

$$\frac{\mu - \mu_\infty}{\mu_0 - \mu_\infty} = \frac{1}{(1 + (K_1\dot{\gamma})^2)^{m_1/2}}. \tag{2.54}$$

where K_1 and m_1 have similar physical significances to the K and m in the Cross model. Yasuda et al. [161] introduced a parameter a in the Carreau model later,

$$\frac{\mu - \mu_\infty}{\mu_0 - \eta_\infty} = \frac{1}{(1 + (K_{CY}\dot{\gamma})^a)^{n/a}}, \tag{2.55}$$

which is called the 'Carreau-Yasuda' model or more simply the 'CY' model, where K_{CY} is a constant with a dimension of time representing the onset of shear-thinning. The flow curve of shear-thinning fluids can be described more precisely using the CY model since it contains five parameters whilst there are only four parameters in both Cross model and Carreau model. Based on the advantage of CY model over other models, the CY model has been selected to characterise the rheological behaviours of the shear-thinning fluids used in the present study. Examples of shear-thinning fluids are food thickeners (e.g. xanthan gum), paints (e.g. nail polish) and paper pulp.

Shear-thickening fluids

The act of external forces may cause the rearrangement of microstructures of a material such that the viscosity increases with shear rate. This rheological

behaviour is called 'shear-thickening'. Particle suspensions are the most common type of shear-thickening fluids.

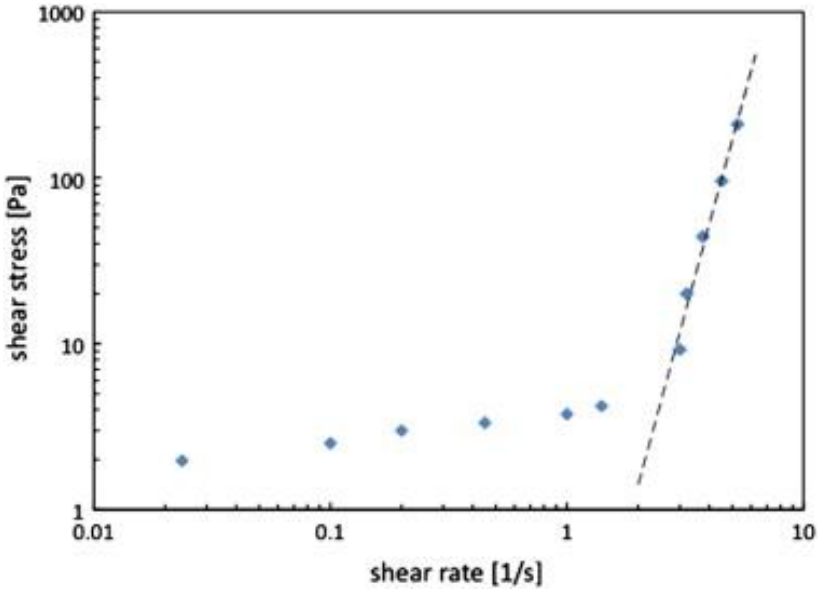

Figure 2.21: Flow curve of a colloid suspension with volume fraction of 0.603. (Adapted from [23])

For particulate systems, the action of shear stress can cause the rearrangement of the particles such that the resistance to flow increases with shear rate. Figure 2.21 displays the flow curve of a colloidal suspension with volume fraction of 0.603 measured using a rotational rheometer [23]. The dashed line represents a power-law model fit with a value of n greater than unity to the last five points of the flow curve. In almost all known cases of shear-thickening, there is a region of shear-thinning at lower shear rates. This feature can also be observed in Figure 2.21.

In a colloidal system, shear-thickening is related to a mechanism called dilatancy, which depends on the competition between interparticle forces such as Van der Waals forces and shear forces. If the applied shear forces are very low and the interparticle forces still dominate, the suspended particles are kept in an

ordered, layered and equilibrium structure by the interparticle forces and the colloidal system remains in a stable state. However, as the shear forces increase and once exceed a threshold value the particles are forced out of their equilibrium positions and pushed together to form hydroclusters as shown in Figure 2.22. These hydroculsters are irregular, rod-like chains of particles, which cause 'traffic jam' and finally lead to the dramatic increase of viscosity. Thus the shear-thickening effect is a result of the transition from an order structure of suspended particles to a disordered structure [36, 64, 118]. Examples of shear-thickening fluids are cornstarch-water mixtures and silica nanoparticles suspensions.

2.5.2 Viscoplastic fluids

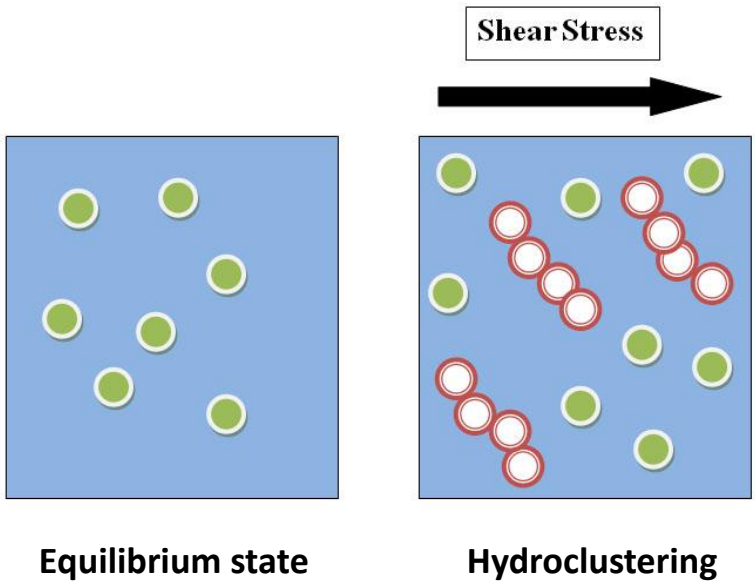

Figure 2.22: Schematic of hydroclustering process.

Viscoplatic fluids are an important type of non-Newtonian fluids, which respond like an elastic solid when the applied stress is below a threshold value (called the yield stress), and start to flow when the yield stress is overcome. In practice, many soft materials in industrial or everyday products exhibit such

property, including slurries and suspensions, crystallizing lavas, some polymer solutions, muds and clays, heavy oils, cosmetic creams, hair gel, liquid chocolate, and toothpaste [7, 52]. Due to this special property viscoplastic fluids have important applications in various fields ranging from the oil and chemical industries, to food processing, cosmetics, and geophysical fluid dynamics. Currently, there is a growing interest in studying the behaviour of viscoplastic fluids in the drop-on-demand process [53, 77, 88] because it is relevant to additive manufacturing (3D printing).

The Bingham model is the simplest model to describe the viscoplastic or yield-stress nature. The full constitutive equation of the Bingham model as mentioned previously in Equation 2.53 is

$$\begin{cases} \dot{\gamma} = 0 & \tau \leq \tau_0 \\ \tau = \tau_0 + \mu_p \dot{\gamma} & \tau > \tau_0 \end{cases}, \tag{2.56}$$

where a linear relationship between shear stress and shear rate is established once the yield stress is overcome. However, another popular viscoplastic model called the Herschel-Bulkley model relates the shear rate experienced by the fluid to the shear stress according to a power law:

$$\begin{cases} \tau = G\gamma & \tau \leq \tau_0 \\ \tau = \tau_0 + K\dot{\gamma}^n & \tau > \tau_0 \end{cases}, \tag{2.57}$$

where K denotes the consistency coefficient and n the flow index similar to the parameters in power-law model, and G is the elastic modulus. As shown in Equation 2.57, the material is assumed to respond like elastic solid, where the shear rate is proportional to the applied shear stress, when the shear stress is lower the yield stress. The typical flow curves of both Bingham and Herschel-Bulkley model fluids are schematically shown in Figure 2.23. Beside the yield-stress property, the Herschel-Bulkley model also describes shear-thinning behaviours once it starts to flow provided that the flow index n is smaller than one. Since most viscoplastic fluids exhibit shear-thinning effect rather than Newtonian behaviour,

the Hershel-Bulkley model is able to better describe real materials. For this reason, the Herschel-Bulkley model (HB model) has been selected to characterise the rheological behaviours of the viscoplastic fluids used in the present research.

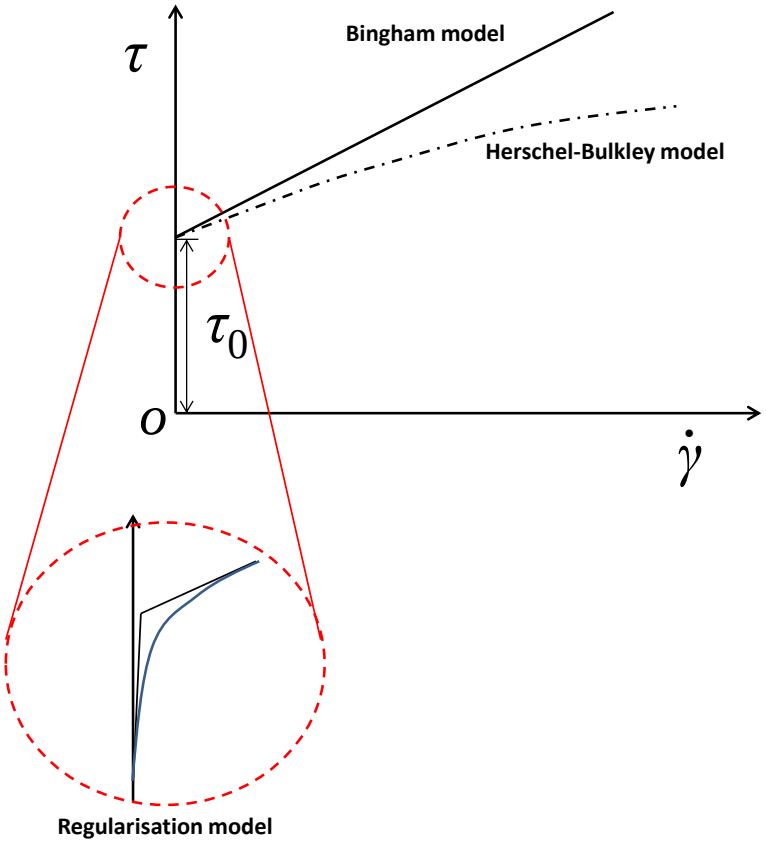

Figure 2.23: Flow curves of Bingham model and Hershel-Bulkley model.

When Bingham model (or Hershel-Bulkley model) is adopted in numerical simulations of viscoplastic flows, in order to avoid discontinuity problem in first derivative, regularisation methods are commonly used as shown by the inset in Figure 2.23. Among the available regularisation models in literature, the Papanastasiou regularisation model can best approximate the ideal discontinuous model [70]. The exponential regularisation of Bingham model was proposed by Papanastasiou as [121]:

$$\tau = \tau_0(1 - e^{-m\dot{\gamma}}) + K\dot{\gamma}, \tag{2.58}$$

where the parameter K controls the exponential growth of stress as shown in Figure 2.24.

In an experiment study on the solid-fluid transition in a yield-stress gel (Carbopol 940), a clear hysteresis upon increasing and decreasing external forces was observed [129]. A simple kinetic model based on an analogy between the solid-fluid transition and a first order phase transition was proposed to describe the structural hysteresis in the solid-fluid transition. More recently, a Gibbs random field model for the microscopic interactions in a viscoplastic fluid was presented in a theoretical and experimental investigation [141]. This model contains three parameters: the internal energy if the material is sufficiently described by only two parameters; and a constant externally applied stress is controlled by a third parameter. Despite the limited number of parameters involved in this model, a decent agreement between the predictions of the model and the experimental data was found for various yield-stress materials.

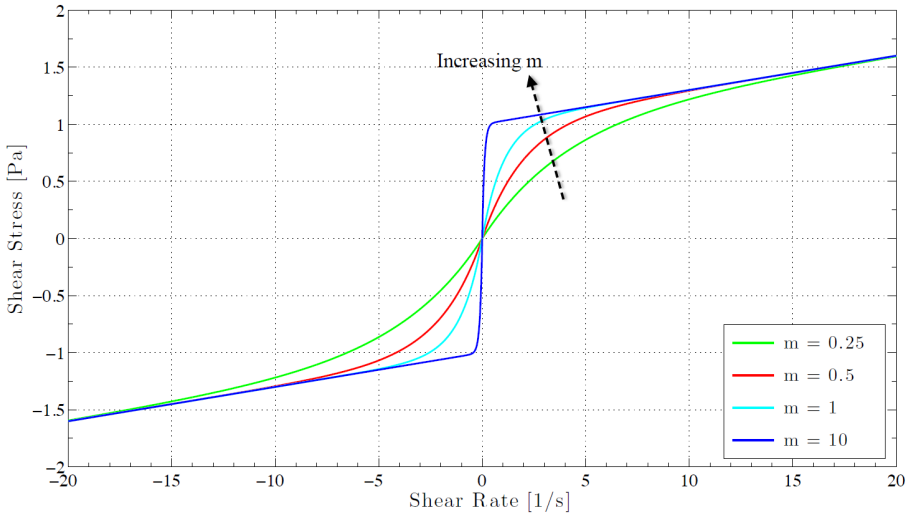

Figure 2.24: Papanastasiou regularisation of Bingham model for different values of m (adapted from [57]).

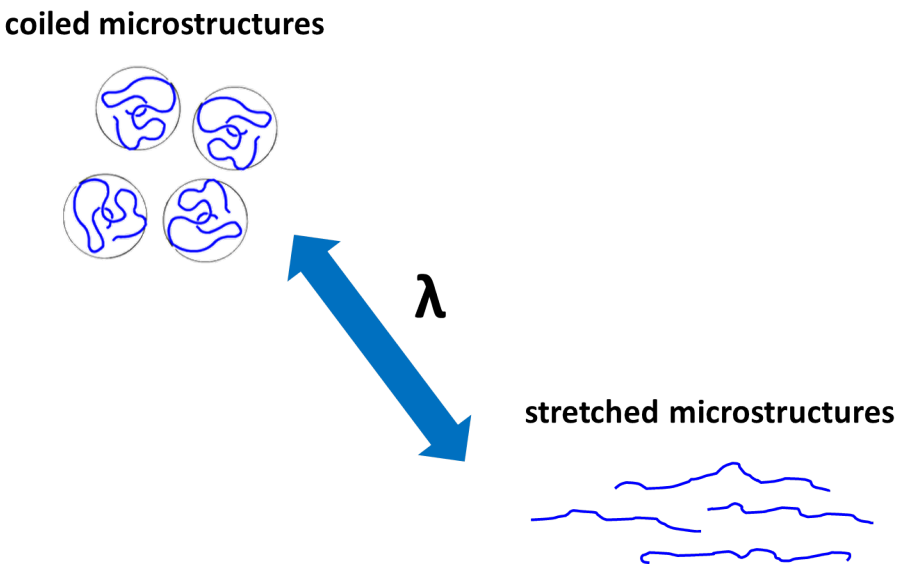

Figure 2.25: Schematic of the conformational rearrangement of microstructures.

2.5.3 Viscoelastic fluids

The term 'viscoelastic ' means the simultaneous existence of viscous and elastic properties in a material. When a viscoelastic liquid is subject to shear stress, a part of the deformation energy is stored as elastic energy, and released with a certain delay depending on the relaxation time of the fluid. From the microscopic point of view, the action of hydrodynamic forces causes the conformational rearrangement of microstructures such that the elastic energy is stored in the rearranged microstructures as shown in Figure 2.25. The observable microscopic time scale of the relaxation time (λ) for simple fluids is extremely short: $\lambda \sim 10^{-15}$ s. Thus the viscoelastic effect is negligible. However in the case of some complex fluids, depending on the properties of the microstructures the time scale of λ can be considerably long : $\lambda \sim 10^{-3} - 10^{3}$ s. The most common dimensionless number used to characterise the viscoelasticity is called the Weissenberg number:

$$Wi = \frac{\text{elastic forces}}{\text{viscous forces}} = \lambda\dot{\gamma} \quad (\text{or} \quad \lambda\dot{\epsilon}), \tag{2.59}$$

which compares the elastic forces to the viscous forces. Since this number is derived from scaling the evolution of stress, it can be defined by either shear rate

($\dot{\gamma}$) or elongation rate ($\dot{\epsilon}$).

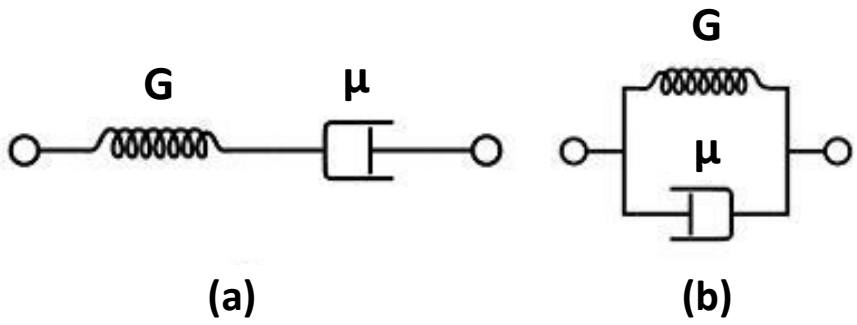

Figure 2.26: Schematic of the viscoelastic models: (a) Maxwell model; (b) Kelvin-Voigt model.

One of the simplest constitutive models of viscoelasticity is the 'Kelvin-Voigt' model,

$$\tau = G\gamma + \mu\dot{\gamma}, \tag{2.60}$$

where G is the elastic modulus, γ the shear strain, and μ the viscosity. The Kelvin-Voigt model can be derived from a parallel combination of a spring and a dashpot. In this model the shear (tensile) rates in elastic and viscous elements are the same whilst the total stress is equal to the sum of stresses in the two elements. Similar to the Kelvin-Voigt model, Maxwell introduced another simple model of a spring and a dashpot but in series connection:

$$\tau + (\mu/G)\dot{\tau} = \tau + \lambda\dot{\tau} = \mu\dot{\gamma}, \tag{2.61}$$

where $\mu/G = \lambda$ is the so-called the 'relaxation time'. Contrary to the Kelvin-Voigt model, the total shear (strain) rate is equal to the sum of strain rates in elastic and viscous elements while the shear (tensile) stresses in the two elements are the same. The two basic viscoelastic models are schematically contrasted in Figure 2.26.

2.5.4 Polymer solutions

The academic literatures relevant to rheology are dominated by the investigations of rheological behaviours of the polymer solutions. This is due to both their great importance in various industrial applications and a wide range of rheological phenomena exhibited by them. A better understanding of the rheological behaviours of the polymer solutions will also enable us to tailor-make them to facilitate fundamental rheological research.

The wide range of observed rheological phenomena is attributed the long chain molecules dissolved in the solvent, which are a unique characteristic of polymer solutions. The viscosity of the polymer solution increases with the mass concentration of the polymers. However the increase rates have been observed to be inconsistent for different regimes of concentration. For instance, Figure 2.27 shows the measured viscosities of water-based Polyvinyl alcohol (PVA) solutions as a function of the polymer mass concentration [120], from which it is clear that the viscosity grows much faster after a critical value of concentration called the 'overlap concentration', which depends on the 'intrinsic viscosity' as discussed below.

Firstly, we define a quantity called relative viscosity (μ_r), which is simply the ratio of the solution viscosity (μ) to the solvent viscosity (μ_{sol}):

$$\mu_r = \frac{\mu}{\mu_{sol}}. \tag{2.62}$$

This quantity is greater than one ($\mu_r > 1$) since adding polymers to a Newtonian solvent will always increase the viscosity ($\mu > \mu_{sol}$). And the specific viscosity is determined by subtracting one from the relative viscosity:

$$\mu_{sp} = \mu_r - 1 = \frac{\mu - \mu_{sol}}{\mu_{sol}}, \tag{2.63}$$

which expresses the relative viscosity increase due to polymer additives compared to the solvent viscosity. Then if one divides the specific viscosity by the mass

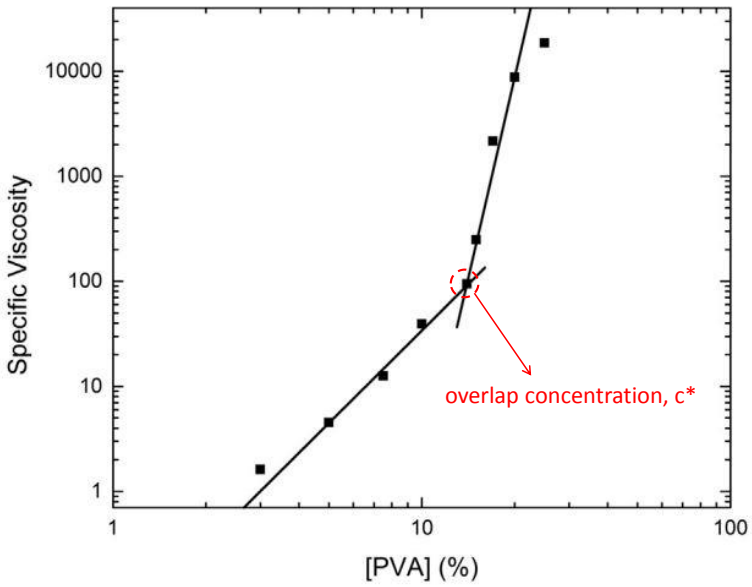

Figure 2.27: Viscosity versus Polyvinyl alcohol (PVA) concentration showing polymer overlap concentration (c*). (Adapted from [120])

concentration c (w/w) of the polymers, the reduced viscosity (or reduced specific viscosity) is obtained:

$$\mu_{red} = \frac{\mu_{sp}}{c}. \tag{2.64}$$

Finally the limit of $c \to 0$ of μ_{red} is defined as the intrinsic viscosity ($[\mu]$):

$$[\mu] = \lim_{c \to 0} \mu_{red} = \lim_{c \to 0} \frac{\mu - \mu_{sol}}{c \cdot \mu_{sol}}. \tag{2.65}$$

Note that the quantities here (such as μ, μ_{sol} etc.) are all zero-shear-rate viscosities. Where there is a dependence of the apparent viscosities on the shear rate for non-Newtonian fluids, an extrapolation to zero shear rate using appropriate model is required. A simple correlation between the overlap concentration and the intrinsic viscosity was provided by Graessley in 1980 [82]:

$$c^* = \frac{0.77}{[\mu]}. \tag{2.66}$$

The intrinsic viscosity $[\mu]$ is so named because it is an intrinsic function of the dissolved macromolecules. One of the most important properties of the macromolecules is the molecular weight. The famous Mark-Houwink equation, also

known as the Mark-Houwink-Sakurada equation, provides a correlation between the intrinsic viscosity $[\mu]$ and the molecular weight M [89]:

$$[\mu] = K_{MH} M^a, \tag{2.67}$$

where K_{MH} and a are constant parameters, and the values of them depend on the particular polymer-solvent system. A value of $a = 0.5$ is an indicator of the so-called 'theta solvent' (θ solvent), where the polymer coils act like ideal chains. For most flexible polymers, a is in the range of $0.5 \sim 0.8$. However for semi-flexible polymers, $a \geq 0.8$. In case of polymers acting like absolute rigid rods, e.g., tobacco mosaic virus, $a = 2.0$.

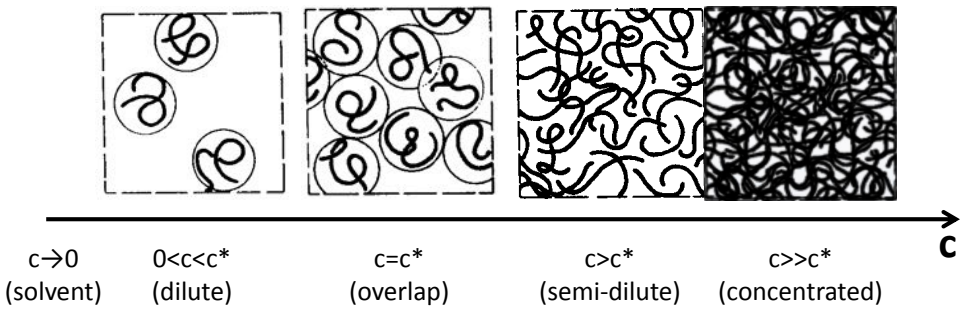

Figure 2.28: Different regimes of solutions of flexible polymers as a function of polymer concentration.

A schematic showing different regimes of solutions of flexible polymers as a function of polymer concentration is plotted in Figure 2.28. If the polymer concentration is sufficiently low ($0 < c < c^*$), there is very weak interaction between the macromolecules (*dilute regime*). As the concentration starts to increase, the macromolecules begin to feel the existence of their neighbours and there is intermediate interaction between them (*overlap regime*). If the concentration increases even further, the macromolecules can no longer remain the coiled state individually and join together to form an entangled and cross-linked structure (*semi-dilute*

or concentrated regime), which dramatically increases the viscosity of the solution. All the model fluids of polymer solutions used in the present research are within the dilute regime.

2.6 Non-Newtonian Leidenfrost drops

2.6.1 Effect of polymer additives

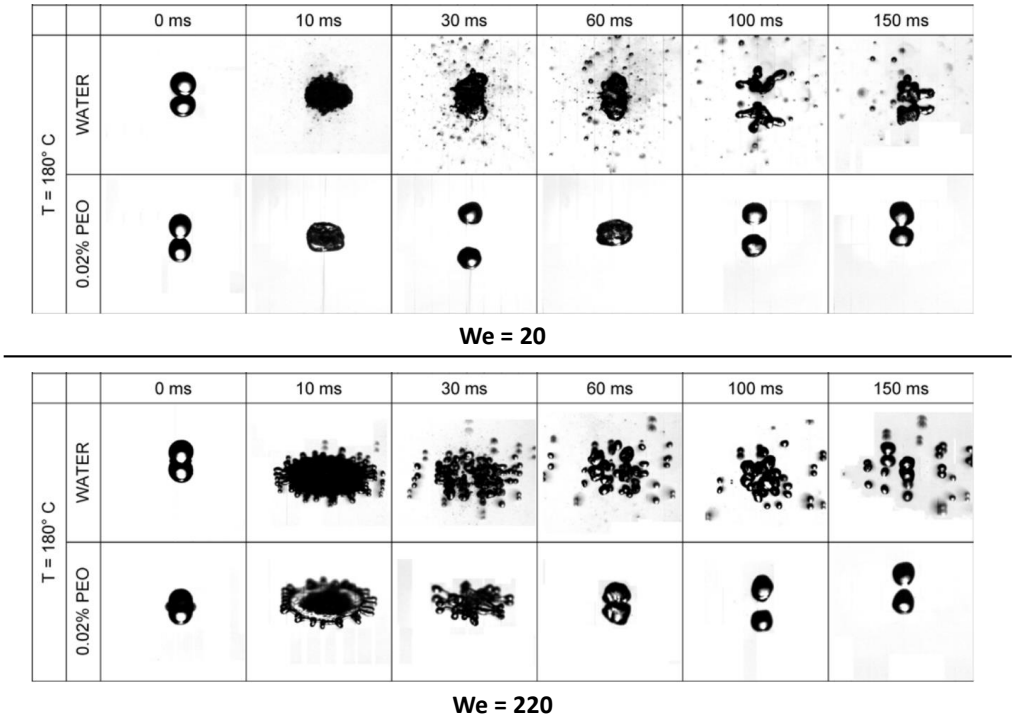

Figure 2.29: Comparison of the impact morphologies between a drop of pure water and one of polymer solution (200 ppm PEO: polyethylene oxide) at surface temperature T = 180^{o}C for different Weber numbers (We = 20&220). (Adapted from [15])

After the first description about the 'Leidenfrost effect' in 1756 [100], the Leidenfrost drops have been extensively studied for simple Newtonian fluids (such as water). However there is a growing interest in Leidenfrost drops of complex fluids (i.e., non-Newtonian fluids) in both industry and academia due to the effect of their intriguing rheological behaviours on impact outcomes. Early investigations on drop impact of non-Newtonian fluids in Leidenfrost regime qualitatively de-

scribe that by adding very small amount of polymer additives the impacting drops may exhibit completely different morphologies [15, 20]. For instance, the polymer additives (PEO: polyethylene oxide) are observed to inhibit secondary atomization (the scattering of secondary droplets from the free surface of the liquid) at impact Weber number, We = 20 and to prevent splashing (the disintegration of the drop into numerous small droplets) at We = 220 as demonstrated by Figure 2.29. It should be noted that although the surface temperature (T = 180^{o}C) in Figure 2.29 is below the dynamic Leidenfrost temperature of water drops, the behaviours of non-Newtonian drops are still in the Leidenfrost regime (the bouncing back of the impact drops off the surface), which suggests the dynamic Leidenfrost temperature is lower for a drop of dilute polymer solution compared to one of pure water.

2.6.2 Comparative energy balance approach

In Leidenfrost drops, the energy dissipation during the whole impact process (including impact, spreading, retraction, and rebound) can be easily calculated by the difference between the gravity potential energies of the drop when it is released from the needle and when it reaches the maximum bouncing height. Thus the ratio of the total energy dissipation to the initial potential energy which also equals the initial impact kinetic energy can be written as

$$\frac{E_{diss}}{E_0} = 1 - \frac{H_{\mathrm{m}}}{H_0}, \tag{2.68}$$

where E_{diss} denotes the total energy dissipation during the whole impact process, E_0 the initial impact kinetic energy, H_{m} the maximum bouncing height, and H_0 the vertical distance between the surface and the released point.

In order to get a deeper insight of the energy re-distribution during impact and rebound, one can adopt the comparative energy balance approach to conduct the energy analysis between two drops of different fluids with the same kinetic energy before impact [22]. The effect of the elasticity of the vapour layer [133]

can be neglected since this effect is similar for drops with different fluids at the same Weber number. In particular, a comparative energy balance analysis between water drops and polymer solution (XG, 300 ppm) drops was presented in [30]. At the end of spreading, the kinetic energy of the impacting drop is partially converted into the surface energy, and partially dissipated due to viscous resistances. Consequently for the water-XG drop pair, the energy balance can be expressed as:

$$E_{\sigma}^{W} + E_{diss-sp}^{W} = E_{\sigma}^{XG} + E_{diss-sp}^{XG}, \tag{2.69}$$

where E_{σ}^{W} (or E_{σ}^{XG}) and $E_{diss-sp}^{W}$ (or $E_{diss-sp}^{XG}$) denote the surface energy of the water (or XG) drop at maximum spreading and the energy dissipation for the water (or XG) drop during the spreading phase, respectively. Since the difference between the maximum spreading diameter of water drops and that of XG drops is very small [30], the surface energies of these two different drops are approximately equal:

$$E_{\sigma}^{W} \approx E_{\sigma}^{XG}, \tag{2.70}$$

which leads to the same energy dissipation during the spreading stage:

$$E_{diss-sp}^{W} = E_{diss-sp}^{XG}. \tag{2.71}$$

After maximum spreading, the drop starts to retract and rebound, converting the surface energy stored at the end of spreading into mechanical energy. When the drop reaches the maximum bouncing point, all the mechanical energy available for drop rebound is entirely converted into the potential energy which is proportional to the maximum bouncing height, H_{m}. Based on energy balance, the potential energy at maximum bouncing height is equal to the net available surface energy at maximum spreading, minus the viscous dissipation during the retracting phase ($E_{diss-ret}^{W}$ or $E_{diss-ret}^{XG}$). Since the polymer solution (XG) drops are observed to bounce higher than the water drops, the potential energy restored

at the maximum bouncing height for them is greater:

$$E_{\sigma}^{XG} - E_{diss-ret}^{XG} > E_{\sigma}^{W} - E_{diss-ret}^{W}. \tag{2.72}$$

Combining Equation 2.70 and Equation 2.72 yields:

$$E_{diss-ret}^{XG} < E_{diss-ret}^{W}. \tag{2.73}$$

As shown in Equation 2.73, the polymer additives cause smaller viscous energy dissipation during the retraction and rebound stages, which results in greater maximum bouncing height compared to water drops.

2.6.3 Effect of polymer concentration

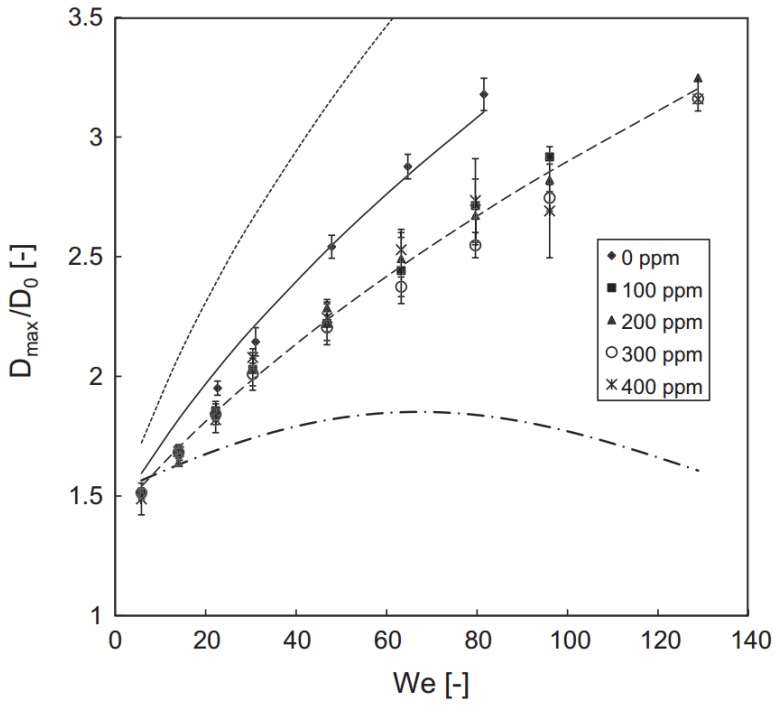

Figure 2.30: Maximum spreading diameter as a function of the Weber number for different polymer concentrations. The lines of different types represent the trends predicted by $D_m/D_0 = \sqrt{(\alpha^2/6)\mathrm{We} + 2}$ [133] for different values of restitution coefficient (α, the ratio between the rebound and impact velocities): (a) solid line: α = 0.75; (b) long dashed line: α = 0.62; (c) short dashed line: α = 1; (d) dash-dot line: measured values of α. (Adapted from [18])

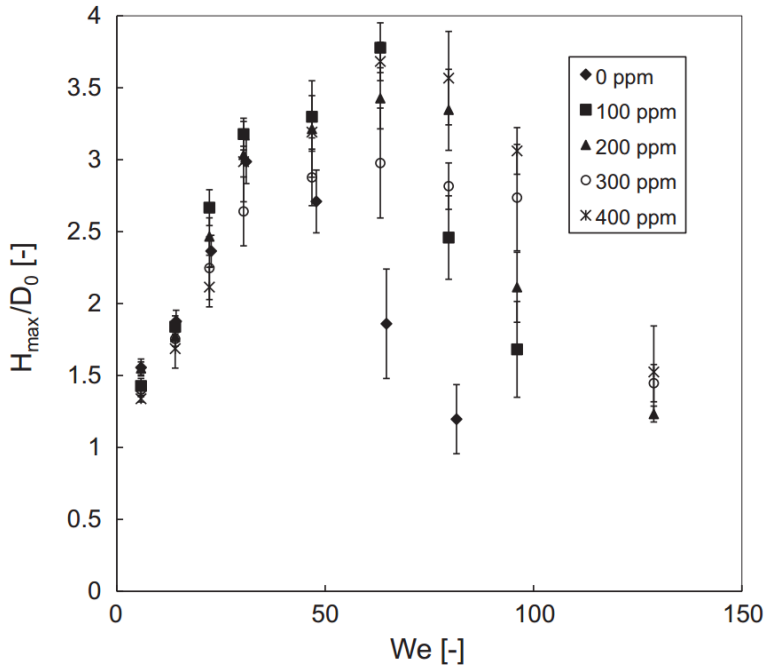

Figure 2.31: Maximum bouncing height as a function of the Weber number for different polymer concentrations. (Adapted from [18])

Recently, a systematic investigation of the effect of polymer solution on the dynamics of Leidenfrost drops of dilute polymer solution was reported in [18]. Polymer solutions (PEO: polyethylene oxide) of different mass concentrations at 100 ppm, 200 ppm, 300 ppm and 400 ppm were obtained by preparing and diluting a master solution with a concentration of 400 ppm. Drops with equilibrium diameter ~3 mm were released from a blunt hypodermic needle and impacted on a polished aluminium surface heated up to 400^{o}C. It was found that the polymer additives cause a slight reduction of the maximum spreading diameter of the impacting drops, however the dependence of the magnitude of reduction on polymer concentration is very weak as shown in Figure 2.30. Compared to the effect of polymer concentration on maximum spreading diameter, the effect on maximum bouncing height is relatively stronger. Figure 2.31 compares the maximum bouncing height as a function of the Weber number for different polymer concentrations, in which it is clearly observed that if the Weber number is beyond

a critical value (We > 50) the polymer additives enable the impacting drops to bounce higher. Although the data seem to show that the magnitude of increase in maximum bouncing height is greater as the polymer solution becomes more concentrated (especially for We > 50), these differences are comparable with the experimental error. In the same study, the frequency of free oscillations was measured and compared between the drops with different polymer concentrations. It was observed that the effect of polymer additives on the frequency of free oscillations is not significant, the oscillation behaviours can still be predicted by the well-known model for Newtonian fluids.

2.7 Capillary flows of viscoplastic fluids

2.7.1 Viscoplastic drops

The process of formation and detachment of viscoplastic drops from a capillary nozzle is experimentally studied through high-speed imaging in [77]. The results of viscoplastic drops are compared with Newtonian drops and shear-thinning drops. The capillary nozzle is made of a flat-ended metallic hypodermic needle with 1.27 mm outside diameter and 0.838 mm inner diameter (needle gauge 18). The model yield-stress fluids are prepared by mixing a commercial hairdressing gel with de-ionized water. Fluids with different values of yield-stress are achieved by different mixing mass fractions. The drop shape during detachment for three different fluids (Newtonian, shear-thinning and viscoplastic) is shown in Figure 2.32.

The formation and detachment behaviours of Newtonian and shear-thinning drops are qualitatively similar, which leads to spherical drops at the end. However viscoplastic drops exhibit strongly prolate shapes and a significantly different breakup dynamics of the capillary filament initially connecting drops to the nozzle.

In a subsequent study on viscoplastic drops [78], the drop dynamics during

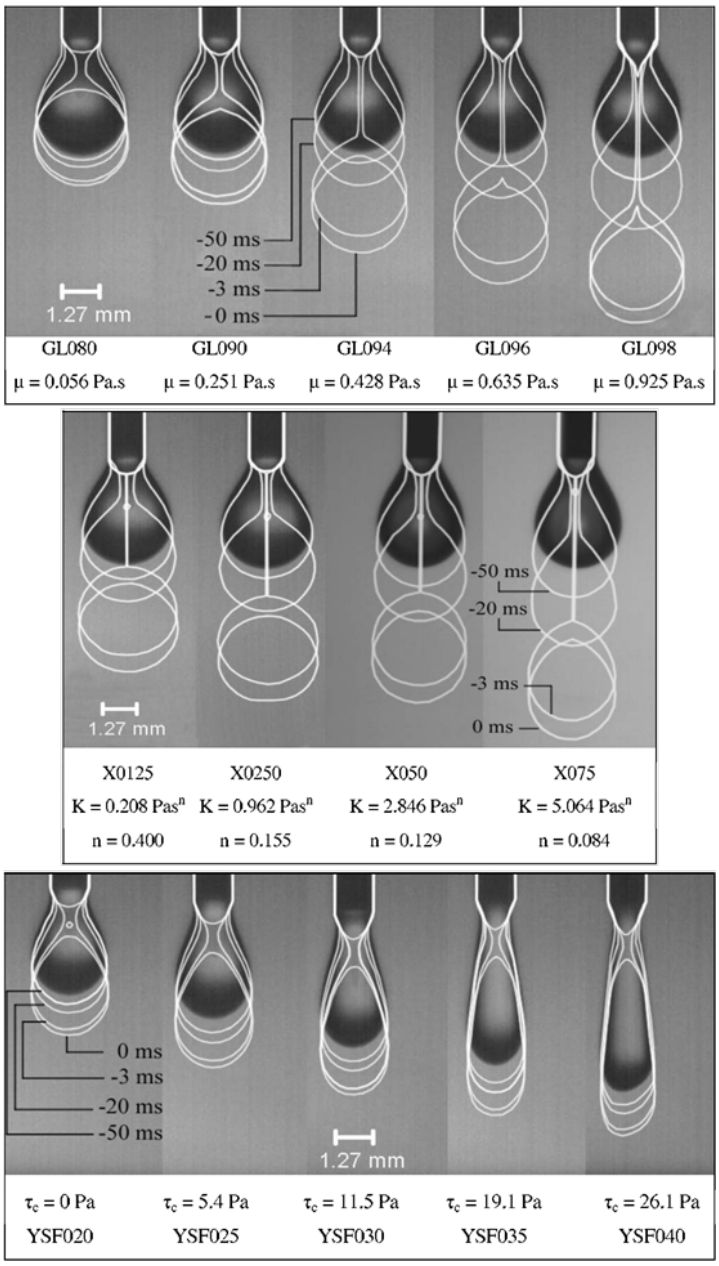

Figure 2.32: Drop shape during detachment (Upper: Newtonian fluid; Middle: shear-thinning fluid; Lower: yield-stress fluid). (Adapted from [77]).

free-fall is experimentally investigated using high-speed imaging. The behaviours of yield-stress drops are compared with Newtonian drops. A dimensionless number as a function of time referred as the 'shape factor' is introduced to characterise the drop shape during free-fall:

$$S(t) = \frac{H(t) - L(t)}{H(t) + L(t)}, \tag{2.74}$$

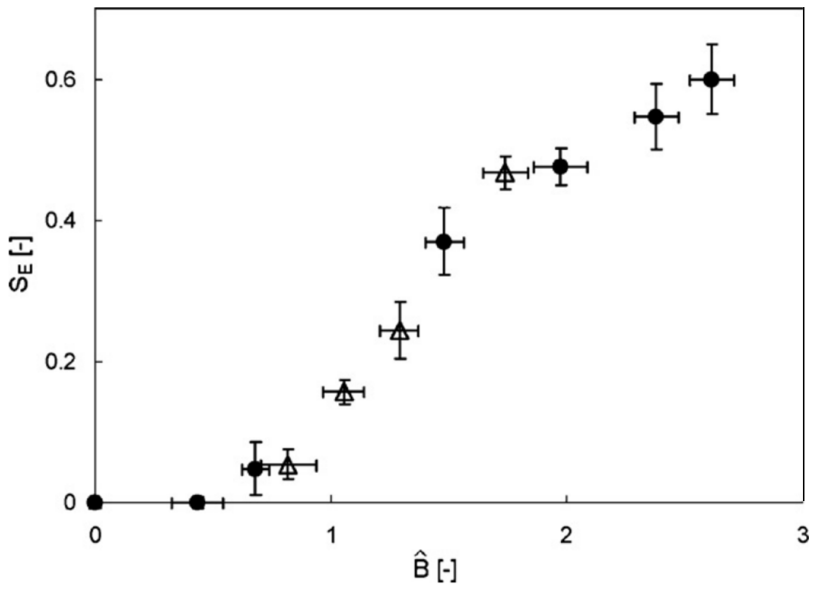

Figure 2.33: The equilibrium drop shape factor as a function of Bingham-Capillary number. Open symbols represent the data from a nozzle of inner diameter 0.838 mm while filled symbols are the data from a nozzle of inner diameter 0.495 mm. (Adapted from [78]).

where H and L represent the horizontal dimension and vertical dimension of the drop respectively. The drop shape of viscoplastic fluids during free-fall is observed to be significantly affected the yield-stress magnitudes. This effect is interpreted by the Bingham-Capillary number $\widehat{B}$ (Equation 1.2) which compares the yield stress with the Laplace pressure. The equilibrium shape factor (S_E) at the end of the transient as a function of Bingham-Capillary number is displayed in Figure 2.33. A transition of the equilibrium shape factor is observed at around $\widehat{B} \approx 1$, where the capillary forces equal those arising from the yield stress.

The motion and shape of an axisymmetric viscoplastic drop slowly falling through an infinite viscous fluid is numerically studied in [146]. In the numerical simulations, the Green function for the Stokes equation is utilized and the non-Newtonian stress is treated as a source term. It is found that, the presence of yield stress is able to stabilize the deformations of initially deformed drop (finally leads to a steady shape) even at sufficiently high Ca numbers, where

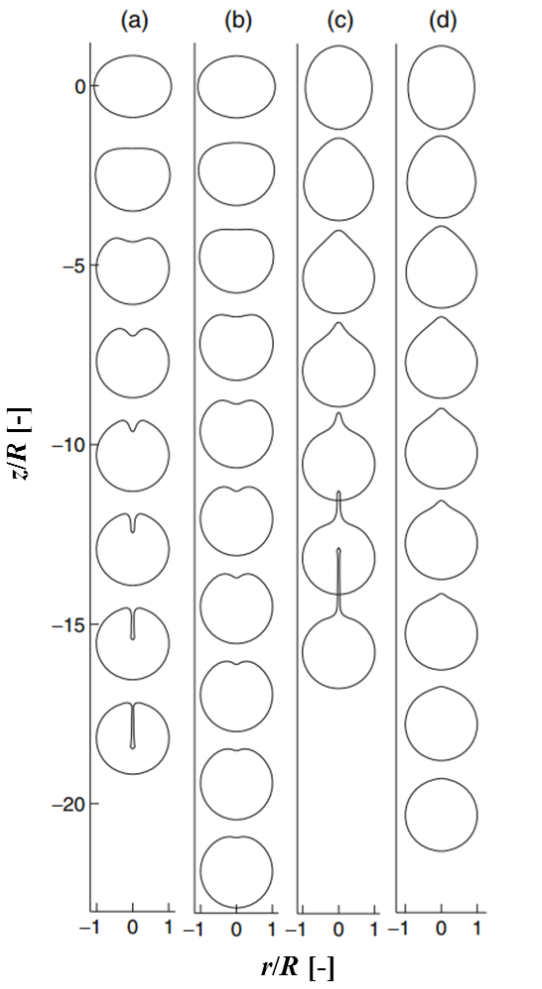

Figure 2.34: Evolution of the shapes of viscoplastic drops slowly falling through a Newtonian fluid: (a) initially oblate drop, Ca=20, Bm=0.05; (b) initially oblate drop, Ca=20, Bm=0.15; (c) initially prolate drop, Ca=14, Bm=0.05; (d) initially prolate drop, Ca=14, Bm=0.1. (Adapted from [146]).

the Newtonian drop breaks up. The numerical results showing the evolution of shapes of viscoplastic drops slowly falling through a Newtonian fluid for different combinations of Ca, Bm number and initial shape condition are displayed in Figure 2.34. All cases in Figure 2.34 are numerically solved at sufficient high Ca numbers, in which the Newtonian drops with the same viscosity ratio would break up [98]. However, if the Bm number is beyond a critical value ((b) and (d) in Figure 2.34), the yield-stress drops behave similar to the Newtonian drops at sufficient low Ca number and finally reach a steady shape. It is proposed that the

existence of unyielded zones inside the falling drops which grow with Bm number causes this strong stabilization.

The impact morphology of viscoplastic drops on solid flat surfaces is experimentally investigated by means of high-speed imaging in [76]. The results are compared with Newtonian and shear-thinning drops at different impact Weber numbers. One interesting observation of the impact morphology of viscoplastic drops is the formation of central drop peaks at the end of inertial spreading, while the impact morphology of shear-thinning drops is qualitatively similar to that of Newtonian drops. Through measuring the dimensions of these central drop peaks, the role of yield stress magnitude in the impact morphology of viscoplastic drops is qualitatively characterised. In another experimental study on the spreading behaviour of capillary driven viscoplastic drops [79], through the comparison with purely shear-thinning drops, the spreading rate is shown to be influenced independently both by the degree of shear-thinning and by the yield-stress magnitude. In addition, it is observed that the spreading can be inhibited if the yield stress is beyond a critical value, preventing drops from reaching a shape of spherical cap.

The spreading of axisymmetric viscoplastic droplets extruded slowly on glass surfaces is investigated experimentally using shadowgraphy and swept-field confocal microscopy [93]. In this study, the confocal microscopy system enables one to directly measure the vertical profile of the radial velocity, revealing apparent slip of spreading drops of viscoplastic fluids (Carbopol solutions) over untreated glass surfaces (as shown in Figure 2.35), which is a factor that has not always been considered explicitly.

A lattice Boltzmann model is used to simulate multiphase viscoplastic fluid flow in [157]. Good agreements between the simulation results and the corresponding theoretical solutions are obtained for different cases, including droplet(s) falling and interaction in Bingham fluid, and sessile viscoplastic droplet motion.

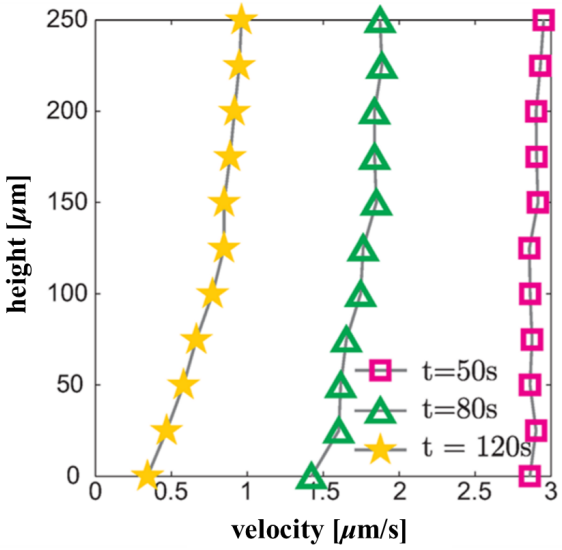

Figure 2.35: Vertical velocity profile of Carbopol droplet (0.036 % w/w) spreading on a glass surface at different moments. (Adapted from [93]).

More recently, the free oscillation of a yield-stress drop is theoretically investigated in [47]. In particular, the question of whether there exists a finite stopping time for an unforced motion of a viscoplastic drop is addressed. The dynamics of viscoplastic fluid with a free surface is described by a variational inequality formulation which leads to an energy balance equation. It is proved that under certain assumptions the finite stopping time of oscillations exists if the yield stress is positive and the flow index is above or equal to one.

2.7.2 Flows of viscoplastic fluids in microchannels

The flow of viscoplastic fluids (yield stress range: 5~21 Pa) in horizontal glass tubes with different diameters (diameter range: 0.46~1.5 mm) under the action of capillarity is experimentally studied in [16]. It is observed that the motion of fluid stops after it penetrates a few centimetres. The normalised maximum length of penetration (measured from where the fluid stops to the starting point) with respect to tube diameter is plotted as a function of Bingham-Capillary number ($\widehat{B}$) as shown in Figure 2.36. The experimental data exhibit different scaling

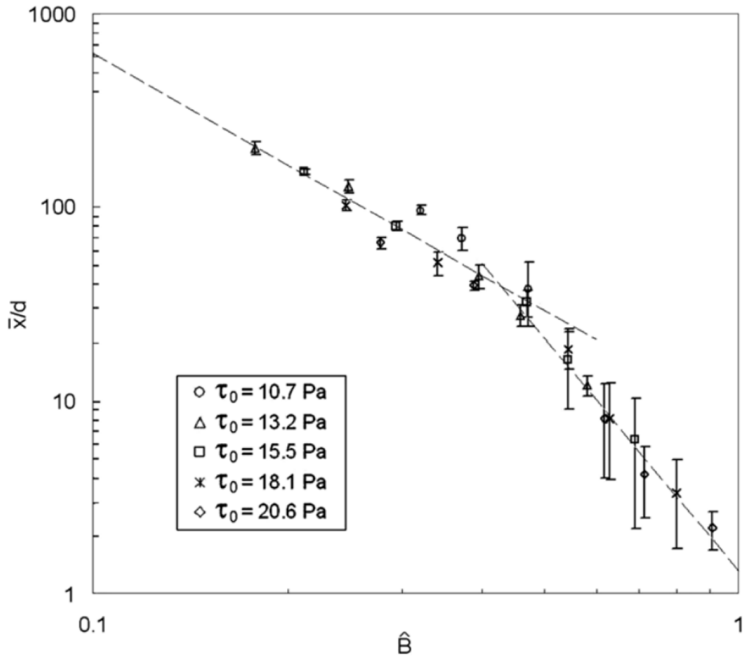

Figure 2.36: Dimensionless maximum length of penetration as a function of Bingham-Capillary number. The dashed lines represent the power-law best fits of the experimental data: $\bar{x}/d = 7.8\widehat{B}^{-1.9}$ $(\widehat{B} < 0.5)$ and $\bar{x}/d = 3.1\widehat{B}^{-4.1}$ $(\widehat{B} > 0.5)$. (Adapted from [16]).

laws (dashed lines in Figure 2.36) with respect to $\widehat{B}$ number which compares the yield stress with the Laplace pressure. However the experimental data of maximum length of penetration is found to be much higher than the predicted values obtained by a simple model based on the balance between capillary and frictional forces. It is suggested that such behaviour is due to the apparent wall slip which is a well-known mechanism for viscoplastic flows.

The inertialess immiscible displacement of vicoplastic fluid by a second viscoplastic fluid in a pressure-driven plane channel with interfacial tension effects is numerically studied in [69]. The viscoplastic fluids are modeled as Bingham materials (Equation 2.56) with an exponential regularisation proposed by Papanastasiou (Equation 2.58). In particular, the fraction of mass attached to the wall and the flow regimes as functions of the Ca number, the viscosity ratio and the yield number (defined as the ratio of yield stress to the characteristic

viscous stress) of the displacing and displaced fluids are investigated. The yielding/unyielding zones are also captured by the classical criterion $\tau \geq \tau_0$ for the yielding zones. It is shown that the variation of the yield number of the displaced fluid has a greater effect on the mass fraction attached to the wall and the flow regimes than that of the displacing fluid. In addition, the effects of yield number and Capillary number on the yielding/unyielding zones are investigated. It is observed that increasing the yield number will always cause the growing of unyielding zones in the corresponding fluid domain. However the role of Capillary number is more complex. On one hand, the local stress can be increased by increasing the interfacial forces (i.e., increasing the Capillary number), which leads to higher probability of overcoming the yield stress. On the other hand, the increase in the interfacial tension will lower the strain-rate of the flow and the viscous stress, which induces the decrease of probability of overcoming the yield stress.

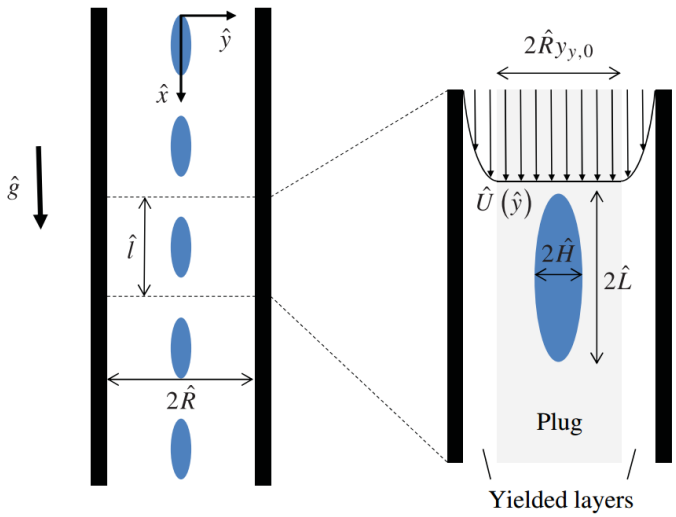

Figure 2.37: Schematic of the encapsulated droplet train in viscoplastic fluid. (Adapted from [110]).

More recently, the encapsulation of droplets within a viscoplastic fluid for the purpose of transportation is explored both analytically and computationally in [110]. The geometry of the physical set-up is schematically shown in Figure

2.37. It is found that the stability of the encapsulated droplets is governed by the length scale of the flow and yield stress of the encapsulating fluid.

2.8 Drop impact on viscoplastic surfaces

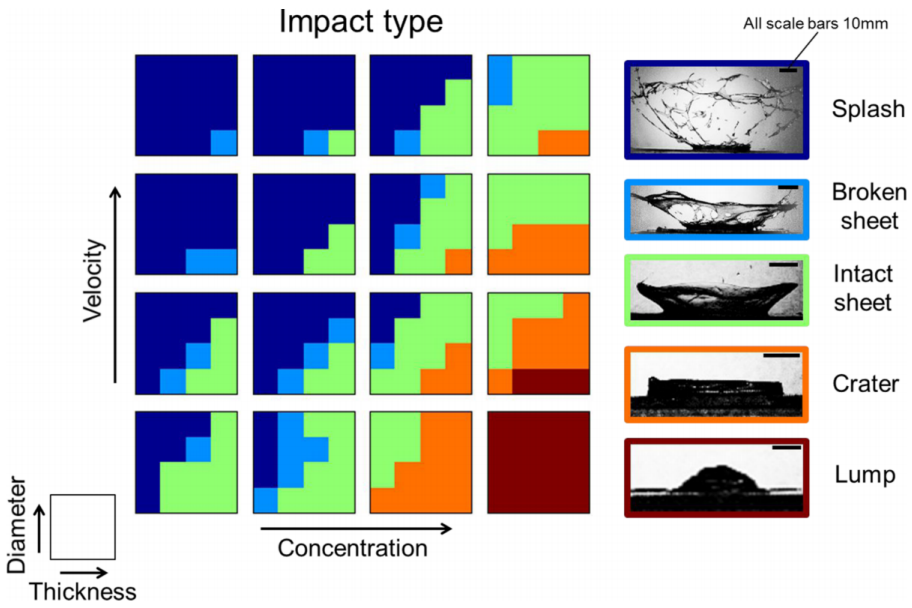

Figure 2.38: Impact outcome as a function of four independent parameters. (Adapted from [31]).

Blackwell et al. experimentally investigate the impact of yield stress fluid drops on horizontal surfaces coated with a layer of the same material [31]. In this study the large long-lifetime ejection sheets with redirected momentum which extend away from the impact location are observed under certain impact parameters. In addition, the sheet may breakup and small droplets of threadlike shapes can be ejected from the rim of liquid sheet under critical splash conditions. In particular, the effect of four independent parameters on impact outcomes is investigated, including impact velocity, thickness of coating material, droplet size and concentration of Carbopol solution (i.e., rheological properties). Figure 2.38 maps the impact regimes of these four parameters. Each subplot in Figure 2.38 shows a specific impact outcome (indicated by the colour-coded box as: splash,

broken sheet, intact sheet, crater and lump) as a function of coating thickness and droplet size. The subplots are arranged as a grid with Cartesian coordinates of solution concentration and impact velocity.

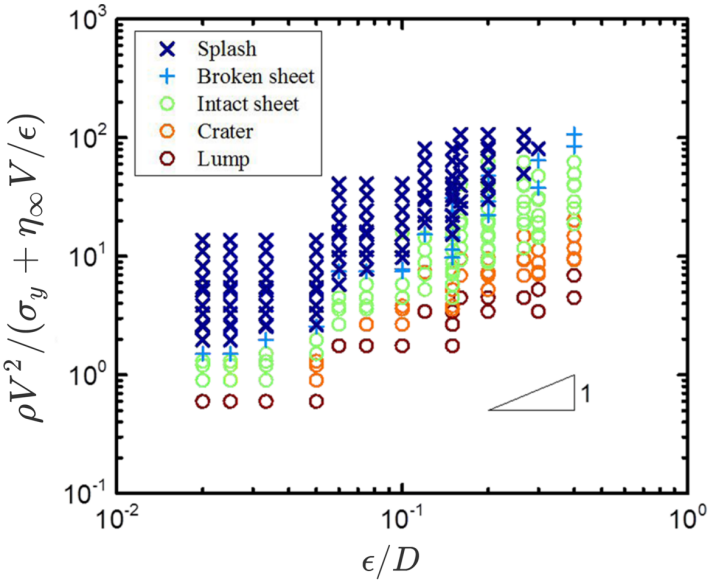

Figure 2.39: Reduced impact regime map by the introduction of a single dimensionless number which represents the ratio of the inertial force to flow force. (Adapted from [31]).

A single dimensionless number is proposed to predict the transition between splashing and sticking behaviours:

$$\mathrm{IF}^* = \frac{\rho u_i^2}{\sigma_0 + \mu_\infty u_i/\epsilon}\left(\frac{D_0}{\epsilon}\right), \tag{2.75}$$

where ϵ denotes the thickness of the coated material, σ_0 is the yield stress, and μ_∞ is the infinite shear rate viscosity. This quantity expresses the competition between the inertial force ($\sim \rho u_i^2 \times D_0^2$) and dissipative flow force ($(\sigma_0 + \mu_\infty u_i/\epsilon) \times D_0\epsilon$) which is contributed by both the force resulted from yield stress and the viscous force. The dimensionality of the impact regime map is reduced to one by the introduction of this single dimensionless number (IF^*) as shown in Figure 2.39, in which it is observed the transition regime scales as:

$$\frac{\rho u_i^2}{\sigma_0 + \mu_\infty u_i/\epsilon} \sim \frac{\epsilon}{D_0} \tag{2.76}$$

Furthermore, beyond the identification of sticking/splashing transition, the quantitative measures, such as impact event duration time, material rebound height, maximum radial spread distance, and final crater diameter are investigated in [32] by plotting these measures as a function of the same dimensionless number which reduced the impact regime map (Equation 2.75). The scaling laws are observed and the dimensionless number is found to be capable of describing the impact behaviours characterised by these quantitative measures.

2.9 Drop impact on PDMS surfaces

PDMS (Polydimethylsiloxane) is perhaps the most widely used silicon-based organic polymer in scientific research. It optically clear and elastic. Its Youngs modulus is determined by the mixing ratio of the 'base' and 'curing agent' (sometimes also referred as 'crosslinker'). For this reason, it is often adopted to manufacture model elastic materials with a wide range of elastic modulus in various types of experiments (e.g., drop behaviours on elastic surfaces) by altering the mixing ratios. This section reviews some recent works on the drop impact on PDMS surfaces.

Mangili et al. have experimentally studied the impacts of water drops (diameter ~ 2.85mm) on flat PDMS substrates with different softness and surface roughness [112]. Particularly the effect of substrate softness on drop behaviours and the maximum deformation of the substrate during impact are investigated. With the observation of the same maximum spreading diameter for drop impacts on both hard and soft substrates, it is found that the effect of substrate softness on the spreading behaviour is almost negligible. However the retraction stage and the post-spreading oscillations can be considerably affected by the substrate softness. The recoiling of impacting drops on a relatively hard substrate (i.e., high elastic modulus) is more pronounced compared to that on a soft substrate. The oscillation of the impacting drop after the initial spreading is also observed

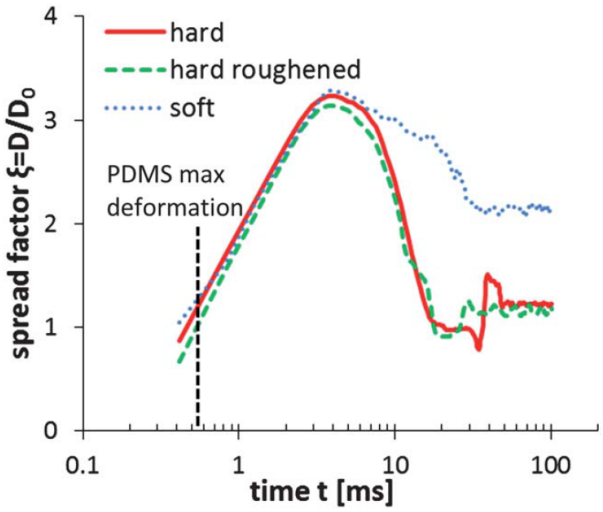

Figure 2.40: Spreading factor ($\xi(t) = D(t)/D_0$) as a function of time for different substrates: hard (red line), hard roughened (green dashed line) and soft (blue dotted line). (Adapted from [112]).

to be largely inhibited by the substrate softness (the fluctuation time of the impacting drop on soft substrate is only half of that on hard substrate). The effect of substrate softness on drop behaviours can be clearly seen in Figure 2.40 which plots the spreading factor ($\xi(t) = D(t)/D_0$) as a function of time for different substrates (hard, hard roughened and soft).

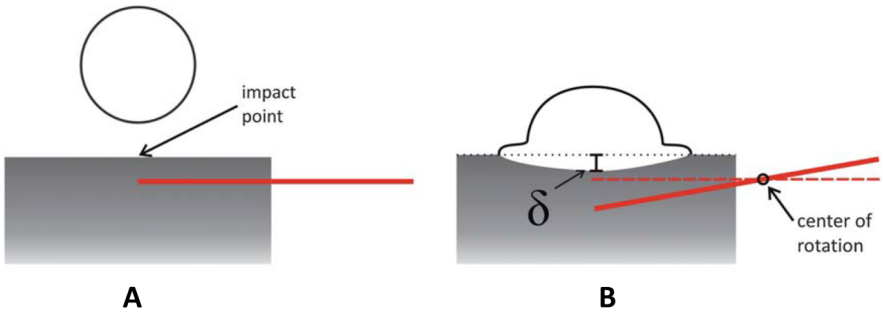

Figure 2.41: Schematic of the operating mechanism of the inserted cantilever system to measure the substrate deformation: (A) before impact, (B) during impact. The substrate deformation δ (Adapted from [112]).

The substrate deformation is measured by inserting a cantilever into the PDMS substrate just under the impact point and calculating the deformation from the displacement of the free end of the cantilever. The operating mech-

anism of the inserted cantilever system to measure the substrate deformation is schematically shown in Figure 2.41: (A) before impact, (B) during impact. The measured data of maximum substrate deformation as a function of impact velocity (u_i) are fitted to a power law, which gives:

$$\delta = 13.8 u_i^{1.56}. \tag{2.77}$$

As a result, a nonlinear correlation between the maximum substrate deformation and the impact kinetic energy is found: $\delta \sim E_{\mathrm{k}}^{0.78}$.

The fact that the retraction of impacting drops decreases with decreasing substrate elasticity is confirmed by the work of Alizadeh et al. [1], however in this study it is also shown that the substrate elasticity has very little effect on the dynamics of impacting drops on textured surfaces with periodic arrays of microstructures (i.e., superhydrophobic surfaces). In another experimental study of drop impact on soft PDMS surfaces [46], the evolution of the entrapped air under an impact droplet is investigated. A thin air film during the impact is observed due to the shear-thinning property of the surface, which reduces the surface energy and leads to the rebound of the droplet.

2.10 Drop impact on surfaces with arbitrary shapes

Hardalupas et al. conduct experiments on sub-millimetre droplet impingement onto spherical surfaces with diameters of the order of 1 mm, and it was found that the onset of reatomisation is promoted with the increase of surface curvature [85]. Motivated by the aim to measure the spatial and temporal variation of film thickness during drop impact, which is extremely difficult for drop impact on a flat surface, Bakshi et al. [6] investigate the impact of a droplet onto a spherical target experimentally and theoretically. Reynolds number and target-to-drop size ratio are observed to affect the dynamics of the film flow on the surface of the target. Additionally, an experimental study on the drop impact of heptane and butanol

on wetted spheres shows that the spreading factor defined as the ratio between the spreading area and the drop surface area increases as the curvature ratio grows or liquid viscosity reduces [103].More recently the dynamics of drop impact on spherical surfaces has been simulated numerically using different methods including Lattice-Boltzmann method and Volume of Fluid method [111, 162, 163], results show good agreement with the existing experimental data in literatures. Besides a spherical shape of the impact surface, the drop impact on substrates of other arbitrary shapes has also been investigated experimentally and numerically, such as cylindrical surfaces [104, 105, 122] or rectangular microcavities [106, 148]. Figure 2.42 displays some examples of drop impact on surfaces with arbitrary shapes in literature: (A) spherical surface, (B) rectangular microcavity & (C) cylindrical surface.

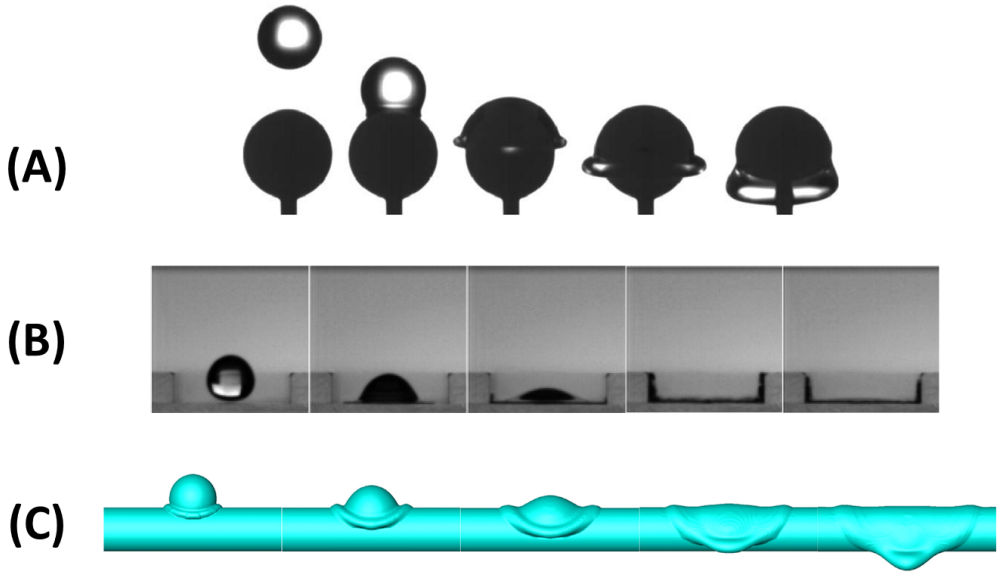

Figure 2.42: Examples of drop impact on surfaces with arbitrary shapes: (A) spherical surface (experiment from [6]), (B) rectangular microcavity (experiment from [148]) & (C) cylindrical surface (numerical simulation from [104]).

2.11 A novel image-processing technique based on a goniometric mask

Recently, a novel image-processing scheme based on a goniometric mask has been proposed to measure the dynamic contact angle during the impact process [26, 27, 28]. In conventional goniometry methods, contact angles are generally measured by fitting one or more analytical functions to the drop shape (e.g., the Axisymmetric Drop Analysis method) [58, 90, 139]. Compared to these methods, the novel technique does not require either the drop symmetry or the drop shape of a spherical cap, which is desirable when measuring the dynamic contact angle of drop impact on convex surfaces.

2.11.1 Angle-area correlation in a Cartesian coordinate system

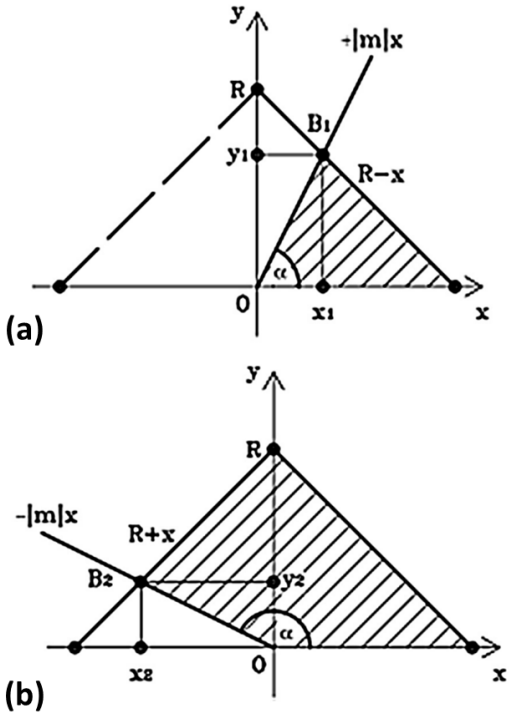

Figure 2.43: Geometric schematic for the correlation between angle α and area of polygon (represented by the shaded area): (a) acute angle ($\alpha < 90^o$), (b) obtuse angle ($\alpha > 90^o$). (Adapted from [27])

In a Cartesian coordinate system, the angle α between the x-axis and a straight line $y = mx$ is normally formulated as: $\alpha = \arctan(m)$. However, this angle can also be correlated to the area of a polygon enclosed by the x-axis and three straight lines $y = mx$, $y = R - x$, $y = R + x$, where R represents a positive constant. The type of the polygon is determined by the values of m: a triangle for $m > 0$ and a quadrangle for $m < 0$ (as shown in Figure 2.43(a) and Figure 2.43(b), respectively). The formula which correlates the angle α to the polygon area A_λ is derived as [27]:

$$\alpha = \frac{\pi}{2}(1 - \lambda) + \arctan[\lambda \frac{R^2(1 - \lambda) - 2A_\lambda}{2A_\lambda - R^2}], \tag{2.78}$$

where λ is the sign function of m: $\lambda = \mathrm{sgn}(m)$.

As a result, the triangle formed by the lines $y = R \pm x$ and x-axis can be conceived as an ideal goniometer, which is able to measure the angle between a line through the origin of the Cartesian coordinate system and x-axis.

2.11.2 Goniometric mask

The angle-area correlation discussed in last section can be utilized to measure the angle between the tangent line to any point of a contour line in a binary image and the horizontal line. As shown in Figure 2.44(a), the triangle goniometer in the Cartesian coordinate system can be represented by a smaller binary image containing a triangle made up of pixels with value 1 (referred as the *goniometric mask*). The area can be readily obtained by counting the number of pixels in the region where the target object and the reference triangle overlap. In the case of a binary image, the count of pixels within a certain region can be achieved through a two-dimensional convolution operation. The discrete convolution operation between two matrices gives a matrix whose elements are the sums of the products of the elements of these two matrices. As shown in Figure 2.44(b), the goniometric mask must be flipped both vertically and horizontally since the convolution operation reverses the order of the rows and columns of the second matrix. Hence

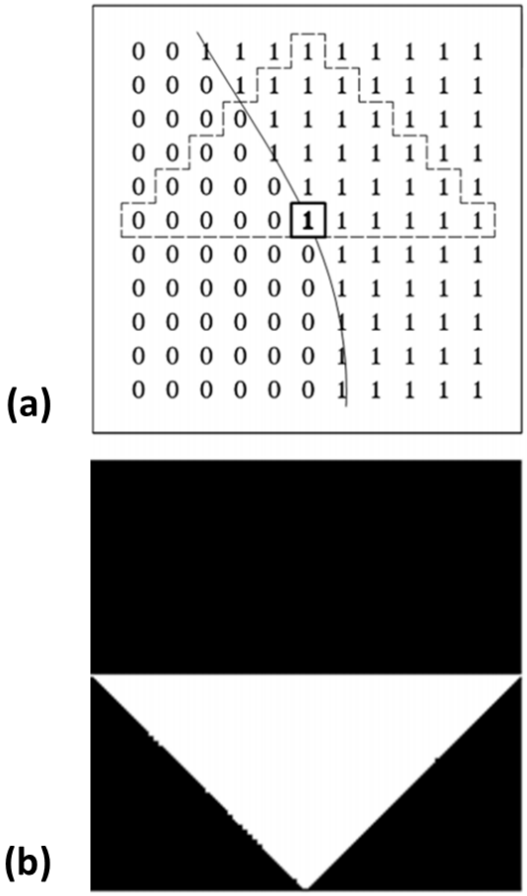

Figure 2.44: Example of angle measurement by a goniometric mask on a binary image: (a) A sampling window of the binary image, the solid line indicates the contour line of the target object, and the elements enclosed by the dashed line are considered for angle-area calculation. (b) The binary image generated by the matrix of the goniometric mask. (Adapted from [27])

the general form of the goniometric mask matrix is written as:

$$\begin{bmatrix} 0 & 0 & 0 & \dots & 0 & 0 & 0 \\ \vdots & \vdots & \vdots & \dots & \vdots & \vdots & \vdots \\ 0 & 0 & 0 & \dots & 0 & 0 & 0 \\ 1 & 1 & 1 & \dots & 1 & 1 & 1 \\ 0 & 1 & \dots & 1 & \dots & 1 & 0 \\ \vdots & 0 & \ddots & 1 & \iddots & 0 & \vdots \\ 0 & \dots & 0 & 1 & 0 & \dots & 0 \end{bmatrix}, \tag{2.79}$$

where the mask size z (i.e., the number rows or columns of the matrix) is $2n+1$ (n is an integer number).

Chapter 3

Experimental Techniques

3.1 Fluid preparation

All the non-Newtonian model fluids used in the present research are water-based polymer solutions. The solvent water was de-ionised using a purifier (Barnstead Easypure II 7136) before mixing.

Xanthan gum solutions were chosen as pure shear-thinning model fluids since they only exhibit shear-thinning behaviour due to the rigid rod-like conformation of dissolved molecules. The mixture of xanthan gum power (Sigma-Aldrich, ρ = 1500 kg/m^3, average molecular weight: $4\times10^6 - 12\times10^6$ Da) and de-ionised water was stirred by a magnetic stirrer (Stuart CB162) for about four hours to ensure homogeneity.

Polyacrylamide solutions were chosen as viscoelastic model fluids. However except the viscoelastic behaviour, they also exhibit shear-thinning behaviour like the xanthan gum solutions. The mixture of polyacrylamide power (Sigma-Aldrich, ρ = 1130 kg/m^3, average molecular weight: 27×10^6 Da) and de-ionised water was stirred by the same magnetic stirrer for about four hours to ensure homogeneity.

Glycerol solutions were chosen as Newtonian model fluids. The mixture of glycerol (Sigma-Aldrich, ρ = 1250 kg/m^3) and de-ionised water was stirred by the same magnetic stirrer for about one hour to ensure homogeneity.

Carbopol solutions were chosen as viscoplastic model fluids. They were pre-

pared by dispersing Carbopol 940 powder (Lubrizol, true density: ρ = 1400 kg/m^3) into de-ionised water. Carbopol solutions must be neutralised in order to achieve maximum viscosity (see Appendix B for reference). Aqueous NaOH solution (30% w/w) was then used to neutralise the Carbopol dispersions [55, 137].

3.2 Equilibrium drop diameter measurement

Table 3.1: Average single drop weights and equilibrium diameters with standard deviations for different model fluids.

Fluid	**Drop mass,** m **[mg]**	**Density,** ρ **[kg/m^3]**	**Diameter,** D_0 **[mm]**
100 ppm XG	14.96±0.70	1000	3.06±0.05
400 ppm XG	14.82±0.92	1000	3.05±0.06
80 ppm PAA	13.70±1.83	1000	2.97±0.13
300 ppm PAA	13.00±1.70	1000	2.92±0.13
6.39% GLY	14.20±1.32	1030	2.97±0.09
21.9% GLY	14.40±0.84	1060	2.96±0.06
74.0% GLY	16.20±1.40	1190	2.96±0.08
85.9% GLY	15.80±1.23	1240	2.90±0.08
0.067% CA	14.75±1.16	1000	3.04±0.08
0.079% CA	13.95±0.60	1000	2.99±0.04
0.086% CA	13.95±0.69	1000	2.99±0.05
0.1% CA	13.55±1.67	1000	2.96±0.12
0.113% CA	10.80±0.70	1000	2.74±0.06
0.124% CA	10.00±0.65	1000	2.67±0.06
0.142% CA	9.65±0.59	1000	2.64±0.05
water	15.40±1.36	1000	3.09±0.09

The value of the equilibrium drop diameter is of great importance in drop impact experiments both because of its role in the accurate calculation of impact Weber number ($We = \rho v_i^2 D_0/\sigma$) and in the normalization of morphological parameters (e.g., maximum spreading diameter, maximum bouncing height etc.).

In order to minimize the experimental error, the equilibrium diameter of a single drop was calculated based on the assumption that the drop is spherical, $D_0 = \sqrt[3]{6m/\pi\rho}$. A precision balance (Denver Instrument TP-124A) was used to measure the drop weight. Table 3.1 displays the average single drop weights over

50 samples (released from a blunt hypodermic needle: gauge 21, i.d. 0.495 mm) and the calculated equilibrium diameters with standard deviations for all the model fluids used in experiments (XG: xanthan gum solutions; PAA: polyacrylamide solutions; GLY: glycerol solutions; CA: Carbopol solutions).

3.3 Surface tension measurement

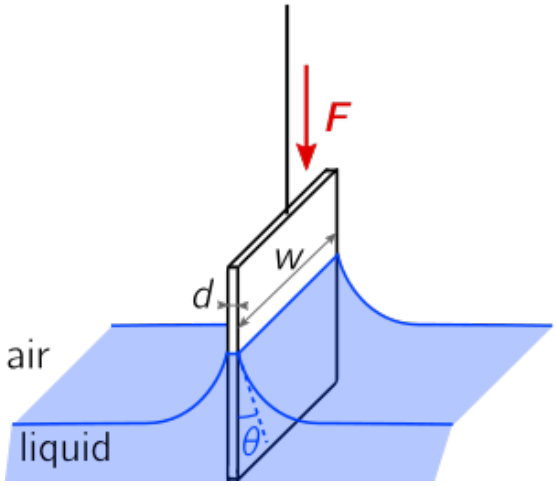

Figure 3.1: Schematic diagram of the Wilhelmy plate method.

The calculation of impact Weber numbers requires accurate values of the surface tensions of model fluids. In the present study, the surface tensions were measured by a tensiometer (Kruss K20 EasyDyne) using the Wilhelmy plate method. A schematic diagram of the Wilhelmy plate method is shown in Figure 3.1. In this method, a platinum plate is used to perpendicularly contact the interface between air and fluid to ensure complete wetting. The force exerted on the plate is measured by a sensitive force sensor. The surface tension is calculated by the Wilhelmy equation:

$$\sigma = \frac{F}{l\cos\theta}, \tag{3.1}$$

where l represents the wetted perimeter, $l = 2w + 2d$ (w: plate width & d: plate thickness), and θ is the contact angle between the plated and liquid. However in practice the contact angle is often not measured based on the assumption of

complete wetting ($\theta = 0$).

Table 3.2: Measured values of surface tensions and calculated capillary lengths of model fluids (* value taken from [38]).

Fluid	**Surface tension, σ [mN/m]**	**Capillary length, $l_c = \sqrt{\sigma/(\rho g)}$ [mm]**
100 ppm XG	72.70	2.72
400 ppm XG	71.50	2.70
80 ppm PAA	72.70	2.72
300 ppm PAA	71.40	2.70
6.39% GLY	72.30	2.68
21.9% GLY	71.50	2.62
74.0% GLY	66.90	2.40
85.9% GLY	65.60	2.32
CA (all concentrations)	66.00*	2.60
water	72.75	2.72

Table 3.2 displays the measured values of surface tensions at room temperature 20 °C and calculated capillary lengths of model fluids of different weight concentrations used in all the experiments. However so far there has not been a consensus on the definition of surface tension of the yield-stress fluids. This is due to the difficult task of isolating the contribution of yield stress when measuring the surface tension of a yield-stress fluid using conventional technique. Recently a systematic investigation on the measurements of the surface tension of viscoplastic fluids by Boujlel et al. showed that Carbopol gels appear to have almost the same value (0.066 N/m) of surface tension irrespective of their yield stress, but this value is only about 10% smaller than that of pure water at ambient temperature: 23 °C [38]. This value of the surface tension of Carbopol gels is used in the calculation of Weber number in the present work since our experiments were conducted at a close ambient temperature of 20 °C.

3.4 Rheology characterization

3.4.1 Shear-thinning & viscoelastic model fluids

Polyacrylamide (PAA) solutions were chosen as model viscoelastic fluids because they are also shear-thinning, therefore it was possible to isolate the effects of viscoelasticity by comparing them with purely shear-thinning fluids. To obtain fluids with matching rheology, two xanthan solutions (XG) with mass concentrations of 100 ppm (XG1) and 400 ppm (XG2) were prepared, and their flow curves were measured using an MCR302 rheometer (Anton Paar) equipped with cone-plate geometry (cone angle: 2°; diameter: 75 mm). A set of polyacrylamide

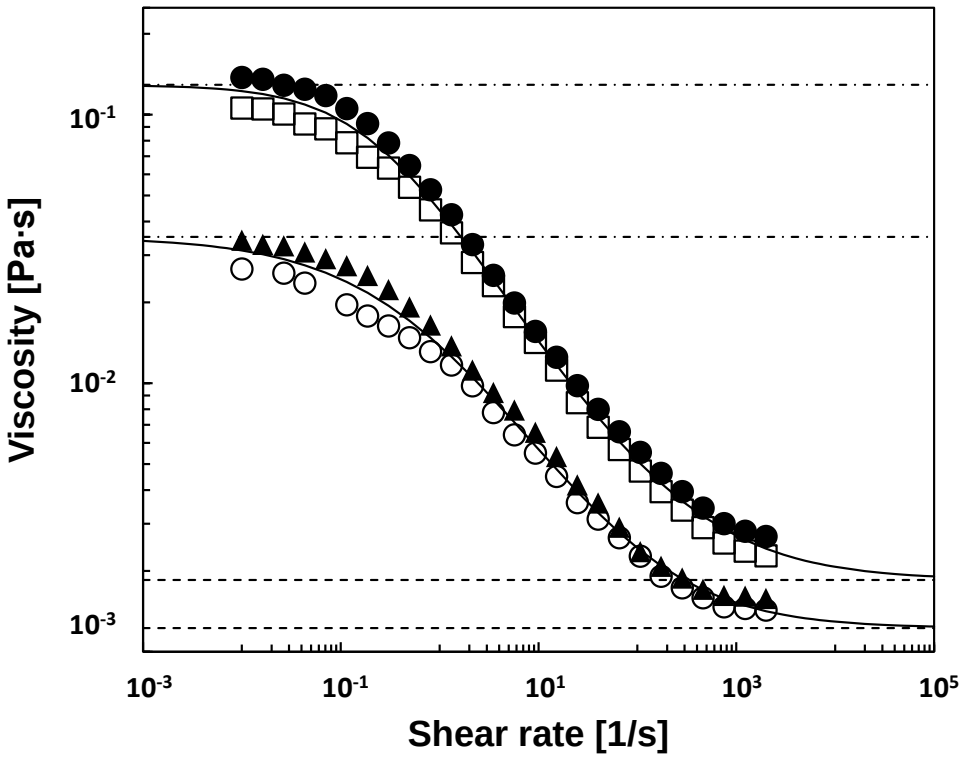

Figure 3.2: Flow curves of the model fluids measured with an MCR302 rheometer (Anton Paar) equipped with a cone-plate geometry (75 mm diameter; 2° angle): ○, 100 ppm XG, ▲, 80 ppm PAA, □, 400 ppm XG, and ●, 300 ppm PAA. Solid lines represent the Carreau-Yasuda model fit curves of the average values of measured XG and PAA data. Dashed lines and dot-dashed lines indicate the constant viscosities of GLY with infinite-shear viscosity and GLY with zero-shear viscosity, respectively.

Table 3.3: Rheological parameters obtained from CY model fitting.

Parameter	XG1 & PAA1	XG2 & PAA2
μ_0, [mPa·s]	33	129
μ_∞, [mPa·s]	1.2	1.9
λ_{CY}, [s]	1.71	4.93
a, [-]	0.54	0.84
n, [-]	0.63	0.59

solutions of different concentration was then prepared from successive dilutions of a master solution with mass concentration of 1600 ppm. The flow curves of these solutions were measured and compared with those of xanthan solutions; the procedure was repeated until 80 ppm (PAA1) and 300 ppm (PAA2) polyacrylamide solutions with flow curves matching those of xanthan solutions were identified. The average values of measured XG and PAA data were fitted with the Carreau-Yasuda model, to obtain the values of the zero-shear rate (μ_0) and infinite shear rate (μ_∞) viscosities:

$$\mu_{\mathrm{CY}} = \mu_\infty + \frac{\mu_0 - \mu_\infty}{\left[1 + (\lambda_{\mathrm{CY}} \cdot \dot{\gamma})^a\right]^{\frac{n}{a}}}. \tag{3.2}$$

The values of zero-shear-rate viscosities, μ_0, infinite-shear-rate viscosities, μ_∞, and other rheological parameters obtained from the Carreau-Yasuda model fitting are shown in Table 3.3.

Table 3.4: Rheological properties of shear-thinning, viscoelastic & Newtonian model fluids.

Fluid	Concentration [w/w]	Newtonian viscosity [mPa·s]	μ_0 [mPa·s]	μ_∞ [mPa·s]
GLY1	6.39%	1.2	-	-
GLY2	21.9%	1.9	-	-
GLY3	74.0%	33	-	-
GLY4	85.9%	129	-	-
XG1	100 ppm	-	33	1.2
XG2	400 ppm	-	129	1.9
PAA1	80 ppm	-	33	1.2
PAA1	300 ppm	-	129	1.9

Finally, Newtonian glycerol solutions (GLY) were prepared with viscosities

equal to the zero-shear-rate viscosity (μ_0) and infinite-shear-rate viscosity (μ_∞) of the corresponding XG and PAA solutions. A synopsis of the model fluid parameters is reported in Table 3.4, while Figure 3.2 shows their flow curves. Open and filled symbols represent the measured data of XG and PAA solutions, respectively, and solid lines are the Carreau-Yasuda model fit curves of the average values of measured XG and PAA data. The dashed lines represent the constant viscosities of the GLY solutions matching μ_0 and μ_∞ for each corresponding XG solutions.

3.4.2 Viscoplastic model fluids

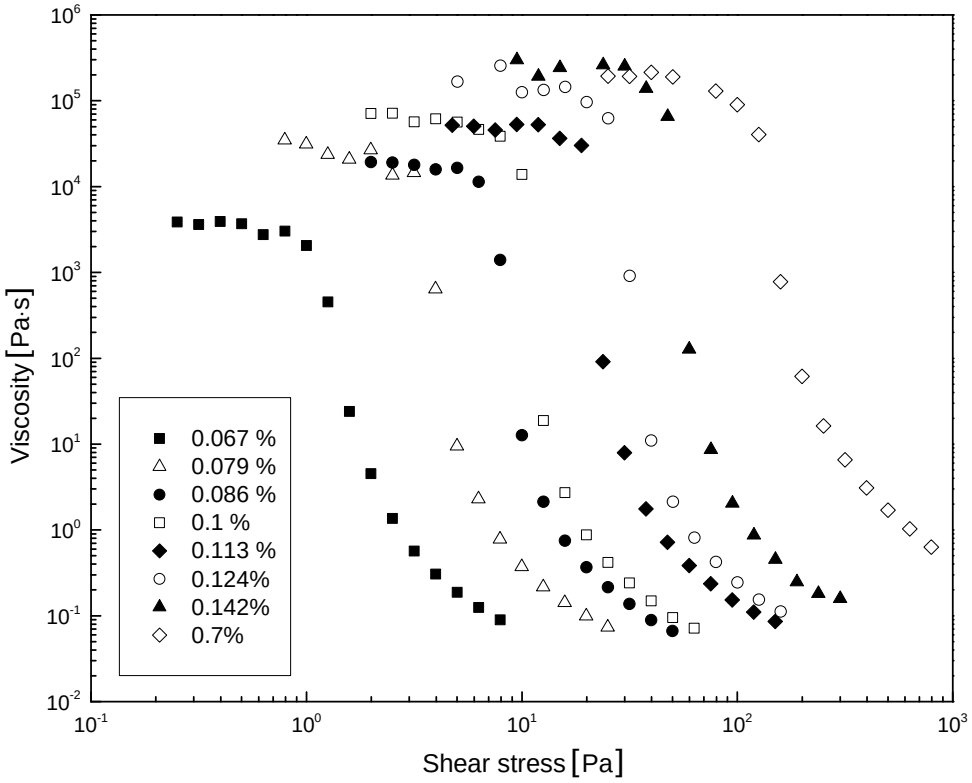

Figure 3.3: Flow curves of the model viscoplastic fluids of different concentrations.

Fluids with eight different concentrations of Carbopol (Ca 0.067%, 0.079%, 0.086%, 0.1%, 0.113%, 0.124%, 0.142% w/w and 0.7% w/w, respectively) were prepared in order to study the effect of large variations of the yield stress on drop

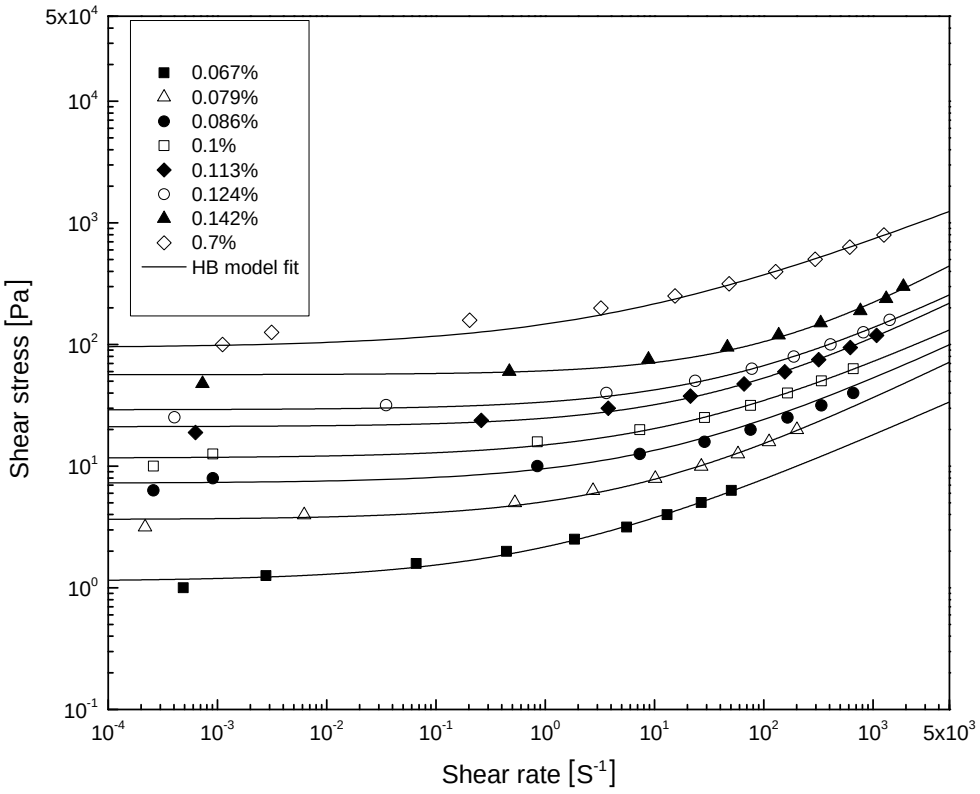

Figure 3.4: Shear stresses of the model fluids as a function of shear rates and the corresponding H-B fit curve.

impact behaviour. Viscosities of the model viscoplastic fluids were measured using a rotational rheometer (TA Instruments AR 1000) with a parallel plate geometry (diameter: 40 mm) with rough surfaces to avoid wall slip artefacts. The measured flow curves are shown in Figure 3.3. To identify the yield stress, viscosity data obtained for shear stresses above the yield point were fitted with the Herschel-Bulkley (H-B) model, as shown in Figure 3.4:

$$\tau = \tau_0 + k\dot{\gamma}^n. \tag{3.3}$$

where τ is the shear stress, τ_0 the yield stress, $\dot{\gamma}$ the shear rate, k the consistency index, and n the flow index. The resulting yield stress values for Carbopol solutions of different concentrations were shown in Table 3.5, which is consistent with values reported in the reference literature [137]. The concentrations of the Carbopol solutions were intentionally selected to yield a Bingham-Capillary

number range covering unity, which ensured that the yield stress was comparable with or higher than the Laplace pressure at relatively high B numbers.

Table 3.5: Properties of model viscoplastic fluids.

Ca	k [**Pa·s^n**]	n [-]	**Yield stress,** τ_0 [**Pa**]	**Bingham-Capillary number,** $B = \tau_0 D_0/\sigma$ [-]
0.067%	1.04	0.40	1.13	0.052
0.079%	1.48	0.45	3.64	0.16
0.086%	2.32	0.43	7.24	0.33
0.1%	3.31	0.42	11.7	0.52
0.113%	3.74	0.47	21.1	0.88
0.124%	4.66	0.46	29.1	1.2
0.142%	4.31	0.53	56.5	2.3
0.7%	53.3	0.36	94.0	-

3.5 Convex hemispherical elastic substrates

3.5.1 Selection of elastic modulus & manufacturing

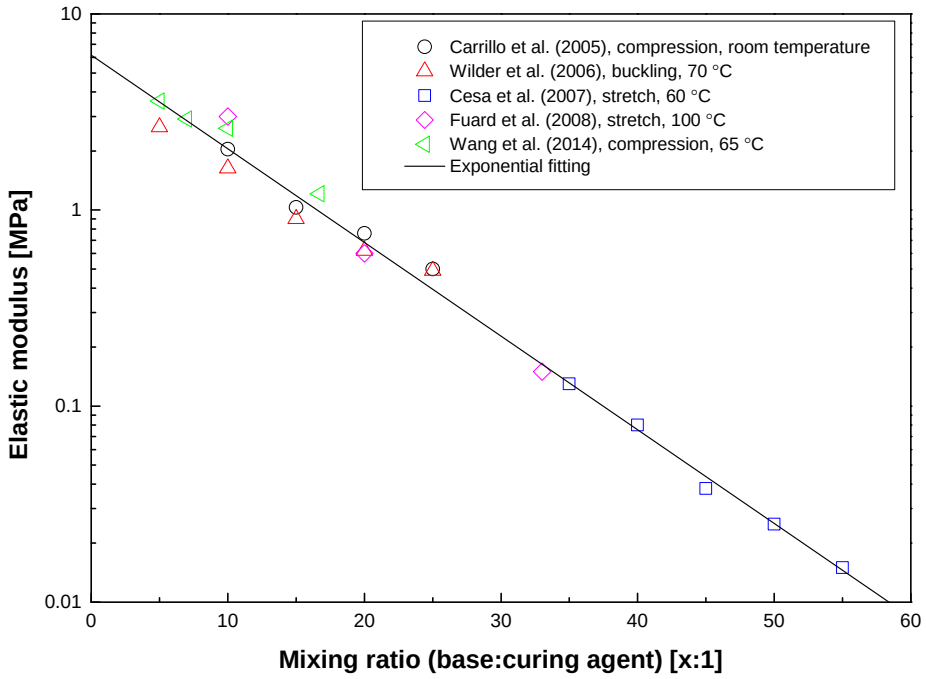

Figure 3.5: The measured elastic modulus of PDMS as a function of mixing ratio reported by different research groups.

Table 3.6: Elastic modulus of PDMS of different mixing ratios.

Mixing ratio	**Elastic modulus,** E **[Mpa]**
10:1	2.05
30:1	0.23
40:1	0.08

The convex hemisphere elastic substrates were manufactured using polydimethylsiloxane (PDMS). The commercial product Sylgard 184 (SigmaAldrich) was selected since it has been widely used in previous works. The elastic modulus of PDMS can be adjusted by changing the mixing ratio of the base polymer and the crosslinker. Figure 3.5 shows the measured experimental data of the elastic moduli of PDMS as a function of the mixing ratio reported by five research groups [40, 43, 71, 153, 155]. The methods for measurement include compression, stretch and buckling. The baking temperatures range from room temperature to 100 °C. It is observed that the experimental data obtained by different researchers show

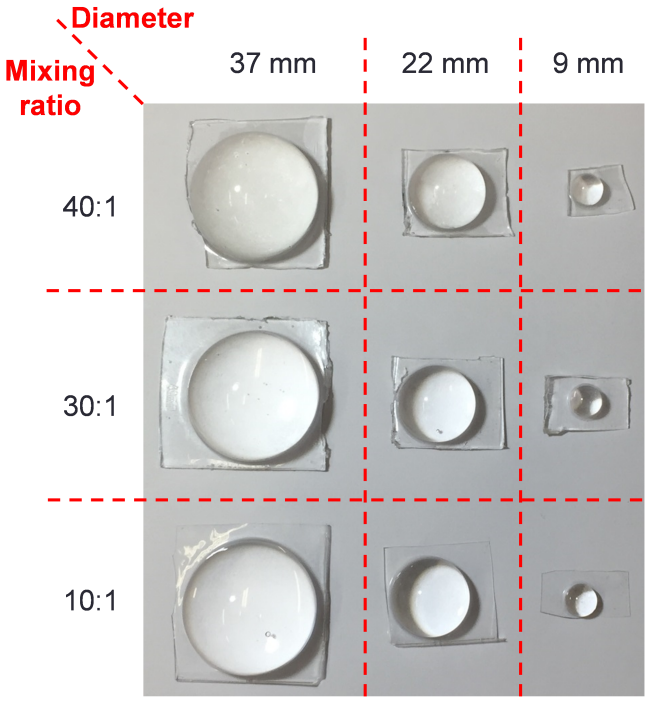

Figure 3.6: Manufactured samples of hemispherical PDMS substrates of different diameters and mixing ratios.

very good consistency and the elastic modulus decreases exponentially as the mixing ratio grows. Thus all the data are fitted into an exponential model, which yields a coefficient of determination $R^2 = 0.988$:

$$\mathrm{E} = 6.17 \cdot e^{-0.11\mathrm{x}}, \tag{3.4}$$

where x represents the mixing ratio of the base and the curing agent. In order to study the effect of the elastic modulus on the impact morphology of the drop, three different mixing ratios are selected to manufacture the substrates: 10:1, 30:1 & 40:1. The corresponding elastic moduli of the PDMS of different mixing ratios are calculated using Equation 3.4 and the values are shown in Table 3.6.

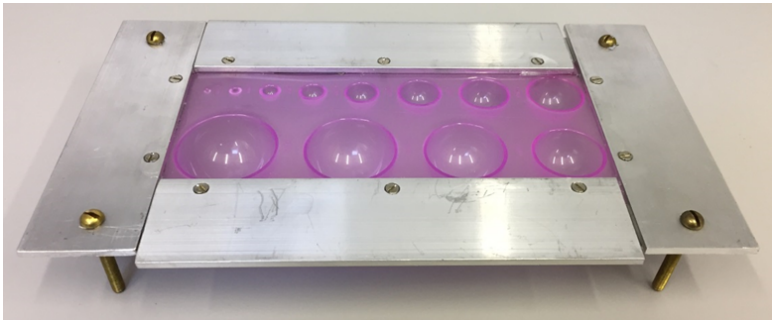

Figure 3.7: Photograph of the mould for manufacturing PDMS substrates.

PDMS hemispheres of different diameter were produced by curing the Sylgard 184 compound in a suitable mould (Figure 3.7). After the mould was filled with the mixture of base and curing agent, it was baked in an oven at 65 °C for 24 hours to make sure the sample was completely cured [71]. Some manufactured samples of hemispherical PDMS substrates of different diameters and mixing ratios are displayed in Figure 3.6.

3.5.2 Wetting properties of PDMS

It has been experimentally shown that the contact angle hysteresis ($\Delta\theta = \theta_{\mathrm{ad}} - \theta_{\mathrm{re}}$, where θ_{ad} represents the advancing contact angle and θ_{re} the receding contact angle) changes with the elastic modulus of the soft substrates [63]. The static

Table 3.7: Static, advancing & receding contact angle (θ_0, θ_{ad} & θ_{re}) and contact angle hysteresis ($\Delta\theta$) of flat substrates with the same elastic moduli in experiments.

E [MPa]	θ_0 [°]	$\theta_{\mathbf{ad}}$ [°]	$\theta_{\mathbf{re}}$ [°]	$\Delta\theta$ [°]
2.05	104 ± 3	118 ± 2	81 ± 3	38 ± 5
0.23	115 ± 6	123 ± 5	49 ± 4	73 ± 5
0.08	114 ± 2	128 ± 3	0	128 ± 3

contact angle and contact angle hysteresis of water drop on flat PDMS substrates with the same elastic moduli as the hemispherical substrates used in the present experiments were measured, and their values are reported in Table 3.7. Advancing and receding contact angles were measured using the volume change method; the advancing contact angle was measured by recording the gradually growing droplet (increasing volume) through the injection of liquid from a needle, whereas the receding contact angle was measured by decreasing the volume. As shown in Table 3.7, the contact angle hysteresis increases significantly as the elastic modulus decreases. Especially in the case of the softest surface (E=0.08 MPa), the decrease in the drop volume does not lead to retraction of the contact line and the liquid periphery remains pinned until the volume reduces to zero; thus, in this case the receding contact angle is almost zero. The experimental data in Table 3.7 is consistent with the data reported in a previous experimental investigation [112].

3.6 Leidenfrost drop impact

3.6.1 Experimental setup

The experimental setup for Leidenfrost drop impacts is schematically described in Figure 3.8. The drop dispensing system consists of a syringe, a blunt hypodermic needle (gauge 21, i.d. 0.495 mm) and a flexible tube which connects the syringe to the needle. The surface of the aluminium block was well polished and kept at the temperature of 400 °C. Temperature could be controlled within ±1°C by a PID

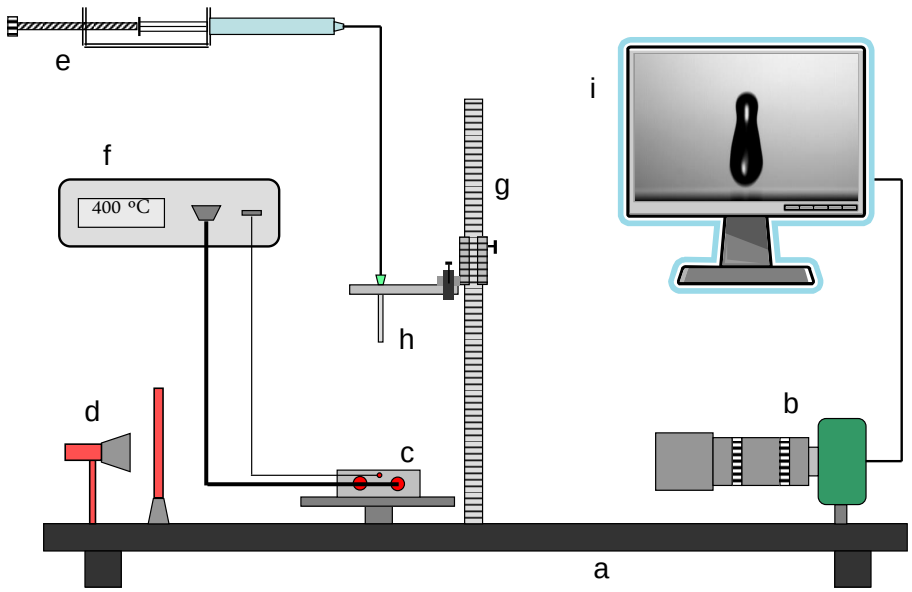

Figure 3.8: Schematic of the experimental setup for Leidenfrost drop impacts: (a) optical breadboard; (b) high-speed camera; (c) heated aluminium block; (d) LED backlight; (e) drop dispensing system; (f) temperature controller; (g) height gauge; (h) needle; (i) computer.

controller driven by a K thermocouple placed 1 mm below the point of impact. This temperature is high enough to keep the vapour film stable and avoid the formation of secondary droplets [13, 19, 133]. The photograph of experimental rig is displayed in Figure 3.9.

The digital height gauge (indicted by 'g' in Figure 3.8) allowed one to adjust the vertical distance between the needle and the aluminium surface hence the impact velocity and the Weber number, $We = \rho D_0 u_i^2/\sigma$, which represents the competition between kinetic energy and surface energy. It has been proved that the impact velocity is almost identical to the theoretical free fall velocity, $u = \sqrt{2g(H_0 - D_0)}$, if the falling heights are smaller than 15cm in the previous work [17]. Thus the Weber number can be calculated as

$$We = \frac{2\rho g D_0 (H_0 - D_0)}{\sigma}. \tag{3.5}$$

In this study, the impact velocities of 300 ppm PAA drops are reduced due to the

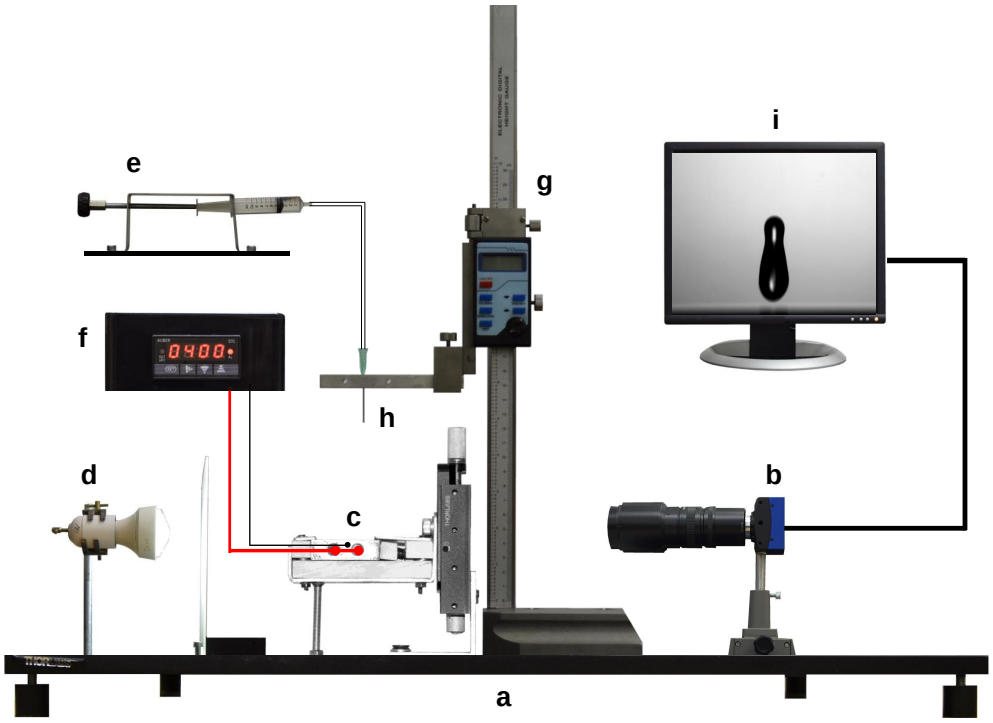

Figure 3.9: Photograph of the experimental rig for Leidenfrost drop impacts: (a) optical breadboard; (b) high-speed camera; (c) heated aluminium block; (d) LED backlight; (e) drop dispensing system; (f) temperature controller; (g) height gauge; (h) needle; (i) computer.

creation of a long filament after the drops are released because of high viscoelastic effect. Thus instead of the calculated We numbers, the impact Weber numbers based on the true impact velocity (measured from digital image processing) were used for 300 ppm PAA drops. For Leidenfrost drop impact experiments, the impact Weber numbers were in the range between 8 and 110. For each set of experimental parameters (i.e., fluid concentration and Weber number), the drop impact experiment was repeated five times for the sake of statistical analysis.

To determine the properties of the fluids during impact on a hot surface, it is necessary to estimate the drop temperature with a reasonable precision. Since there is a co-existence of the liquid and the vapour phase, and neglecting non-equilibrium effects, in the Leidenfrost regime the drop should be at saturation (100°C for water at atmospheric pressure). However, the impact duration is very short; typically, the contact time of Leidenfrost drops with $D_0 = 3$ mm is about

15 ms [17]. Thus, the temperature distribution in the drop may not be uniform, so that only the part directly exposed to the heat flux from the impact surface reaches the saturation temperature. An estimate of the heat transfer between the drop and the surface suggests that, even for drop diameters of few millimetres, and in the most favourable heating conditions, the average temperature of the drop increases by only about 10°C with respect to the ambient temperature [18]. Thus, one can evaluate the fluid properties at ambient temperature as a first approximation.

The impacts of single drops were recorded using a high-speed CMOS camera (Mikrotron MC1310) equipped with a 18-108/2.5 zoom lens (Navitar Zoom 7000) at the rate of 1000 frames per second and a resolution of 480×576 pixels, which allowed measurements with a typical spatial resolution of 27 μm per pixel. The camera was horizontally aligned with the impact surface in order to measure the bouncing height of the drop with precision. Back-to-front illumination was provided by a LED lamp (Philips Accent LED), which ensured a uniform intensity in the field of view.

3.6.2 Image processing

Drop impact movies were analysed using a custom-built LabView application operating in two stages: in the first stage, the background is subtracted from each frame, and the image brightness, contrast, gamma correction and digital gain can be adjusted manually; in the second stage, the application extracts from each frame the gap between the drop and the surface, G, and the horizontal and vertical dimensions of the drop, D_H and D_V, normalized with respect to the equilibrium drop diameter, as shown in Figure 3.10. From these measurements, the height of the drop centre of mass was calculated as $H_C = G + D_V/2$ (note that such definition relies on the assumption drops are symmetric during rebound, which is not always the case).

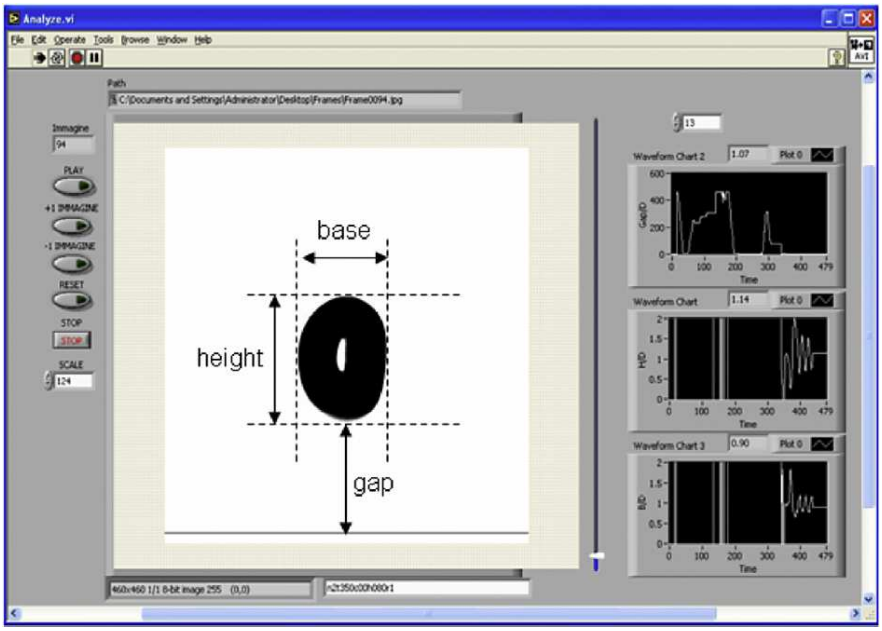

Figure 3.10: Digital image processing software and definition of measured lengths.

For the case in which the drop does not break up into smaller droplets during the bouncing phase after the impact on the heated surface, the maximum bouncing height can be easily obtained by finding the maximum value of the H_C series. However this method can not be applied to the case in which a satellite drop is created during rebound (as shown in Figure 3.11) due to the incorrectly measured values of D_V (the length from the bottom of the major drop to the top of the satellite drop) in the software. The high vertical velocity of the satellite drop, V_S, enables the satellite drop to reach a much larger bouncing height than the major drop thus it will 'escape' from the upper limit of the recording area and reappear in the recording area again when it falls back. The maximum bouncing height of the major drop can be obtained by selecting the maximum value of the certain H_C series which are measured without the satellite drop during rebound. However if one wants to calculate the energy dissipation during impact for this case using Equation (2.68), the calculated value would be inaccurate due to the neglected kinetic energy of the satellite drop. Here an approach which is devised to modify the measured maximum value of H_C series based on energy

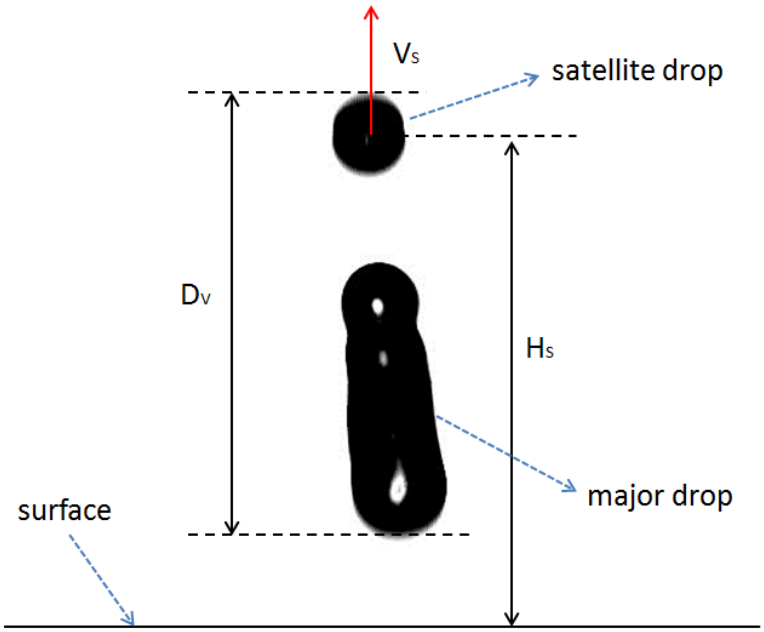

Figure 3.11: The creation of satellite drop during rebound.

conservation is proposed as follows.

Let M_0 denote the total mass of the original drop before break-up, M_S the mass of the satellite drop, M_M the mass of the major drop, $H_{max}^{(mea)}$ the measured maximum bouncing height of the major drop, $H_{max}^{(mod)}$ the modified maximum bouncing height, H_S the height of the centre of mass of the satellite drop, V_S the instantaneous vertical velocity of the satellite drop (the velocity can be calculated by the displacement of the centre of mass between two consecutive images), g the acceleration of gravity. According to energy conservation, the sum of the mechanical energy of major and the mechanical energy of satellite drop equals the maximum possible gravitational potential energy of the original drop if it did not break up into two drops,

$$(M_S g H_S + \frac{1}{2} M_S V_S^2) + M_M g H_{max}^{(mea)} = M_0 g H_{max}^{(mod)}. \tag{3.6}$$

Define a parameter k as the ratio of the mass of the satellite drop to the mass of the original drop, $k = \frac{M_S}{M_0} = (\frac{D_S}{D_0})^3$, where D_S and D_0 denote the diameter of satellite drop and original drop respectively. Then Equation (3.6) can be rewritten

as

$$H_{max}^{(mod)} = kH_S + (1-k)H_{max}^{(mea)} + \frac{kV_S^2}{2g}. \tag{3.7}$$

The Equation (3.7) is the derived formula for the calculation of the modified maximum bouncing height for the case of 'one satellite drop' and it can be easily extended to the case of two or more satellite drops. The formula for the case of two satellite drops is presented as

$$H_{max}^{(mod)} = k_1H_{S1} + k_2H_{S2} + (1-k_1-k_2)H_{max}^{(mea)} + \frac{k_1V_{S1}^2 + k_2V_{S2}^2}{2g}, \tag{3.8}$$

where the subscripts '1' and '2' are used to distinguish the symbols of the first satellite drop and those of the second satellite drop. The experimental data of the maximum bouncing heights presented in this work are all modified values if not specified.

3.7 Drop impact on liquid substrates

3.7.1 Experimental setup

Replacing the heated aluminium surface in the experimental setup for the Leidenfrost drop impact shown in Figure 3.8 with a liquid substrate contained in a transparent box, one can get the experimental setup for drop impact on liquid substrates as described schematically in Figure 3.12. The corresponding photograph of experimental rig is shown in Figure 3.13.

Drops were released from a blunt hypodermic needle (gauge 21, i.d. 0.495 mm) and impacted on a viscoplastic fluid layer contained in a cubic transparent plastic box (10cm×10cm×10cm). For drop impact experiments on liquid substrates, the impact Weber numbers were in the range between 15 and 176. The depth of the liquid substrate was always set to 1 cm since in preliminary experiments it was found that the substrate depth had negligible effect on the morphology of drop impact if the depth was more than three times the equilibrium drop diameter. The impacts of single drops were recorded using a high-speed CMOS

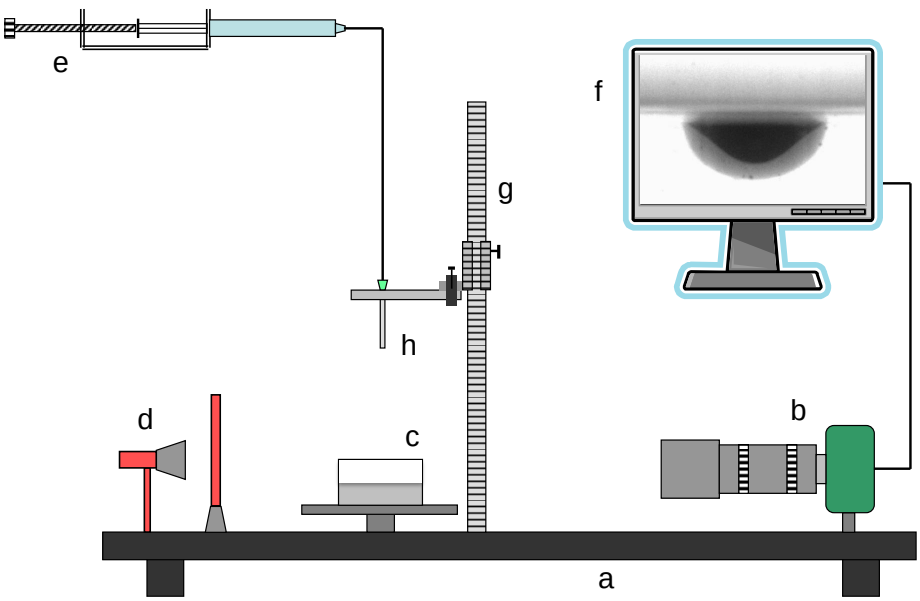

Figure 3.12: Schematic of the experimental setup for drop impacts on liquid substrates: (a) optical breadboard; (b) high-speed camera; (c) transparent plastic box filled with model fluids; (d) LED backlight; (e) drop dispensing system; (f) computer; (g) height gauge; (h) needle.

camera (Phantom v9000) at the rate of 4000 frames per second; this yields an uncertainty on time, and in particular on the impact time, t_0, of ± 0.125 ms. The camera was horizontally aligned with the impact surface in order to measure the dimensions of both drop fluid and crater with precision, and was inclined to around 20° with respect to the horizontal plane in order to capture the contour of the spreading drop above the substrate surface. Corrections of measured data were properly made by considering the magnification change due to the variation of the refraction index (from the substrate, through the plastic wall, to the air). Back-to-front illumination was provided by an LED lamp (Philips Accent LED), which ensured a uniform intensity in the field of view. Drops were dyed with 0.1% (w/w) black ink in order to distinguish the drop fluid from the substrate/crater; the effect of the dye on the fluid yield stress and surface tension was negligible.

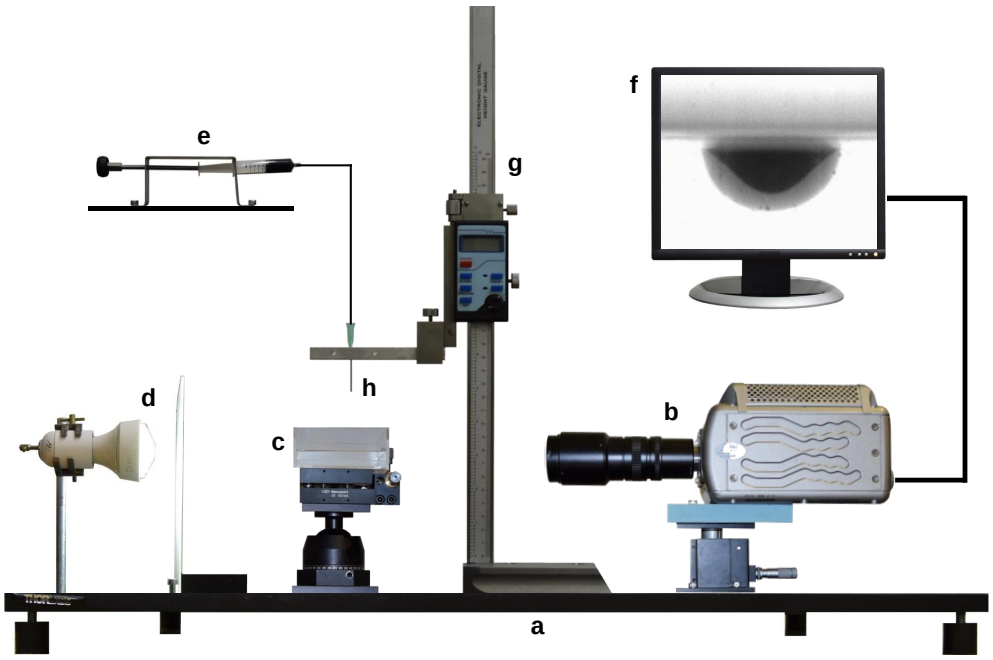

Figure 3.13: Photograph of the experimental rig for drop impacts on liquid substrates: (a) optical breadboard; (b) high-speed camera; (c) transparent plastic box filled with model fluids; (d) LED backlight; (e) drop dispensing system; (f) computer; (g) height gauge; (h) needle.

3.7.2 Image processing

Drop impact movies were analysed by digital image processing in two stages (see Appendix A.1 for the corresponding code): in the first stage, the background is subtracted from each frame and the image brightness, contrast, gamma correction, and digital gain were adjusted manually in order to get clear profiles of both the crater and the drop fluid, represented by the dark and grey regions in the left part of Figure 3.14, respectively. In the second stage, the image is processed further to capture both the profiles of the crater and the drop fluid through basic image segmentation algorithms; in particular, boundaries were identified as the lines corresponding to maximum intensity gradients as shown by the close-ups in Figure 3.14. Three different colours are used to denote different regions (red: crater; dark blue: drop; & light blue: substrate). The measurements of the crater

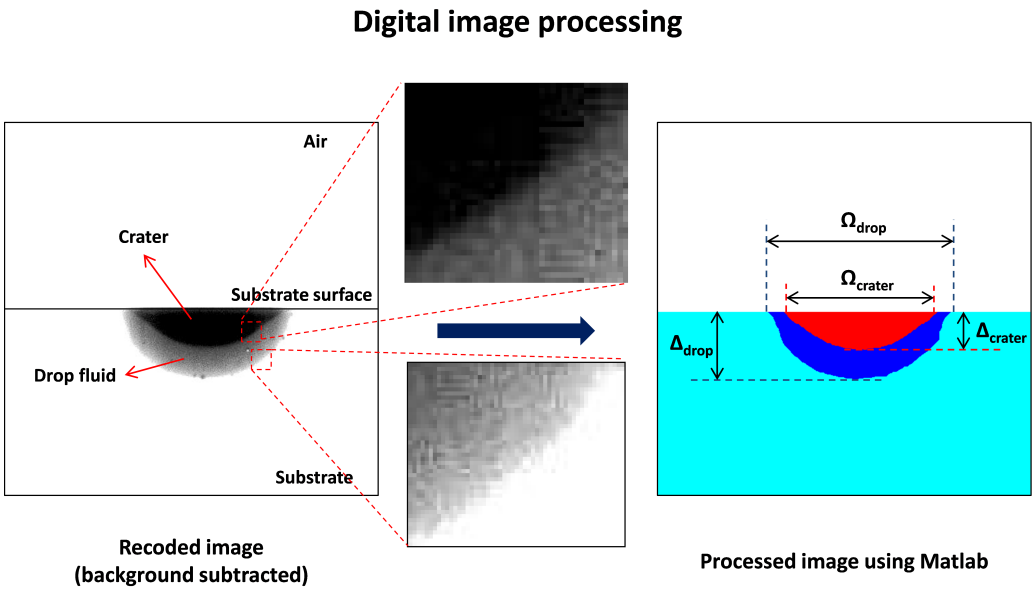

Figure 3.14: Schematic of the digital image processing: background-subtracted image (left); processed image using self-developed Matlab code (right).

dimensions (Ω_{crater}, Δ_{crater}) and drop fluid dimensions (Ω_{drop}, Δ_{drop}) can be easily obtained from the processed image displayed in the right part of Figure 3.14.

3.8 Drop impact on spherical elastic surfaces

3.8.1 Experimental setup

The experimental setup was conceptually similar to that of the Leidenfrost drop impact experiments (Figures 3.8 & 3.9). Drops of de-ionized water were released from a blunt hypodermic needle (gauge 21, i.d. 0.495 mm) and impacted on the centre ("north pole") of the hemispherical PDMS substrate (see Section 3.5 for details about the PDMS substrate). The impact velocities u_i were measured through digital image processing.

In this study, each set of experimental parameters contains three variables: (a), the elastic modulus of the substrate; (b), the diameter ratio, which is defined as the ratio of the hemispherical substrate diameter (D_{sub}) to the drop equilibrium diameter $D^* = D_{sub}/D_0$; (c), the impact Weber number. Values of the impact parameters are presented in Table 3.8. For each set of experimental parameters

Table 3.8: Values of the impact parameters.

Elastic modulus, E [**MPa**]	**Diameter ratio**, D^* [-]	**Weber number**, We [-]
		14
2.05	2.91	47
0.23	7.12	81
0.08	12.0	114
		147

(i.e., elastic modulus, diameter ratio and Weber number), the impact experiment is repeated five times for the sake of statistical analysis.

The impacts of single drops are recorded using a high-speed CMOS camera (Mikrotron MC1310) with a resolution of 640×365 pixels at the rate of 2000 frames per second. Magnification was kept constant throughout all experiments and lengths on the image could be calculated by comparison with the reference length of the substrate diameter (spatial resolution: 21 μm/pixel). The camera is horizontally aligned with the north pole of the substrate in order to obtain precise measurements. Back-to-front illumination is provided by an LED lamp (Philips Accent LED), which ensures a uniform intensity in the field of view.

3.8.2 Image processing

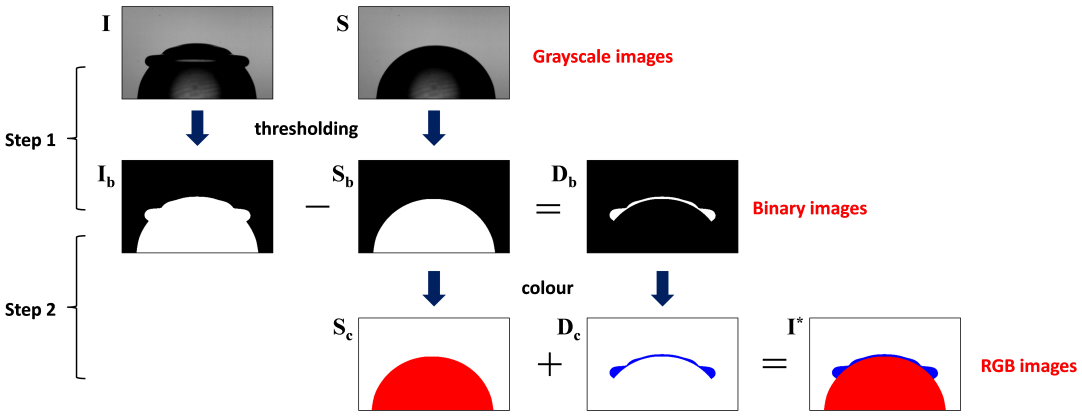

Figure 3.15: Schematic of the image processing.

The recorded images by high-speed camera were processed through a self-developed Matlab program (see Appendix A.2 for the corresponding code), which

allows one to observe the contour of the deforming drop and obtain quantitative measurements. Figure 3.15 shows an example of how the recorded grayscale image ($\mathbf{I}$) is converted to the processed RGB image ($\mathbf{I}^*$). Image $\mathbf{I}$ represents a snapshot which is taken 6 ms after impact at Weber number 47, elastic modulus 2.05 MPa & diameter ratio 2.91. The whole process consists of two steps. In the first step, both the image during impact ($\mathbf{I}$, drop & substrate) and the image before impact ($\mathbf{S}$, substrate) are converted into binary images through image thresholding. Then the contour of the deforming drop ($\mathbf{D_b}$) is obtained by subtracting the hemispherical substrate ($\mathbf{S_b}$) from the binary image containing both the drop and the substrate ($\mathbf{I_b}$). In the second step, the binary images of the substrate and the drop ($\mathbf{S_b}$ & $\mathbf{D_b}$) are coloured into RGB images ($\mathbf{S_c}$ & $\mathbf{D_c}$). In order to differentiate between the substrate and the drop, they are coloured red and blue respectively. Finally the RGB image of the drop is superimposed on the RGB image of the substrate, which produces the processed RGB image ($\mathbf{I}^*$).

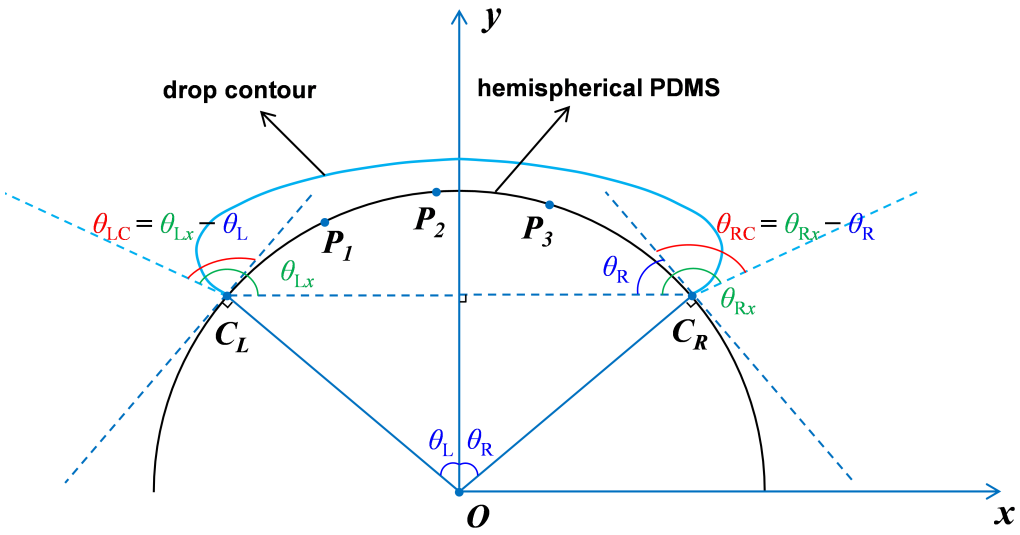

Figure 3.16: Schematic of the contact angle measurement procedure.

A schematic of the contact angle measurement procedure is shown in Figure 3.16. Firstly the centre of the hemispherical substrate must be found before any further measurements can be done. This is achieved by solving the coordinates of

the centre using the coordinates of three randomly selected points (e.g., P_1, P_2 & P_3) on the arc of the substrate since three noncollinear points determine a circle. Secondly the left & right contact points, C_L & C_R, are identified and the value of the angle $\angle C_L O C_R$ (referred as the 'base angle', $\alpha = \theta_{\mathrm{L}} + \theta_{\mathrm{R}}$) is measured.

3.8.3 Quantitative measurements

The dynamic contact angle measurement is achieved by goniometric-mask method (see Section 2.11 for details). However this method is only able to measure the angle with respect to the horizontal line (e.g., $\theta_{\mathrm{R}x}$ & $\theta_{\mathrm{L}x}$ in Figure 3.16) from the digital image. By means of some simple geometrical analysis, the actual dynamic contact angles can be calculated as follows:

$$\theta_{\mathrm{RC}} = \theta_{\mathrm{R}x} - \theta_{\mathrm{R}} \ (\theta_{\mathrm{LC}} = \theta_{\mathrm{L}x} - \theta_{\mathrm{L}}), \tag{3.9}$$

where θ_{RC} (or θ_{LC}) represents the dynamic contact angle on the right (or left) side of the view, and $\theta_{\mathrm{R}x}$ (or $\theta_{\mathrm{L}x}$) denotes the measured angle of the tangential line of the drop contour at the contact point with respect to x-axis, and θ_{R} (or θ_{L}) is the angle between line $\overline{OC}_{\mathrm{R}}$ (or $\overline{OC}_{\mathrm{L}}$) and y-axis.

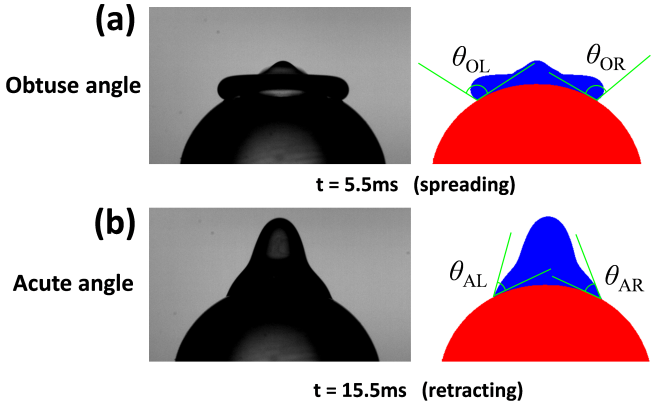

Figure 3.17: Contact angles at different stages: (a) spreading, (b) retracting.

The contact angle measurement via the goniometric mask method depends on the mask size [27, 28]. The mask size, z, strongly affects the angle measurement because a discrete mask can resolve a maximum number of discrete angle values

equal to the number of pixels in the triangle, $(z+1)^2/4$. Thus, the minimum value (in radians) that can be measured, corresponding to one pixel, is $4/(z+1)^2$; for example, to measure an angle of 1°, the mask size should be $z = \sqrt{180} - 1 = 25$. Thus, a mask size of 25×25 pixels is the minimum size to achieve a resolution of 1°. The algorithm performance is a trade-off between the mask size and the mask size/image size ratio; on one hand, increasing the mask size pays back in terms of accuracy but, on the other hand, if the image size to mask size ratio is too small angles are not measurable. In other words, the optimal mask size is a trade-off between the need to capture the drop contour curvature near the contact point, which requires a smaller mask, and the need to obtain more accurate measurement, which requires a larger mask. For this reason, the measurements of the dynamic contact angles are taken in a range of mask size from 1 to 81 pixels with the following impact parameters: We = 14, E = 2.05 MPa & D^* = 2.91. In particular, two snapshots after impact are selected as shown in Figure 3.17: (a), t = 5.5 ms (in spreading phase); (b), t = 15.5 ms (in retracting phase). In case (a) the measured contact angles on both left and right sides (θ_{OL} & θ_{OR}) are obtuse,

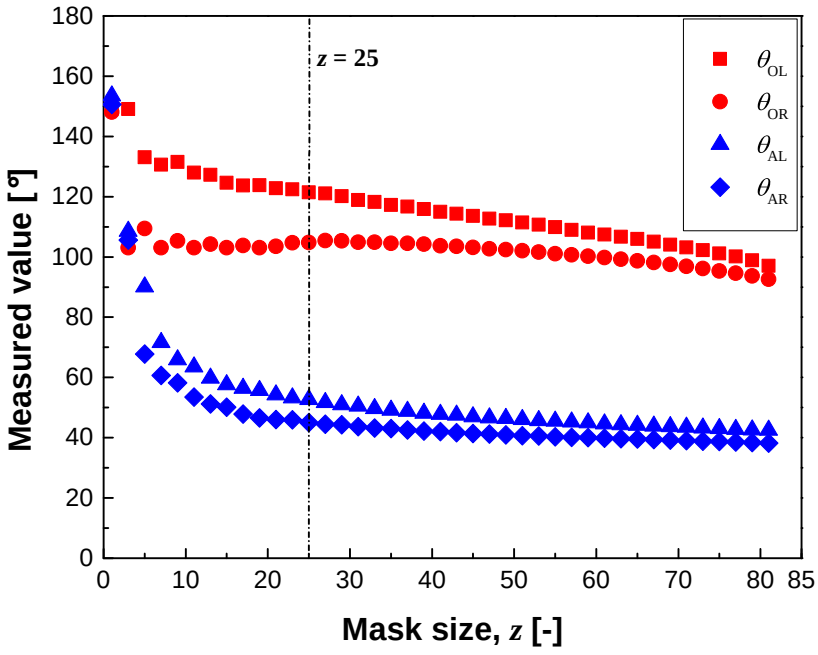

Figure 3.18: Measured contact angles as a function of mask size.

while in case (b) two acute angles are measured (θ_{AL} & θ_{AR}). The measured results of four contact angles as a function of mask size z are shown in Figure 3.18. The mask size was set to 25 pixels for all the contact angle measurements in this study. In order to further validate the measurement method, the temporal variation of left dynamic contact angle in the same case is measured at z=25 pixels as shown in Figure 3.19. The results are compared with the results of a smaller mask size z=19 pixels and a bigger mask size z=31 pixels. The high consistency among the results implies that the measurement method is valid and the choice of mask size is reasonable.

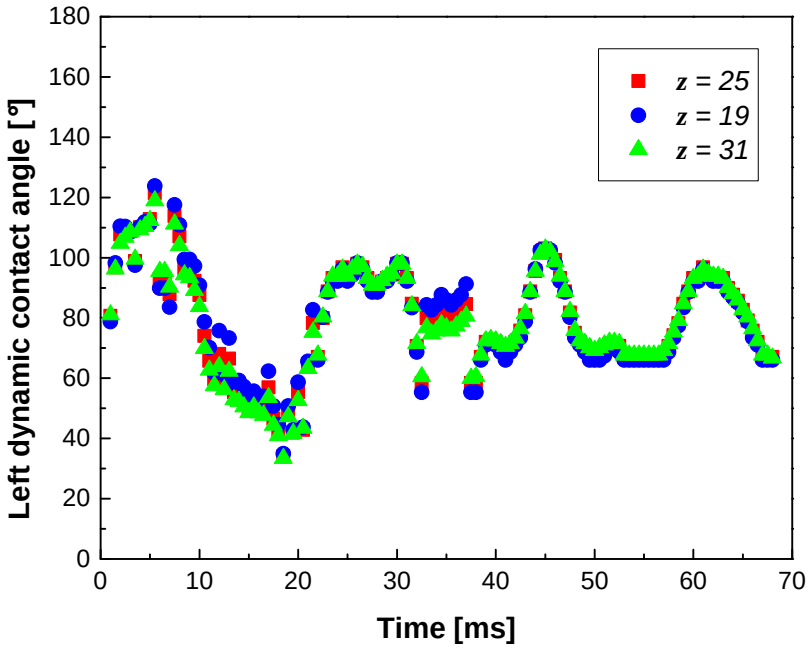

Figure 3.19: Measured dynamic contact angles (left) as a function of time after impact.

Furthermore, as shown in Table 3.9, the measured data using the goniometric mask method (z = 25 in Figure 3.19) in the initial oscillation stage after maximum spreading are compared with the measured values of contact angles through a conventional tangent line method [61]. It is shown that the maximum difference of measured values between these two methods is around 3°. Thus it is estimated that the potential experimental error of the goniometric mask method

is within 5°. One of the advantages of goniometric mask method is that it is more efficient to analyse large stacks of images. In conventional tangent line method, the curve fitting of the drop contour with polynomial functions requires the selection of suitable nodes on the drop edge. At present the position of nodes on the drop edge cannot be automatically generated, but must be designated manually. Another advantage of this novel technique is that it is able to measure the dynamic contact angles of drops which undergo large and non-symmetric deformations, which cannot be achieved by the Axisymmetric Drop Shape Analysis method [139]. The major disadvantage of the goniometric mask method is that the measurement accuracy depends on the mask size and the image resolution. Inappropriate selection of the mask size or low resolution of the image may cause large experimental errors.

Table 3.9: Comparison of contact angle measurements between goniometric mask method and tangent line method.

Time, t **[ms]**	**Goniometric mask**, $\theta_{\mathbf{G}}$ [°]	**Tangent line**, $\theta_{\mathbf{T}}$ [°]	**Difference**, $\mid \theta_{\mathbf{G}} - \theta_{\mathbf{T}} \mid$ [°]
7.0	113.77	111.04	2.73
7.5	107.08	107.40	0.32
8.0	96.28	96.55	0.27
8.5	96.28	95.91	0.37
9.0	92.33	90.00	2.33
9.5	87.56	85.60	1.96
10.0	73.99	74.74	0.75
10.5	65.74	63.43	2.31
11.0	59.70	60.26	0.56
11.5	68.08	70.35	2.27
12.0	58.25	56.31	1.94
12.5	66.52	63.43	3.09
13.0	55.40	53.13	2.27
13.5	55.21	56.31	1.10
14.0	53.27	51.65	1.62
14.5	50.19	48.80	1.39
15.0	52.71	50.11	2.60
15.5	50.46	49.70	0.76
16.0	50.07	49.72	0.35
16.5	56.98	56.58	0.40

Another obvious quantity of interest is the substrate deformation caused by drop impact. In the case of a flat substrate, the substrate deformation can be calculated by inserting a cantilever into the PDMS substrate just under the impact point, and measuring the displacement of the free end of the cantilever [112]. Unfortunately, in the case of spherical substrate this method cannot be used, because due to the substrate curvature the impact surface is not parallel to the cantilever, and the cantilever would be moved by the expanding drop, which causes a displacement of the free end at least one order of magnitude larger than the displacement caused by the PDMS deformation only. According to the experimental results by Mangili et al. [112], in case of a flat PDMS substrate with an elastic modulus of 0.017 MPa an impacting drop with vertical velocity of about 2m/s ($We \approx 152$) will cause a maximum substrate deformation of ≈ 40 μm. In the present work, the maximum Weber number is 147 and the lowest elastic modulus is 0.08 MPa (i.e., almost five times larger than 0.017 MPa), hence one can estimate a maximum deformation of the order of 8-9μm, which is below the spatial resolution of these measurements (21μm/pixel).

Chapter 4

Results and Discussion

4.1 Symmetry breaking and somersaults in Leidenfrost drops

The results presented in this section are obtained through the experimental setup described in Section 3.6.1.

4.1.1 Morphology

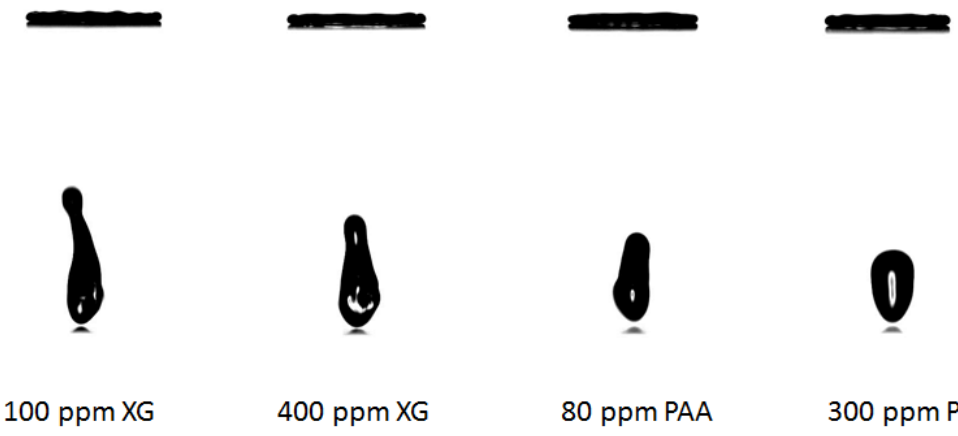

Figure 4.1: Impact morphology of XG and PAA drops with different concentrations at Weber number ~65. Top: lamellae at maximum spreading; bottom: prolate shapes of the drops at the beginning of rebound.

For xanthan gum (XG) and polyacrylamide (PAA) solutions, generally the outlines of the drops of the high concentration solutions at low Weber numbers

during impact and rebound are smoother than those of the drops of low concentration solutions at high Weber numbers, and the amplitude of the deformation of the drops in former cases is much smaller than that in later cases. Figure 4.1 displays the impact morphology of XG and PAA drops with different concentrations at the moment of maximum spreading and the moment of the onset of rebound at the same Weber number ~65. The diameter of lamella for low concentration solution at maximum spreading is slightly larger than the diameter of lamella for high concentration solution. The length of the prolate shape of the drop along the vertical direction at the beginning of rebound decreases with the increase of the concentration. The shape of the drops of PAA solutions during rebound are smoother and more symmetric compared to the XG drops with similar rheology due to the viscoelastic effect. The drop of the 100 ppm XG solution was observed to break up into two drops (i.e., one satellite drop was created) during the later stage of rebound whilst the drops of PAA solutions and the higher concentration solutions of XG maintained as 'one drop' for the whole impact and rebound process. Moreover the creation of satellite drop was also observed both at a lower Weber number ~50 and higher Weber number ~80 for the drop impacts of 100 ppm XG solution. No creation of satellite drop was observed for the drop impacts of 400 ppm XG solution in the considered Weber number range. This may be due to the high energy dissipation during impact resulted from the high viscosity of the high concentration solution.

Table 4.1: Regime map of impact morphology in terms of the creation of satellite drop(s).

GLY [w/w]	We **~15**	We **~30**	We **~50**	We **~70**	We **~85**
6.39%	-	one	-	-	-
21.9%	-	one	-	-	-
74.0%	-	two$^+$	two$^+$	two$^+$	two$^+$
85.9%	-	-	-	-	one

For Newtonian glycerol (GLY) solutions, the situation is even more compli-

cated. Table 4.1 shows the regime map of impact morphology in terms of the creation of satellite drop(s) for glycerol drops with different concentrations (i.e., different viscosities) and different Weber numbers, where 'one' denotes the case that only one satellite drop was created, 'two^{+}' denotes the case that two or more satellite drops were created and '-' denotes the case that no break-up was observed. The creation of one satellite drop was observed for the drop impacts of two low concentration GLY solutions (6.39% & 21.9%), however no satellite drop was created at higher Weber numbers (~50, ~70 and ~85). It is also surprising that from the drop impact experiments of 74.0% GLY solution the creation of two or more satellite drops was observed in a wide Weber number range (from ~30 to ~85) even if the viscosity of 74.0% GLY solution is much higher than the viscosities of the two low concentration solutions. The typical process of the creation of two satellite drops for drop impact of 74.0% GLY solution is shown in Figure 4.2.

Figure 4.2: Typical process of the creation of two satellite drops for drop impact of 74.0% GLY solution (We ~70).

4.1.2 Maximum spreading diameter

The diameter of the lamella formed at the end of the spreading stage is called the maximum spreading diameter. The value of this parameter is proportional to the surface energy of the drop at the end of spreading hence it is also an indicator of the energy dissipation during the spreading process if the initial kinetic energy (i.e., the We) of the drop remains unchanged [30]. Figure 4.3 shows the

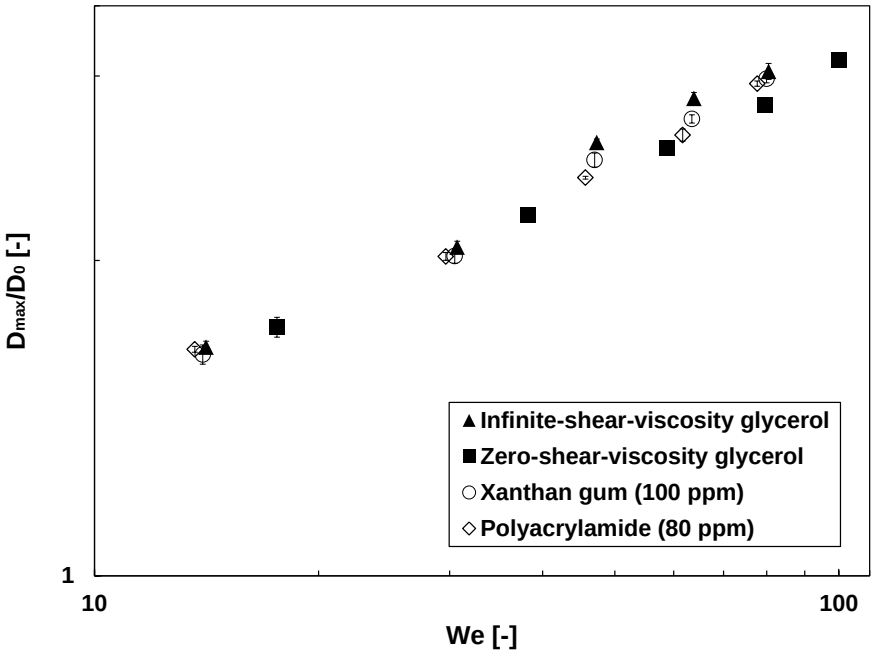

(a)

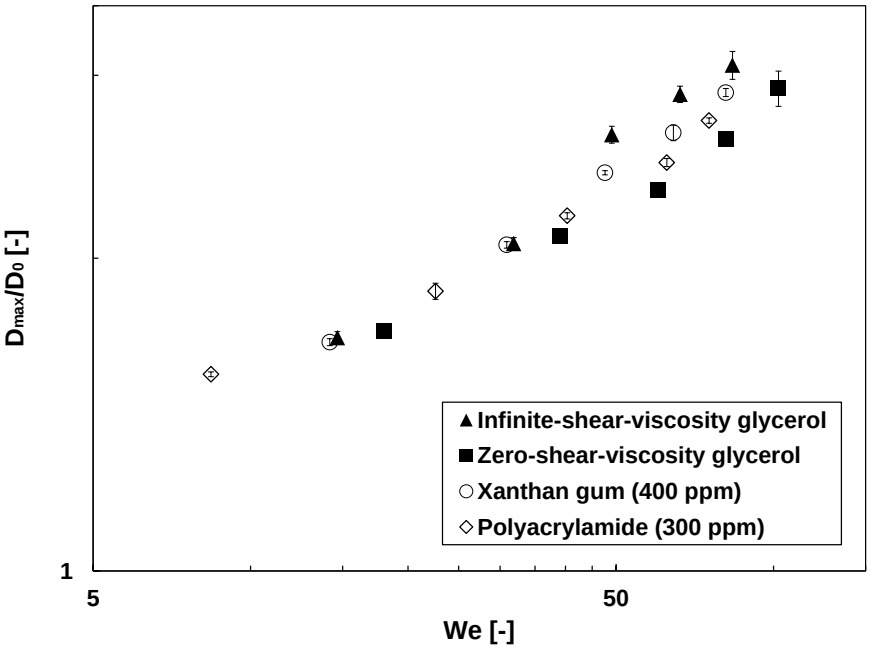

(b)

Figure 4.3: Normalised maximum spreading diameter of the drops of model fluids as a function of the impact Weber number: (a) 100 ppm XG, 80 ppm PAA and matching GLY solutions; (b) 400 ppm XG, 300 ppm PAA and matching GLY solutions.

normalised maximum spreading diameter with respect to the equilibrium drop diameter of the drops of model fluids as a function of the impact Weber number. For the case of low concentration (Figure 4.3(a)), the maximum spreading diameters of the drops of all the model fluids are almost consistent. However for high concentration (Figure 4.3(b)), the maximum spreading diameters of infinite-shear-viscosity GLY drops are systematically higher than those of XG, PAA and zero-shear-viscosity GLY drops in the considered Weber number range, which indicates that the viscosity dominates the energy dissipation of the spreading stage (i.e., higher viscosity leads to higher energy dissipation).

4.1.3 Maximum bouncing height

Figure 4.4 displays the normalized maximum bouncing height of XG, PAA, and the matching GLY drops as a function of the impact Weber number. The maximum bouncing height (H_{max}) denotes the maximum height reached by the drop centre of mass during rebound. Under certain conditions satellite drop(s) may be created during rebound (see Section 4.1.1), therefore the corresponding reported data in Figure 4.4 were corrected by taking the kinetic energy of satellite drop(s) into account (see Section 3.6.2 for details). As shown in Figure 4.4(a), the maximum bouncing heights of 100 ppm XG, and 80 ppm PAA and GLY with zero-shear viscosity drops are almost consistent in the considered Weber number range. It can also be observed that the maximum bouncing height tends to reach a constant value at high Weber numbers for these three fluids. However, the maximum bouncing height of GLY with infinite-shear viscosity drops starts to decrease at a critical Weber number ~30. Coincidentally, this feature can also be seen in a higher concentration case with the same critical Weber number as shown in Figure 4.4(b). One may conclude that the GLY with infinite-shear viscosity drops (i.e., those with the lowest viscosity) are subjected to large energy dissipation during impact, which leads to less potential energy restored when reaching

maximum height.

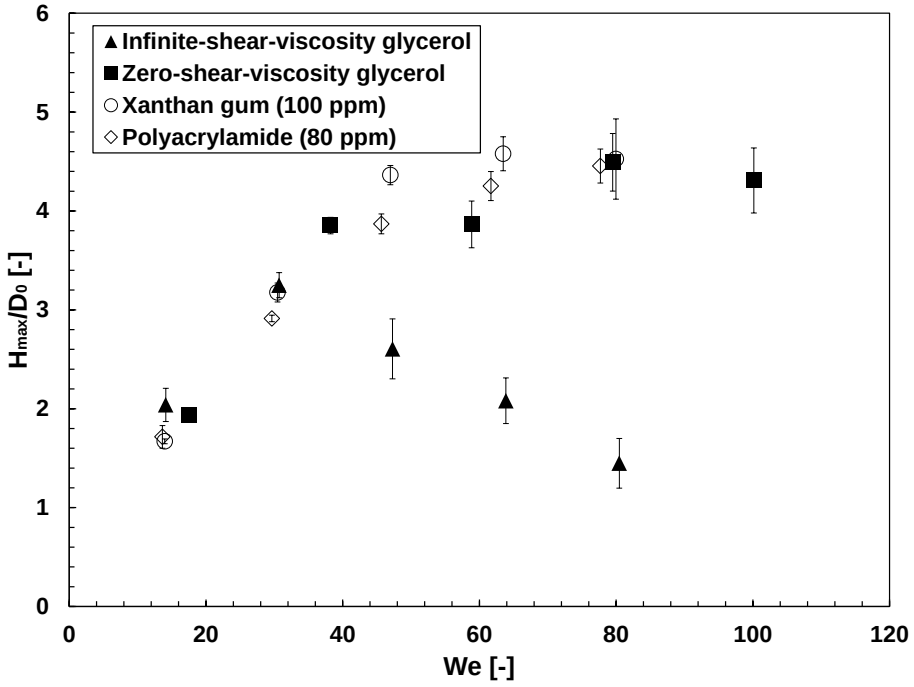

(a)

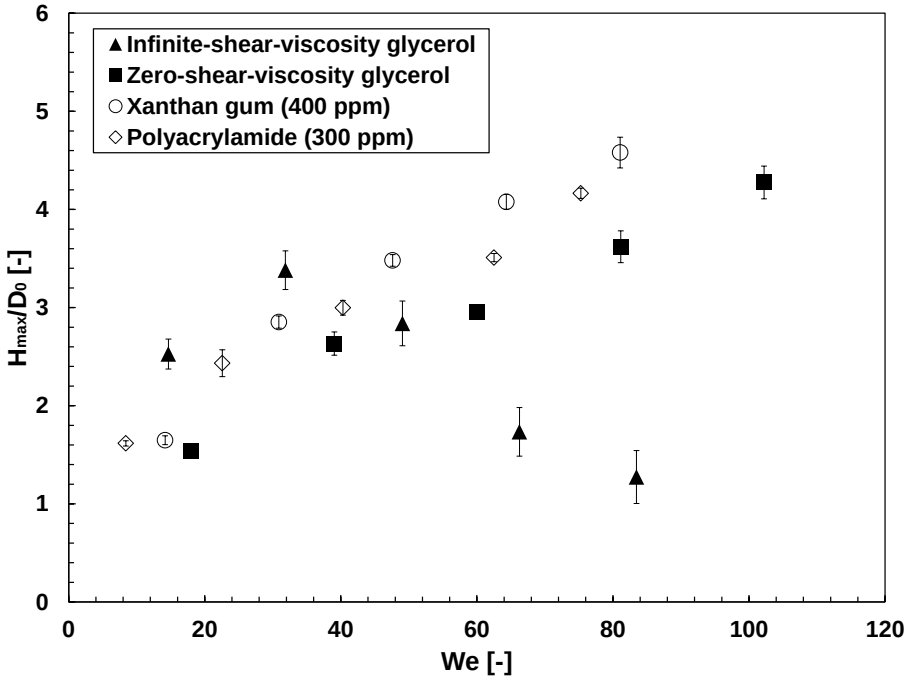

(b)

Figure 4.4: Normalised maximum bouncing height of the drops of model fluids as a function of the impact Weber number: (a) 100 ppm XG, 80 ppm PAA and matching GLY solutions; (b) 400 ppm XG, 300 ppm PAA and matching GLY solutions.

4.1.4 Retraction velocity

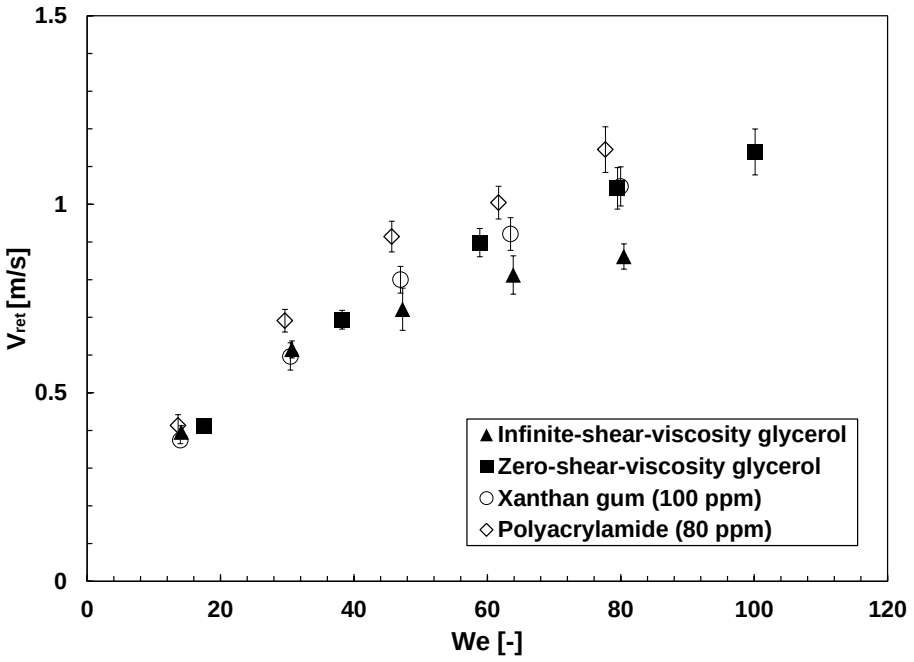

(a)

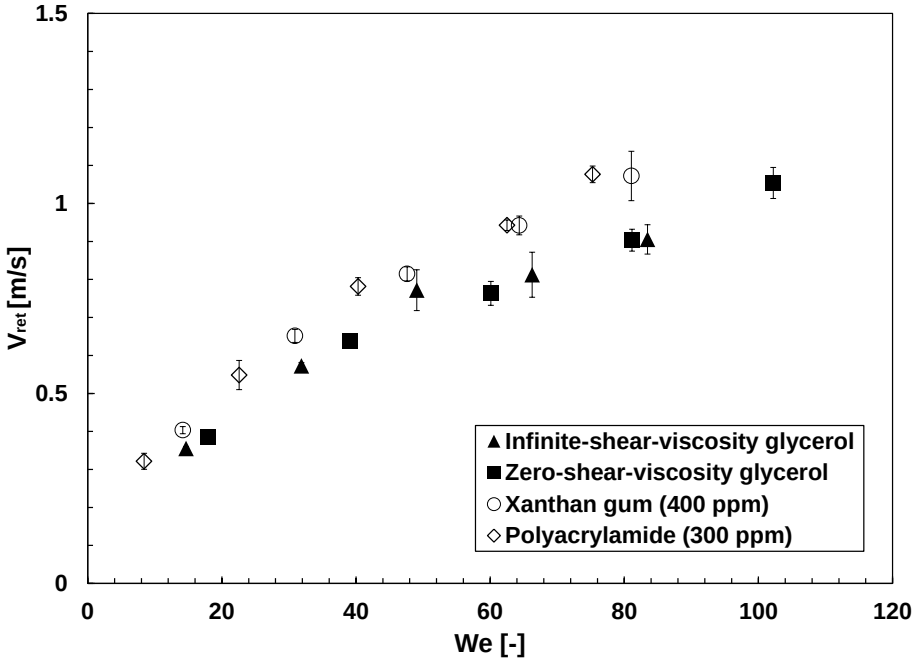

(b)

Figure 4.5: Retraction velocity of the drops of model fluids as a function of the impact Weber number: (a) 100 ppm XG, 80 ppm PAA and matching GLY solutions; (b) 400 ppm XG, 300 ppm PAA and matching GLY solutions.

The retraction velocity of drops after maximum spreading is displayed in Figure 4.5 with respect to the Weber number. This quantity plays a major role in the phenomenon of drop rebound, because drops will bounce only if the rim retraction is fast enough, and no rebound can be observed if the retraction velocity is lower than a certain value. The values in Figure 4.5 represent the slope of the base diameter vs. time curve in the linear range observed after maximum spreading, showing a linear growth for $We < 100$ except the case of infinite-viscosity GLY drops. The retraction velocity of infinite-viscosity GLY drops is observed to increase more slowly (slower than the initial linear increase at low Weber numbers) and be moderately less in magnitude compared to other three model fluids at high Weber numbers in both Figure 4.5(a) and Figure 4.5(b). However the discrepancy of retraction velocities among all the model fluids is much smaller than the discrepancy of the maximum bouncing height (see Figure 4.4) at high Weber numbers, which is unexpected since the kinetic energy which is proportional to the square of retraction velocity of the low viscosity Newtonian drops during retraction is not significantly different from that of the other three model fluids while the energy stored as gravitational potential energy which is proportional to the maximum bouncing height after impact of the low viscosity Newtonian drops is found to be considerably less than that of the other model fluids.

4.1.5 Somersaulting of bouncing drops

Interestingly, the bouncing drops of glycerol with infinite-shear viscosity were observed to "somersault" beyond this critical Weber number (~30) and no distinct rotational motion can be observed below this critical Weber number for all types of drops. Figure 4.6 shows the rebound morphology of Leidenfrost drops of different model fluids at $We \approx 70$. It can be clearly seen that the GLY with infinite-shear viscosity drops rotate during rebound, while drops of the other three

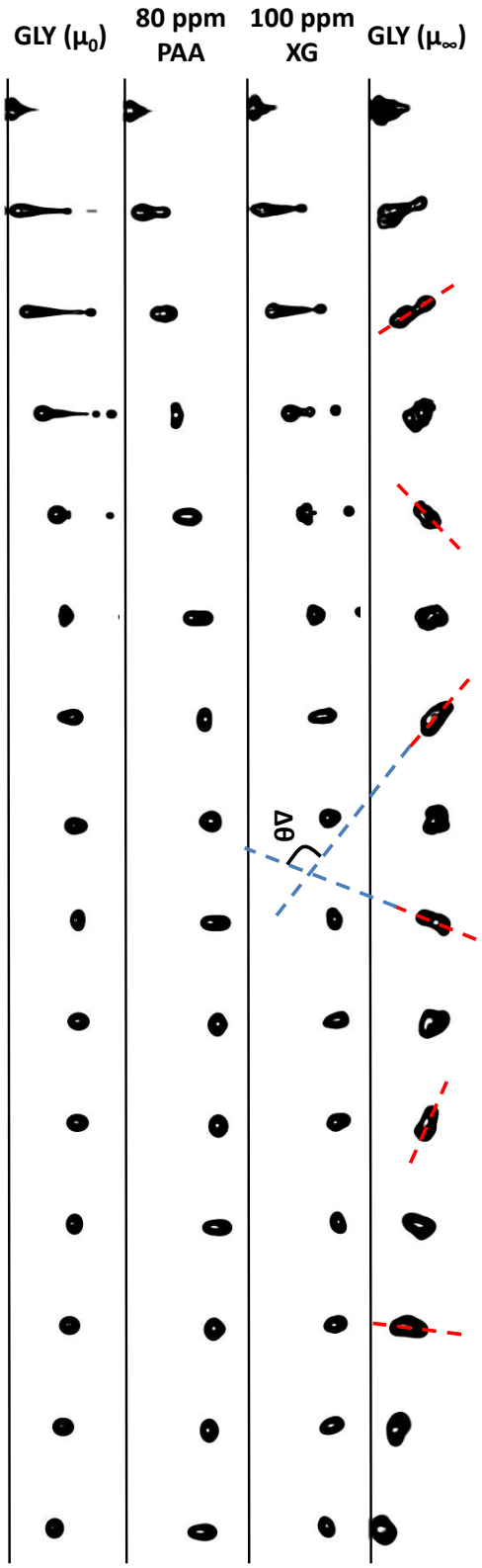

Figure 4.6: Rebound morphology of Leidenfrost drops of different model fluids at $We \approx 70$. The time between two consecutive images is 5 ms.

model fluids exhibit only symmetric oscillations in the direction of rebound. The dashed red lines parallel to the stretching direction of the drops in the first row of images in Figure 4.6 approximately represent the transient vibrational direction of the bouncing drops while the vibrational directions of other three types of drops remain almost vertical. Thus, the angular velocity of the rotating drops can be roughly estimated as the ratio of the angle of rotation in two images over the time between the images: $\omega = \Delta\theta/\Delta t$. In general, this introduces an error because the rotation angle is measured in the plane of the field of view, while the actual rotation occurs in a three-dimensional space; however, the error can be removed provided the rotation angle is measured taking reference points on the axes of an orthogonal Cartesian coordinate system (for example, the angle corresponding to one revolution, $\Delta\theta = 2\pi$, remains the same for any reciprocal position of the rotation plane and the field of view). Thus, there is only one case where the angular velocity is not measurable, that is, when the rotation is exactly in the plane perpendicular to the field of view.

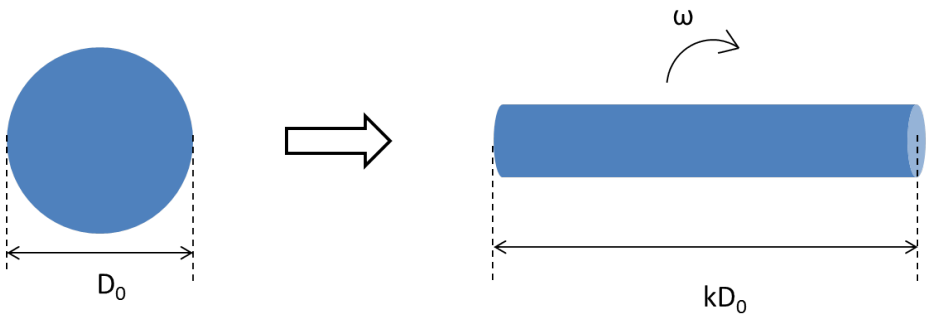

Figure 4.7: Cylindrical-shape approximation of the bouncing drop.

The calculated values of mean angular velocities of infinite-viscosity GLY drops are displayed in Figure 4.8 for Weber numbers beyond ~30 (critical We). The overall result of this complex oscillation dynamics is that the drop centre of mass does not move along the same vertical trajectory during drop rebound, but combines the vertical, ascending movement with a rotational movement of smaller amplitude. The energy associated with the drop dynamics must be independent

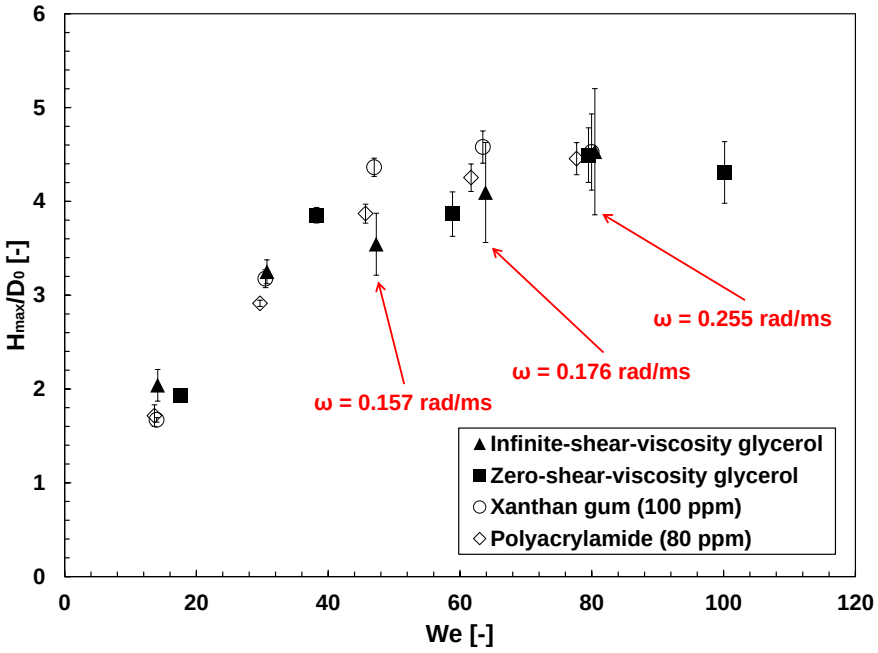

(a)

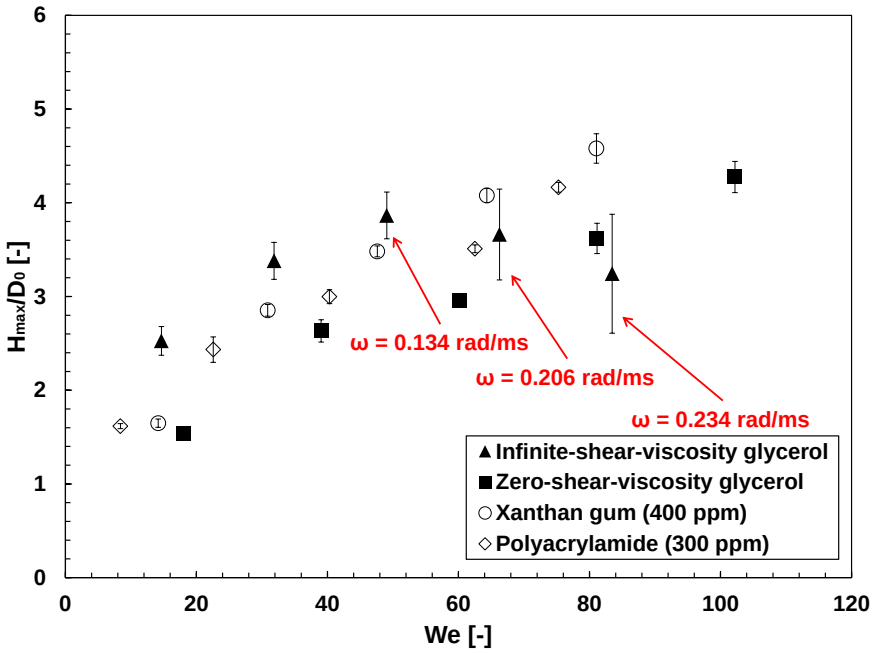

(b)

Figure 4.8: Normalised maximum bouncing height (modified data for GLY with infinite-shear viscosity) of the drops of model fluids as a function of the impact Weber number: (a) 100 ppm XG, 80 ppm PAA and matching GLY solutions; (b) 400 ppm XG, 300 ppm PAA and matching GLY solutions. Error bars represent the mean square value of the errors on the centre of mass height and on the virtual lengths obtained from Eq. 4.3.

of the reference frame; thus, we estimate this energy in a reference frame moving with the drop centre of mass, as if the drop was rotating instead of oscillating. In order to estimate the rotational kinetic energy of the tumbling drops we use the moment of inertia of a solid cylinder as an approximation (see Figure 4.7), although the shape of the bouncing drop is changing due to vibration:

$$I = m\left(\frac{R^2}{4} + \frac{l^2}{12}\right) = \frac{1}{72}\pi\rho D_0^5\left(\frac{1+2k^3}{2k}\right). \tag{4.1}$$

where $l = kD_0$ is the cylinder length, measured from images, and R is the cylinder radius, calculated imposing volume conservation. By inserting the moment of inertia into Equation 4.1 the rotational kinetic energy can then be expressed as:

$$E_{rot} = \frac{1}{2}I\omega^2 = \frac{1}{144}\pi\rho\omega^2 D_0^5\left(\frac{1+2k^3}{2k}\right). \tag{4.2}$$

The increment in maximum bouncing height (normalised with respect to the equilibrium drop diameter) if all the rotational kinetic energy was converted into potential energy can be written as:

$$\frac{\Delta h}{D_0} = \frac{E_{rot}}{mgD_0} = \frac{D_0\omega^2}{24g}\left(\frac{1+2k^3}{2k}\right), \tag{4.3}$$

where ω denotes the mean angular velocity, and g the gravity acceleration.

If $\Delta h/D_0$ defined by Equation 4.3 is added to the original maximum bouncing height data of the infinite-viscosity GLY drops for Weber numbers higher than ~30, a new graph which displays the normalised maximum bouncing height of XG, PAA and the matching GLY drops with respect to the equilibrium drop diameter as a function of the impact Weber number can be plotted (see Figure 4.8).

It is important to observe that the measured angular velocities are in quantitative agreement with the shape oscillation frequencies reported in [18], which confirms that the drop rotation in the relative coordinate system corresponds to non-symmetric drop oscillations/deformations in a fixed reference frame.

The fact the "virtual maximum bouncing height" of infinite-viscosity GLY drops are consistent with measured maximum bouncing height of other types of drops indicates that the total kinetic energy carried by low-viscosity Newtonian drops during retraction is only partly transformed into rotational kinetic energy rather than dissipated. The small difference of maximum bouncing height between Newtonian and non-Newtonian drops in Figure 4.8 implies that non-Newtonian effects play little role in the energy distribution.

4.1.6 Symmetry breaking in retraction stage

To investigate the physical mechanism of symmetry break (i.e., why some drops exhibit symmetric oscillations during rebound, and others do not), the high-speed camera was inclined with respect to the impact surface with an angle of $\sim 20^\circ$ in order to view the morphology of spreading and retracting drop from the top (see Figure 4.9). One can observe distinct finger-like protrusions on the rim in the case of GLY with infinite-shear viscosity drops at Weber numbers beyond ~30, which indicate the onset of the well-known rim instability eventually leading to splashing. Similar disturbances on the rim are also observed for drop impact onto a solid surface [131] and, as it is well-known, they become more pronounced in case of low-viscosity fluids [131, 159]. These protrusions grow during the inertial spreading stage, and form an axisymmetric crown at maximum spreading; however, at the onset of recoil one can observe that some of the protrusions coalesce to create bigger fingers during retraction, while others do not. This is likely to be caused by another instability of the rim, which can be modelled as a toroidal ring subject to radial compression. Thus, the mass distribution in the retracting droplet becomes non-uniform, which induces asymmetries both in the drop shape and in the internal flows, and eventually causes the drop to rotate during rebound.

Figure 4.9: Spreading and retracting morphology of Leidenfrost drops of different model fluids at $We \approx 70$. The time between two consecutive images is 1 ms.

4.2 Viscoplastic Leidenfrost drops

The results presented in this section are obtained through the experimental setup described in Section 3.6.1.

4.2.1 Morphology

The impact morphology of different viscoplastic Leidenfrost drops at low impact Weber number (10~20) and high impact Weber number (100~120) are shown respectively in Figure 4.10(a) and Figure 4.10(b). Specifically four important moments during the whole impact process are selected: beginning of impact, maximum spreading, beginning of bouncing and maximum bouncing. The shape of viscoplastic drop produced from a capillary nozzle becomes more prolate when B increases [Figure 4.10(a)] since the surface tension is not able to deform the natural prolate shape forming under the needle due to the existence of high yield-stress [77]. This effect weakens at high impact Weber number, due to a longer falling time for drops to reach spherical shape at higher releasing position (i.e., higher Weber). It is obvious that the spreading is inhibited for drops with high values of B: at low We drops with high B (B = 1.2 & 2.3) end up with a conical shape during spreading while others form a disk-like shape; at high We drop with higher B tend to achieve a thicker liquid lamella with shorter radius. This is associated with high viscous energy dissipation in drops with a high value of yield-stress. Retracting behaviours of low B drops are much more pronounced as revealed by the long prolate shapes at the beginning of bouncing. They also bounce higher compared with high B drops. In the middle range of B (0.16~1.2), there is a monotonous decrease in the maximum bouncing height with respect to the B number.

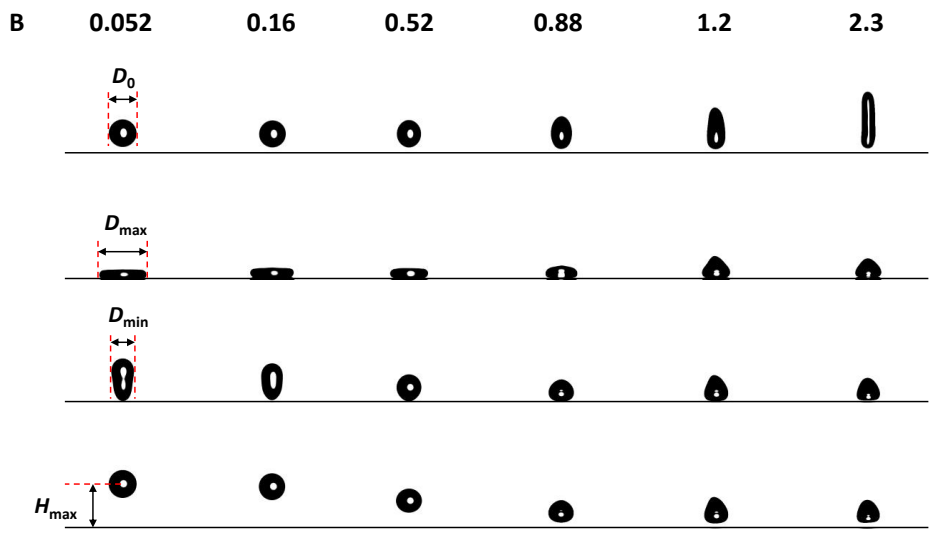

(a)

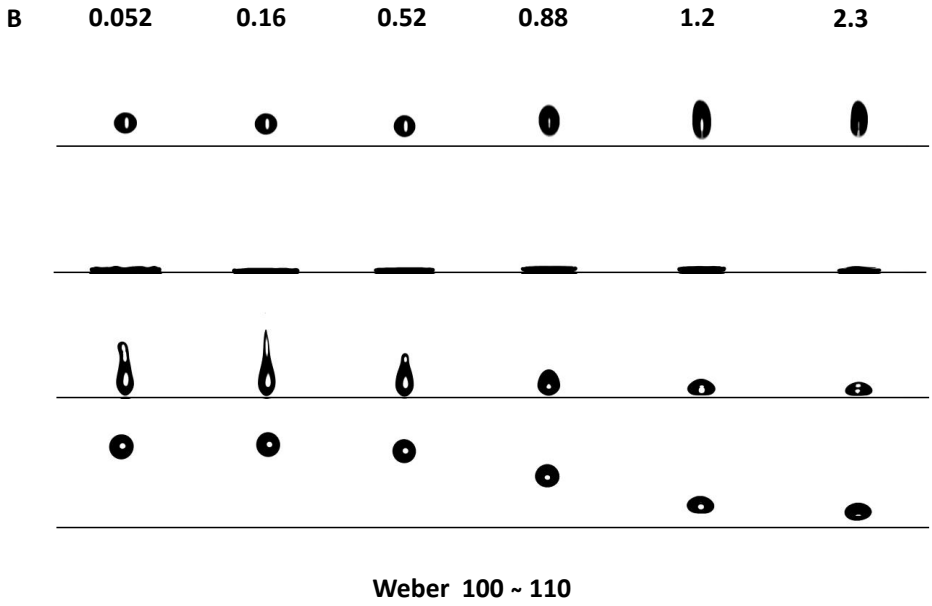

(b)

Figure 4.10: Impact morphology of Leidenfrost different viscoplastic drops with different Bingham-Capillary numbers: (a) Weber number 10~20; (b) Weber number 100~110. The first row indicates the Bingham-Capillary number of impacting drop, second the beginning of impact, third the maximum spreading, fourth the beginning of bouncing and last the maximum bouncing.

4.2.2 Temporal variation of drop diameter

Figure 4.11(a) and Figure 4.11(b) show the drop diameter (horizontal dimension) normalised with respect to the equilibrium drop diameter as a function of impact

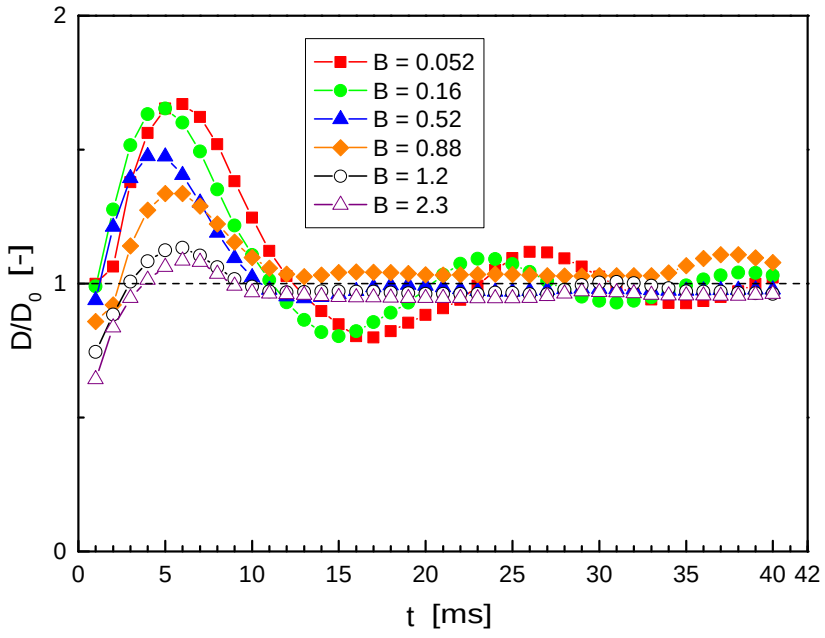

(a)

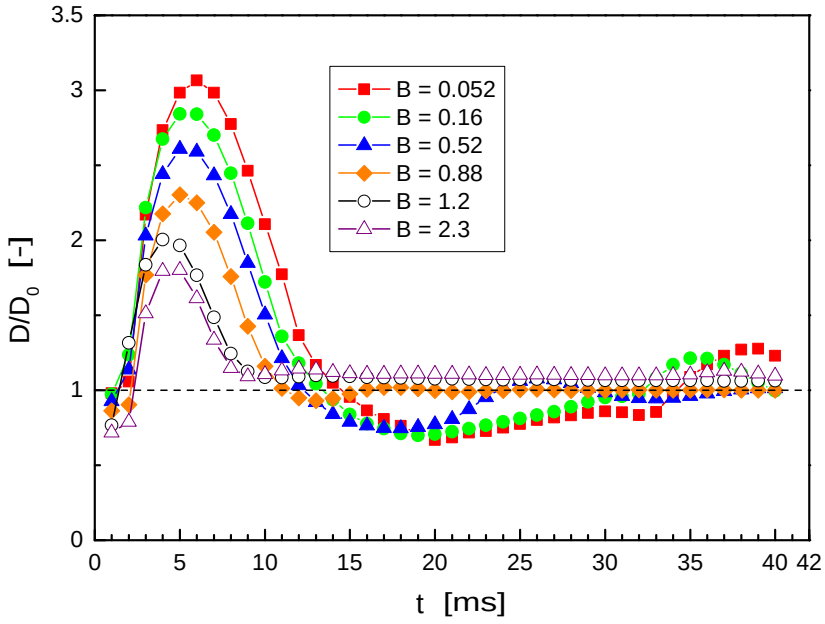

(b)

Figure 4.11: Normalised drop diameter (horizontal dimension) of model fluids as a function of impact time: (a) Weber number 10~20; (b) Weber number 100~110.

time at low Weber number (10~20) and high Weber number (100~120). The time is measured from the moment when impacting drop makes contact with the hot surface. For drops with low values of B [B = 0.052, 0.16 in Figure 4.11(a); B = 0.052, 0.16&0.52 in Figure 4.11(b)], the drop diameter continues to oscillate

after the initial spreading and retracting phases. A wave trough is observed after the initial retraction stage where the drop diameter is noticeably smaller than the equilibrium drop diameter ($D/D_0 < 1$). Then a secondary expansion of the drop diameter follows, as a result the drop keeps oscillating during rebound. However as the yield stress increases (B = 1.2, 2.3), the drop diameter remains almost constant after the initial spreading and retracting stages. No noticeable oscillation is observed for drop with a B number of 1.2 at high impact Weber number [see Figure 4.11(b)] though the maximum spreading diameter is around twice the equilibrium drop diameter. In this case the spreading drop is not able to retract to its equilibrium diameter ($D/D_0 > 1$), resulting in an oblate bouncing drop [see Figure 4.10(b)].

4.2.3 Maximum spreading diameter

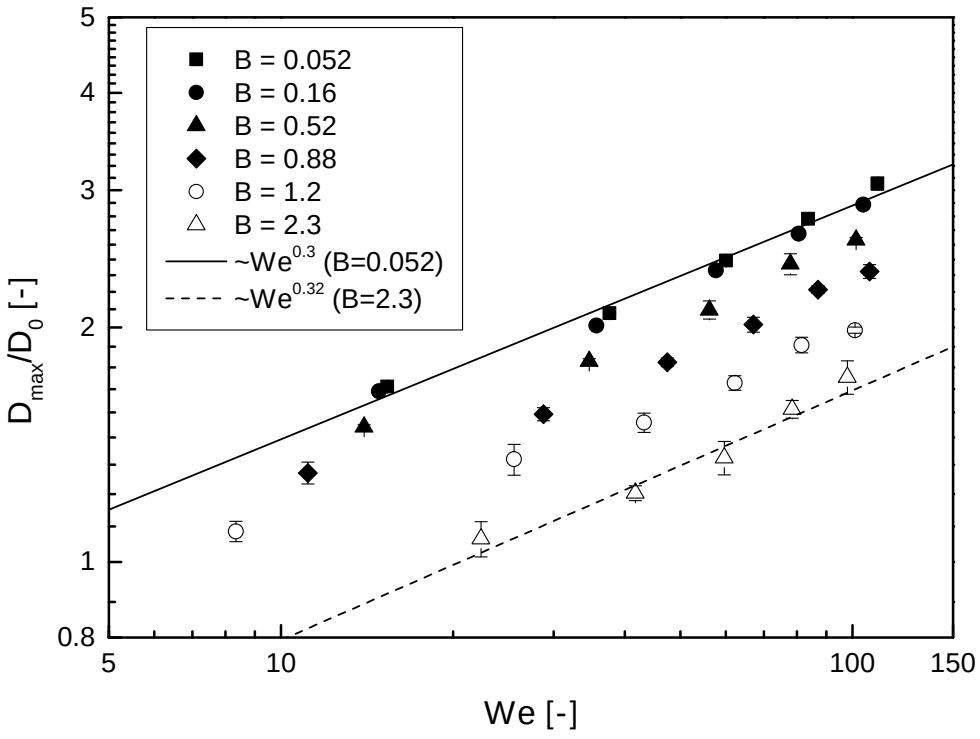

Figure 4.12: Maximum spreading diameter of the drops of model fluids as a function of the impact Weber number. Lines represent the fitting results of scaling law for B = 0.052 (solid) and B = 2.3 (dashed).

Figure 4.12 shows the normalised maximum spreading diameter with respect to the equilibrium drop diameter ($D_{\max}/D_0$) of the drops of model fluids as a function of the impact Weber number. The maximum spreading diameter decreases monotonously with respect to B number since larger B number means more viscous energy dissipation during spreading. For each model viscoplastic drop (i.e., the same B), the correlation between $D_{\max}/D_0$ and We follows the scaling law: $D_{\max}/D_0 \sim We^{\alpha}$ [24]. The experimental data of the most concentrated solution (B = 2.3) and the least (B = 0.052) are fitted to the scaling law and yield values of α as 0.32 and 0.3 (see solid and dashed lines in Figure 4.12). However the obtained index (α) for viscoplastic drops is slightly higher than the value (α = 0.25) of Newtonian cases reported in literature [24]. Similar effect has also been observed for other type (shear-thinning) of non-Newtonian drops [30]. Though the yield stress does inhibit the spreading of liquid lamella to some degree, a monotonous increase of maximum spreading diameter with respect to We is observed for all viscoplastic drops. This is due to the dominance of inertial force during spreading. The considered range of Weber numbers is from 10 to 150, which means inertial force is at least one order of magnitude higher than surface tension. While the yield stress is either smaller than or comparable with surface tension (check B values in Table 3.5), inertial force always plays a major role in spreading for all cases.

4.2.4 Maximum bouncing height

The maximum bouncing height ($H_{\max}$) denotes the maximum height reached by the drop centre of mass during rebound. While the maximum spreading diameter indicates how much of the initial impact kinetic energy is stored as surface energy as the drop is deformed, the maximum bouncing height indicates how much energy remains after the impact or, alternatively, can give a measure of the total energy dissipation during impact when subtracted from the impact

kinetic energy [30].

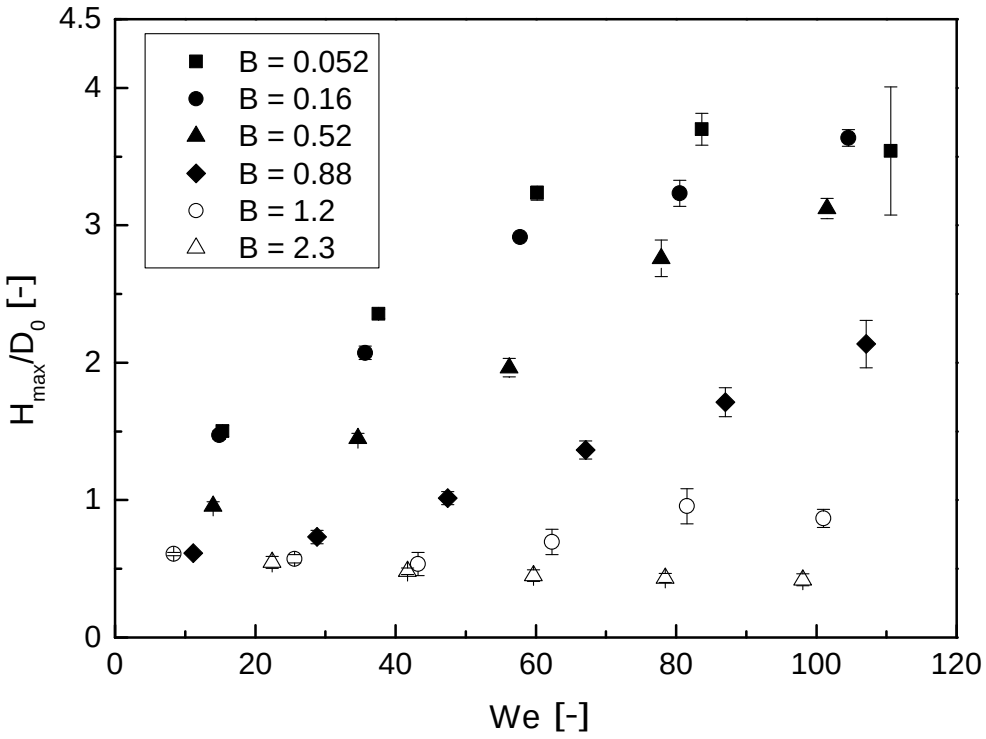

Figure 4.13: Maximum bouncing height of the drops of model fluids as a function of the impact Weber number.

The normalised maximum bouncing height ($H_{\max}/D_0$) of drops of model fluids with respect to the equilibrium drop diameter is displayed in Figure 4.13 as a function of the impact Weber number. The data of drops with a Bingham-Capillary number higher than unity (B = 1.2&2.3) are labelled using open symbols while others are represented by filled symbols. For drops with a relatively low yield stress (B = $0.052, 0.16$&0.52), the rebound behaviour is similar to high viscosity Newtonian drops: after an initial almost linear increase with respect to We the maximum bouncing height tends to reach a plateau at high impact Weber numbers [see Figure 4.4(a)]. This behaviour is probably due to the fact that the viscous dissipation during impact becomes large enough to compensate the increment in bouncing height, due to the increase of surface energy stored during impact.

When the yield stress force is close to but still slightly lower than surface

tension (B = 0.88), no sign of plateau is observed in the considered We range except for the linear increase. Nevertheless the rebound behaviour of drops with values of B over unity (B = 1.2&2.3) is totally different from others: the maximum bouncing height of drop with a yield stress force slightly higher than surface tension (B = 1.2) fluctuates between $0.5D_0$ and D_0 whilst that of drop with an even higher Bingham-Capillary number (B = 2.3) stays around $0.5D_0$ regardless of the change of impact Weber number. It is observed that for higher yield stress magnitudes (B = 1.2&2.3) drops keep a prolate morphology at impact, therefore the definition of Weber number based on the equivalent equilibrium drop diameter is not as accurate as in other cases. However, even a large correction of the Weber number for these points would not affect the main results; with reference to Figure 4.13, for example, this would cause a horizontal shift of the points in the two corresponding series (open symbols), which would not change the conclusion either qualitatively or quantitatively.

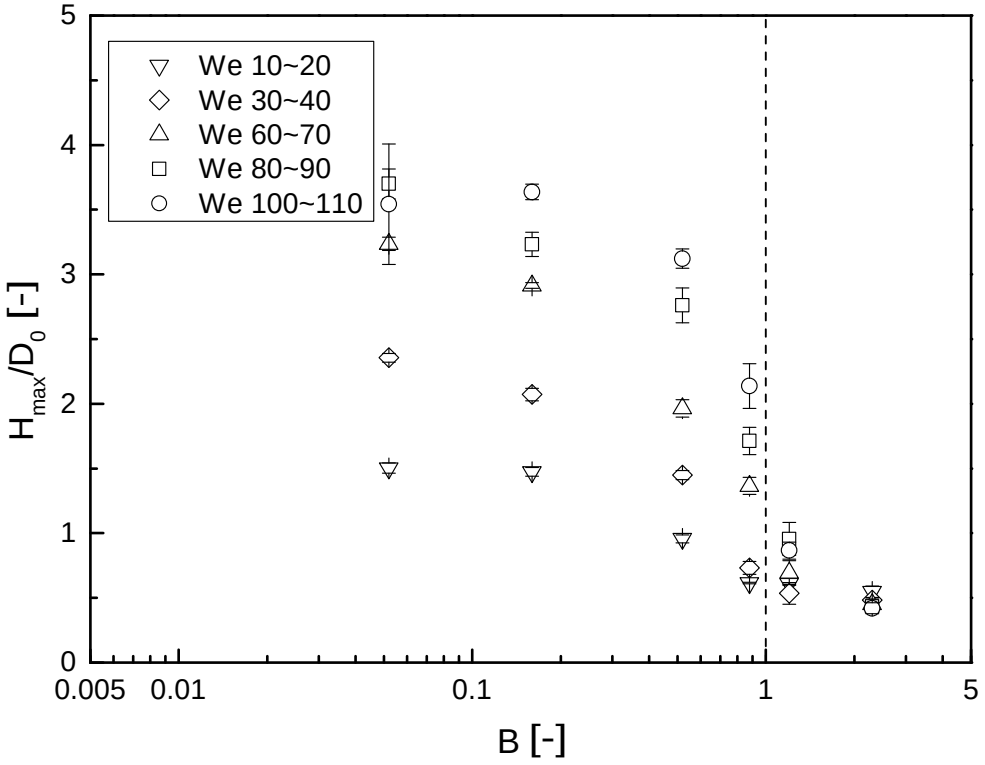

Figure 4.14: Maximum bouncing height of the drops of model fluids as a function of the Bingham-Capillary number.

Figure 4.13 can be replotted as Figure 4.14 by replacing the Weber number with the Bingham-Capillary number for x-axis in order to show the effect of B on maximum bouncing height directly. The data are regrouped into five sets according to impact We range. The varying trend of $H_{\max}/D_0$ with respect to B is similar for all We range groups: after an initial plateau at low Bingham-Capillary numbers, the maximum bouncing height drops considerably as B exceeds unity. This is related to the high resistance of yield stress to counter the retraction driven by surface tension, which will be discussed in Section 4.2.5. In addition, an interesting phenomenon observed here is the complete inhibition of drop rebound at sufficiently high Bingham-Capillary numbers regardless of the impact Weber numbers. This could lead to important potential industrial applications. For example, the delivery of pesticides in agriculture requires the inhibition of drop bouncing in order to reduce the quantities of pesticides used per unit area. Furthermore, the soil can be polluted due to the rebound of pesticides drops. Another important engineering implication is spray printing. The no-rebound nature of drops with high Bingham-Capillary numbers can considerably reduce the quantities of waste materials due to drop rebound during the printing process.

4.2.5 Minimum retracting diameter

The diameter of the prolate bouncing drop formed at the beginning of rebound is called the 'minimum retracting diameter' ($D_{\min}$). This parameter can qualitatively describe the magnitude of retraction after the spreading phase, in other words, the effect of yield stress to counter the retraction driven by surface tension. Figure 4.15 shows the normalised minimum retracting diameter ($D_{\min}/D_0$) with respect to the equilibrium drop diameter of the drops of model fluids as a function of the impact Weber number. For cases of low Bingham-Capillary numbers (B = 0.052, 0.16 & 0.52), the variation of minimum retracting diameter with respect to impact Weber number follows the same pattern: after an initial drop the

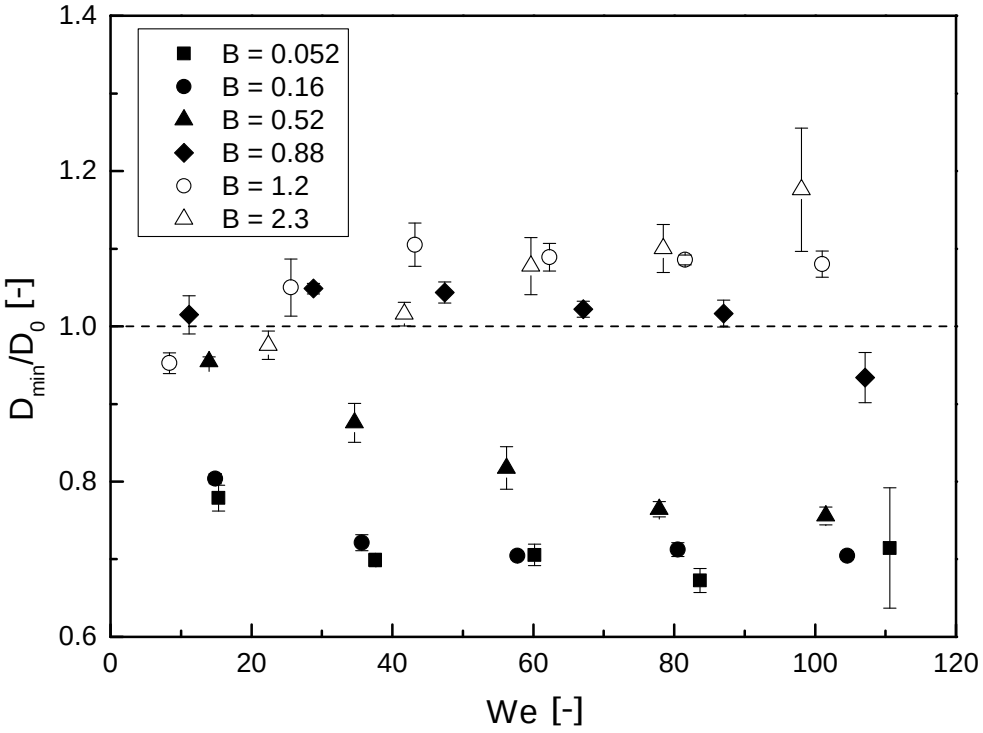

Figure 4.15: Minimum retracting diameter of the drops of model fluids as a function of the impact Weber number.

$D_{\min}/D_0$ reaches a plateau as We increases. In addition, the minimum retracting diameter is always smaller than the equilibrium drop diameter ($D_{\min}/D_0 < 1$), which means the surface tension still dominates during the retraction process for low B numbers. However when B increases to 0.88, the value of $D_{\min}$ fluctuates around the equilibrium drop diameter ($D_{\min}/D_0 \approx 1$) indicating that the resistant yield stress is comparable to the surface tension. As the Bingham-Capillary number becomes larger (B = 2.3), the minimum retracting diameter even increases monotonously with respect to the Weber number in the considered We range. At high impact We (60 ~ 100), the spreading drop is not able to retract to its equilibrium diameter due to the existence of high yield stress ($D_{\min}/D_0 > 1$) and the inertial deformation upon impact becomes permanent, resulting in an oblate bouncing drop [see Figure 4.10(b)]. Here the ratio of the maximum spreading diameter to the minimum retracting diameter is defined as the 'retraction coefficient' ($D_{\max}/D_{\min}$) and its correlation with the maximum bouncing height is

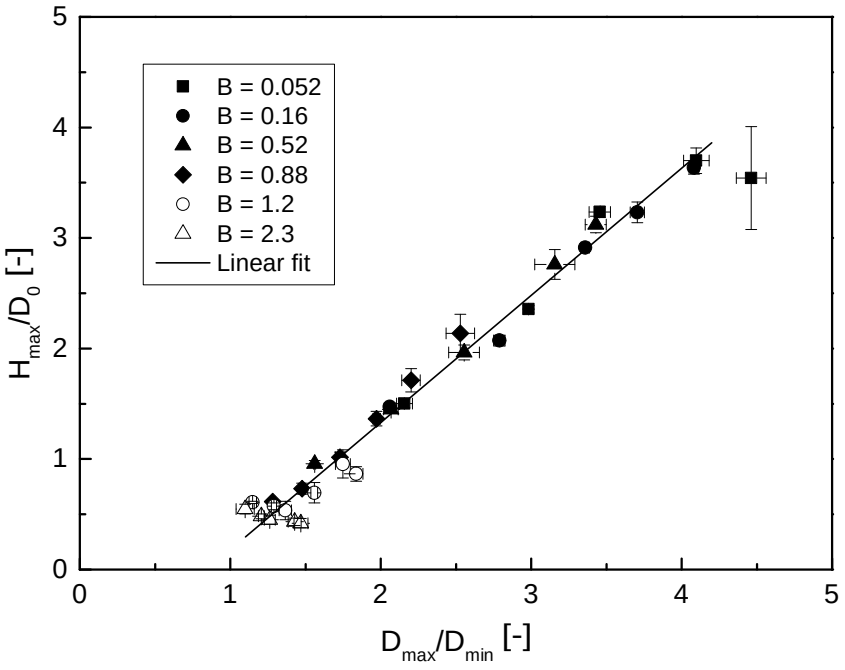

(a)

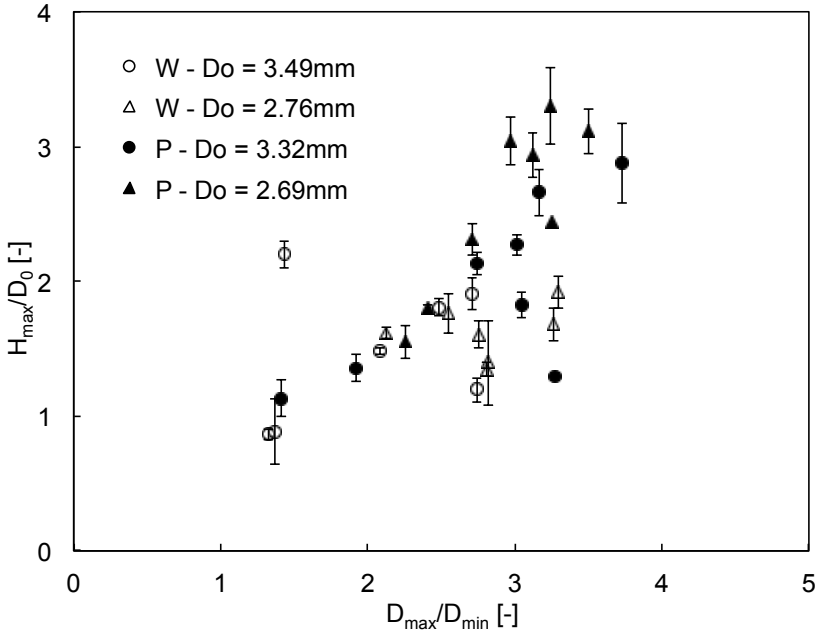

(b)

Figure 4.16: Maximum bouncing height of the drops of model fluids as a function of the retraction coefficient: (a) viscoplastic drops; (b) water and dilute polymer solution drops of different diameter [17].

plotted in Figure 4.16(a). A linear correlation between these two parameters is obtained:

$$H_{max}/D_0 = 1.15(D_{max}/D_{min}) - 0.968. \quad (4.4)$$

This feature indicates that the deformation of the drop during retraction stage is crucial to the bouncing behaviour while the assumption that the disk-like drop remains rigid in the so-called disk model (e.g., [133]) may not be physical. Thus, the major contribution to the rebound of a drop impacting onto a heated surface is the surface tension whilst the contribution of intrinsic elasticity of the vapour cushion between the drop and the surface is negligible. It should be noted that when the same analysis is done on drops of water or dilute polymer solutions [Figure 4.16(b)], data do not display a clear linear correlation, except in the lower limit of the bouncing height (Weber number), both because of the lower viscosity, which makes the drop shape highly irregular at the beginning of rebound, and to the more complex energy dissipation mechanism [17, 30, 18].

4.3 Spreading behaviours of drop impact on viscoplastic surfaces

The results presented in this section are obtained through the experimental setup described in Section 3.7.1 with an inclined high-speed camera (around 20° with respect to the horizontal plane).

4.3.1 Morphology

Examples of the impact morphology of drops on different viscoplastic substrates are displayed in Figures 4.17 and 4.18. In the first experimental set (Figure 4.17), water was chosen as the working fluid for drops while the substrate varies from the softest case (τ_0 = 1.13 Pa) to the hardest (hydrophilic glass). In the second experimental set (Figure 4.18), the 0.1% Carbopol gel (τ_0 = 11.7 Pa) was selected as the drop fluid and the impact morphology on a more solid gel substrate (0.7% Carbopol, τ_0 = 94.0 Pa) was investigated at three different Weber numbers: 15,

Figure 4.17: Image sequences showing the impact morphology of water drops onto the substrates varying gradually from soft to solid: the values at the top of each image sequence are the yield stress values of the substrates while the time after impact is shown at the right.

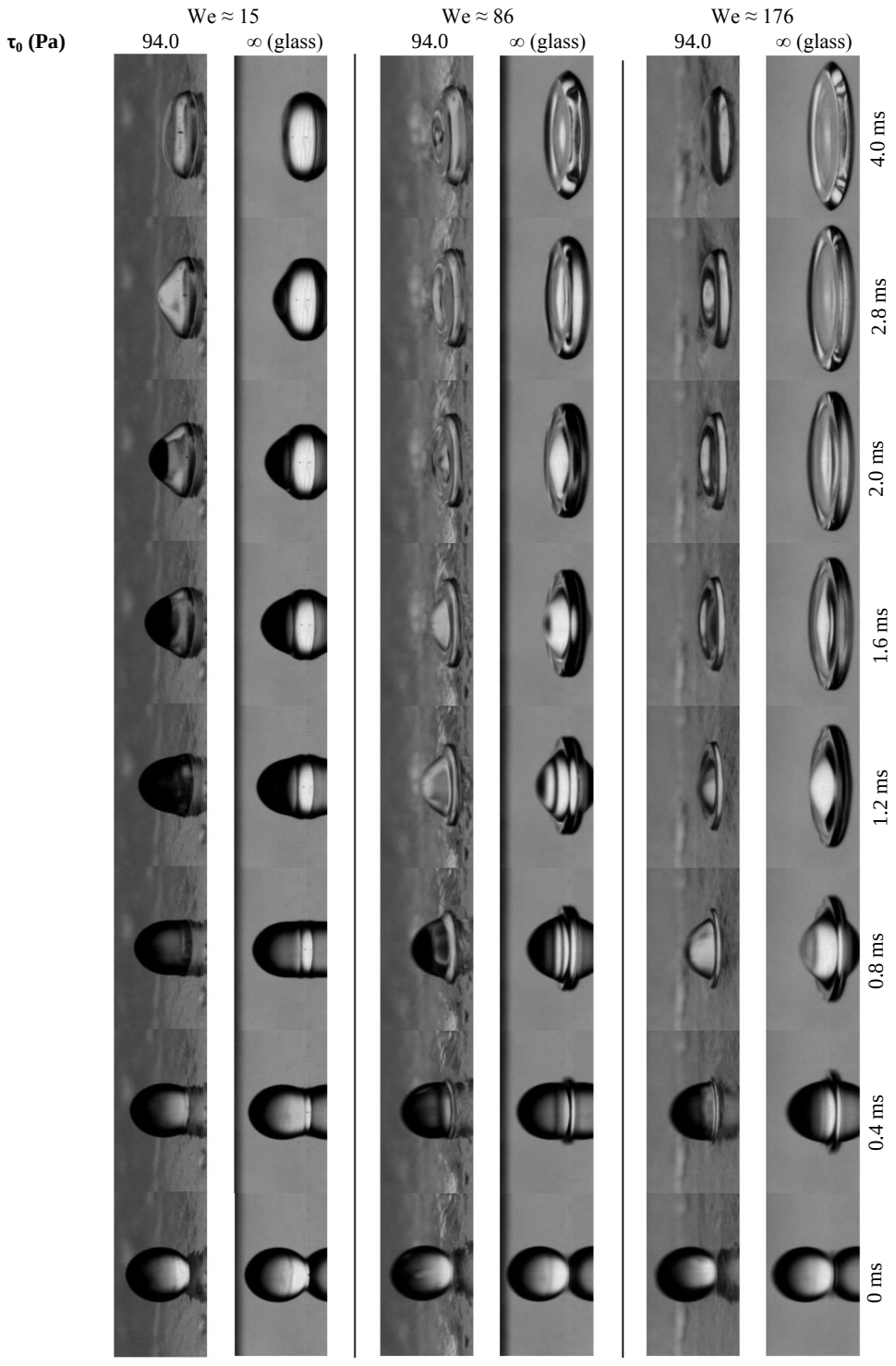

Figure 4.18: Image sequences demonstrating comparisons of impact morphologies of the same gel drops (τ_0 = 11.7 Pa) onto a more solid gel (τ_0 = 94.0 Pa) substrate and hydrophilic glass substrate at different Weber numbers: 15, 86 and 176. The time after impact is shown at the right.

86 and 176, while the glass substrate was used as a comparison.

The image sequences in Figure 4.17 display the impact morphology of water drops onto the substrates varying gradually from soft to solid (i.e., with the increase of the yield stress). The impact height was set to 2 cm which gives a value of impact velocity at $u_i = \sqrt{2g(H - D_0)} \approx 0.6$ m/s and of Weber number at $We = \rho D_0 u_i^2/\sigma \approx 15$. As shown in Figure 4.17, the impact morphology for the very soft substrates ($\tau_0 = 1.13$ & 7.24 Pa) is similar to that of a water drop impact into a water substrate. As the drop penetrates the substrate capillary waves are stimulated and crater is formed. Finally the drop cannot be distinguished from the substrate anymore. However when the yield stress is increased to $\tau_0 = 11.7$ Pa the drop partially stays on the surface of the substrate as shown by the liquid disk in the last image of the third sequence. The profiles of the spreading liquid disk become clearer for the cases of more concentrated gels ($\tau_0 = 29.1$ & 94.0 Pa) which indicates major part of the drop stays over the surface of the substrate during inertia spreading.

4.3.2 Spreading behaviours

The spreading base diameter D_B/D_0 (the diameter of the interface of drop and substrate) of water drops normalised with respect to the equilibrium drop diameter as a function of spreading time t for cases of different substrates (Carbopol gels: $\tau_0 = 11.7,\ 29.1,\ 94.0$ Pa and hydrophilic glass) is plotted in Figure 4.19. An obvious feature which can be found in Figure 4.19 by comparing the data for three gel substrates ($\tau_0 = 11.7,\ 29.1,\ 94.0$ Pa) is that the Newtonian drop spread faster when the gel substrates become more solid. And the explanation for such phenomenon is simple: the magnitude of deformation rises with the increase of the softness of the substrate under the same impact Weber number. When a softer substrate is considered: first, larger volume of drop fluid penetrates the surface of the substrate, which leaves less volume of fluid for spreading; second,

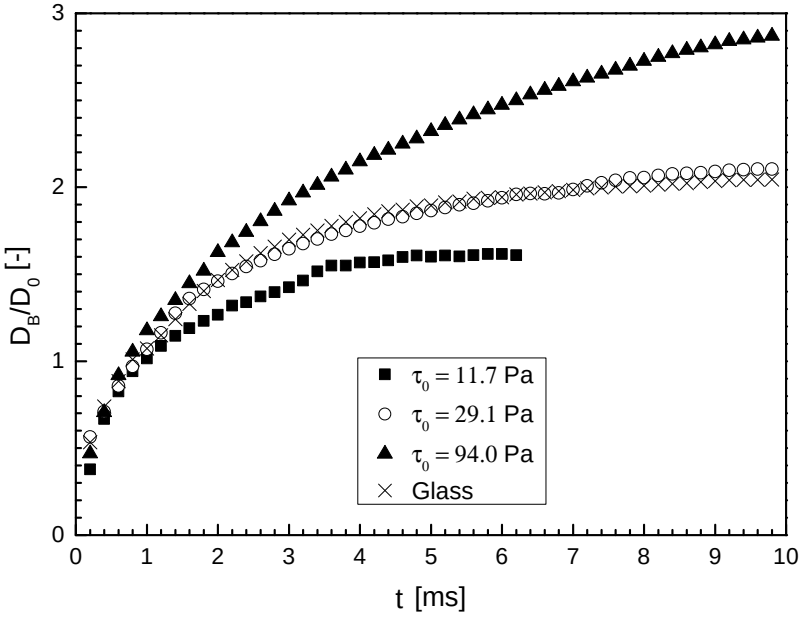

Figure 4.19: The normalised spreading base diameter D_{B}/D_0 of water drops as a function of spreading time t for substrates with different softness.

the kinetic energy which is dissipated through the deformation of the substrate is proportional to the magnitude of deformation, which further slows the spreading speed of the drop. The unexpected phenomenon is that when the substrate becomes totally solid (glass), which leads to zero deformation of the substrate, the drop spreads slower than the case of the most concentrated gel (τ_0 = 94.0 Pa) though it spreads faster than the most soft case (τ_0 = 11.7 Pa).

The image sequences in Figure 4.18 demonstrate comparisons of impact morphologies of the same gel drops (τ_0 = 11.7 Pa) onto a more solid gel (τ_0 = 94.0 Pa) substrate and hydrophilic glass substrate at different Weber numbers. The normalised spreading base diameter D_{B}/D_0 as a function of spreading time t for those cases is plotted in Figure 4.20. The impact morphology at low Weber number ($We \approx 15$) is similar for two substrates; however, in the case of glass substrate the spreading speed of gel drop rises significantly with the increase of the Weber number (see Figure 4.20) while gel drop appears to have the same maximum

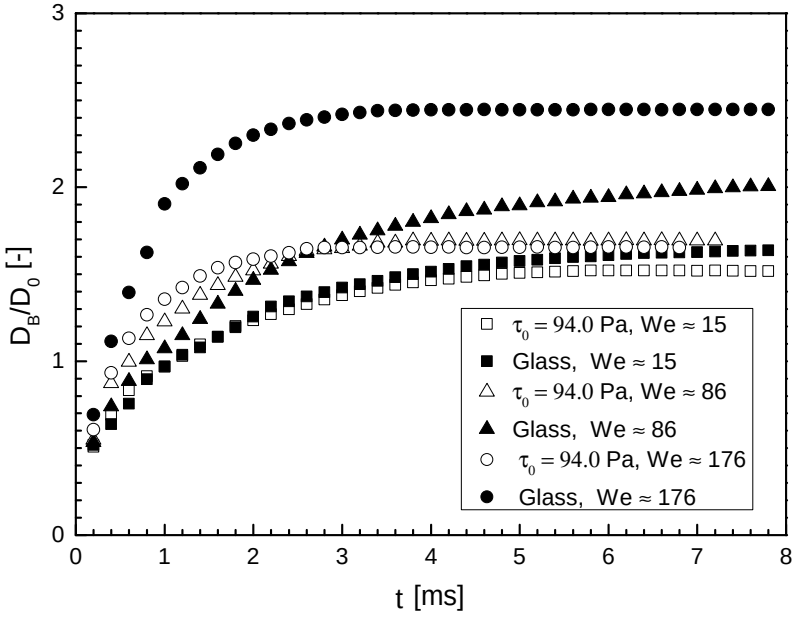

Figure 4.20: The normalised spreading base diameter D_B/D_0 of water drops as a function of spreading time t for substrates with different softness.

spreading diameter at high Weber numbers ($We \approx 86$ and $We \approx 176$) indicated by the minor changes of open triangle and circles. Further experiments at Weber numbers between 86 and 176 were conducted and no distinct changes in the maximum spreading diameter were found. Even compared to the very low Weber number case ($We \approx 15$) the maximum spreading diameter at high Weber numbers does not increase much (within 15%). A yield-stress fluid drop stops spreading on a gel substrate with higher yield stress regardless of the impact velocity, which is quite different from the case of Newtonian fluid with low viscosity (water) as reported in Figure 4.19. Large portion of kinetic energy of the drop is dissipated during impact as indicated by the large deformation of the substrate at high Weber numbers (see the last several images of third and fifth image sequences in Figure 4.18). Due to the complicated non-Newtonian nature of the viscoplastic fluid more detailed investigation on the flow field inside the gel drop is needed in order to fully understand the mechanism.

4.3.3 Possible mechanism for spreading behaviours

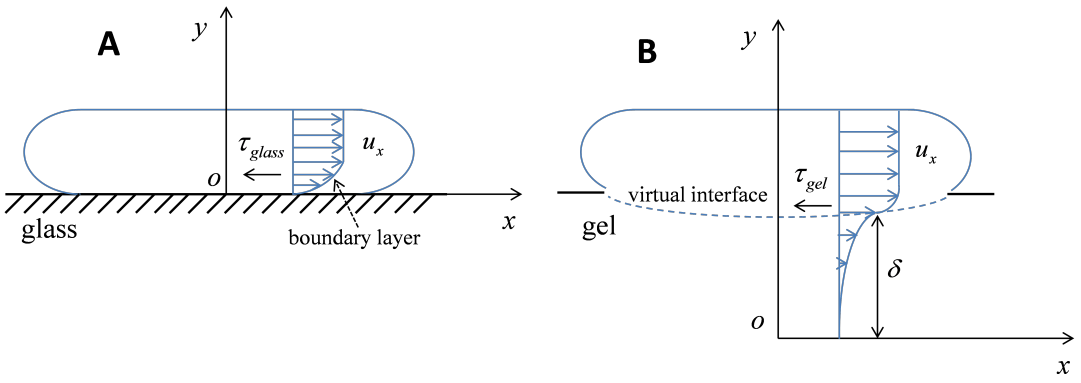

Figure 4.21: The schematic displaying the velocity profile during inertial spreading: (A) a spreading Newtonian drop on a solid glass substrate; (B) a spreading Newtonian drop on a soft gel substrate.

Here we propose a possible mechanism which explains the spreading behaviours of Newtonian drops impacting on different substrates as follows: (i) for the case of a glass substrate, a velocity boundary layer is formed close to the solid wall during spreading as displayed by the schematic in Figure 4.21. The velocity gradient at the wall surface is large, which leads to large local shear stress:

$$\tau_{glass} = \mu \frac{\mathrm{d}u_x}{\mathrm{d}y} \mid_{y=0} . \tag{4.5}$$

Thus, the drop is subjected to large friction force during spreading. (ii) In the case of a gel substrate, the boundary layer is different since the momentum of the drop fluid can be transferred to the substrate fluid. The horizontal velocity increases more gently within a larger range of y axis, as shown schematically in Figure 4.21. It should be noted that the value of δ (Figure 4.21) can be very small or even negligible compared with the equilibrium diameter of the drop, especially at sufficient low Weber numbers. As a consequence the velocity gradient at the virtual interface is lower:

$$\tau_{gel} = \mu \frac{\mathrm{d}u_x}{\mathrm{d}y} \mid_{y=\delta} < \tau_{glass}, \tag{4.6}$$

and the drop is subject to a smaller friction force. The spreading of an impacting Newtonian drop on a gel is a result of the competition between the deformation of the substrate and the drag reduction resulting from the gel surface. For a soft substrate (τ_0 = 11.7 Pa), the deformation effect dominates hence it spreads slower than a solid surface. Nevertheless for a much more solid substrate (τ_0 = 94.0 Pa) the drag reduction effect becomes dominant, which leads to faster spreading. In the case of intermediately soft substrate (τ_0 = 29.1 Pa), the drag reduction effect compensates the deformation effect, as a result the inertia spreading stage is similar to the case of glass substrate (see Figure 4.19).

4.4 Cavity evolution and permanent nestling of viscoplastic drop impact on viscoplastic surfaces

The results presented in this section are obtained through the experimental setup described in Section 3.7.1 with a high-speed camera which is horizontally aligned with the impact surface.

4.4.1 Morphology

The impact morphology of viscoplastic drops onto viscoplastic substrates is shown in Figure 4.22 & 4.23. In particular, six cases are selected: (1) an impacting drop with yield stress τ_0 = 1.13 Pa on substrate with the same yield stress at impact Weber number 15 [Figure 4.22(a)]; (2) an impacting drop with yield stress τ_0 = 1.13 Pa on substrate with the same yield stress at impact Weber number 85 [Figure 4.22(b)]; (3) an impacting drop with yield stress τ_0 = 3.64 Pa on substrate with the same yield stress at impact Weber number 15 [Figure 4.22(c)]; (4) an impacting drop with yield stress τ_0 = 3.64 Pa on substrate with the same yield stress at impact Weber number 85 [Figure 4.23(a)]; (5) an impacting drop with yield stress τ_0 = 1.13 Pa on substrate with τ_0 = 3.64 Pa at impact Weber number 50

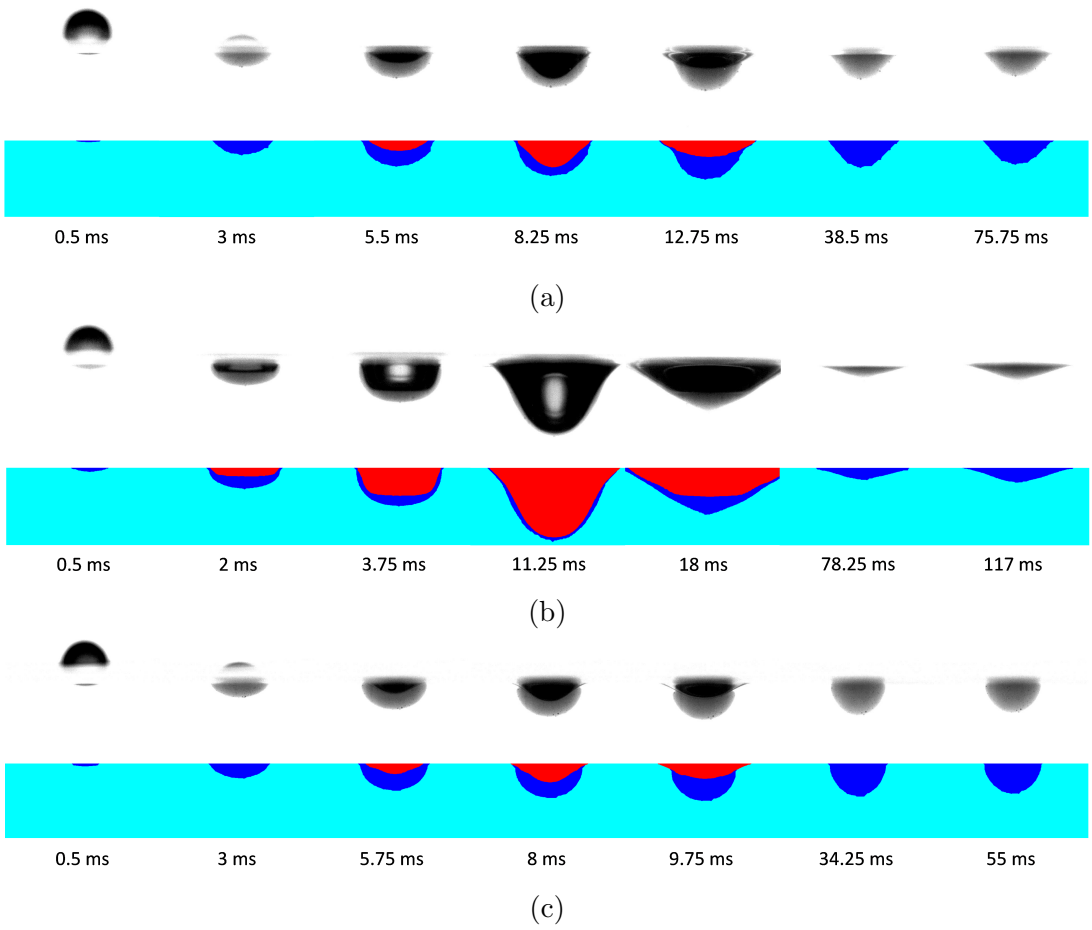

Figure 4.22: Impact morphology of viscoplastic drops onto gel substrates: (a) drop (τ_0 = 1.13 Pa), substrate (τ_0 = 1.13 Pa) & We = 15; (b) drop (τ_0 = 1.13 Pa), substrate (τ_0 = 1.13 Pa) & We = 85; (c) drop (τ_0 = 3.64 Pa), substrate (τ_0 = 3.64 Pa) & We = 15. The first row displays original images and the second row the same images after processing; the time after impact is shown at the bottom.

[Figure 4.23(b)]; (6) an impacting drop with yield stress τ_0 = 3.64 Pa on substrate with τ_0 = 1.13 Pa at impact Weber number 50 [Figure 4.23(c)]. From these image sequences the common feature of the morphology of a viscoplastic drop impacting on a viscoplastic substrate can be summarized: first, the drop fluid penetrates the substrate with an approximately hemispherical shape; second, a crater is developed due to the large kinetic energy of the impacting drop which deforms the free surface; last, the crater retracts due to the combined effects of buoyancy and surface energy minimisation and finally disappears, however some of the drop fluid remains permanently nestled into the substrate (see the last two images for

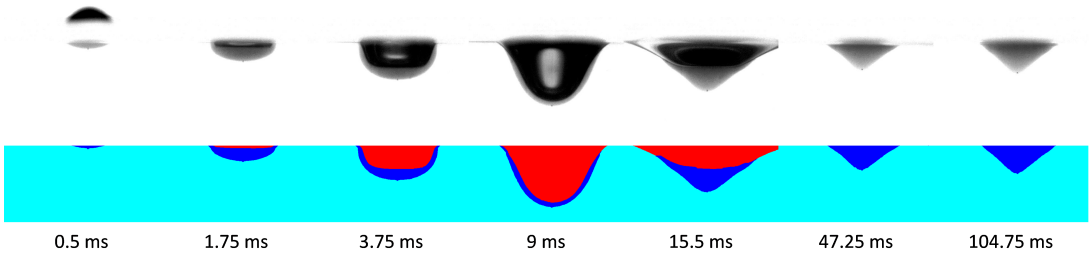

(a)

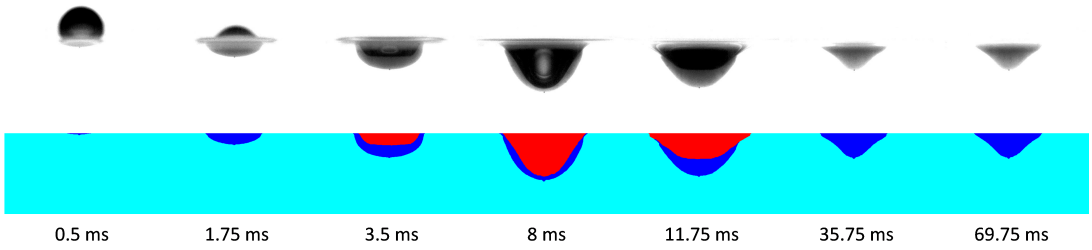

(b)

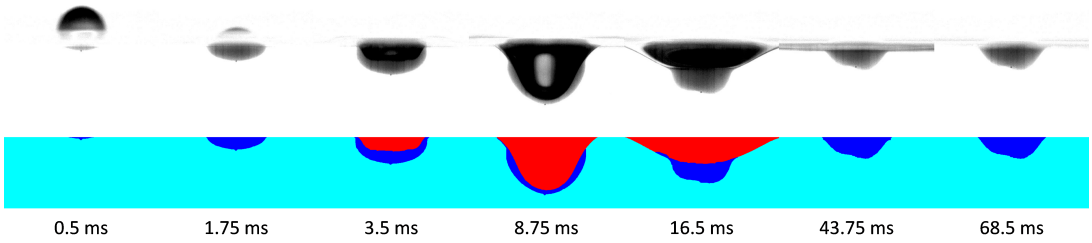

(c)

Figure 4.23: Impact morphology of viscoplastic drops onto gel substrates: (a) drop (τ_0 = 3.64 Pa), substrate (τ_0 = 3.64 Pa) & We = 85; (b) drop (τ_0 = 1.13 Pa), substrate (τ_0 = 3.64 Pa) & We = 50; (c) drop (τ_0 = 3.64 Pa), substrate (τ_0 = 1.13 Pa) & We = 50. The first row displays original images and the second row the same images after processing; the time after impact is shown at the bottom.

each case).

Although the interface between the gel substrate and air is of difficult interpretation, both because of the change in the refractive index and because of some blurring due to background subtraction, one can observe capillary waves [132] propagating in the radial direction from the impact point. Previous studies showed that viscoplastic drops may have highly non-spherical shapes prior to impact [76, 78, 77], which may affect significantly the crater evolution; however the relatively low yield stresses of the fluids used in the present work ensure the drop

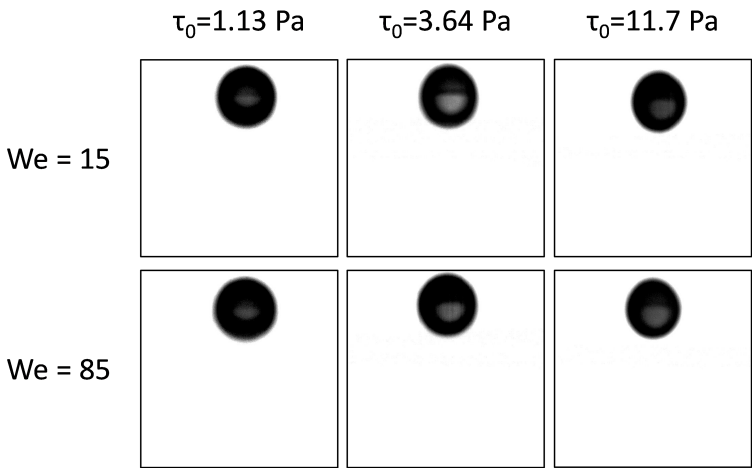

Figure 4.24: Drop shapes before impact. Impact Weber number We=15 & 85.

shape before impact is spherical irrespective of the Weber number, as shown in Figure 4.24 (note that the optical system is focused on the drop profile below the surface so the drop profile above the liquid surface is less sharp).

The morphology of a softer drop impacting on a harder surface is compared with that of a harder drop impacting on a softer surface at the same impact Weber number in Figures 4.23(b) and 4.23(c). The initial development is almost identical. However a larger crater is formed for the case of harder-drop/softer-surface combination due to the softness of the surface which leads to greater deformation. The final shape at the end of impact becomes asymmetric compared to the softer-drop/harder-surface case (note this asymmetry is observed systematically in repeated experiments).

Figure 4.25 and 4.26 plot the temporal variations of the normalised dimensions (Δ & Ω) with respect to equilibrium drop diameter of both the drop fluid and the crater for four different cases. An almost linear increase of the depth of both the crater and the drop fluid with respect to time is observed in the initial stage for all cases. The growth rate of the crater depth is higher than that of the drop fluid in case of low Weber numbers [Figure 4.25(a) & Figure 4.25(b)] whilst the growth rates are almost the same at high impact We numbers [Figure 4.26(a)

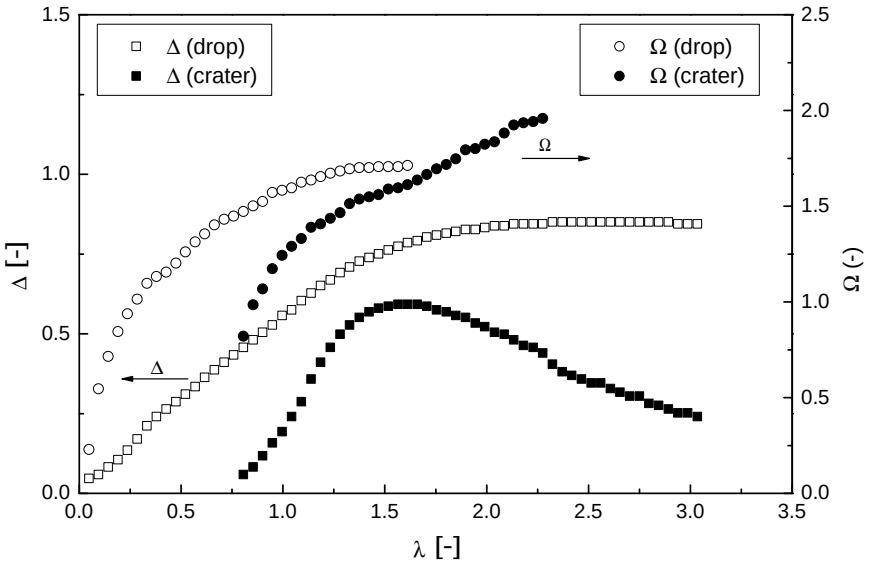

(a)

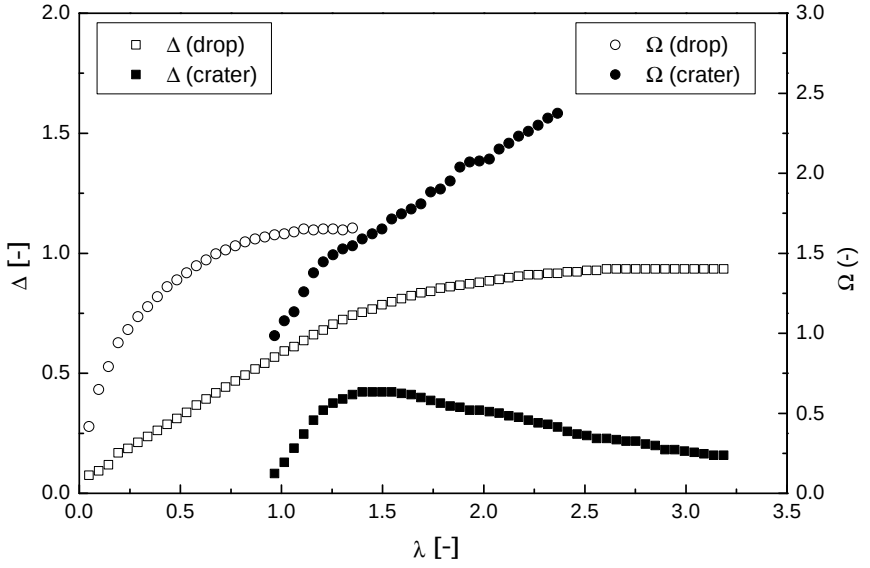

(b)

Figure 4.25: The normalised dimensions (Δ & Ω) of both drop fluid (open symbols) and crater (filled symbols) as a function of dimensionless time (λ) for different cases: (a) $\tau_{0,drop}$ = 1.13 Pa, $\tau_{0,substrate}$ = 1.13 Pa, We = 15; (b) $\tau_{0,drop}$ = 3.64 Pa, $\tau_{0,substrate}$ = 3.64 Pa, We = 15.

& Figure 4.26(b)]. A systematic comparison between the experimental data and the prediction of crater evolution model for Newtonian drops by Bisighini et al. [29] will be discussed in Section 4.4.4.

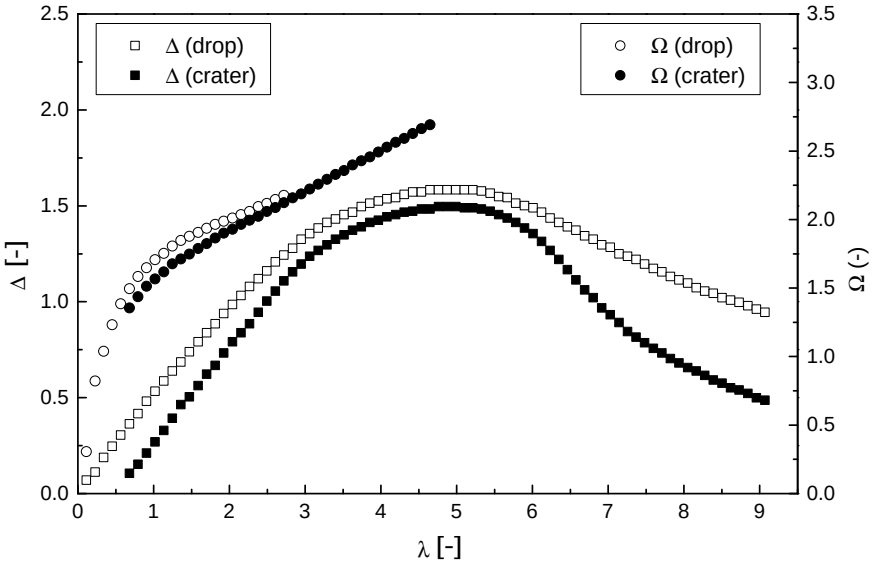

(a)

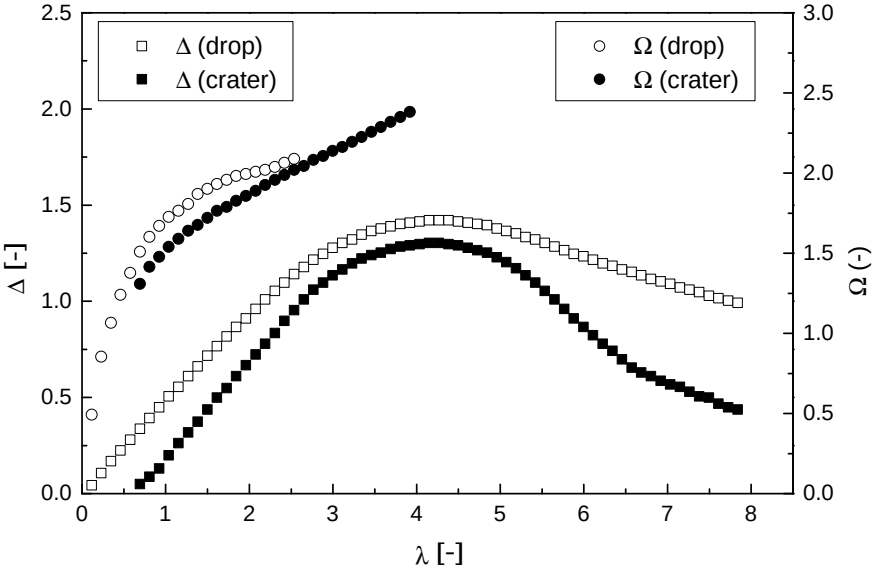

(b)

Figure 4.26: The normalised dimensions (Δ & Ω) of both drop fluid (open symbols) and crater (filled symbols) as a function of dimensionless time (λ) for different cases: (a) $\tau_{0,drop}$ = 1.13 Pa, $\tau_{0,substrate}$ = 1.13 Pa, We = 85; (b) $\tau_{0,drop}$ = 3.64 Pa, $\tau_{0,substrate}$ = 3.64 Pa, We = 85.

4.4.2 Permanent nestling

An interesting phenomenon observed here is the permanent nestling of the drop fluid in the substrate under the impact point. The drop fluid remains confined within a volume with either conical, irregular, or spherical-cap shape, which is

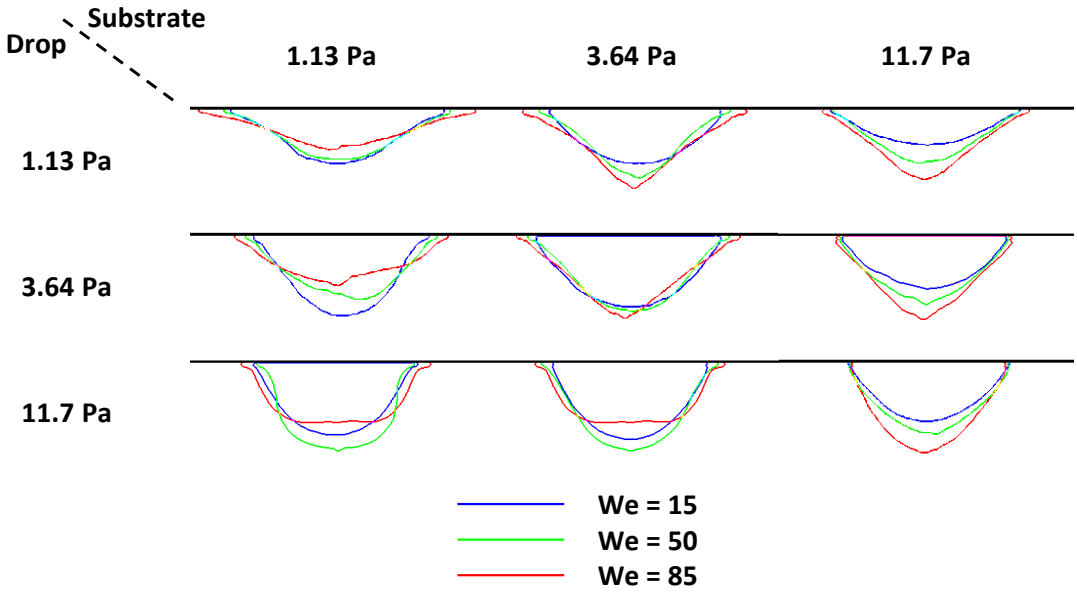

Figure 4.27: The morphology map of impacting drops for different drop/substrate combinations at low (We=15, blue line), intermediate (We=50, green line) and high (We=85, red line) Weber numbers. The top row indicates the yield stress values of the substrate while the column on the left denotes the values of impacting drops.

preserved in time due to the intrinsic yield-stress nature of both the drop and the substrate, which reduces significantly molecular diffusion and advection in comparison with low-viscosity Newtonian fluids. The final shape of a drop deposited onto a partially cured substrate is of great importance in the inkjet manufacturing process. For this reason, the final profiles of the impacting drops for different drop/surface yield stress combinations and different Weber numbers (We = 15, 50&85) are displayed in Figure 4.27. One can observe that the final shape of the impacting drops has is approximately a spherical cap at low Weber numbers, but tends to evolve into a conical or truncated-conical shape as the Weber number increases for all combinations of drop/substrate yield stresses.

The depth of the impacting drop grows with the Weber number for drop impacts on harder substrate (τ_0 = 11.7 Pa), however for softer substrates (e.g., τ_0 = 1.13 Pa) the impacting drop expands horizontally instead of penetrating vertically at high impact Weber numbers. As a consequence, in the case of softer

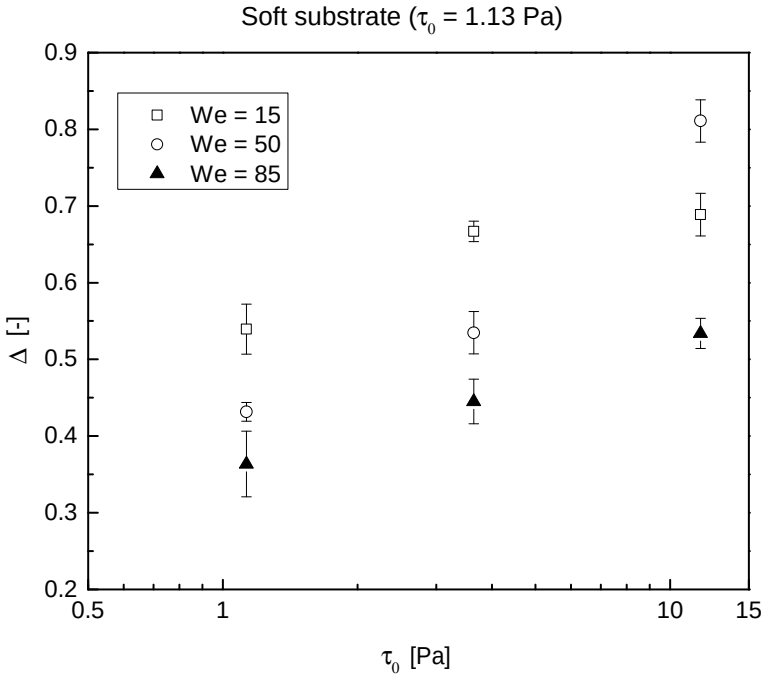

Figure 4.28: Depth of final profiles of impact drops as a function of the yield stress of impacting drops at three different Weber numbers for a soft substrate (τ_0 = 1.13 Pa).

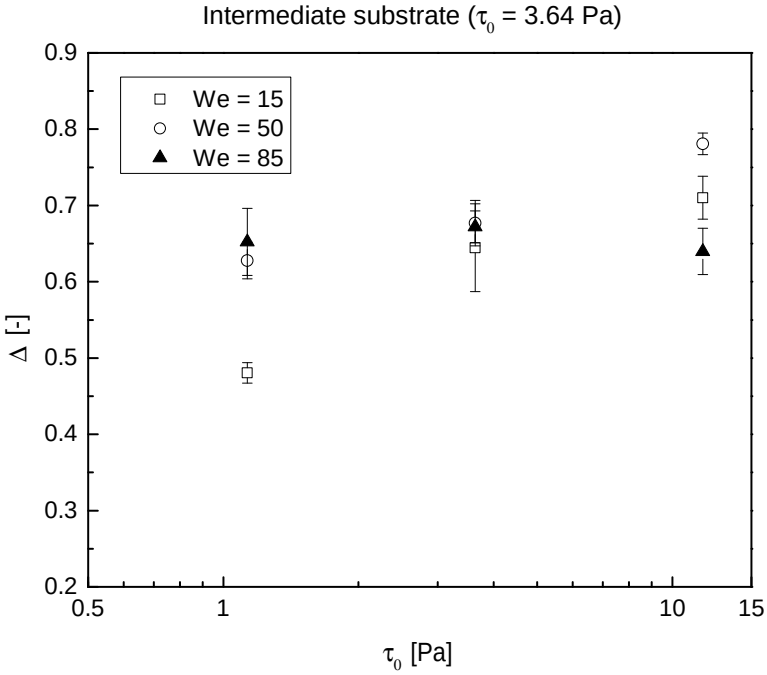

Figure 4.29: Depth of final profiles of impact drops as a function of the yield stress of impacting drops at three different Weber numbers for an intermediate substrate (τ_0 = 3.64 Pa).

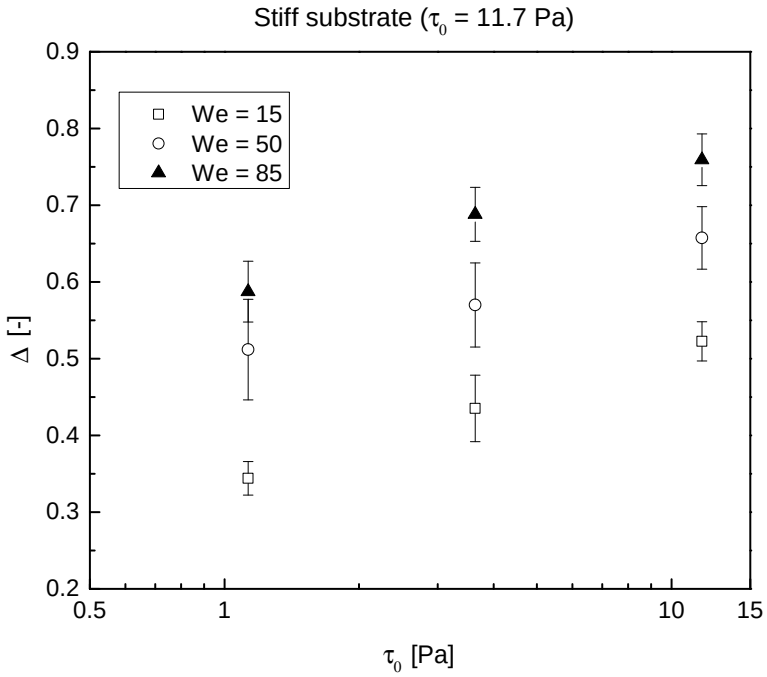

Figure 4.30: Depth of final profiles of impact drops as a function of the yield stress of impacting drops at three different Weber numbers for a stiff substrate (τ_0 = 11.7 Pa).

substrates the penetration depth of the impacting drop surprisingly decreases with respect to the increase of the Weber number, as shown in Figure 4.28, which plots the depth of final profiles of impacting drops as a function of the yield stress at three different Weber numbers. The experimental data averaged over five experiments per set are divided into three groups according to the stiffness of the substrate (soft: τ_0 = 1.13 Pa in Figure 4.28, intermediate :τ_0 = 3.64 Pa in Figure 4.29 and hard: τ_0 = 11.7 Pa in Figure 4.30). It is observed that the depth of the impacting drop increases monotonically as the drop becomes harder (i.e., higher yield stress) except in the case of the intermediate substrate at We = 85, which does not show significant changes.

4.4.3 Volume of final shape

The volume of the final shape of the drop fluid underneath the surface of the substrate can be estimated through the digital information extracted from the

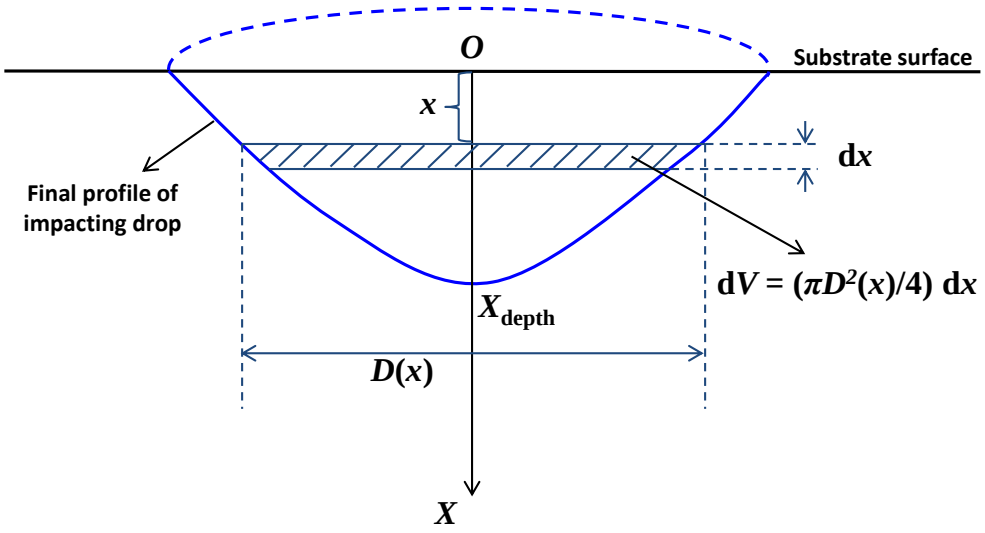

Figure 4.31: Schematic of the volume calculation of drop fluid.

processed images (Figures 4.22 & 4.23) at the end of impact. Under the assumption that the final shape is axisymmetric, the total volume of the depositing drop material below the substrate surface can be calculated from the sum of the volumes of several thin disks as shown in Figure 4.31. The integral expression of the total volume can be discretised by the sum of finite small disks with thickness of one pixel:

$$V_{\text{final}} = \int_0^{X_{\text{depth}}} \mathrm{d}V = \int_0^{X_{\text{depth}}} \frac{\pi D^2(x)}{4} \mathrm{d}x \approx \sum_{i=1}^{n} \frac{\pi D^2(i)}{4} \Delta x, \tag{4.7}$$

where $D(i)$ denotes the local diameter of the disk measured by image processing, Δx the thickness of the disk (size of one pixel) and n the number of disks.

The ratio of this quantity to the original volume of the drop released from the needle (V_{final}/V_0) can be used as an indicator of the degree of penetration or diffusion. For a case of $V_{\text{final}}/V_0 < 1$, the drop partially penetrates the substrate leaving a part of the original fluid material over the surface of the substrate (a bump over the substrate surface is observed). However if $V_{\text{final}}/V_0 \approx 1$, it is suggested all the drop material is immersed in the substrate (i.e., full penetration), which occurs when the apparent drop volume (calculated from the grey region, see Figure 3.14) is almost the same as the volume of the original drop. This quantity is

closely related to two parameters: (i) the impact Weber number ($We = \rho D_0 u_i^2/\sigma$); (ii) the ratio of the yield stress magnitude of the drop to that of the substrate ($\beta = \tau_{0,\,\mathrm{drp}}/\tau_{0,\,\mathrm{sub}}$). The former expresses the magnitude of kinetic energy carried by the impacting drop since the surface tension is approximately the same for all model fluids (Table 3.5). The latter indicates the relative stiffness of the impacting drop compared to the substrate. At higher impact Weber numbers, a high value of V_{final}/V_0 is expected due to the large crater formation induced by high kinetic energy. Since the substrate is more likely to deform if the relatively stiffness of the drop is higher, it is anticipated that V_{final}/V_0 grows as the yield stress ratio, β, increases.

Figure 4.32 shows the normalized drop volume beneath the surface as a function of the yield stress ratio at different impact Weber numbers. These data suggest the amount of drop fluid penetrated into the substrate increases as a

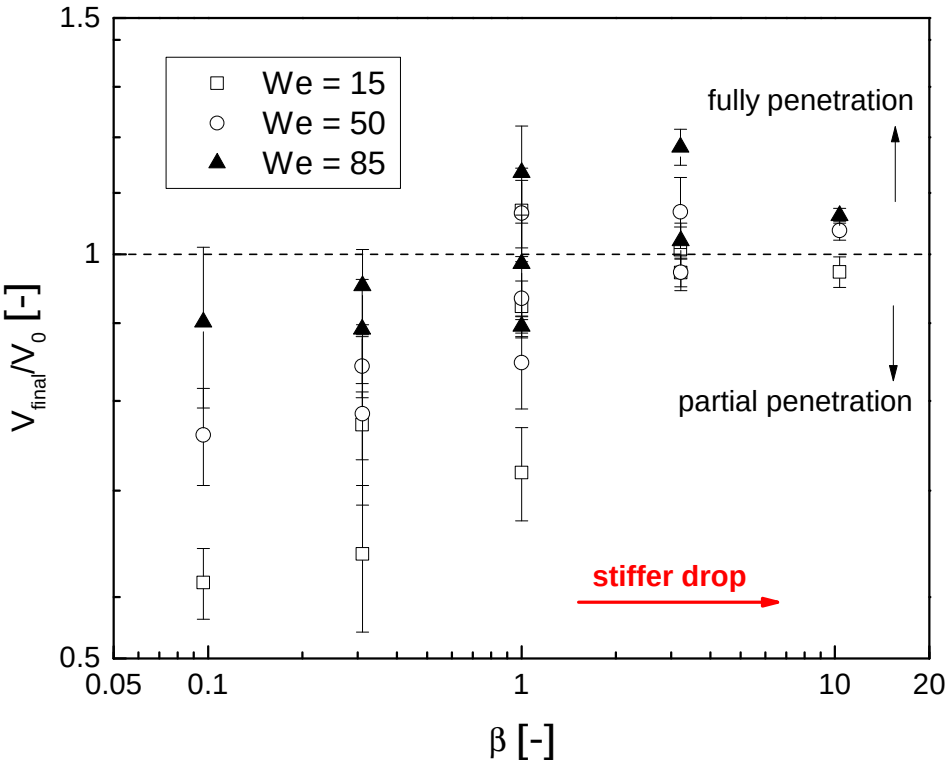

Figure 4.32: Normalized drop volume beneath the surface as a function of β at different impact Weber numbers.

function of the yield stress ratio; this becomes more evident when data corresponding to drop/substrate combinations with similar values of β (e.g., the combination with $\tau_{0,\,\mathrm{drp}}/\tau_{0,\,\mathrm{sub}} = 1.13/3.64 \approx 0.310$ and the combination with $\tau_{0,\,\mathrm{drp}}/\tau_{0,\,\mathrm{sub}} = 3.64/11.7 \approx 0.311$) are grouped together, as shown in Figure 4.33. The horizontal dashed line is provided as a guide to the eye to distinguish the 'full penetration' ($V_{\mathrm{final}}/V_0 \approx 1$) regime and the 'partial penetration' ($V_{\mathrm{final}}/V_0 < 1$) regime. As expected, V_{final}/V_0 increases monotonically with respect to both We and β, therefore this quantity can be conveniently re-plotted as a function of a single dimensionless parameter, i.e., the product (βWe); the experimental data of normalized drop volume as a function of βWe is plotted in Figure 4.34. Considering a function representing these experimental data $V_{\mathrm{final}}/V_0 = f(\beta We)$ with the following asymptotic properties, $\lim_{\beta We \to 0} V_{\mathrm{final}}/V_0 = 0$ and $\lim_{\beta We \to \infty} V_{\mathrm{final}}/V_0 = 1$, one can propose an empirical correlation:

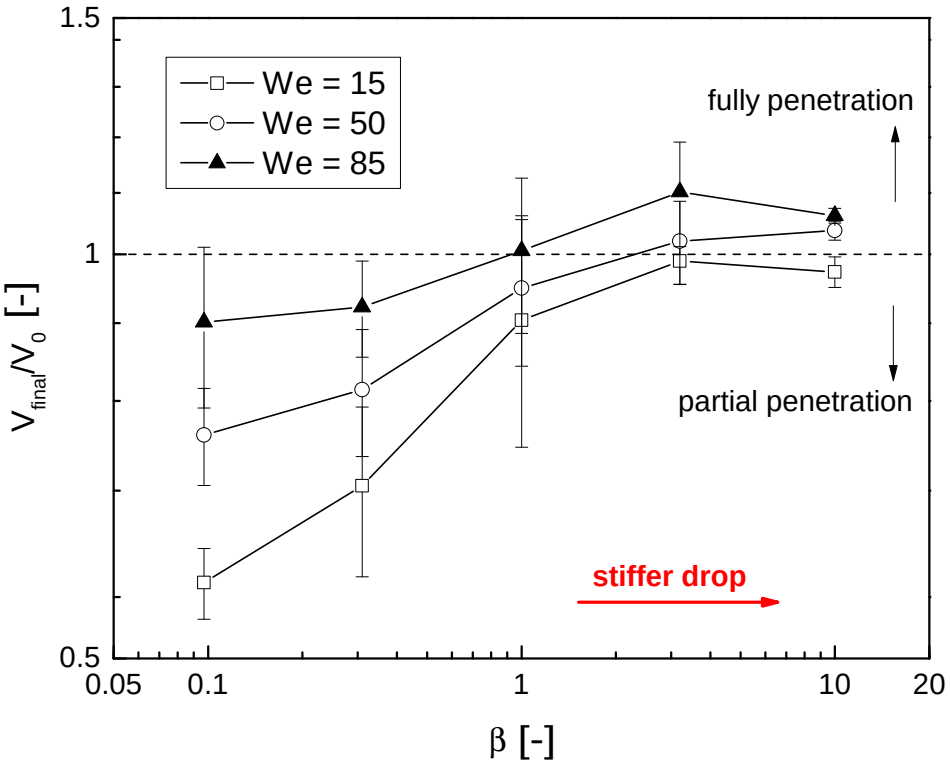

Figure 4.33: Normalized drop volume beneath the surface as a function of β at different impact Weber numbers. Data with close values of yield stress ratios are grouped together for clarity.

$$V_{\text{final}}/V_0 = \frac{1}{1 + m(\beta We)^{-n}}, \tag{4.8}$$

where m and n are constants obtained from least-squares fitting, and their numerical values are $m = 1.2$ & $n = 0.82$, with a correlation coefficient 0.92.

4.4.4 Crater evolution

Experimental data are compared with the prediction of a crater evolution model developed for Newtonian fluids [29]. Since the model assumes the same fluid for the drop and the impact surface, only the drop/substrate combinations with the same yield stress are considered. The temporal evolution of the dimensionless diameter (or width), Ω, during the initial stage can be approximated as:

$$\Omega \approx 2\sqrt{(\alpha_0 + 0.17\lambda)^2 - (0.27\lambda - \alpha_0)^2}, \tag{4.9}$$

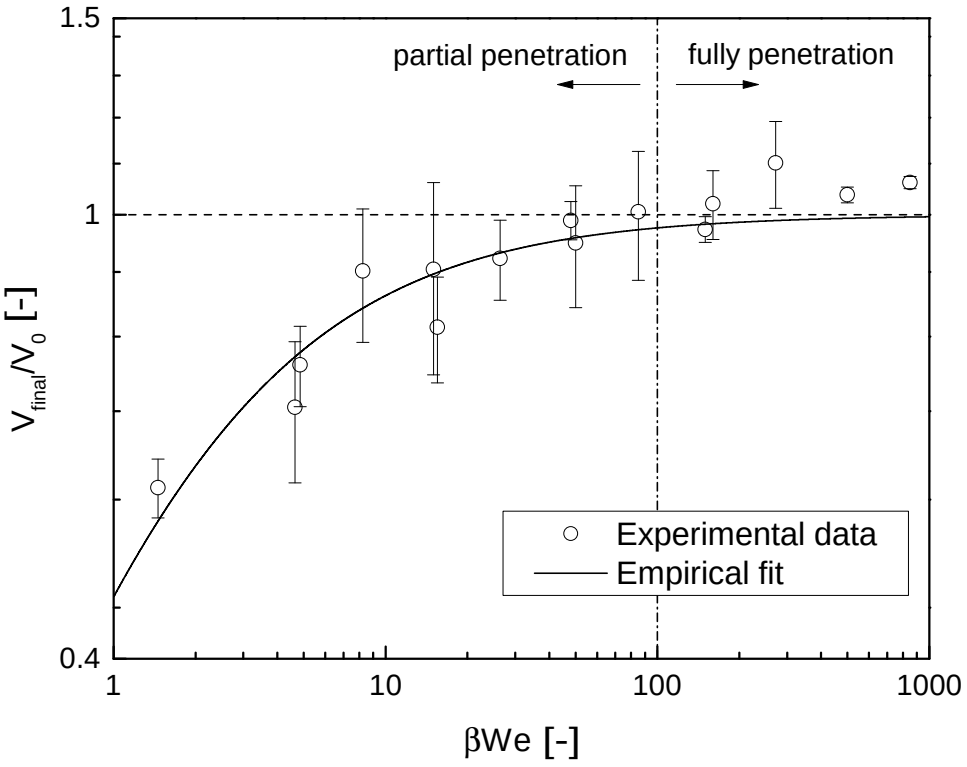

Figure 4.34: Normalized drop volume beneath the surface as a function of βWe. Experimental data are represented by open circles while solid line indicates the empirical fit.

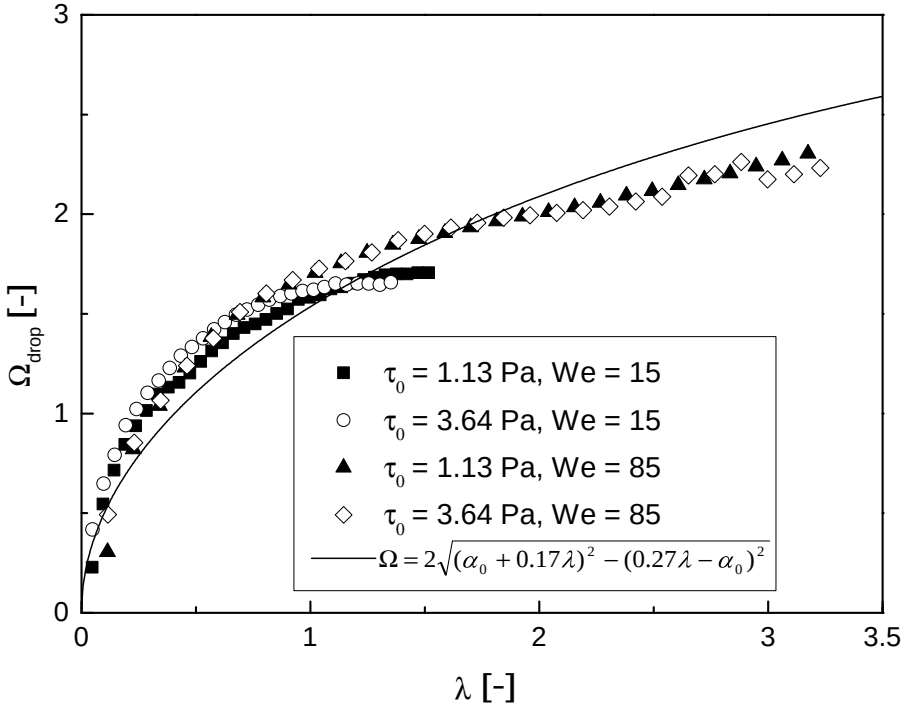

(a)

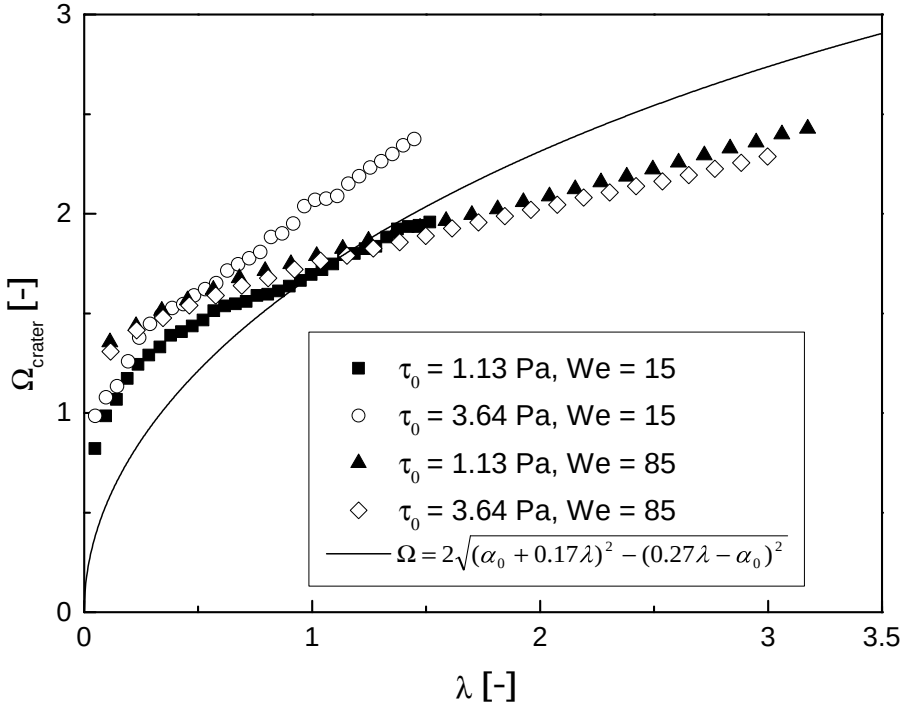

(b)

Figure 4.35: Temporal evolution of the dimensionless diameter of drop/crater for different impact parameters and the fit curve by crater evolution model: (a) drop fluid; (b) crater.

where λ is the dimensionless time and α_0 a constant associated with the initial cavity radius. Measurements of the temporal evolution of the crater and drop fluid diameters in the initial stage reported in Figures 4.25 & 4.26 were fitted to Equation 4.9 separately, as shown in Figure 4.35 (note dimensionless time is used). Fitting experimental data relative to Newtonian fluids using the same model yields a constant $\alpha_0 = 0.77$ [29]. Here, a constant $\alpha_0 = 0.71$ with standard error 0.011 (Figure 4.35a) was obtained for the temporal evolution of drop fluid diameter, while a value $\alpha_0 = 0.85$ with standard error 0.027 (Figure 4.35b) for the crater diameter evolution. Thus, the model is in better agreement with the drop fluid diameter rather than the crater diameter.

In the crater evolution model (see Section 2.3.3), the dimensionless depth grows linearly with respect to dimensionless time in the initial stage ($\lambda < \lambda^*$):

$$\Delta = 0.44\lambda. \tag{4.10}$$

In the second stage ($\lambda > \lambda^*$) the crater evolution for inviscid flow can be described by the following differential equations (where $\Delta = \alpha + \zeta$):

$$\ddot{\alpha} = -\frac{3}{2}\frac{\dot{\alpha}^2}{\alpha} - \frac{2}{\alpha^2 We} - \frac{1}{Fr}\frac{\zeta}{\alpha} + \frac{7}{4}\frac{\dot{\zeta}^2}{\alpha}, \tag{4.11}$$

$$\ddot{\zeta} = -3\frac{\dot{\alpha}\dot{\zeta}}{\alpha} - \frac{9}{2}\frac{\dot{\zeta}^2}{\alpha} - \frac{2}{Fr}. \tag{4.12}$$

Viscous effects can be taken into account by introducing the viscous energy dissipation terms into Equation 4.11 and Equation 4.12:

$$\ddot{\alpha} = -\frac{3}{2}\frac{\dot{\alpha}^2}{\alpha} - \frac{2}{\alpha^2 We} - \frac{1}{Fr}\frac{\zeta}{\alpha} + \frac{7}{4}\frac{\dot{\zeta}^2}{\alpha} - \frac{4\dot{\alpha}}{\alpha^2 Re}, \tag{4.13}$$

$$\ddot{\zeta} = -3\frac{\dot{\alpha}\dot{\zeta}}{\alpha} - \frac{9}{2}\frac{\dot{\zeta}^2}{\alpha} - \frac{2}{Fr} - \frac{12\dot{\zeta}}{\alpha^2 Re}. \tag{4.14}$$

Initial conditions can be obtained from the linear approximation in the first stage of impact [29]:

$$\dot{\alpha} \approx 0.17,\ \alpha \approx \alpha_0 + 0.17\lambda,\ \dot{\zeta} \approx 0.27,\ \zeta \approx -\alpha_0 + 0.27\lambda. \tag{4.15}$$

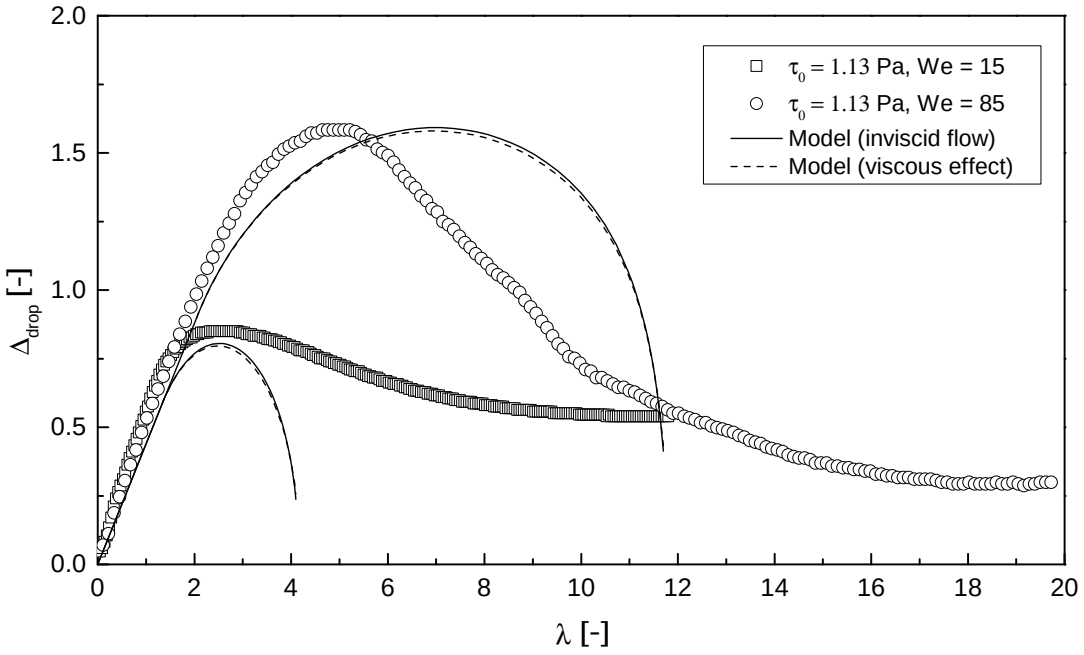

(a)

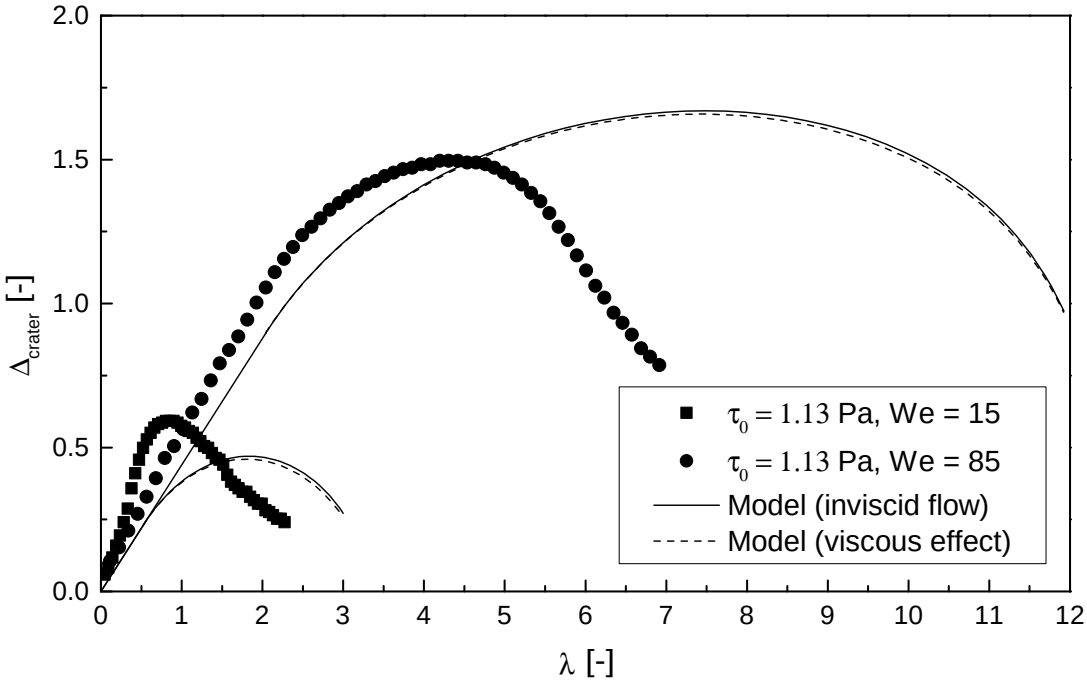

(b)

Figure 4.36: The dimensionless depth of crater/drop as a function of dimensionless time at various impact parameters: (a) dimension of drop fluid, τ_0 = 1.13 Pa; (b) dimension of crater, τ_0 = 1.13 Pa. The experimental data are represented by symbols. Solid lines indicate the model prediction for inviscid flow while the dashed lines show the difference if viscous effect is taken into account.

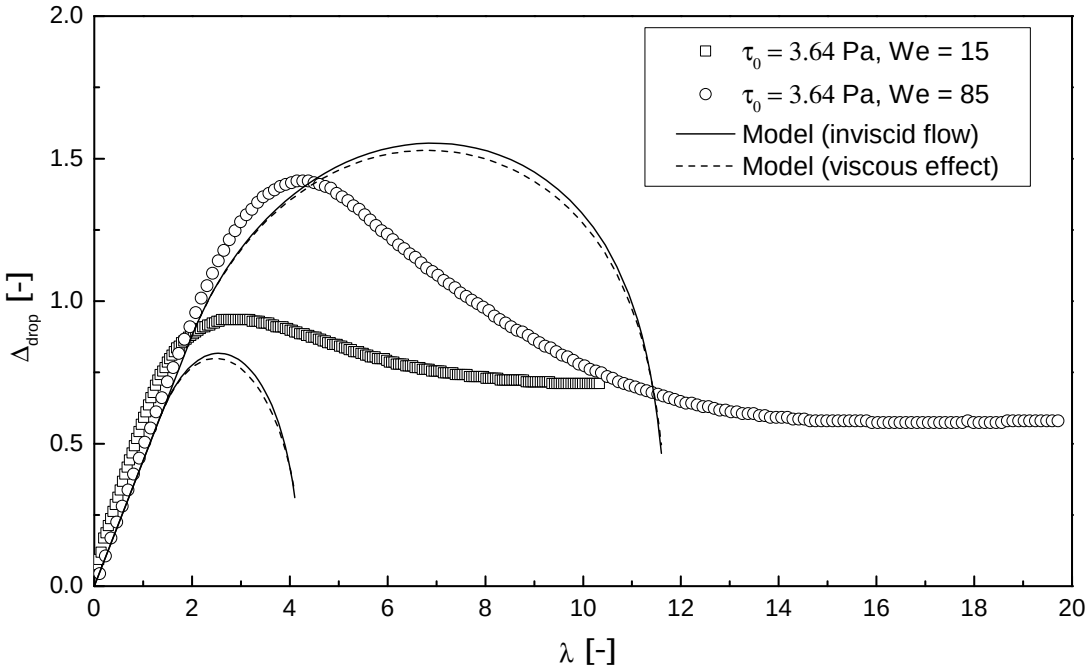

(a)

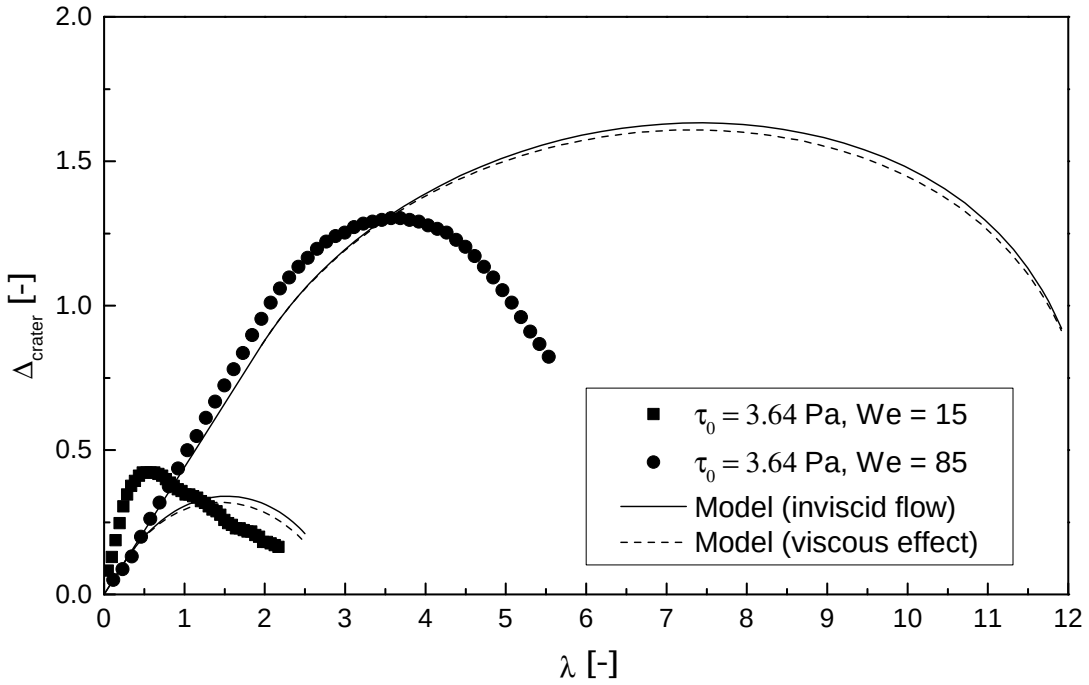

(b)

Figure 4.37: The dimensionless depth of crater/drop as a function of dimensionless time at various impact parameters: (a) dimension of drop fluid, τ_0 = 3.64 Pa; (b) dimension of crater, τ_0 = 3.64 Pa. The experimental data are represented by symbols. Solid lines indicate the model prediction for inviscid flow while the dashed lines show the difference if viscous effect is taken into account.

The model prediction of the crater evolution can be calculated by numerical integration of the system of ordinary differential Equations 4.11 and 4.12 (Equations 4.13 and 4.14 if considering viscous effects) using the initial condition from Equation 4.15 at $\lambda = \lambda^*$. For instance $\lambda^* = 1.3$ is observed for the case of the evolution of drop fluid in Figure 4.25(a). Together with $\alpha_0 = 0.72$ obtained from the diameter evolution model fit for drop fluid (Figure 4.35a), the initial condition for this case can be calculated as: $\dot{\alpha}(1.3) = 0.17$, $\alpha(1.3) = 0.941$, $\dot{\zeta}(1.3) = 0.27$, $\zeta(1.3) = -0.369$. The predicted dimensionless depth as a function of dimensionless time is compared with the experimental data for both drop fluid and crater in Figures 4.36 & 4.37. The Reynolds numbers in Equation 4.13 and 4.14 are calculated using the generalized definition of Reynolds number for the flow of a Herschel-Bulkley fluid derived by Madlener et al. [109]:

$$Re_{\mathrm{HB}} = \frac{\rho u_i^{2-n} D_0^n}{(\tau_0/8)(D_0/u_i)^n + K((3m+1)/(4m))^n 8^{n-1}}. \tag{4.16}$$

where K and n are flow parameters in Equation 2.57, u_i the impact velocity and $m = (nK(8u_i/D_0)^n)/(\tau_0 + K(8u_i/D_0)^n)$. As shown in Figure 4.36(a) and 4.37(a), the agreement between the experimental data the model prediction for the dimension of the drop fluid is reasonable at least in the first stage. The linear growth predicted by the model (Eq. 4.10) in the first stage is observed and the maximum depth is also correctly predicted. However for the case of crater dimension [Figures 4.36(b) and 4.37(b)], the depth grows faster than the model prediction in the first stage at low impact Weber number [see the filled square symbols in Figures 4.36(b) and 4.37(b)]. Also the crater evolution model underpredicts the maximum crater depth at $We = 15$ while at a higher impact Weber number the maximum depth is overpredicted. The discrepancy between the model predictions of inviscid flow and those obtained considering viscous effect is negligibly small, therefore viscous effects do not play a major role in the model, which is not obvious a priori. Nevertheless the fact that the maximum

depth for both cases of drop fluid and crater decreases as the yield stress increases indicates the magnitude of yield stress still plays an important role in case of viscoplastic fluids. The overall agreement between the experimental data and model prediction is better when describing the dimension of drop fluid than the crater.

At high impact Weber number, the drop fluid distributes almost uniformly over the large surface of the crater, forming a thin layer; thus, the difference between the dimensions of the crater and those of the drop fluid are negligibly small. For this reason, the crater evolution model is better at predicting the crater evolution at high impact Weber numbers, where the crater and the drop fluid are almost coincident. However, when the impact Weber number is low the drop forms a thick layer, hence there are greater differences between the evolution of the crater and that of the drop fluid. This behaviour was not observed in previous studies using low-viscosity Newtonian fluids, where there is an almost instantaneous mixing of the drop into the liquid substrate.

4.5 Drop impact on spherical elastic surfaces

The results presented in this section are obtained through the experimental setup described in Section 3.8.1.

4.5.1 Morphology

Effect of elastic modulus on morphology

The morphology of drop impact on elastic convex surfaces showing the effect of elastic modulus is displayed in Figures 4.38 & 4.39. In particular, four groups of image sequence are selected: Group A & Group B (Figure 4.38) compare the results at the same Weber number but different diameter ratios while Group C & Group D (Figure 4.39) compare the results at the same diameter ratio but different Weber numbers. The impact morphologies of the two cases of high

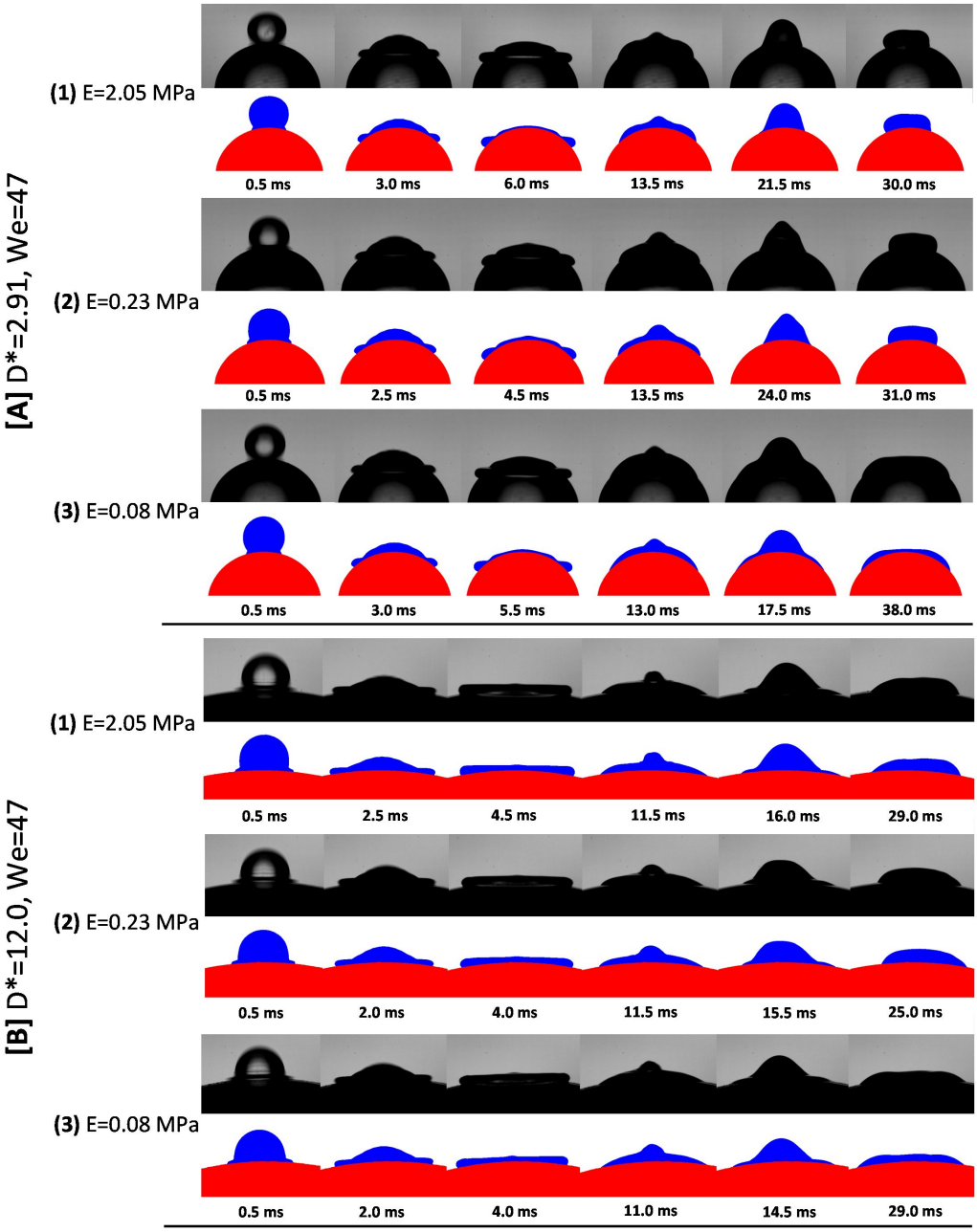

Figure 4.38: Morphology of drop impact on elastic convex surfaces showing the effect of **elastic modulus**. For each group of image sequences, the elastic modulus decreases from **(1)** to **(3)**: **(1)** E = 2.05 MPa, **(2)** E = 0.23 MPa & **(3)** E = 0.08 MPa. In order to show the effect of E under various conditions, different combinations of the other two impact parameters (D^* & We) are chosen for each group: **A**, D^* = 2.91, We = 47; **B**, D^* = 12.0, We = 47. The first row in each case represents the recorded images and the second row shows the processed images.

elastic moduli in Group A [A(1) & A(2)] are almost the same: the drop firstly spreads on the convex surface until the spreading angle reaches its maximum

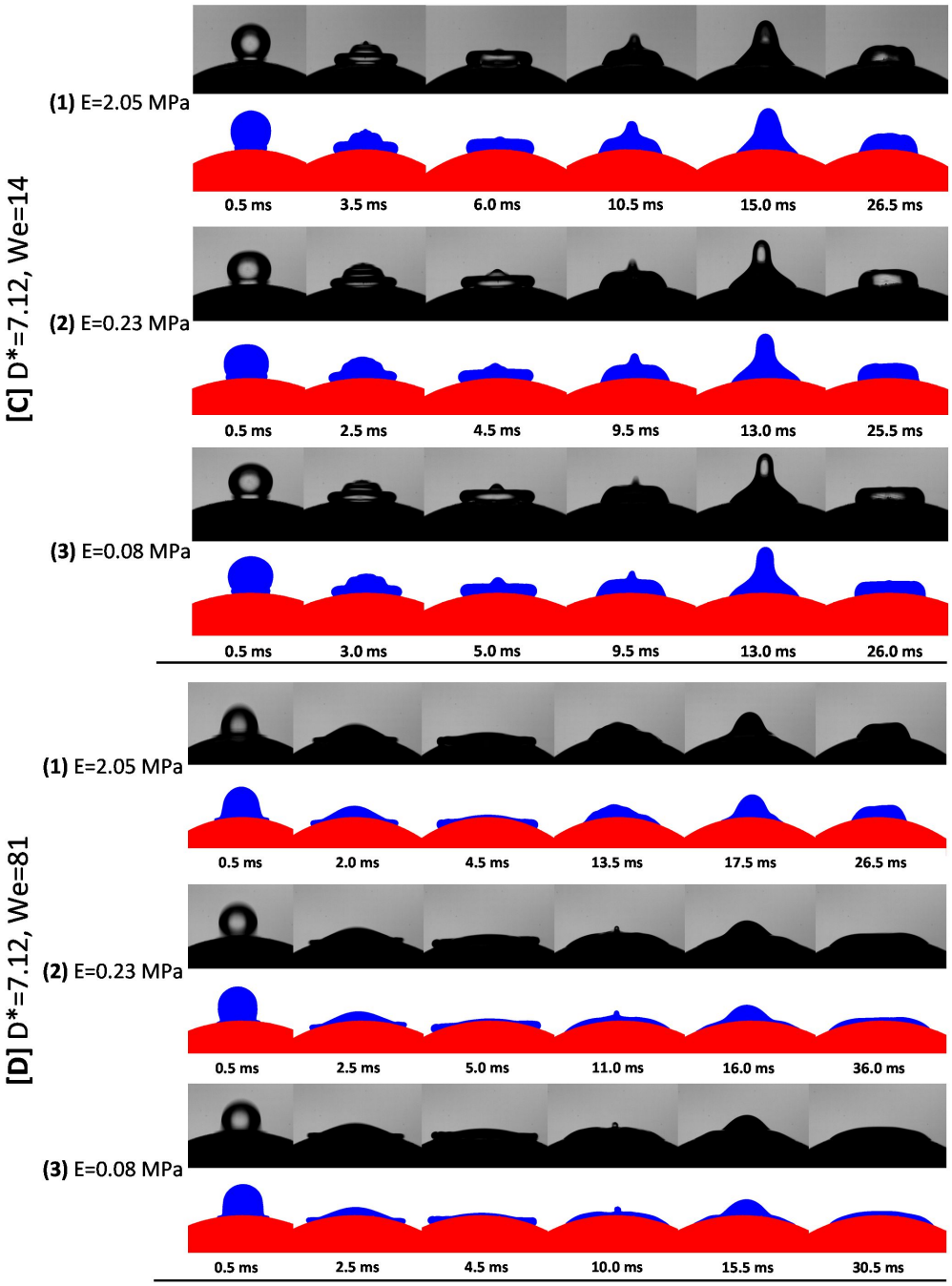

Figure 4.39: Morphology of drop impact on elastic convex surfaces showing the effect of **elastic modulus**. For each group of image sequences, the elastic modulus decreases from **(1)** to **(3)**: **(1)** E = 2.05 MPa, **(2)** E = 0.23 MPa & **(3)** E = 0.08 MPa. In order to show the effect of E under various conditions, different combinations of the other two impact parameters (D^* & We) are chosen for each group: **C**, D^* = 7.12, We = 14; **D**, D^* = 7.12, We = 81. The first row in each case represents the recorded images and the second row shows the processed images.

and then the thin liquid cap starts to recoil as the contact angle decreases. A central column of liquid may be observed at the end of the retraction stage (as shown by the last but one image). After the initial retraction the drop sits on the top of the hemisphere and oscillate periodically between horizontal direction and vertical direction. This stage is dominated by capillary forces. But for the case of low elastic modulus [A(3)], the liquid cap fails to retract and the rim of the liquid is almost pinned at the maximum spreading location. The height of central liquid column is also smaller than other two cases due to this pinning effect. However in the case of a higher impact Weber number (We = 81) and a greater diameter ratio (D^* = 7.12) as shown in Group C, besides the substrate with the lowest elastic modulus, the substrate with the intermediate elastic modulus [D(2)] also exhibits the 'pinned effect'. This effect becomes less pronounced at a relatively low impact Weber number and high diameter ratio (e.g., see Group B & C). Generally the spreading phase is not affected greatly by the elastic modulus. No splashing or breakup was observed in the range of Weber numbers considered, in agreement with other studied that demonstrated a strong increase of the splashing threshold due to the absorption of the kinetic energy of the impacting drop by the deformation of the substrate [125, 91].

Effect of diameter ratio on morphology

Figures 4.40 & 4.41 show the effect of diameter ratio on the morphology of drop impact on elastic convex surfaces. Specifically four groups of image sequence are selected: Group A & Group B (Figure 4.40) compare the results at the same Weber number but different elastic moduli while Group C & Group D (Figure 4.41) compare the results at the same elastic modulus but different Weber numbers. In Group A, surprisingly the case with the smallest diameter ratio [A(1)] exhibits the largest degree of retraction even though the gravity component applied on the liquid rim along the tangential direction is higher during both

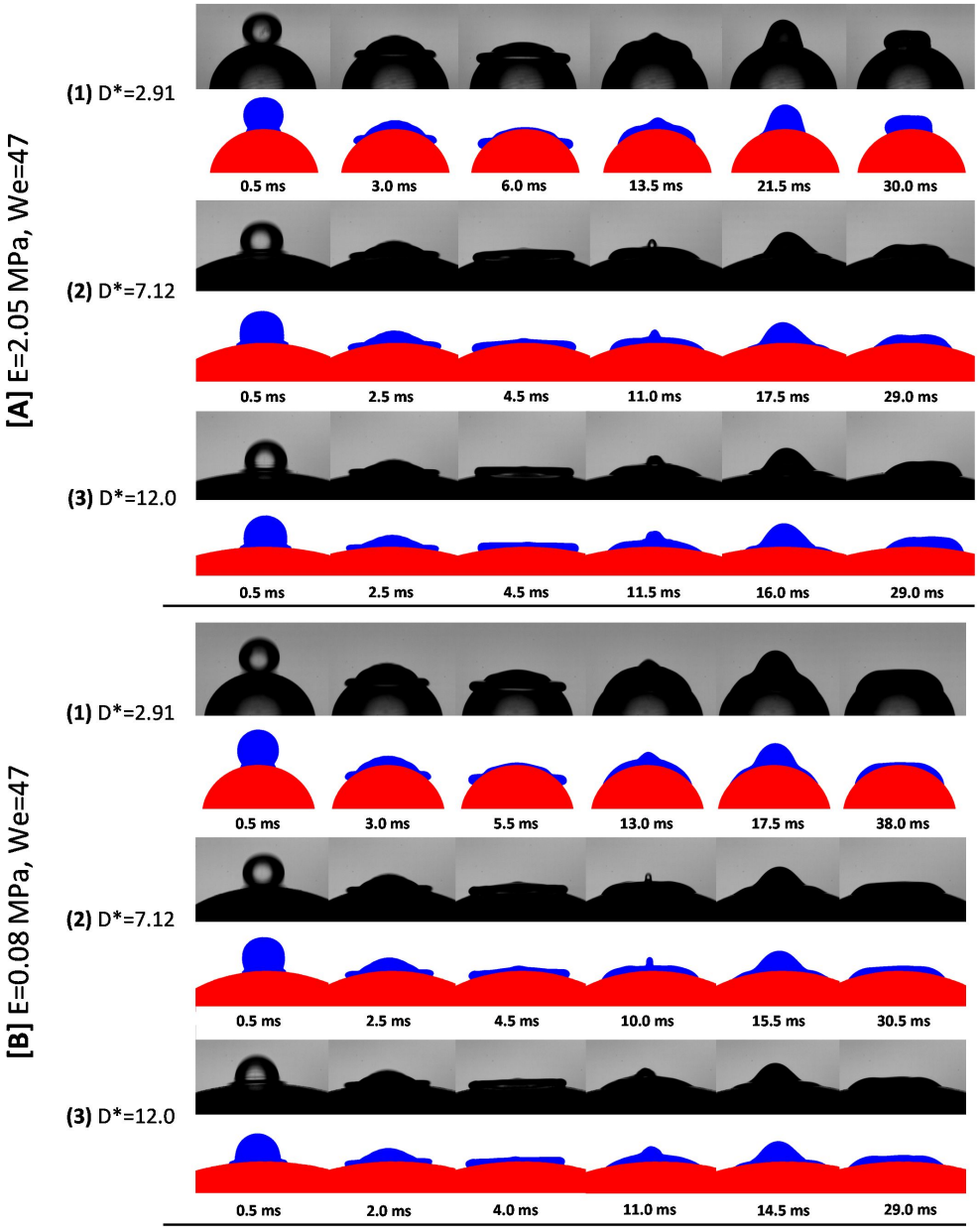

Figure 4.40: Morphology of drop impact on elastic convex surfaces showing the effect of **diameter ratio**. For each group of image sequences, the diameter ratio increases from **(1)** to **(3)**: **(1)** D^* = 2.91, **(2)** D^* = 7.12 & **(3)** D^* = 12.0. In order to show the effect of D^* under various conditions, different combinations of the other two impact parameters (E & We) are chosen for each group: **A**, E = 2.05 MPa, We = 47; **B**, E = 0.08 MPa, We = 47. The first row in each case represents the recorded images and the second row shows the processed images.

spreading and retracting phases than the other two cases. And the height of the liquid column formed after recoiling is greater compared to large diameter ratio

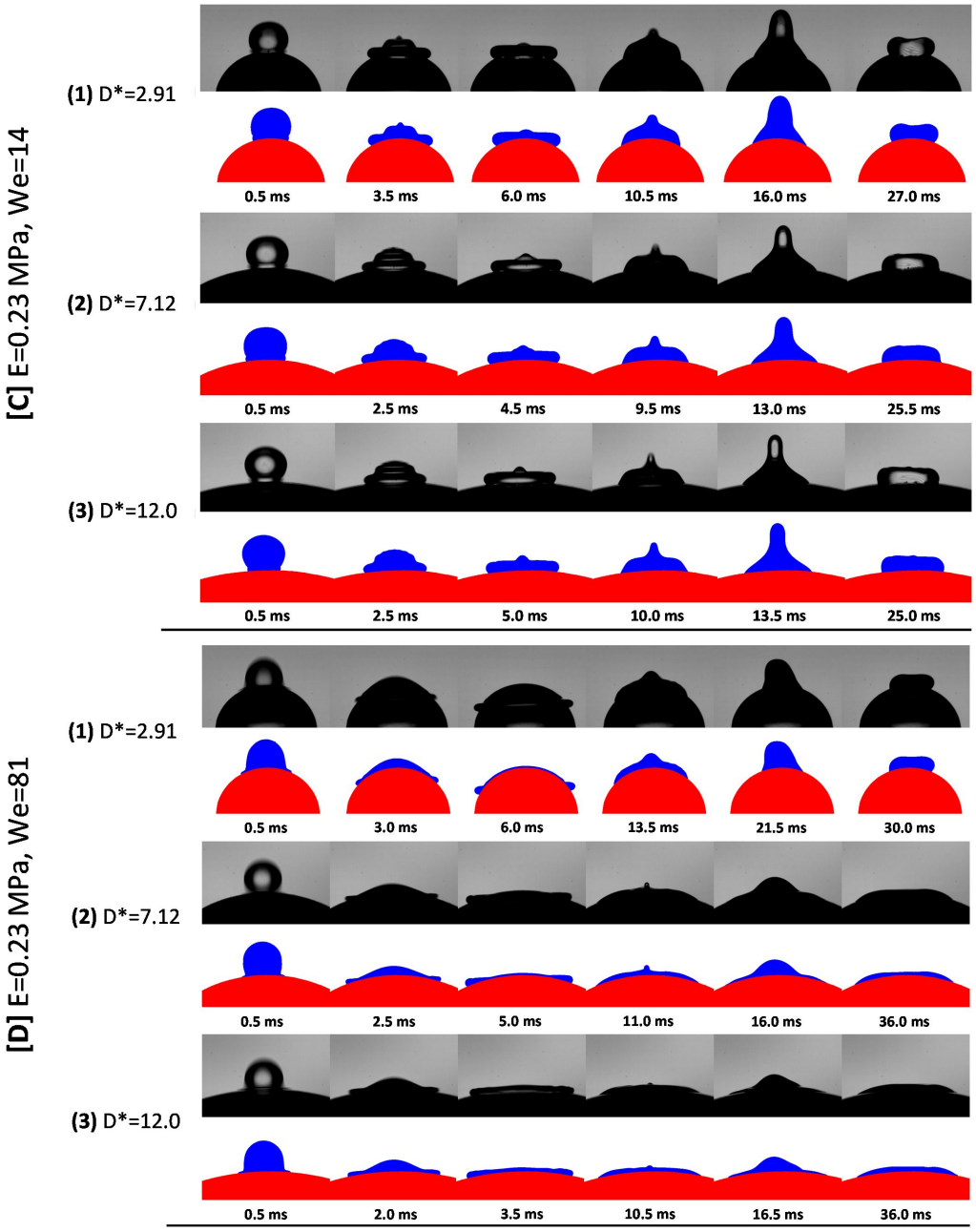

Figure 4.41: Morphology of drop impact on elastic convex surfaces showing the effect of **diameter ratio**. For each group of image sequences, the diameter ratio increases from **(1)** to **(3)**: **(1)** D^* = 2.91, **(2)** D^* = 7.12 & **(3)** D^* = 12.0. In order to show the effect of D^* under various conditions, different combinations of the other two impact parameters (E & We) are chosen for each group: **C**, E = 0.23 MPa, We = 14; **D**, E = 0.23 MPa, We = 81. The first row in each case represents the recorded images and the second row shows the processed images.

cases. This effect has also been observed in Group D. Here it is proposed that this 'de-wetting effect' is due to the combinational influence of gravity and large

curvature of the impact surface, which leads to a large dynamic contact angle at the beginning of retraction. For cases with very low elastic modulus, where the 'pinned effect' dominates, and very low impact Weber number (e.g., Group B & C) the 'de-wetting effect' becomes less significant.

Effect of Weber number on morphology

The effect of the impact Weber number on the impact morphology is displayed in Figures 4.42 & 4.43. Four groups of image sequences are selected: Group A & Group B (Figure 4.42) compare the results at the same diameter ratio but different elastic moduli, while Group C & Group D (Figure 4.43) compare the results at the same elastic modulus but different diameter ratios. As the impact Weber number increases, due to the curvature of the surface, the central part of the liquid lamella is no longer covered by the rim and becomes visible (e.g., Group A, B & D). Moreover flow instabilities are observed at high impact Weber number during the spreading stage as indicated by the wavy shape near the rim of the spreading lamella in (3) for all groups. In case C(3), the flow instabilities cause symmetry breaking during the retraction. As a result the drop partially slide off the top of the hemisphere.

4.5.2 Maximum spreading & minimum retracting

After impact the drop spreads radially from the top of the hemisphere to form a cap, and the base angle attains its maximum value at the end of the spreading stage. The maximum spreading angle ($\alpha_{\max}$) for different impact parameters is measured through digital image processing. If the same liquid lamella (i.e., the same surface energy) is deposited on hemispheres with different diameters, obviously the hemisphere with the lowest diameter will give the largest spreading angle. Thus the maximum spreading angle is very dependent of D^* and it is more reasonable to plot the normalised maximum length of the wetted arc (denoted by $\widehat{C_L C_R}$ in Figure 3.16): $L_{\max} = (\alpha_{\max}/180°) \cdot \pi \cdot (D_{sub}/2)$, which is proportional

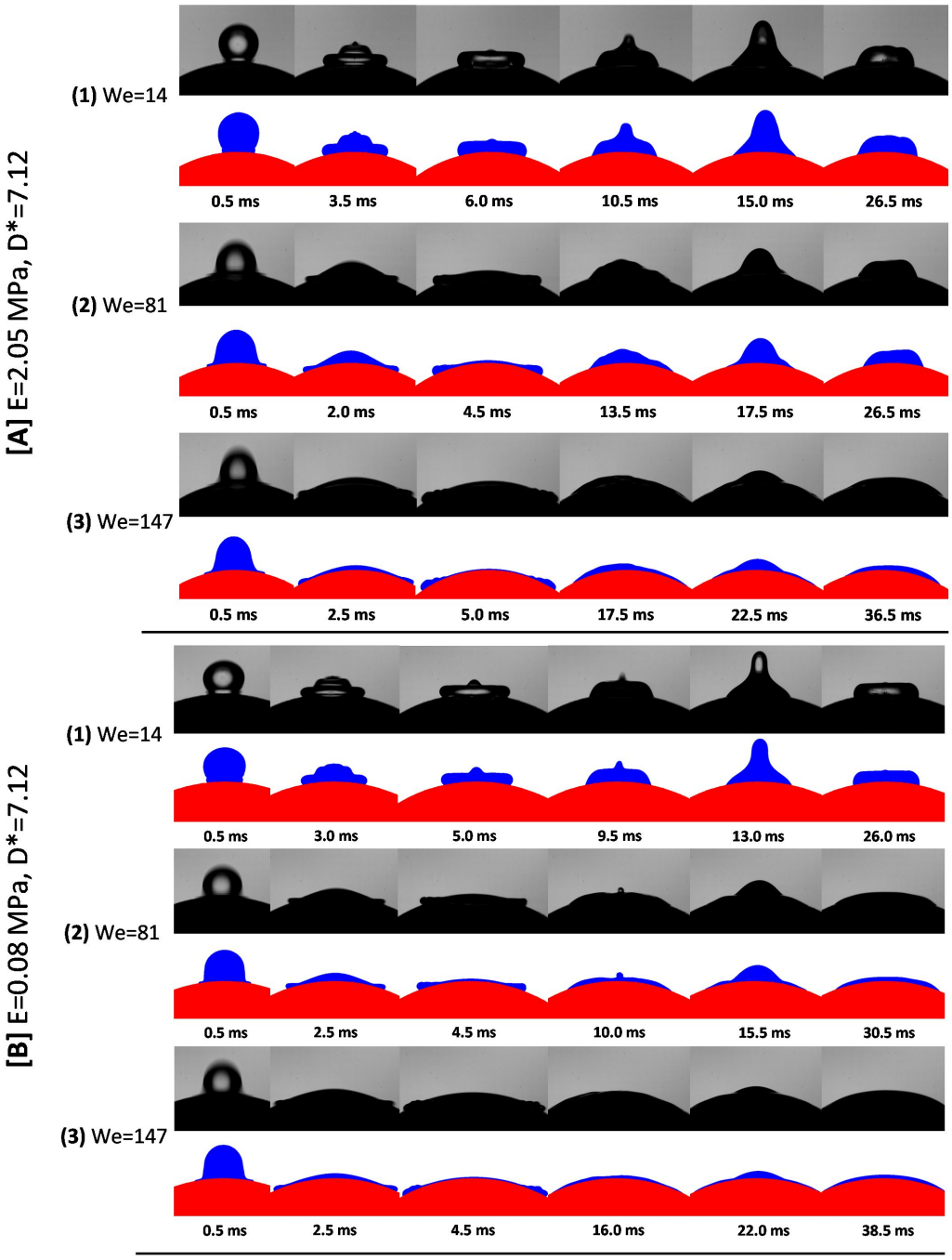

Figure 4.42: Morphology of drop impact on elastic convex surfaces showing the effect of **impact Weber number**. For each group of image sequences, the Weber number increases from **(1)** to **(3)**: **(1)** We = 14, **(2)** We = 81 & **(3)** We = 147. In order to show the effect of D^* under various conditions, different combinations of the other two impact parameters (E & D^*) are chosen for each group: **A**, E = 2.05 MPa, D^* = 7.12; **B**, E = 0.08 MPa, D^* = 7.12. The first row in each case represents the recorded images and the second row shows the processed images.

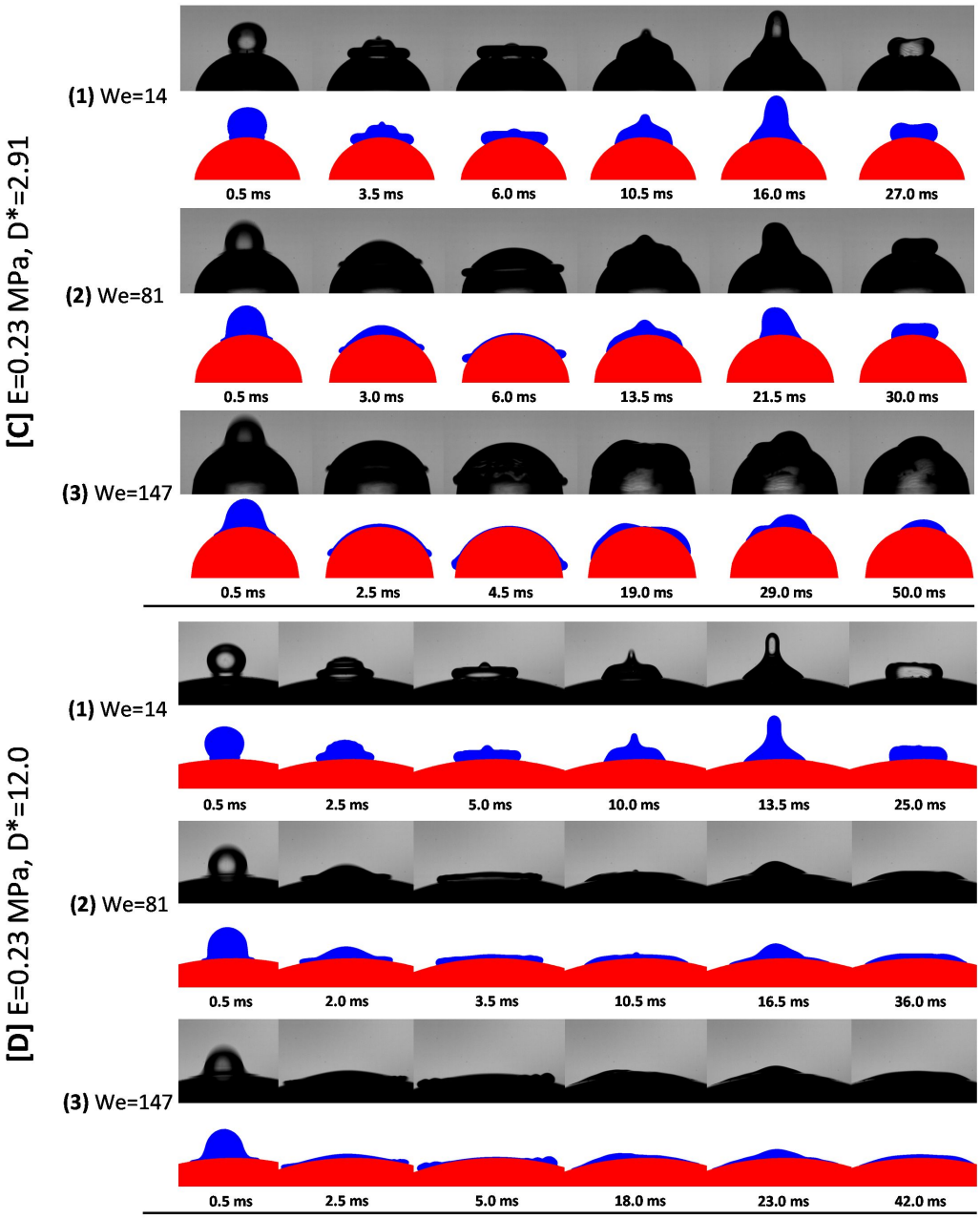

Figure 4.43: Morphology of drop impact on elastic convex surfaces showing the effect of **impact Weber number**. For each group of image sequences, the Weber number increases from **(1)** to **(3)**: **(1)** We = 14, **(2)** We = 81 & **(3)** We = 147. In order to show the effect of D^* under various conditions, different combinations of the other two impact parameters (E & D^*) are chosen for each group: **C**, E = 0.23 MPa, D^* = 2.91; **D**, E = 0.23 MPa, D^* = 12.0. The first row in each case represents the recorded images and the second row shows the processed images.

to the surface energy of the liquid cap, as a function of the Weber number for different impact parameters as shown in Figure 4.44. Data with the same diameter

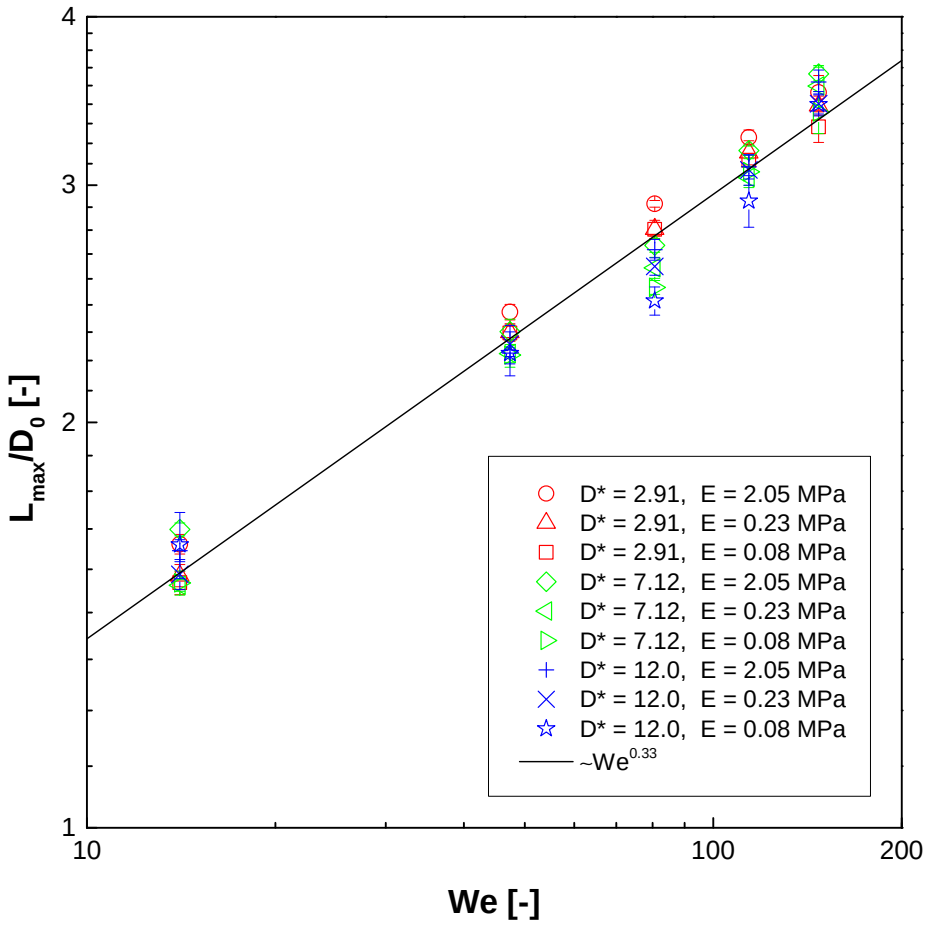

Figure 4.44: Maximum length of the wetted arc (normalized by equilibrium drop diameter) as a function of impact Weber number for cases of different diameter ratios and elastic moduli.

ratio are marked using the same colour (red: D^* = 2.91, green: D^* = 7.12 & blue: D^* = 12.0). Good consistency is exhibited by the experimental data in the considered Weber number range, where follow a scaling law [24] ($L_{\max}/D_0 \sim We^{0.33}$) indicated by the solid line, which implies that the spreading behaviours are still dominated by the Weber number (i.e., the effect of elastic modulus and diameter ratio is negligible). In addition, the curvature effect on the spreading behaviours of impacting drops observed in our experiments is in consistent with the results from a recent numerical investigation [97].

After maximum spreading, the drop recoils to the top of the hemisphere and starts to oscillate. The minimum base angle reached at the end of the initial

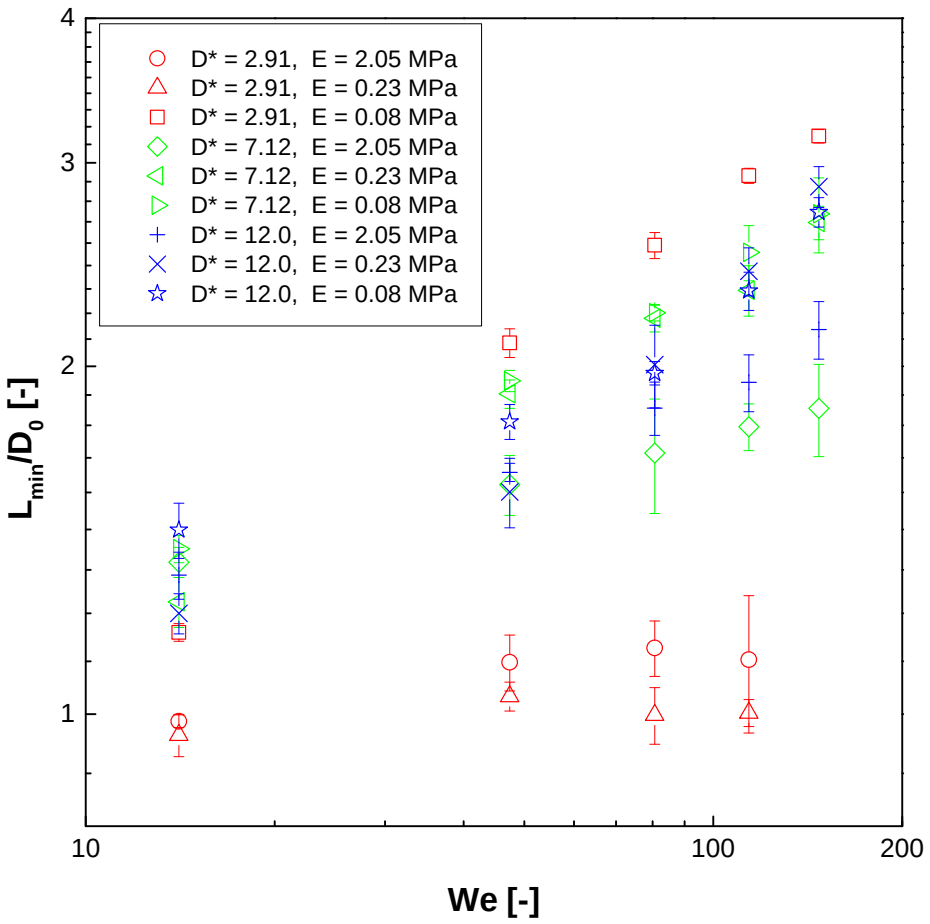

Figure 4.45: Minimum length of the wetted arc (normalized by equilibrium drop diameter) as a function of impact Weber number for cases of different diameter ratios and elastic moduli.

retraction phase is referred to as the 'minimum retracting angle' ($\alpha_{\min}$). The normalised minimum length of the wetted arc (defined the same way as $L_{\max}$ but with $\alpha_{\min}$) as a function of impact Weber number for different impact parameters is plotted in Figure 4.45. Unlike the spreading behaviour, the retracting behaviour is strongly affected by the magnitude of the elastic modulus of the substrate. Especially in the case of the lowest diameter ratio (red symbols), the minimum length of the wetted arc for substrates with high/intermediate stiffness (E=2.05 MPa or E=0.23 MPa) remains around 1 regardless of the increase of Weber number. The data for Weber number ~147 are unavailable since the flow instabilities at high impact velocity lead to symmetry break during the re-

traction of the drop, and the drop partially or completely slide off the top of the hemispherical substrate (see case **C (3)** in Figure 4.43 for example). However the minimum length of the wetted arc for the case of most soft substrate (E=0.08 MPa) increases significantly as the Weber number grows and is only slightly smaller than the maximum one (compare the red square data between Figure 4.44 and Figure 4.45), which means the periphery of the drop almost stays pinned after maximum spreading. In case of higher diameter ratios (D^* = 7.12 & D^* = 12.0), although the data for any substrate stiffness seem to rise with the increase of Weber number, the minimum length of the wetted arc for the highest stiffness substrate (E=2.03 MPa) is systematically lower compared to the other two cases of softer substrates.

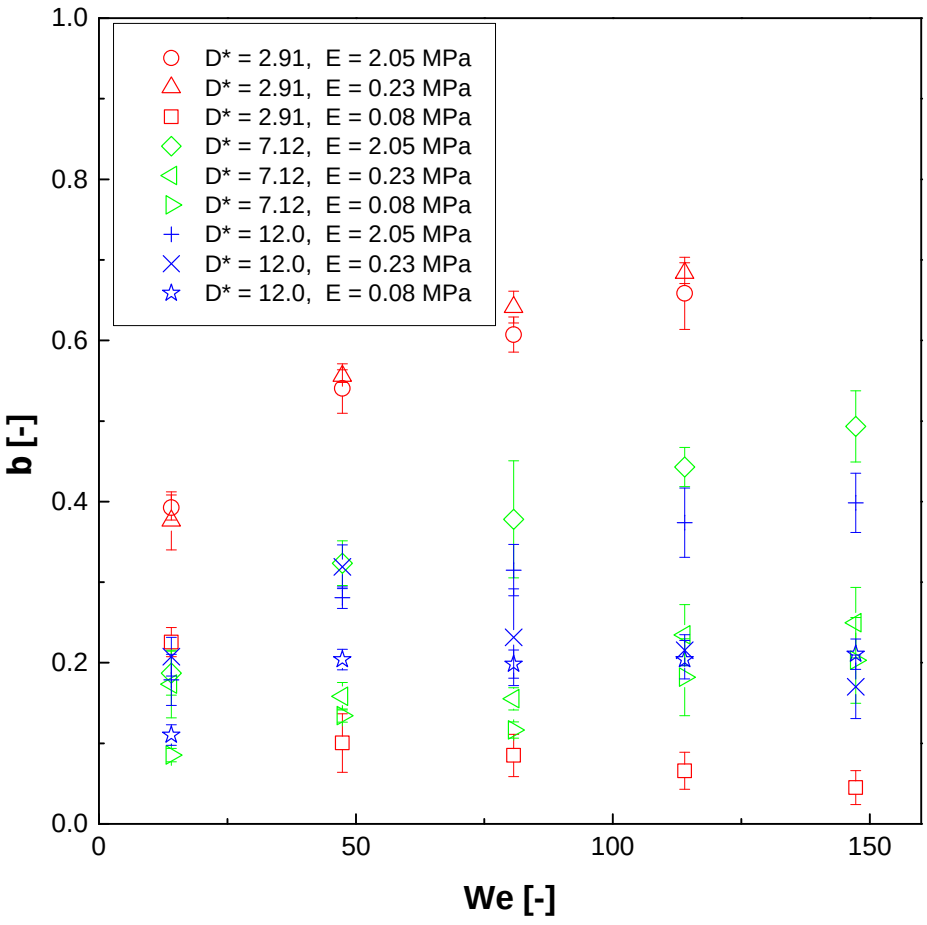

Figure 4.46: Retraction coefficient as a function of impact Weber number for cases of different diameter ratios and elastic moduli.

In order to better characterize the retraction behaviour, a quantity which is referred as the retraction coefficient is defined:

$$\beta = (\alpha_{max} - \alpha_{min})/\alpha_{max}. \tag{4.17}$$

It expresses the relative decrease in the maximum spreading angle due to retraction with respect to the magnitude of maximum spreading angle. Figure 4.46 shows the retraction coefficient as a function of impact Weber number for different impact parameters. In the cases of highest-stiffness substrates (symbols: ○,◇,+), the retraction is more pronounced as the Weber number increases for all diameter ratios, which is reasonable since larger impact velocity will result in higher retraction velocity of the liquid lamella. Surprisingly the data for the smallest diameter ratio (○) are systematically higher than those with larger diameter ratios (◇,+). Here this effect is called the 'de-wetting effect' due to the curvature of the surface, which indicates that impacting drops experience a more significant retraction phase on a substrate with higher curvature. In the case of substrates with intermediate stiffness (△,◁,×), the de-wetting effect is still applicable though some data of highest diameter ratio (×) is comparable or even higher than those with a higher curvature (◁). However the de-wetting effect completely fails in cases of substrates with lowest stiffness (□,▷,☆). The substrate with highest diameter ratio (☆) yields most pronounced retraction. The retraction coefficient of impacting drops on substrate with lowest diameter ratio (□) even decreases with the increase of Weber number, also the values of β are below 0.1 when the Weber number is higher than 50, which means the peripheries of spreading drops almost remain stationary after maximum spreading. Thus the effect of diameter ratio on the retraction behaviours in case of the most soft substrate is totally different from the other two cases with a higher-stiffness substrate.

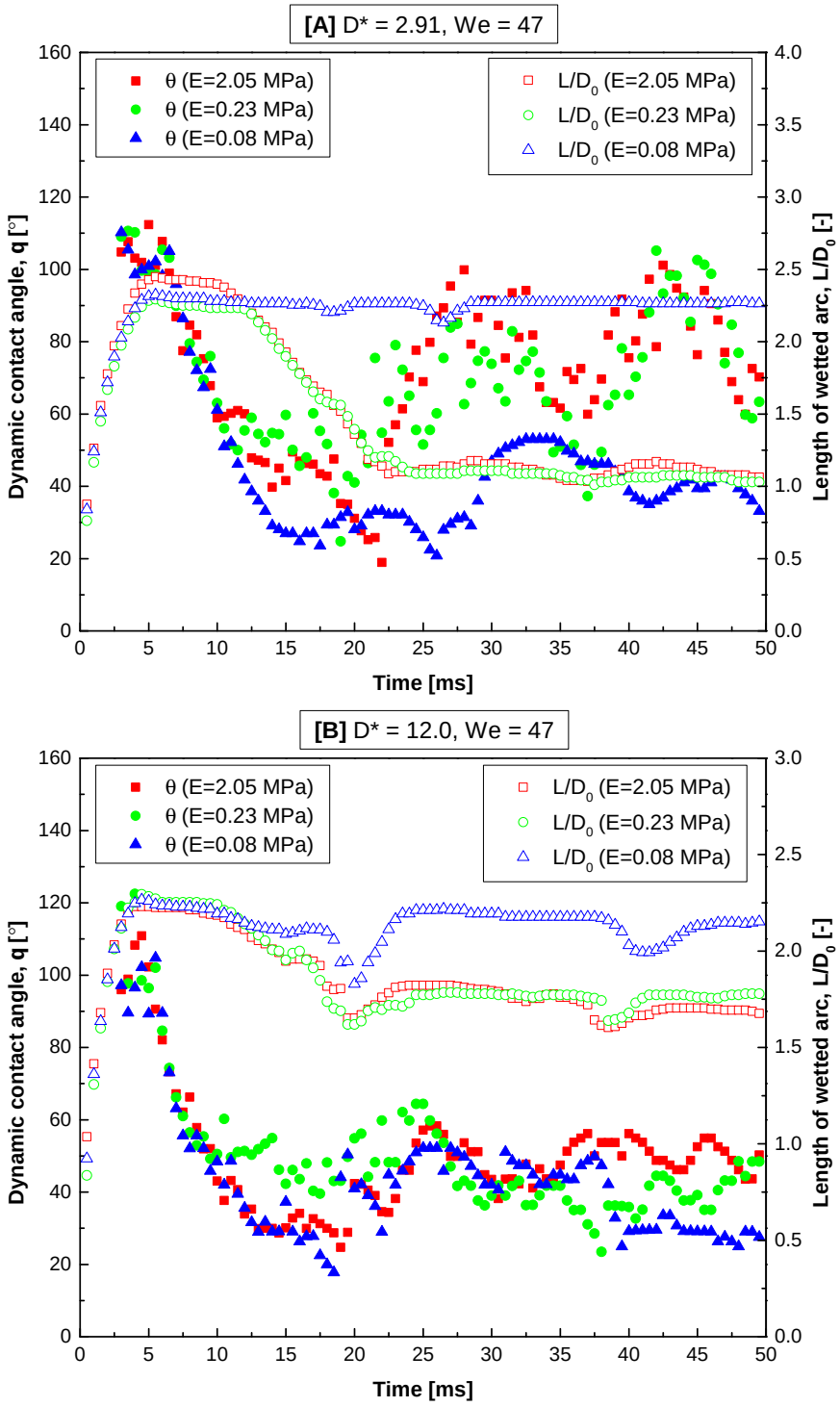

Figure 4.47: Dynamic contact angle as a function of impact time showing the effect of elastic modulus. The impact parameters in each subfigure (A & B) correspond to the image sequence group (A & B) in Figure 4.38. Filled symbols represent the data of dynamic contact angle while the length of wetted arc is denoted by open symbols.

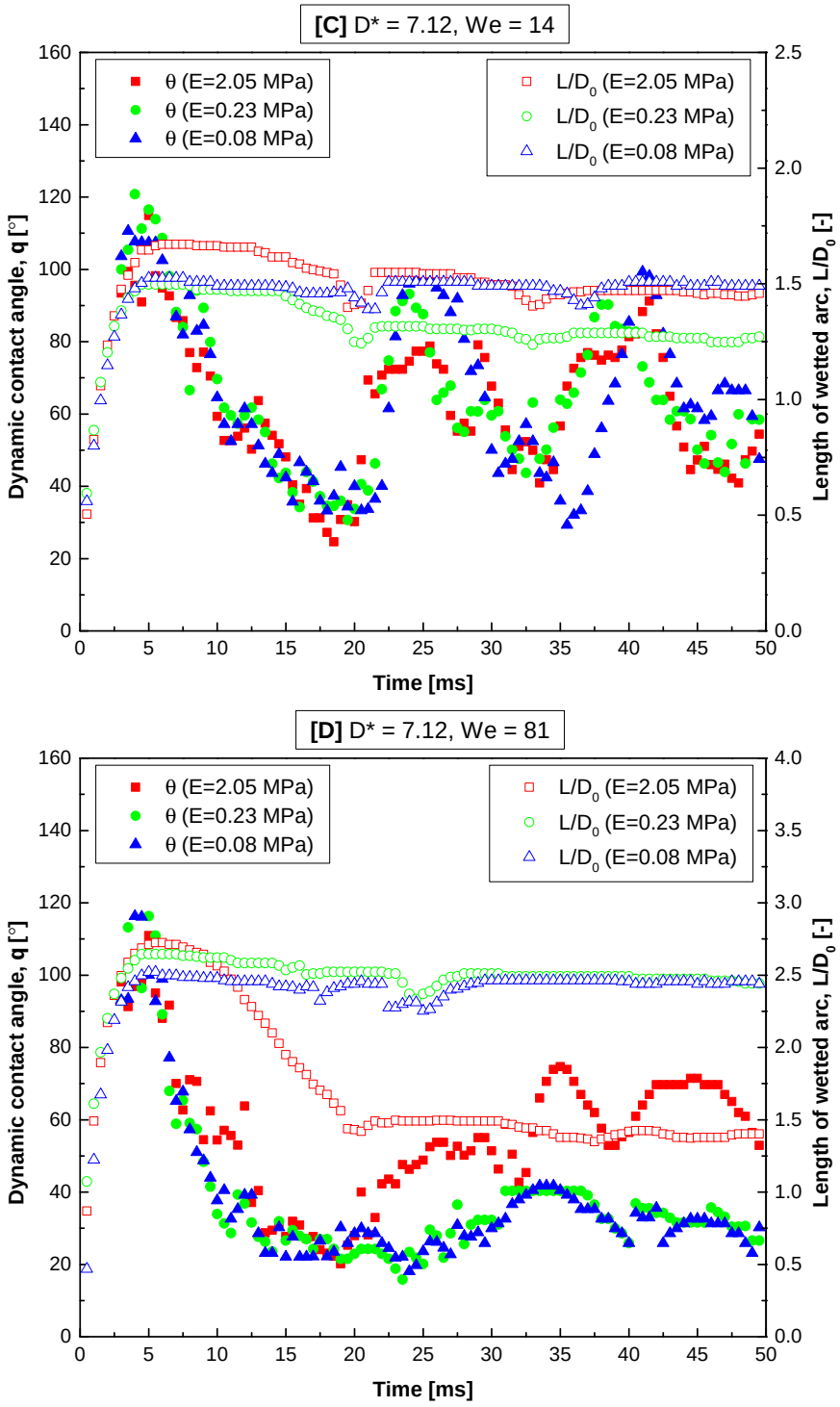

Figure 4.48: Dynamic contact angle as a function of impact time showing the effect of elastic modulus. The impact parameters in each subfigure (C & D) correspond to the image sequence group (C & D) in Figure 4.39. Filled symbols represent the data of dynamic contact angle while the length of wetted arc is denoted by open symbols.

4.5.3 Dynamic contact angle

Effect of elastic modulus on dynamic contact angle

The dynamic contact angle as a function of time showing the effect of elastic modulus is displayed in Figures 4.47 & 4.48 (corresponding to the cases of morphology shown in Figures 4.38 & 4.39). All the experimental data of dynamic contact angle in this study is measured from the left contact point. The length of the wetted arc is also shown as open symbols in order to provide a clear reference of the impact phases (i.e., spreading, retracting & oscillating). The data of contact angles in the initial stage (within ~ 5ms after impact) are not shown since the magnification of our experimental setup (spatial resolution: 21 μm/ pixel) is not high enough to clearly capture the drop contour near the contact line in the early stage. As shown in Figures 4.47 & 4.48, the dynamic contact angle during spreading and the early stages of retraction is almost consistent for all cases. However, as retraction progresses the softness of the substrate is observed to dampen the dynamic contact angle oscillations (see blue triangle data in [**A**] & [**D**] and green circle data in [**D**]). This is due to contact line pinning after maximum spreading (see the corresponding open symbols for length of the wetted arc). The oscillation amplitude of the dynamic contact angle is considerably reduced for a softer substrate since the contact line is fixed. Nevertheless the effect of the substrate stiffness on the dynamic contact angle is much less significant in cases of smaller curvature ([**B**]) and lower impact Weber number ([**C**]).

Effect of diameter ratio on dynamic contact angle

The effect of diameter ratio on the temporal evolution of the dynamic contact angle is shown in Figures 4.49 & 4.50 (corresponding to the cases of morphology shown in Figures 4.40 & 4.41). Similar to the effect of substrate stiffness on the dynamic contact angle, the surface curvature does not play an important role during the spreading and early retracting stages. However the increase in the

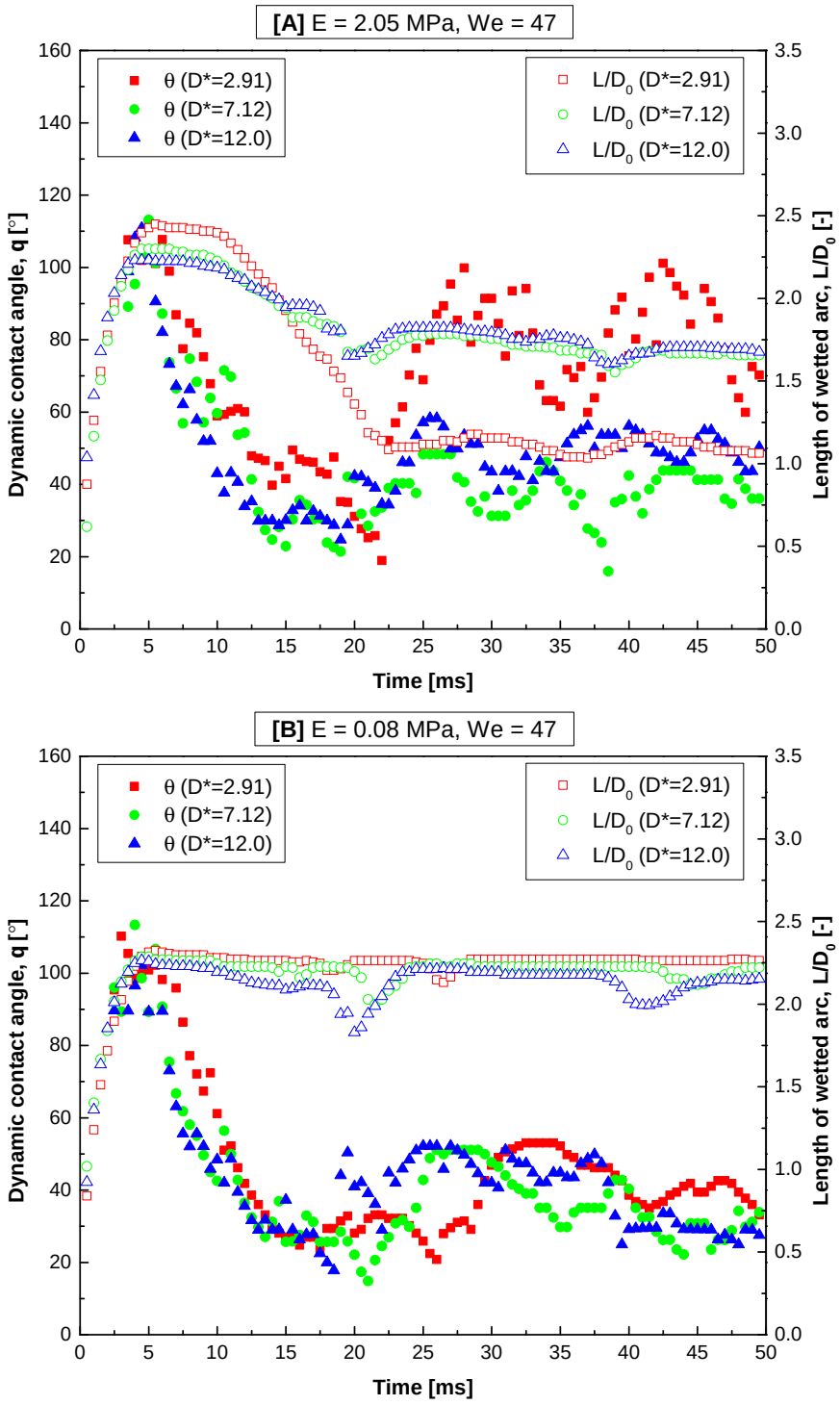

Figure 4.49: Dynamic contact angle as a function of time for different diameter ratios. The impact parameters in each subfigure (A & B) correspond to the image sequence group (A & B) in Figure 4.40. Filled symbols represent the data of dynamic contact angle while the length of wetted arc is denoted by open symbols.

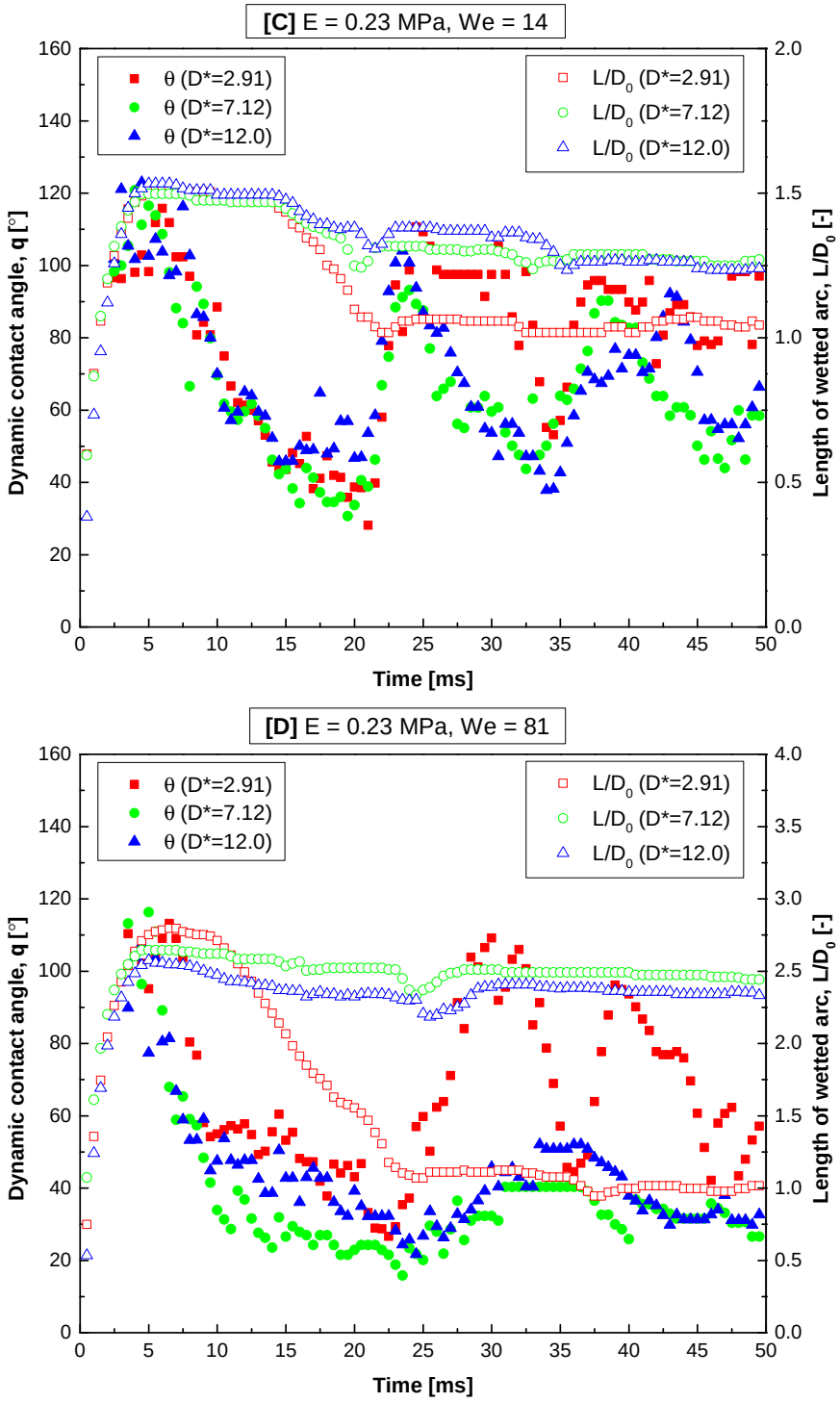

Figure 4.50: Dynamic contact angle as a function of time for different diameter ratios. The impact parameters in each subfigure (C & D) correspond to the image sequence group (C & D) in Figure 4.41. Filled symbols represent the data of dynamic contact angle while the length of wetted arc is denoted by open symbols.

curvature of the surface (i.e., the decrease in the diameter ratio) is observed to enlarge the oscillation amplitude of the dynamic contact angle after the retraction of the drop (see red square data in [**A**] & [**D**]); this is associated with a larger and faster retraction of the contact line (de-wetting). The differences in the de-wetting behaviour can be explained in terms of the surface deformation upon impact, which absorbs part of the impact kinetic energy. In the following section (Section 4.5.4), this mechanism will be discussed in details. Nevertheless the dynamic contact angle is much less affected by the diameter ratio when the stiffness of the substrate is very low ([**B**], where the pinned effect dominates) or the Weber number is small ([**C**]).

Effect of Weber number on dynamic contact angle

The dynamic contact angle as a function of impact time for different Weber numbers is shown in Figures 4.51 & 4.52 (corresponding to the cases of morphology shown in Figures 4.42 & 4.43). The increase in the impact Weber number is observed to systematically reduce the dynamic contact angle in all cases. In addition, the oscillation of the dynamic contact angle after drop retraction is significantly inhibited when the Weber number increases to 147 (see filled blue triangle data in Figures 4.51 & 4.52). However if the Weber number is sufficiently low (see red square data in Figures 4.51 & 4.52), a pronounced oscillation phase with large oscillation amplitude of the dynamic contact angle is observed regardless of the diameter ratio or the elastic modulus of the substrate.

4.5.4 Energy dissipation due to substrate deformation

In this section, the influence of the diameter ratio and of the elastic modulus on the spreading behaviour is interpreted in the light of the substrate deformation energy. Firstly, a simple scenario, schematically shown in Figure 4.53 (A) is considered, where a drop impacts on a flat elastic surface and reaches the maximum spreading diameter. The surface is deformed (as indicated by the dashed line)

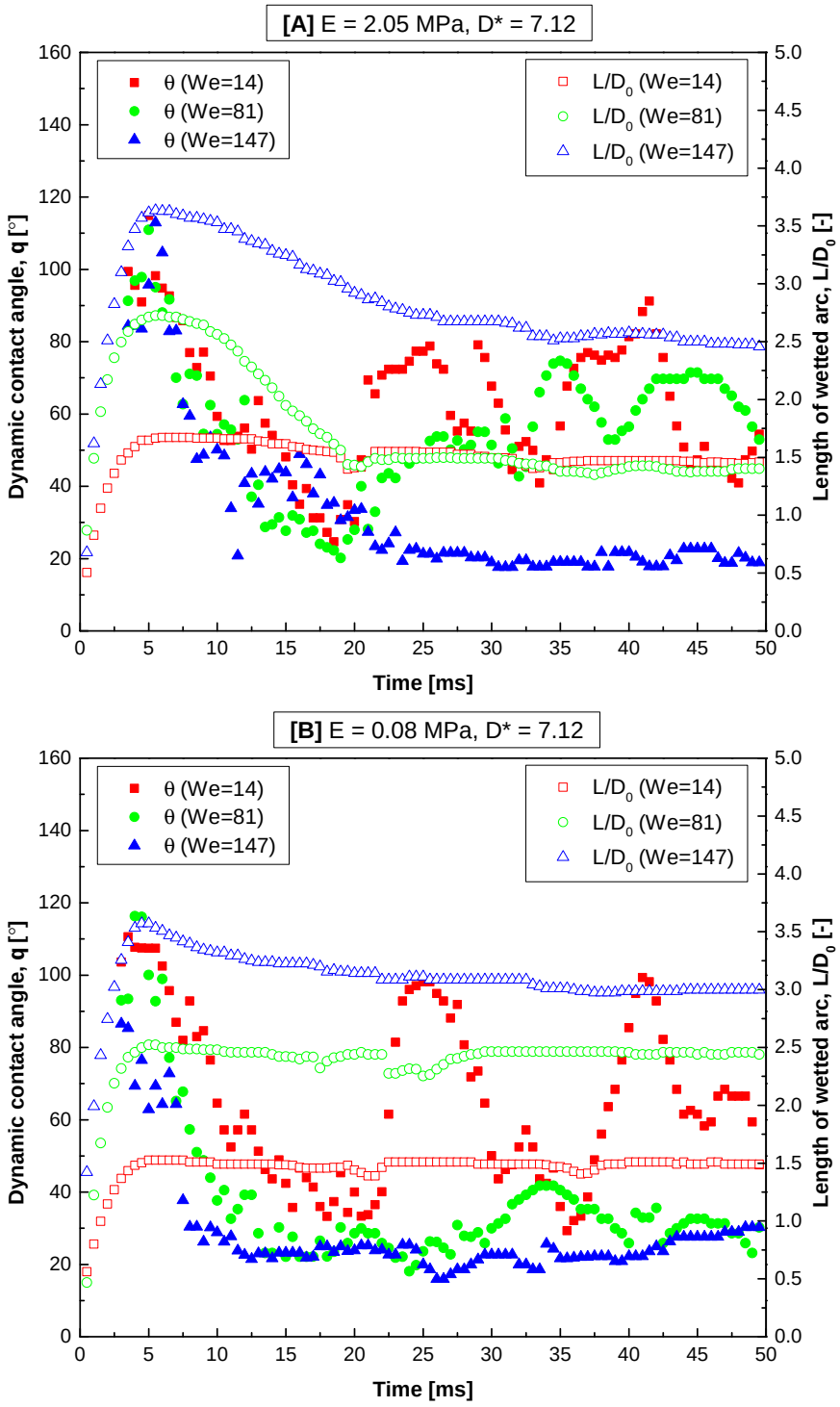

Figure 4.51: Dynamic contact angle as a function of time for different Weber numbers. The impact parameters in each subfigure (A & B) correspond to the image sequence group (A & B) in Figure 4.42. Filled symbols represent the data of dynamic contact angle while the length of wetted arc is denoted by open symbols.

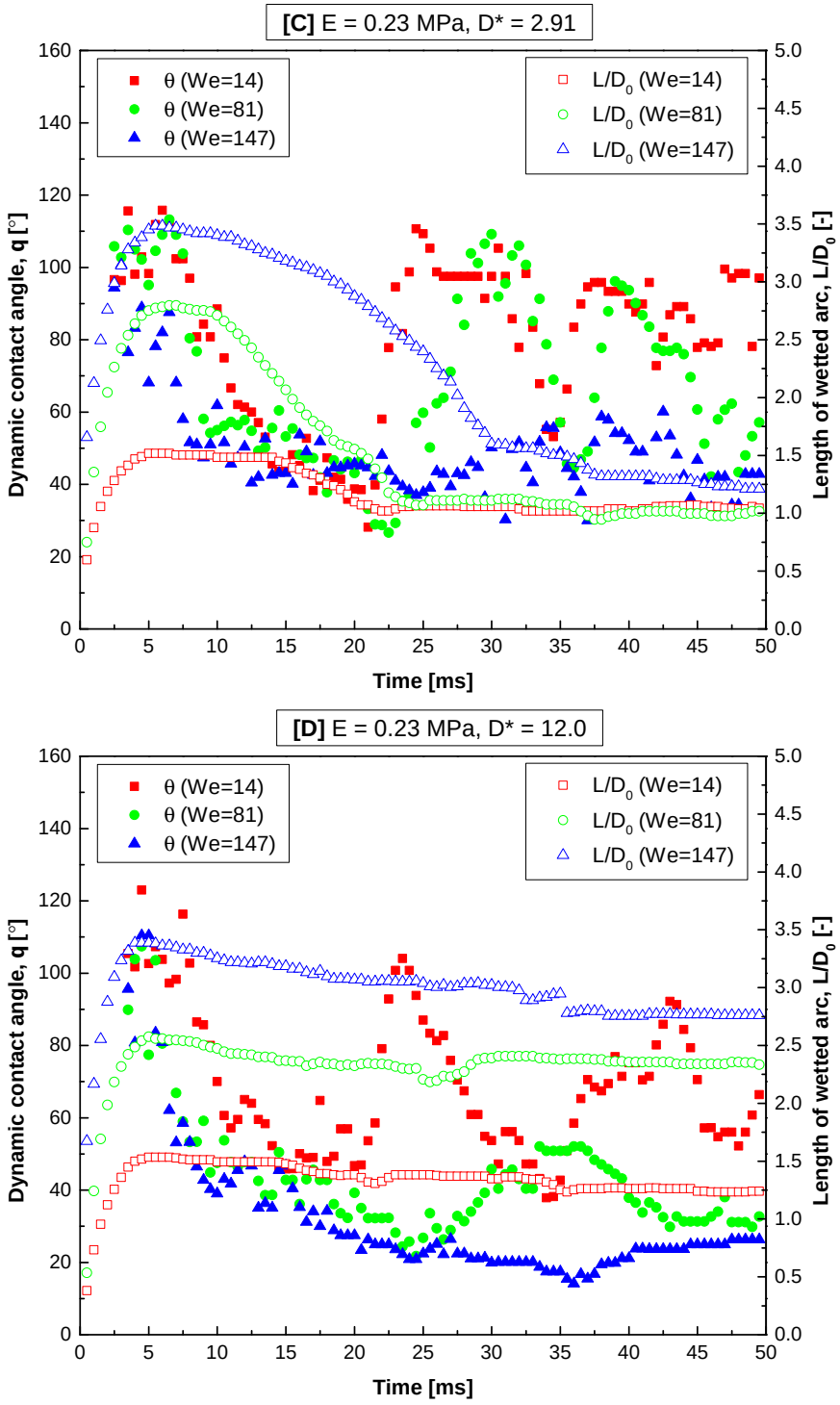

Figure 4.52: Dynamic contact angle as a function of time for different Weber numbers. The impact parameters in each subfigure (C & D) correspond to the image sequence group (C & D) in Figure 4.43. Filled symbols represent the data of dynamic contact angle while the length of wetted arc is denoted by open symbols.

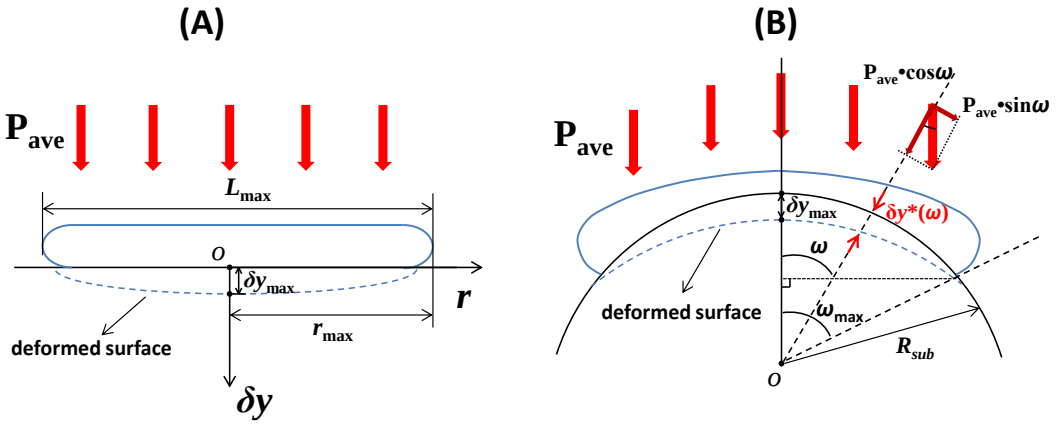

Figure 4.53: Schematic of energy dissipation mechanism due to substrate deformation: (A) drop impact on flat elastic substrate; (B) drop impact on spherical elastic substrate.

due to the pressure exerted by the impacting drop. Since an element of surface which is closer to the impact centre experiences a longer contact time during impact, the magnitude of deformation, $\delta y(r)$ reaches its maximum ($\delta y_{\max}$) at the centre of impact, and decreases radially with the distance from the centre, r, up to a value of zero at maximum spreading radius, $r_{\max}$. To simplify the quantitative estimate of the elastic energy stored by the substrate, the contour of the deformed surface is approximated by a parabola:

$$\delta y(r) = \delta y_{\max}[1 - (\frac{r}{r_{\max}})^2]. \tag{4.18}$$

Let P_{ave} represent the average pressure subjected by the surface with respect to spreading time; then, the normal force on an infinitely small annular surface area can be written as:

$$\mathrm{d}F = P_{\text{ave}} \cdot 2\pi r \mathrm{d}r, \tag{4.19}$$

and the corresponding differential expression of deformation energy is given by:

$$\mathrm{d}W_{\text{def}} = \mathrm{d}F \cdot \delta y = 2\pi P_{\text{ave}} \delta y_{\max}[1 - (\frac{r}{r_{\max}})^2] r \mathrm{d}r. \tag{4.20}$$

Thus the total deformation energy during impact can be obtained by the integral of Equation 4.20 with respect to r:

$$\begin{aligned} W_{\text{def}} &= \int_0^{r_{\max}} \mathrm{d}W_{\text{def}} \\ &= 2\pi P_{\text{ave}} \delta y_{\max} \int_0^{r_{\max}} [1 - (\frac{r}{r_{\max}})^2] r \mathrm{d}r \\ &= \frac{1}{2}\pi P_{\text{ave}} \delta y_{\max} r_{\max}^2 \ (= \frac{1}{8}\pi P_{\text{ave}} \delta y_{\max} L_{\max}^2). \end{aligned} \tag{4.21}$$

Secondly, this simplified model is extended to the case of a spherical elastic surface [Figure 4.53 (B)]. If the impact kinetic energy is the same, i.e., the impacting drops have the same Weber number, one can expect the vertical pressure (P_{ave}) on the impact surface to be almost identical for two cases. However, in the case of a spherical surface, only the normal component of P_{ave} to the target surface is responsible for its deformation, while the tangential component contributes to spreading. As a result, the differential expression of normal force on the substrate surface shown by Equation 4.19 can be modified for the case of a spherical surface as:

$$\begin{aligned} \mathrm{d}F^* &= P_{\text{ave}} \cos\omega \cdot 2\pi R_{sub}^2 \sin\omega \mathrm{d}\omega \\ &= \pi P_{\text{ave}} R_{sub}^2 \sin 2\omega \mathrm{d}\omega, \end{aligned} \tag{4.22}$$

where ω is the polar coordinate measured form the center of the spherical substrate, and R_{sub} denotes the radius of the substrate. Similar to Equation 4.18, a parabolic deformed contour is assumed to radially distribute on the target surface:

$$\delta y^*(\omega) = \delta y_{\max}[1 - (\frac{\omega}{\omega_{\max}})^2], \ (\omega_{\max} = \frac{L_{\max}}{2R_{sub}}). \tag{4.23}$$

By integrating the product of Equation 4.22 and Equation 4.23 with respect to ω, the total deformation energy for the case of a spherical surface can be expressed

as:

$$\begin{aligned} W^*_{\text{def}} &= \int_0^{\omega_{\max}} \mathrm{d}W^*_{\text{def}} \\ &= \int_0^{\omega_{\max}} \mathrm{d}F^* \delta y^*(\omega) \\ &= \pi P_{\text{ave}} R^2_{sub} \delta y_{\max} \\ &\quad \times \int_0^{\omega_{\max}} [1 - (\frac{\omega}{\omega_{\max}})^2] \sin 2\omega \mathrm{d}\omega \\ &= \pi P_{\text{ave}} R^2_{sub} \delta y_{\max} \\ &\quad \times (\frac{1}{2} + \frac{\sin^2 \omega_{\max} - \omega_{\max} \sin 2\omega_{\max}}{2\omega^2_{\max}}) \end{aligned} \tag{4.24}$$

Substituting $R_{sub} = D^* D_0/2$ and $\omega_{\max} = L_{\max}/2R_{sub} = L_{\max}/(D^* D_0)$ into Equation 4.24, the deformation energy as a function of D^* is obtained:

$$\begin{aligned} W^*_{\text{def}} &= \frac{\pi P_{\text{ave}} \delta y_{\max} (D^* D_0)^4}{8 L^2_{\max}} \\ &\quad \times [\frac{L_{\max}}{D^* D_0} (\frac{L_{\max}}{D^* D_0} - \sin \frac{2L_{\max}}{D^* D_0}) + \sin^2 \frac{L_{\max}}{D^* D_0}]. \end{aligned} \tag{4.25}$$

Let $\overline{L}_{\max} = L_{\max}/D_0$ denote the normalized maximum length of the wetted arc, then Equation 4.25 can be simplified as:

$$\begin{aligned} W^*_{\text{def}} &= \frac{\pi P_{\text{ave}} \delta y_{\max} D^2_0 (D^*)^4}{8 \overline{L}^2_{\max}} \\ &\quad \times [\frac{\overline{L}_{\max}}{D^*} (\frac{\overline{L}_{\max}}{D^*} - \sin \frac{2\overline{L}_{\max}}{D^*}) + \sin^2 \frac{\overline{L}_{\max}}{D^*}] \\ &= \frac{\pi P_{\text{ave}} \delta y_{\max} D^2_0}{8} \cdot \Phi(D^*, \overline{L}_{\max}) \end{aligned} \tag{4.26}$$

where

$$\begin{aligned} &\Phi(D^*, \overline{L}_{\max}) = \\ &\frac{(D^*)^4}{\overline{L}^2_{\max}} [\frac{\overline{L}_{\max}}{D^*} (\frac{\overline{L}_{\max}}{D^*} - \sin \frac{2\overline{L}_{\max}}{D^*}) + \sin^2 \frac{\overline{L}_{\max}}{D^*}]. \end{aligned} \tag{4.27}$$

According to the impulse-momentum theorem, the momentum change ($m\Delta u_y$) of the drop in the vertical direction during impact is equal to the average force (F) applied on the drop times its duration (Δt):

$$\begin{aligned} F\Delta t &= P_{\text{ave}} \pi (R_{sub} \sin \omega_{\max})^2 \Delta t \\ &= \frac{\pi P_{\text{ave}} (D_0 D^* \sin \frac{\overline{L}_{\max}}{D^*})^2}{4} \Delta t = m \Delta u_y, \end{aligned} \tag{4.28}$$

where $\Delta u_y = u_i - 0 = u_i$ because the vertical velocity of the drop decreases from the impact velocity (u_i) to zero during impact, and the impact duration can be

approximated by the characteristic time:

$$\Delta t \approx \frac{D_0}{u_i}. \tag{4.29}$$

Thus the average pressure can be estimated as:

$$P_{\text{ave}} \approx \frac{4mu_i^2}{\pi D_0^3 (D^* \sin \frac{\overline{L}_{\max}}{D^*})^2} \tag{4.30}$$

In order to estimate the magnitude of $\delta y_{\max}$, the classical solution for elastic contact mechanics between two spheres is adopted to correlate the force and the maximum deformation [84]:

$$F = \frac{4}{3} \cdot \frac{E}{1-\nu^2} \cdot R_{\text{eff}}^{\frac{1}{2}} \delta y_{\max}^{\frac{3}{2}} \approx \frac{4}{3} \cdot E R_{\text{eff}}^{\frac{1}{2}} \delta y_{\max}^{\frac{3}{2}}, \tag{4.31}$$

where ν is the Poisson's ratio, F (Equation 4.28) is the applied force, and R_{eff} represents the effective radius:

$$R_{\text{eff}} = \frac{R_1 R_2}{R_1 + R_2} = \frac{D^* D_0}{2(1+D^*)}, \tag{4.32}$$

in which R_1 and R_2 denote the radii of the two spheres. Thus, from Equations 4.31 & 4.32 $\delta y_{\max}$ is estimated as:

$$\delta y_{\max} = \frac{u_i}{2 D_0 D^* \sin \frac{\overline{L}_{\max}}{D^*}} \sqrt[3]{\frac{9(1+D^*) m^2 u_i}{D^* E^2}} \tag{4.33}$$

Combing Equations 4.26, 4.30 & 4.33, the deformation energy for the case of a spherical substrate can be rewritten as:

$$W_{\text{def}}^* = \frac{\sqrt[3]{9} m^{\frac{5}{3}} u_i^{\frac{10}{3}}}{4(D_0 D^* \sin \frac{\overline{L}_{\max}}{D^*})^2 E^{\frac{2}{3}}} \sqrt[3]{\frac{1+D*}{D*}} \cdot \Phi(D^*, \overline{L}_{\max}) \tag{4.34}$$

Substituting the drop mass, $m = (1/6)\pi\rho D_0^3$ into Equation 4.34, W_{def}^* can be rewritten as:

$$W_{\text{def}}^* = \frac{\frac{1}{3}(\frac{1}{2})^{\frac{11}{3}} (\pi\sigma We)^{\frac{5}{3}} D_0^{\frac{4}{3}}}{(D^* \sin \frac{\overline{L}_{\max}}{D^*})^2 E^{\frac{2}{3}}} \sqrt[3]{\frac{1+D*}{D*}} \cdot \Phi(D^*, \overline{L}_{\max}), \tag{4.35}$$

where $We = \rho u_i^2 D_0 / \sigma$ is the Weber number.

4.5.5 Considerations on the energy balance

A simple energy balance approach [44, 123, 114] can be used to estimate the maximum length of the wetted arc reached by a water droplet impacting on an elastic spherical substrate. Whilst energy (or momentum) conservation approaches are very popular due to their simplicity, it must be kept in mind their accuracy relies heavily on empirical coefficients. In particular, it is well-known that if the fluid viscosity is not close to that of water, all drop impact models based on energy conservation fail to predict experimental results with an acceptable error [80]; it was also shown that if the model coefficients are judiciously adjusted the scaling $D_{\max}/D_0 \sim We^{1/2}$ can fit experimental data in a very large range of the variables[18]. In other words, if one locks the Weber number exponent and shifts all the empirical input on the other coefficients, it is still possible to obtain very good agreement with experiments, but this does not mean the scaling is true.

Equating the kinetic energy ($E_{\mathrm{k}}^{(b)}$) and surface energy ($E_{\mathrm{s}}^{(b)}$) of a spherical drop before impact to the sum of the kinetic energy (which is assumed to be zero), surface energy ($E_{\mathrm{s}}^{(m)}$), viscous dissipation energy (W_{vis}) and energy dissipation due to substrate deformation (W_{def}^{*}) at maximum spreading, the energy balance yields:

$$E_{\mathrm{k}}^{(b)} + E_{\mathrm{s}}^{(b)} = E_{\mathrm{s}}^{(m)} + W_{\mathrm{vis}} + W_{\mathrm{def}}^{*}. \tag{4.36}$$

The kinetic energy before impact is simply written as:

$$E_{\mathrm{k}}^{(b)} = \frac{1}{2} m u_i^2 = \frac{1}{12}\pi\rho D_0^3 u_i^2 = \frac{1}{12}\pi\sigma D_0^2 We, \tag{4.37}$$

and the surface energy of a spherical drop is:

$$E_{\mathrm{s}}^{(b)} = \pi D_0^2 \sigma. \tag{4.38}$$

The drop shape at maximum spreading is assumed to be a spherical cap with a bottom surface area of $A_b = 2\pi R_{sub}^2(1-\cos\omega_{\max})$, a thickness of $T_c = (1/6\pi D_0^3)/A_b$, and a rim area of $A_r = 2\pi R_{sub}\sin\omega_{\max}\cdot T_c$. The surface energy at maximum

spreading is the sum of surface energy at the liquid-gas interface $E_{\mathrm{s,LG}}^{(m)}$, and the surface energy at the liquid-solid interface $E_{\mathrm{s,LS}}^{(m)}$, minus the surface energy at the solid-gas interface $E_{\mathrm{s,SG}}^{(m)}$, which is gradually lost during the impact process:

$$\begin{aligned} E_{\mathrm{s}}^{(m)} &= E_{\mathrm{s,LG}}^{(m)} + E_{\mathrm{s,LS}}^{(m)} - E_{\mathrm{s,SG}}^{(m)} \\ &= (A_b + A_r)\sigma_{LG} + A_b\sigma_{LS} - A_b\sigma_{SG}, \end{aligned} \tag{4.39}$$

where σ_{LG} is the liquid-gas surface tension, σ_{LS} is the liquid-solid surface tension, and σ_{SG} is the solid-gas surface tension. According to Young's Equation, the difference between σ_{SG} and σ_{LS} can be correlated to σ_{LG} by the static contact angle θ_0:

$$\sigma_{SG} - \sigma_{LS} = \sigma_{LG}\cos\theta_0. \tag{4.40}$$

Combining Equations 4.39 and 4.40, $E_{\mathrm{s}}^{(m)}$ is written as:

$$\begin{aligned} E_{\mathrm{s}}^{(m)} =& [A_b(1-\cos\theta_0) + A_r]\sigma_{LG} \\ =& \frac{\pi(D^*D_0)^2}{2}(1-\cos\frac{\overline{L}_{\max}}{D^*})(1-\cos\theta_0)\sigma \\ &+ \frac{\pi D_0^2 \sin\frac{\overline{L}_{\max}}{D^*}}{3D^*(1-\cos\frac{\overline{L}_{\max}}{D^*})}\sigma, \end{aligned} \tag{4.41}$$

Using the boundary layer thickness (determined from the analytical solution of an axisymmetric stagnation point flow) as the length scale associated with the viscous dissipation term, Pasandideh-Fard et al. derived an expression of the energy lost due to viscous dissipation [123]:

$$W_{\mathrm{vis}} = \frac{\pi}{3}\rho u_i^2 D_0 L_{\max}^2 \frac{1}{\sqrt{Re}} = \frac{\pi}{3}\sigma(\overline{L}_{\max}D_0)^2 We Re^{-\frac{1}{2}}, \tag{4.42}$$

Although Equation 4.42 was obtained for the case of a flat surface, here it is adopted to estimate the viscous energy dissipation for spherical surfaces as an approximation (in particular, the error decreases as the diameter ratio D^* increases).

Substituting $E_{\mathrm{k}}^{(b)}$, $E_{\mathrm{s}}^{(b)}$, $E_{\mathrm{s}}^{(m)}$, W_{vis} and W_{def}^*, given by Equations 4.37, 4.38, 4.41, 4.42 and 4.35, respectively, into the energy balance equation (Equation 4.36), a correlation between the Weber number (We) and normalised maximum

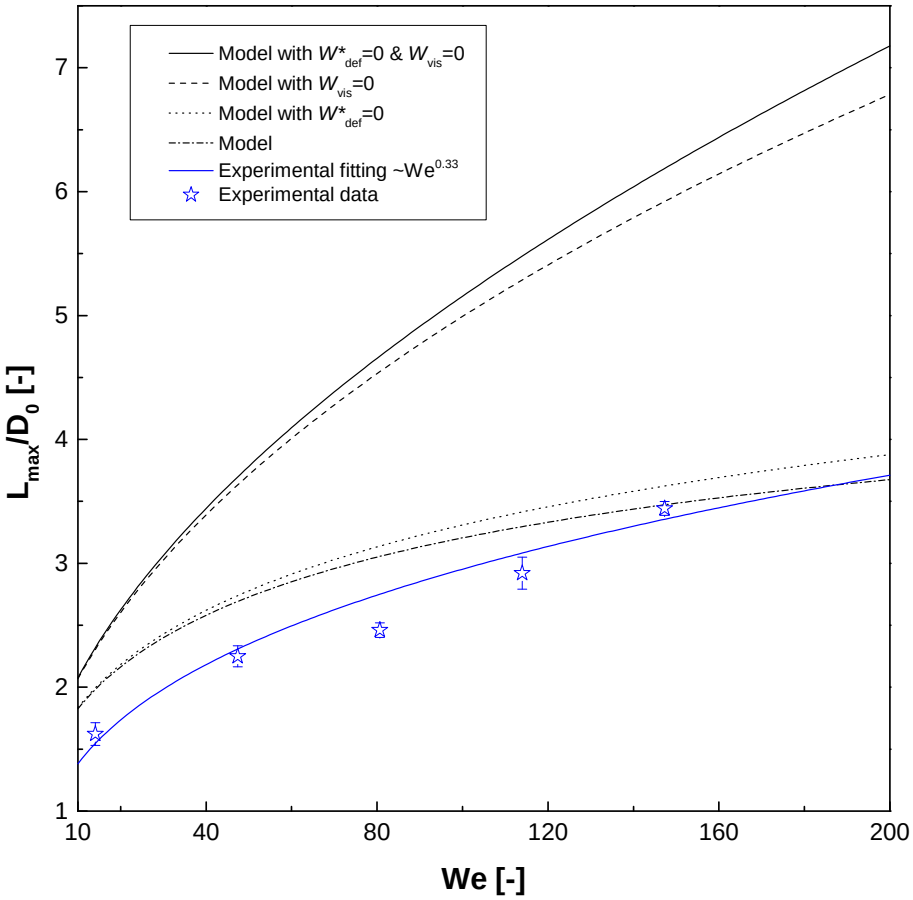

Figure 4.54: The normalised maximum length of the wetted arc as a function of Weber number for a parameter set of E = 0.08 MPa & D^* = 12.0. Lines of different types represent the model predictions with different energy dissipations: no energy dissipation (solid line); only the dissipation due to deformation (dashed line); only viscous dissipation (dotted line); energy dissipations due to both viscous forces and deformation (dash-dot line). Blue star and line indicate the experimental data and fitting, respectively.

length of the wetted arc ($\overline{L}_{\max}$) can be established. Given a certain value of the Weber number, $\overline{L}_{\max}$ can be obtained by Equation 4.36 since all the other parameters are known. The normalised maximum length of the wetted arc is plotted in Figure 4.54 (dash-dot line) as a function of We for a parameter set of E = 0.08 MPa & D^* = 12.0 (i.e., the case where the energy dissipation due to deformation is the highest). The results are compared with different predictions using the same model, and considering: (i) no energy dissipation (solid line); (ii) only the energy dissipation due to substrate deformation (dashed line); (iii)

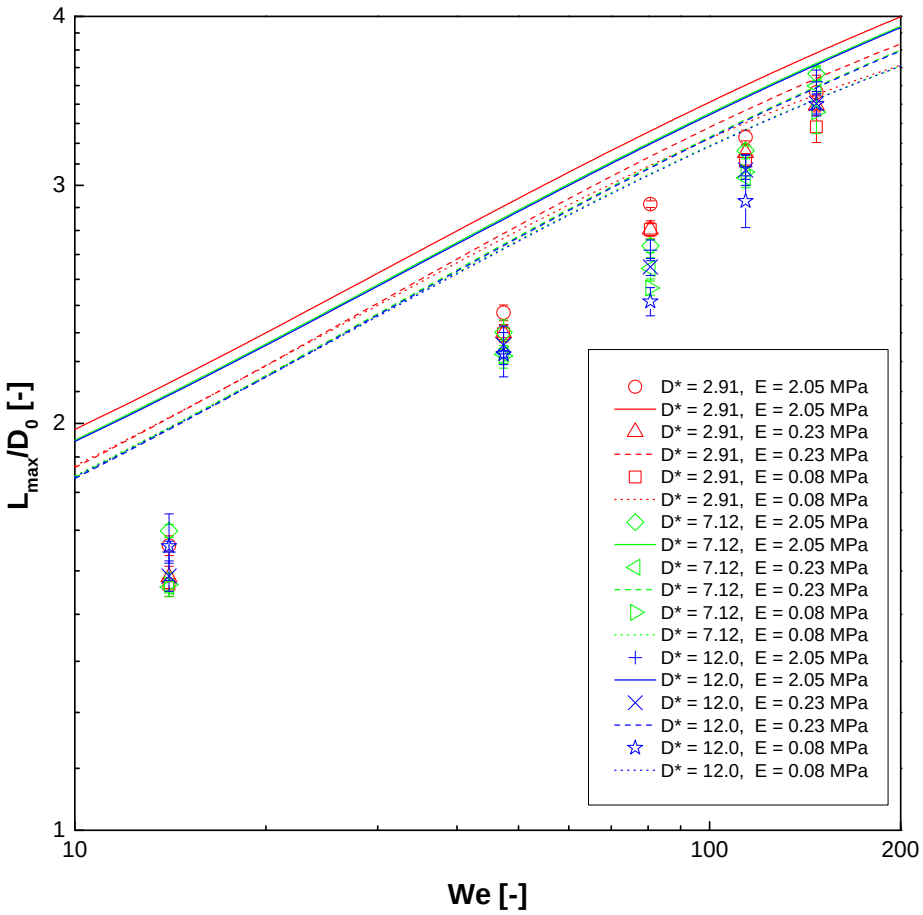

Figure 4.55: The normalised maximum length of the wetted arc as a function of impact Weber number for cases of different diameter ratios and elastic moduli. Lines of different types and colors represent the model predictions, and symbols denote the experimental data.

only the viscous energy dissipation (dotted line). The experimental data for the same parameter set and the best fit line (from Figure 4.44) are also shown for comparison. As shown in Figure 4.54, taking into account the energy dissipation due to deformation without viscous energy dissipation decreases the predicted values only slightly, while the prediction is closer to experimental data if the viscous dissipation is taken into account, because the viscous energy dissipation in the fluid is much larger than the dissipation due to surface deformation. The model predictions of $\overline{L}_{\max}$ for all the cases reported in Figure 4.44 are plotted and compared with the corresponding experimental results in Figure 4.55. The model results confirm the effects of elastic modulus and diameter ratio on the

spreading behaviours are modest and do not change the scaling of the maximum spreading length with respect to the Weber number. However, the proposed energy conservation approach is not able to predict the scaling $L_{\max}/D_0 \sim We^{0.33}$ observed experimentally.

Chapter 5

Conclusions

5.1 Leidenfrost drop impact

5.1.1 Symmetry breaking and somersaults

The impact of Newtonian and non-Newtonian drops on a heated surface in the Leidenfrost regime was studied experimentally to get a deeper understanding of the energy redistribution during the impact process and to investigate separately the effects of different flow behaviours (Newtonian, shear-thinning and viscoelastic) on the energy redistribution by comparing the drop impact process using three model fluids (water solutions of glycerol, xanthan gum and polyacrylamide, respectively).

The main experimental findings are:

• The maximum bouncing height of glycerol drops with infinite-shear viscosity starts to decrease at a critical Weber number (around 30) while those of other types of drops are almost consistent in the considered Weber number range. However the retraction velocity of infinite-shear-viscosity Newtonian drops is only slightly smaller than those of the zero-shear-viscosity Newtonian, xanthan gum and polyacrylamide drops.

• The non-Newtonian effects (shear-thinning and viscoelasticity) have limited influence on the energy redistribution during impact.

• The bouncing drops of glycerol with infinite-shear viscosity are observed to

somersault beyond the critical Weber number (around 30) and no distinct rotational motion can be observed for all the other types of drops. By comparing the virtual maximum bouncing height (calculated by transforming rotational kinetic energy into extra potential energy) and top view images in the retraction phase of low-viscosity Newtonian drops with those of high-viscosity Newtonian and non-Newtonian drops, we show that the somersault effect is due to the symmetry break observed during the retraction of low-viscosity drops.

• The total kinetic energy carried by low-viscosity Newtonian drops during retraction is partly transformed into rotational kinetic energy rather than dissipated when compared with high-viscosity or non-Newtonian drops.

5.1.2 Viscoplastic Leidenfrost drops

The impact morphology of viscoplastic drops onto a heated surface in Leidenfrost regime was studied experimentally though high-speed imaging. Several important parameters which characterize the impact morphology (such as maximum spreading diameter, minimum retracting diameter and maximum bouncing height) were measured by analysing the impact process. In particular six water-based Carbopol solutions with different concentrations were prepared as model fluids in order to study the effect of yield-stress magnitude on morphology.

The main experimental findings are:

• Due to the dominance of inertial force during spreading, the maximum spreading diameter increases monotonously with respect to Weber number for all viscoplastic drops.

• For drops with a relatively low yield stress, the rebound behaviour is similar to high viscosity Newtonian drops. As the yield stress grows, surface forces are no longer able to minimize the free surface of the drop, and the inertial deformation upon impact becomes permanent, resulting in an oblate bouncing drop during rebound. These effects can be interpreted in terms of the Bingham-Capillary

number, which compares the yield stress magnitude and the capillary (Laplace) pressure.

• The linear correlation between retraction coefficient and maximum bouncing height in the considered Weber number range means the deformation of the drop during retraction is crucial to its rebound behaviour and the main contribution to drop rebound is due to surface forces, and not to the intrinsic elasticity of the vapour cushion between the drop and the surface, which is a major assumption in one of the existing models.

5.2 Drop impact on viscoplastic surfaces

5.2.1 Spreading behaviours

The impact morphology of drops Newtonian and yield-stress fluids on viscoplastic surfaces was studied through high-speed imaging. The experimental results were compared with the drop impact morphology on a hydrophilic glass surface. Especially the inertial spreading stage for different combinations of drop and substrate at different impact Weber numbers was carefully investigated.

The main experimental findings are:

• The spreading of an impacting Newtonian drop on a gel is a result of the competition between the deformation of the substrate and the drag reduction resulting from the gel surface. For a relatively soft substrate, the deformation effect dominates hence it spreads slower than a solid surface. Nevertheless for a much more solid substrate, the drag reduction effect becomes dominant, which leads to faster spreading.

• The gel drop stops spreading (tends to have the same maximum spreading diameter) on a gel substrate with higher yield stress regardless of the impact velocity, implying that large portion of kinetic energy of the drop is dissipated during impact at high Weber numbers.

5.2.2 Cavity evolution and permanent nestling

The impact of viscoplastic drops onto viscoplastic substrates characterized by different magnitudes of yield stress was investigated experimentally. The impact morphology of different drop/substrate combinations was studied through high speed imaging for impact Weber numbers between 15 and 85. A map showing the final profiles of the impacting drops for different combinations of drops and substrates at different Weber numbers was constructed. The volumes of the final shapes for different impact parameters were calculated through image processing. Experimental data of the temporal crater evolution were fitted to one of the existing models on crater evolution.

The main experimental findings are:

• The final shapes of the impacting drops transform from a hemisphere to a cone as the Weber number increases for all combinations. Also the magnitude of the yield stress of the substrate strongly affected the penetration depth of drop fluid: depth increases as the impact Weber number grows for stiff surface while decreases for soft surface.

• A single dimensionless parameter has been introduced by the product of drop/substrate yield stress ratio and Weber number to reduce the regime map of behaviour from two parameters to one.

• The comparison between the experimental data of crater evolution and model prediction implies the crater evolution model is more suitable to describe the dimension of the drop fluid rather than the crater.

5.3 Drop impact on spherical elastic surfaces

The impact of water drops on convex, hemispherical, elastic surfaces was investigated experimentally by means of high-speed imaging. Convex hemispherical elastic substrates characterized by different diameters and different elastic moduli

were produced using a polydimethylsiloxane silicone elastomer. The impact morphology was characterized through several quantities, including the maximum and the minimum spreading angles, the length of the wetted curve and the dynamic contact angle. The dynamic contact angle was measured utilizing a novel digital image processing scheme based on a goniometric mask. The morphology of the impacting drop was studied under different impact parameters. In particular, the effect of three independent impact parameters (elastic modulus, diameter ratio and Weber number) on the dynamic contact angle was systematically investigated.

The main experimental findings are:

• The decrease in the elastic modulus of the substrate and the increase in the diameter ratio are observed to inhibit the oscillation of the dynamic contact angle after impact at sufficiently high Weber number, where both the deformation energy and the viscous dissipation become significant. However the effect of elastic modulus (or diameter ratio) is much less significant if the diameter ratio is very high (or the elastic modulus is very low). The increase in the impact Weber number is observed to systematically reduce the dynamic contact angle in all combinations of impact parameters.

• The effect of diameter ratio and elastic modulus on spreading behaviours of the drops is limited.

• The retraction of the drop impacting on the substrate with lowest stiffness is significantly inhibited because of contact line pinning. Drops impacting on a surface with higher curvature are observed to experience a more pronounced retraction phase compared to the case of a small curvature.

• A simple energy conservation approach accounting for the energy dissipation due to substrate deformation has been proposed and is able to explain some of the experimental observations. However it is not able to predict the scaling of the maximum spreading length without further empirical adjustments.

Chapter 6

Outlook and Future Work

6.1 Leidenfrost drop impact

Although a mechanism based on the observation of symmetry breaking and somersaulting in Leidenfrost drops has been proposed to demonstrate the energy redistribution after impact, which successfully explains the fact that the Newtonian drops with infinite-shear viscosity bounce much lower than other types of drops (Section 4.1), the nature of the flow instabilities which lead to the formation of finger-like protrusions and symmetry breaking is still poorly understood. Detailed information of the flow structure inside the retracting drop is needed in order to further understand the mechanism. One possible way is to use the fluorescent particles and track them inside the droplets through a PIV system. However the number of the particles within a single droplet can not be too small to obtain precise measurements and not too large to avoid changing the viscosity. Besides the velocity data measured through the PIV system must be corrected due to the variance of refraction index at the curved interface between the drop fluid and air. Thus measuring the velocity profile experimentally is not a simple task. Another possible approach is numerical simulation. Simulating the impact of drops with sufficient low viscosity on heated surface at sufficiently high Weber number using appropriate two-phase flow numerical methods may reproduce the symmetry breaking and rotating of bouncing drops observed in our experiment.

However the biggest challenge of simulating the Leidenfrost drops is the correct modelling of the dynamics of vapour film which is formed between the droplet and the solid surface during impact.

6.2 Viscoplastic drop impact on viscoplastic surfaces

We propose a possible mechanism which explains the spreading behaviours of Newtonian drops impacting on different substrates based on the difference in velocity profiles (Section 4.3). However, so far we are not able to validate the proposed mechanism experimentally. In order to obtain the velocity profile in both the droplet and the substrate, one could set up a small-scale PIV system as shown schematically by Figure 6.1. Though it would be difficult to visualise the correct movement of particles inside the droplet as mentioned in Section 6.1, the flow field of the substrate under the impact point is much easier to capture since the correction process due to the refraction index change is simpler without curved interface. In addition, with the help of the velocity profile, one is able to identify the yielded/unyielded regions during the drop impact process.

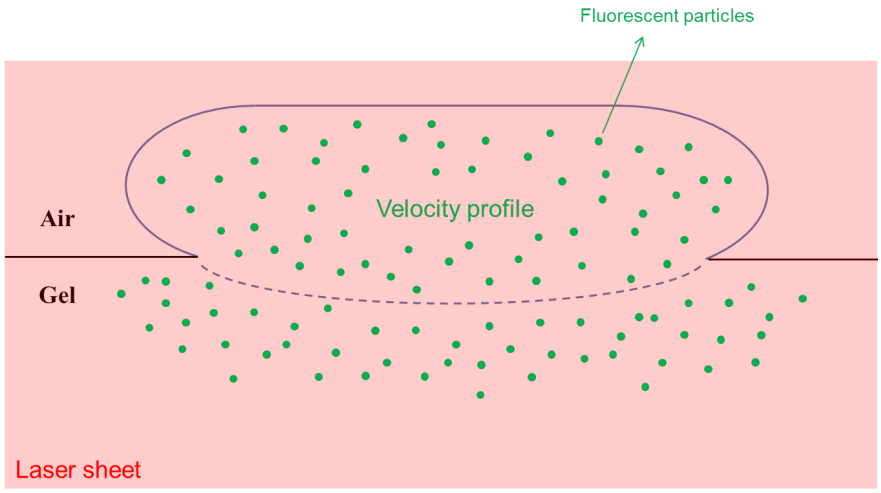

Figure 6.1: Schematic of a small-scale PIV system for measuring the velocity profile.

6.3 Drop impact on spherical soft surface

The deformation of the substrate is negligible compared to the equilibrium drop diameter (i.e., micro-scale substrate deformation) in our drop impact experiments on spherical PDMS substrates (Section 4.5). Thus it is impossible to capture the contour of the deformed surface through digital image processing. However it would be interesting to observe the macro-scale substrate deformation (comparable with the equilibrium drop diameter) during impact. Using PDMS as the convex substrates to achieve macro-scale substrate deformation is not very practical since the liquid behaviours and high stickiness of PDMS at high base/agent mixing ratio (i.e., low elastic modulus) would make it very difficult to separate the PDMS from the mould. One possible future plan is to conduct drop impact experiments on a thin flexible film with a spherical shape as schematically shown in Figure 6.2, in which macro-scale substrate deformation is expected to be observed by a high-speed camera. In addition, the novel digital image processing scheme based on a goniometric mask can be adopted to measure the dynamic contact angle in this scenario where both the drop fluid surface and the solid surface deform during drop impact, which cannot be achieved by conventional techniques of contact angle measurement.

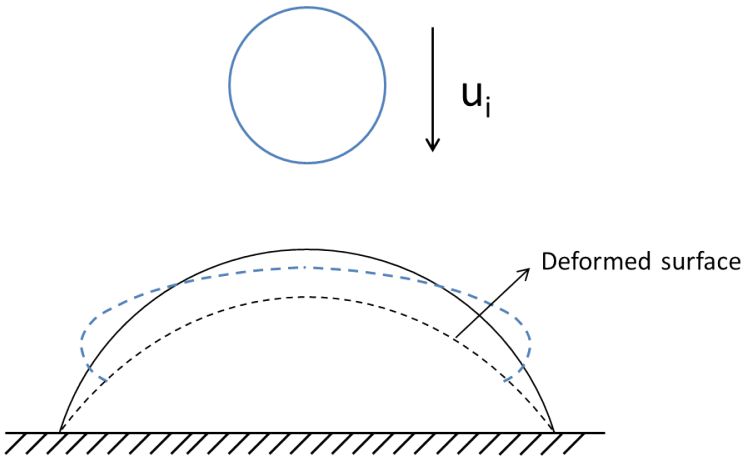

Figure 6.2: Schematic of drop impact on a thin flexible film with a spherical shape.

Bibliography

[1] Azar Alizadeh, Vaibhav Bahadur, Wen Shang, Yun Zhu, Donald Buckley, Ali Dhinojwala, and Manohar Sohal. Influence of substrate elasticity on droplet impact dynamics. *Langmuir*, 29(14):4520–4524, 2013.

[2] K Anders, N Roth, and A Frohn. The velocity change of ethanol droplets during collision with a wall analysed by image processing. *Experiments in Fluids*, 15(2):91–96, 1993.

[3] P Attané, F Girard, and V Morin. An energy balance approach of the dynamics of drop impact on a solid surface. *Physics of Fluids*, 19(1):012101, 2007.

[4] C Thomas Avedisian. The homogeneous nucleation limits of liquids. *Journal of physical and chemical reference data*, 14(3):695–729, 1985.

[5] Chengxin Bai and AD Gosman. Development of methodology for spray impingement simulation. Technical report, SAE Technical Paper, 1995.

[6] Shamit Bakshi, Ilia V Roisman, and Cam Tropea. Investigations on the impact of a drop onto a small spherical target. *Physics of Fluids*, 19(3):032102, 2007.

[7] Neil J Balmforth, Ian A Frigaard, and Guillaume Ovarlez. Yielding to stress: Recent developments in viscoplastic fluid mechanics. *Annual Reviews of Fluid Mechanics*, 46:121–146, 2014.

[8] SE Bechtel, DB Bogy, and FE Talke. Impact of a liquid drop against a flat surface. *IBM Journal of Research and Development*, 25(6):963–971, 1981.

[9] A Bejan and D Gobin. Constructal theory of droplet impact geometry. *International journal of heat and mass transfer*, 49(15):2412–2419, 2006.

[10] Vance Bergeron. Designing intelligent fluids for controlling spray applications. *Comptes Rendus Physique*, 4(2):211–219, 2003.

[11] John D Bernardin and Issam Mudawar. Validation of the quench factor technique in predicting hardness in heat treatable aluminum alloys. *International journal of heat and mass transfer*, 38(5):863–873, 1995.

[12] John D Bernardin and Issam Mudawar. An experimental investigation into the relationship between temperature-time history and surface roughness in the spray quenching of aluminum parts. *Journal of engineering materials and technology*, 118(1):127–134, 1996.

[13] John D Bernardin and Issam Mudawar. A leidenfrost point model for impinging droplets and sprays. *TRANSACTIONS-AMERICAN SOCIETY OF MECHANICAL ENGINEERS JOURNAL OF HEAT TRANSFER*, 126(2):272–278, 2004.

[14] John D Bernardin, Clinton J Stebbins, and Issam Mudawar. Mapping of impact and heat transfer regimes of water drops impinging on a polished surface. *International Journal of Heat and Mass Transfer*, 40(2):247–267, 1997.

[15] V Bertola. Drop impact on a hot surface: effect of a polymer additive. *Experiments in fluids*, 37(5):653–664, 2004.

[16] V Bertola. Wicking with a yield stress fluid. *Journal of Physics: Condensed Matter*, 21(3):035107, 2008.

[17] V Bertola. An experimental study of bouncing leidenfrost drops: comparison between newtonian and viscoelastic liquids. *International Journal of Heat and Mass Transfer*, 52(7):1786–1793, 2009.

[18] V Bertola. Effect of polymer concentration on the dynamics of dilute polymer solution drops impacting on heated surfaces in the leidenfrost regime. *Experimental Thermal and Fluid Science*, 52:259–269, 2014.

[19] V Bertola. An impact regime map for water drops impacting on heated surfaces. *International Journal of Heat and Mass Transfer*, 85:430–437, 2015.

[20] V Bertola and K Sefiane. Controlling secondary atomization during drop impact on hot surfaces by polymer additives. *Physics of Fluids*, 17(10):108104, 2005.

[21] Volfango Bertola. Some applications of controlled drop deposition on solid surfaces. *Recent Patents on Mechanical Engineering*, 1(3):167–174, 2008.

[22] Volfango Bertola. Viscoelastic leidenfrost drops. In *Proc. 22nd European Conference on Liquid Atomization and Spray Systems, Como, Italy*, pages 8–10, 2008.

[23] Volfango Bertola and Mark D Haw. Impact of concentrated colloidal suspension drops on solid surfaces. *Powder Technology*, 2014.

[24] Anne-Laure Biance, Frédéric Chevy, Christophe Clanet, Guillaume Lagubeau, and David Quéré. On the elasticity of an inertial liquid shock. *Journal of Fluid Mechanics*, 554(1):47–66, 2006.

[25] Eugene C Bingham. An investigation of the laws of plastic flow. *Bulletin of the Bureau of Standards*, 13:309–353, 1916.

[26] D Biolè and V Bertola. The fuzzy interface of a drop. *Computing and Visualization in Science*, 17:19–32, 2015.

[27] D Biolè and V Bertola. A goniometric mask to measure contact angles from digital images of liquid drops. *Colloids and Surfaces A: Physicochemical and Engineering Aspects*, 467:149–156, 2015.

[28] D Biolè, M Wang, and V Bertola. Assessment of image processing methods to measure the apparent contact angle of liquid drops. *Experimental Thermal and Fluid Science*, 76:296–305, 2016.

[29] Alfio Bisighini, Gianpietro E Cossali, Cameron Tropea, and Ilia V Roisman. Crater evolution after the impact of a drop onto a semi-infinite liquid target. *Physical Review E*, 82(3):036319, 2010.

[30] Kate Black and Volfango Bertola. Non-newtonian leidenfrost drops. *Atomization and Sprays*, 23(3), 2013.

[31] Brendan C Blackwell, Marc E Deetjen, Joseph E Gaudio, and Randy H Ewoldt. Sticking and splashing in yield-stress fluid drop impacts on coated surfaces. *Physics of Fluids*, 27(4):043101, 2015.

[32] Brendan C Blackwell, Marc E Deetjen, Joseph E Gaudio, and Randy H Ewoldt. Quantitative measures of yield-stress fluid drop impacts on coated surfaces. *Atomization and Sprays*, 27(4), 2017.

[33] TD Blake. Dynamic contact angles and wetting kinetics. *Wettability*, 49:251–309, 1993.

[34] Milton Blander and Joseph L Katz. Bubble nucleation in liquids. *AIChE Journal*, 21(5):833–848, 1975.

[35] Ralf Blossey. Self-cleaning surfacesvirtual realities. *Nature materials*, 2(5):301–306, 2003.

[36] Willem H Boersma, Jozua Laven, and Hans N Stein. Shear thickening (dilatancy) in concentrated dispersions. *AIChE journal*, 36(3):321–332, 1990.

[37] Leon Bolle and J Cl Moureau. Spray cooling of hot surfaces. *Multiphase science and technology*, 1(1-4), 1982.

[38] J Boujlel and Philippe Coussot. Measuring the surface tension of yield stress fluids. *Soft Matter*, 9(25):5898–5908, 2013.

[39] Pierre J Carreau. Rheological equations from molecular network theories. *Transactions of the Society of Rheology (1957-1977)*, 16(1):99–127, 1972.

[40] Fernando Carrillo, Shikha Gupta, Mehdi Balooch, Sally J Marshall, Grayson W Marshall, Lisa Pruitt, and Christian M Puttlitz. Nanoindentation of polydimethylsiloxane elastomers: Effect of crosslinking, work of adhesion, and fluid environment on elastic modulus. *Journal of materials research*, 20(10):2820–2830, 2005.

[41] Kenneth Carroll and Russell Mesler. Splashing liquid drops form vortex rings and not jets at low froude numbers. *Journal of Applied Physics*, 52(1):507–507, 1981.

[42] G Castanet, T Lienart, and F Lemoine. Dynamics and temperature of droplets impacting onto a heated wall. *International Journal of Heat and Mass Transfer*, 52(3):670–679, 2009.

[43] Claudia M Cesa, Norbert Kirchgeßner, Dirk Mayer, Ulrich S Schwarz, Bernd Hoffmann, and Rudolf Merkel. Micropatterned silicone elastomer substrates for high resolution analysis of cellular force patterns. *Review of scientific instruments*, 78(3):034301, 2007.

[44] S Chandra and CT Avedisian. On the collision of a droplet with a solid surface. In *Proceedings of the Royal Society of London A: Mathematical,*

Physical and Engineering Sciences, volume 432, pages 13–41. The Royal Society, 1991.

[45] Longquan Chen, Elmar Bonaccurso, and Martin ER Shanahan. Inertial to viscoelastic transition in early drop spreading on soft surfaces. *Langmuir*, 29(6):1893–1898, 2013.

[46] Longquan Chen, Jun Wu, Zhigang Li, and Shuhuai Yao. Evolution of entrapped air under bouncing droplets on viscoelastic surfaces. *Colloids and Surfaces A: Physicochemical and Engineering Aspects*, 384(1):726–732, 2011.

[47] Wanli Cheng and Maxim A Olshanskii. Finite stopping times for freely oscillating drop of a yield stress fluid. *Journal of Non-Newtonian Fluid Mechanics*, 239:73–84, 2017.

[48] Christophe Clanet, Cédric Béguin, Denis Richard, and David Quéré. Maximal deformation of an impacting drop. *Journal of Fluid Mechanics*, 517:199–208, 2004.

[49] GE Cossali, A Coghe, and M Marengo. The impact of a single drop on a wetted solid surface. *Experiments in fluids*, 22(6):463–472, 1997.

[50] GE Cossali, M Marengo, and M Santini. Secondary atomisation produced by single drop vertical impacts onto heated surfaces. *Experimental thermal and fluid science*, 29(8):937–946, 2005.

[51] GE Cossali, M Marengo, M Santini, and S Fest. Effect of wall effusivity on thermally induced secondary atomisation of single drop impacting onto a tilted surface. *Kyoto: ICLASS*, 2006.

[52] Philippe Coussot. Rheophysics of pastes: a review of microscopic modelling approaches. *Soft Matter*, 3:528–540, 2007.

[53] Philippe Coussot and F. Gaulard. Gravity flow instability of viscoplastic mate- rials: The ketchup drip. *Physical Review E*, 72:031409, 2005.

[54] Malcolm M Cross. Rheology of non-newtonian fluids: a new flow equation for pseudoplastic systems. *Journal of Colloid Science*, 20(5):417–437, 1965.

[55] SJ Curran, RE Hayes, A Afacan, MC Williams, and PA Tanguy. Properties of carbopol solutions as models for yield-stress fluids. *Journal of food science*, 67(1):176–180, 2002.

[56] MAGNUS DAHLBÄCK. Behavior of nebulizing solutions and suspensions. *Journal of Aerosol Medicine*, 7(s1):S–13, 1994.

[57] Grivon Daniel, Civet Yoan, Pataky Zoltan, and Perriard Yves. Bingham-papanastasiou and approximate parallel models comparison for the design of magneto-rheological valves. In *Advanced Intelligent Mechatronics (AIM), 2014 IEEE/ASME International Conference on*, pages 168–173. Ieee, 2014.

[58] OI Del Rıo and AW Neumann. Axisymmetric drop shape analysis: computational methods for the measurement of interfacial properties from the shape and dimensions of pendant and sessile drops. *Journal of colloid and interface science*, 196(2):136–147, 1997.

[59] M Ding, A Kantzas, et al. Capillary number correlations for gas-liquid systems. *Journal of Canadian Petroleum Technology*, 46(02), 2007.

[60] Hongming Dong. *Drop-on-demand inkjet drop formation and deposition.* PhD thesis, Georgia Institute of Technology, 2006.

[61] EB Dussan. On the spreading of liquids on solid surfaces: static and dynamic contact lines. *Annual Review of Fluid Mechanics*, 11(1):371–400, 1979.

[62] Olive G Engel. Crater depth in fluid impacts. *Journal of Applied Physics*, 37(4):1798–1808, 1966.

[63] CW Extrand and Y Kumagai. Contact angles and hysteresis on soft surfaces. *Journal of colloid and interface science*, 184(1):191–200, 1996.

[64] RS Farr, John R Melrose, and RC Ball. Kinetic theory of jamming in hard-sphere startup flows. *Physical Review E*, 55(6):7203, 1997.

[65] Alexander I Fedorchenko and An-Bang Wang. On some common features of drop impact on liquid surfaces. *Physics of Fluids (1994-present)*, 16(5):1349–1365, 2004.

[66] Lin Feng, Shuhong Li, Yingshun Li, Huanjun Li, Lingjuan Zhang, Jin Zhai, Yanlin Song, Biqian Liu, Lei Jiang, and Daoben Zhu. Super-hydrophobic surfaces: from natural to artificial. *Advanced materials*, 14(24):1857–1860, 2002.

[67] JE Field, JP Dear, and JE Ogren. The effects of target compliance on liquid drop impact. *Journal of Applied Physics*, 65(2):533–540, 1989.

[68] RE Ford and CGL Furmidge. Impact and spreading of spray drops on foliar surfaces. *Soc Chem Ind Monogr*, 25:417–32, 1967.

[69] Jackson F Freitas, Edson J Soares, and Roney L Thompson. Viscoplastic–viscoplastic displacement in a plane channel with interfacial tension effects. *Chemical Engineering Science*, 91:54–64, 2013.

[70] IA Frigaard and C Nouar. On the usage of viscosity regularisation methods for visco-plastic fluid flow computation. *Journal of Non-Newtonian Fluid Mechanics*, 127(1):1–26, 2005.

[71] D Fuard, T Tzvetkova-Chevolleau, S Decossas, Philippe Tracqui, and P Schiavone. Optimization of poly-di-methyl-siloxane (pdms) substrates

for studying cellular adhesion and motility. *Microelectronic Engineering*, 85(5):1289–1293, 2008.

[72] Hitoshi Fujimoto and Natsuo Hatta. Deformation and rebounding processes of a water droplet impinging on a flat surface above leidenfrost temperature. *Journal of fluids engineering*, 118(1):142–149, 1996.

[73] Hitoshi Fujimoto, Yosuke Oku, Tomohiro Ogihara, and Hirohiko Takuda. Hydrodynamics and boiling phenomena of water droplets impinging on hot solid. *International Journal of Multiphase Flow*, 36(8):620–642, 2010.

[74] Lichao Gao and Thomas J McCarthy. Contact angle hysteresis explained. *Langmuir*, 22(14):6234–6237, 2006.

[75] Sean Gart, Joseph E Mates, Constantine M Megaridis, and Sunghwan Jung. Droplet impacting a cantilever: A leaf-raindrop system. *Physical Review Applied*, 3(4):044019, 2015.

[76] G German and V Bertola. Impact of shear-thinning and yield-stress drops on solid substrates. *Journal of Physics: Condensed Matter*, 21(37):375111, 2009.

[77] G German and V Bertola. Formation of viscoplastic drops by capillary breakup. *Physics of Fluids*, 22(3):033101, 2010.

[78] G German and V Bertola. The free-fall of viscoplastic drops. *Journal of Non-Newtonian Fluid Mechanics*, 165(13):825–828, 2010.

[79] G German and V Bertola. The spreading behaviour of capillary driven yield-stress drops. *Colloids and Surfaces A: Physicochemical and Engineering Aspects*, 366(1):18–26, 2010.

[80] G German and Volfango Bertola. Review of drop impact models and validation with high-viscosity newtonian fluids. *Atomization and Sprays*, 19(8), 2009.

[81] BS Gottfried, CJ Lee, and KJ Bell. The leidenfrost phenomenon: film boiling of liquid droplets on a flat plate. *International Journal of heat and mass transfer*, 9(11):1167–1188, 1966.

[82] William W Graessley. Polymer chain dimensions and the dependence of viscoelastic properties on concentration, molecular weight and solvent power. *Polymer*, 21(3):258–262, 1980.

[83] G Grant, J Brenton, and D Drysdale. Fire suppression by water sprays. *Progress in energy and combustion science*, 26(2):79–130, 2000.

[84] Dorian AH Hanaor, Yixiang Gan, and Itai Einav. Contact mechanics of fractal surfaces by spline assisted discretisation. *International Journal of Solids and Structures*, 59:121–131, 2015.

[85] Y Hardalupas, AMKP Taylor, and JH Wilkins. Experimental investigation of sub-millimetre droplet impingement on to spherical surfaces. *International journal of heat and fluid flow*, 20(5):477–485, 1999.

[86] Francis H Harlow and John P Shannon. Distortion of a splashing liquid drop. *Science*, 157(3788):547–550, 1967.

[87] Francis H Harlow and John P Shannon. The splash of a liquid drop. *Journal of Applied Physics*, 38(10):3855–3866, 1967.

[88] Lober Hermany, Daniel DallOnder dos Santos, Sérgio Frey, Mônica F Naccache, and Paulo R de Souza Mendes. Flow of yield-stress liquids through an axisymmetric abrupt expansion-contraction. *Journal of Non-Newtonian Fluid Mechanics*, 201:1–9, 2013.

[89] Paul C Hiemenz and Timothy P Lodge. *Polymer chemistry*. CRC press, 2007.

[90] M Hoorfar and AW Neumann. Recent progress in axisymmetric drop shape analysis (adsa). *Advances in colloid and interface science*, 121(1):25–49, 2006.

[91] Christopher J Howland, Arnaud Antkowiak, J Rafael Castrejón-Pita, Sam D Howison, James M Oliver, Robert W Style, and Alfonso A Castrejón-Pita. Its harder to splash on soft solids. *Physical review letters*, 117(18):184502, 2016.

[92] Mingying Hsiao, Seth Lichter, and Luis G Quintero. The critical weber number for vortex and jet formation for drops impinging on a liquid pool. *Physics of Fluids (1958-1988)*, 31(12):3560–3562, 1988.

[93] Maziyar Jalaal, Neil J Balmforth, and Boris Stoeber. Slip of spreading viscoplastic droplets. *Langmuir*, 31(44):12071–12075, 2015.

[94] Elizabeth R Jerison, Ye Xu, Larry A Wilen, and Eric R Dufresne. Deformation of an elastic substrate by a three-phase contact line. *Physical review letters*, 106(18):186103, 2011.

[95] Tadashi Kajiya, Adrian Daerr, Tetsuharu Narita, Laurent Royon, François Lequeux, and Laurent Limat. Dynamics of the contact line in wetting and diffusing processes of water droplets on hydrogel (pamps–paam) substrates. *Soft Matter*, 7(24):11425–11432, 2011.

[96] Alexander Karl, Martin Rieber, Markus Schelkle, Klaus Anders, and Arnold Frohn. Comparison of new numerical results for droplet wall interactions with experimental results. *ASME-PUBLICATIONS-FED*, 236:201–206, 1996.

[97] Danial Khojasteh, Alireza Bordbar, Reza Kamali, and Marco Marengo. Curvature effect on droplet impacting onto hydrophobic and superhydrophobic spheres. *International Journal of Computational Fluid Dynamics*, 31(6-8):310–323, 2017.

[98] CJ Koh and LG Leal. The stability of drop shapes for translation at zero reynolds number through a quiescent fluid. *Physics of Fluids A: Fluid Dynamics*, 1(8):1309–1313, 1989.

[99] Sang Yong Lee and Sung Uk Ryu. Recent progress of spray-wall interaction research. *Journal of mechanical science and technology*, 20(8):1101–1117, 2006.

[100] Johann Gottlob Leidenfrost. *De aquae communis nonnullis qualitatibus tractatus*. Ovenius, 1756.

[101] Johann Gottlob Leidenfrost. On the fixation of water in diverse fire. *International Journal of Heat and Mass Transfer*, 9(11):1153–1166, 1966.

[102] Liow Jong Leng. Splash formation by spherical drops. *Journal of Fluid Mechanics*, 427:73–105, 2001.

[103] Gangtao Liang, Yali Guo, Xingsen Mu, and Shengqiang Shen. Experimental investigation of a drop impacting on wetted spheres. *Experimental Thermal and Fluid Science*, 55:150–157, 2014.

[104] Gangtao Liang, Yali Guo, Yong Yang, Song Guo, and Shengqiang Shen. Special phenomena from a single liquid drop impact on wetted cylindrical surfaces. *Experimental Thermal and Fluid Science*, 51:18–27, 2013.

[105] Gangtao Liang, Yong Yang, Yali Guo, Ni Zhen, and Shengqiang Shen. Rebound and spreading during a drop impact on wetted cylinders. *Experimental Thermal and Fluid Science*, 52:97–103, 2014.

[106] Tong-Miin Liou, Chia-Yen Chan, and Kuan-Cheng Shih. Study of the characteristics of polymer droplet deposition in fabricated rectangular microcavities. *Journal of Micromechanics and Microengineering*, 19(6):065028, 2009.

[107] WC Macklin and PV Hobbs. Subsurface phenomena and the splashing of drops on shallow liquids. *Science*, 166(3901):107–108, 1969.

[108] WC Macklin and GJ Metaxas. Splashing of drops on liquid layers. *Journal of applied physics*, 47(9):3963–3970, 1976.

[109] K Madlener, B Frey, and HK Ciezki. Generalized reynolds number for non-newtonian fluids. In *Progress in Propulsion Physics*, volume 1, pages 237–250. EDP Sciences, 2009.

[110] Amir Maleki, S Hormozi, A Roustaei, and IA Frigaard. Macro-size drop encapsulation. *Journal of Fluid Mechanics*, 769:482–521, 2015.

[111] Ilias Malgarinos, Nikolaos Nikolopoulos, and Manolis Gavaises. A numerical study on droplet-particle collision dynamics. *International Journal of Heat and Fluid Flow*, 61:499–509, 2016.

[112] Simone Mangili, Carlo Antonini, Marco Marengo, and Alidad Amirfazli. Understanding the drop impact phenomenon on soft pdms substrates. *Soft Matter*, 8(39):10045–10054, 2012.

[113] Samuel L Manzello and Jiann C Yang. On the collision dynamics of a water droplet containing an additive on a heated solid surface. In *Proceedings of the Royal Society of London A: Mathematical, Physical and Engineering Sciences*, volume 458, pages 2417–2444. The Royal Society, 2002.

[114] Ted Mao, David Kuhn, and Honghi Tran. Spread and rebound of liquid droplets upon impact on flat surfaces. *AIChE Journal*, 43(9):2169–2179, 1997.

[115] Abraham Marmur. Thermodynamic aspects of contact angle hysteresis. *Advances in colloid and interface science*, 50:121–141, 1994.

[116] AS Moita and ALN Moreira. Drop impacts onto cold and heated rigid surfaces: morphological comparisons, disintegration limits and secondary atomization. *International Journal of Heat and Fluid Flow*, 28(4):735–752, 2007.

[117] ALN Moreira, AS Moita, and MR Panao. Advances and challenges in explaining fuel spray impingement: How much of single droplet impact research is useful? *Progress in energy and combustion science*, 36(5):554–580, 2010.

[118] Ian Douglas Morrison and Sydney Ross. *Colloidal dispersions: suspensions, emulsions, and foams*. Wiley-Interscience, 2002.

[119] Jeffrey D Naber and Patrick V Farrell. Hydrodynamics of droplet impingement on a heated surface. *Training*, 2014:04–28, 1993.

[120] AB Norton, RD Hancocks, and LM Grover. Poly (vinyl alcohol) modification of low acyl gellan hydrogels for applications in tissue regeneration. *Food Hydrocolloids*, 42:373–377, 2014.

[121] Tasos C Papanastasiou. Flows of materials with yield. *Journal of Rheology*, 31(5):385–404, 1987.

[122] M Pasandideh-Fard, M Bussmann, and Sanjeev Chandra. Simulating droplet impact on a substrate of arbitrary shape. *Atomization and sprays*, 11(4), 2001.

[123] M Pasandideh-Fard, YM Qiao, Sanjeev Chandra, and Javad Mostaghimi. Capillary effects during droplet impact on a solid surface. *Physics of fluids*, 8(3):650–659, 1996.

[124] CO Pedersen. An experimental study of the dynamic behavior and heat transfer characteristics of water droplets impinging upon a heated surface. *International Journal of Heat and Mass Transfer*, 13(2):369IN3373–372IN5381, 1970.

[125] Rachel E Pepper, Laurent Courbin, and Howard A Stone. Splashing on elastic membranes: The importance of early-time dynamics. *Physics of Fluids*, 20(8):082103, 2008.

[126] Ramon Pericet-Camara, Günter K Auernhammer, Kaloian Koynov, Simone Lorenzoni, Roberto Raiteri, and Elmar Bonaccurso. Solid-supported thin elastomer films deformed by microdrops. *Soft Matter*, 5(19):3611–3617, 2009.

[127] Ramón Pericet-Cámara, Andreas Best, Hans-Jurgen Butt, and Elmar Bonaccurso. Effect of capillary pressure and surface tension on the deformation of elastic surfaces by sessile liquid microdrops: an experimental investigation. *Langmuir*, 24(19):10565–10568, 2008.

[128] Andrea Prosperetti and Hasan N Oguz. The impact of drops on liquid surfaces and the underwater noise of rain. *Annual Review of Fluid Mechanics*, 25(1):577–602, 1993.

[129] Andreas MV Putz and Teodor I Burghelea. The solid–fluid transition in a yield stress shear thinning physical gel. *Rheologica Acta*, 48(6):673–689, 2009.

[130] David Quéré. Leidenfrost dynamics. *Annual Review of Fluid Mechanics*, 45:197–215, 2013.

[131] Martin Rein. Phenomena of liquid drop impact on solid and liquid surfaces. *Fluid Dynamics Research*, 12(2):61, 1993.

[132] Martin Rein. Capillary effects at newly formed liquid–liquid contacts. *Physics of Fluids*, 14(1):411–414, 2002.

[133] Martin Rein. Interactions between drops and hot surfaces. In *Drop-Surface Interactions*, pages 185–217. Springer, 2002.

[134] Osborne Reynolds. On the floating of drops on the surface of water depending only on the purity of the surface. *Proc. Manchester Lit. Phil. Soc*, 21(1), 1881.

[135] D Richard and D Quéré. Bouncing water drops. *EPL (Europhysics Letters)*, 50(6):769, 2000.

[136] Romain Rioboo, Cameron Tropea, and Marco Marengo. Outcomes from a drop impact on solid surfaces. *Atomization and Sprays*, 11(2), 2001.

[137] Geraint P Roberts and Howard A Barnes. New measurements of the flow-curves for carbopol dispersions without slip artefacts. *Rheologica Acta*, 40(5):499–503, 2001.

[138] Francisco Rodriguez and Russell Mesler. Some drops don't splash. *Journal of colloid and interface science*, 106(2):347–352, 1985.

[139] Y Rotenberg, Lr Boruvka, and AW Neumann. Determination of surface tension and contact angle from the shapes of axisymmetric fluid interfaces. *Journal of colloid and interface science*, 93(1):169–183, 1983.

[140] JF Sacadura. Initiation aux transferts thermiques, tec. *Et Doc, Lavoisier*, 1993.

[141] Raazesh Sainudiin, Miguel Moyers-Gonzalez, and Teodor Burghelea. A microscopic gibbs field model for the macroscopic yielding behaviour of a viscoplastic fluid. *Soft matter*, 11(27):5531–5545, 2015.

[142] S Sampath and X Jiang. Splat formation and microstructure development during plasma spraying: deposition temperature effects. *Materials Science and Engineering: A*, 304:144–150, 2001.

[143] Stefano Schiaffino and Ain A Sonin. Molten droplet deposition and solidification at low weber numbers. *Physics of Fluids (1994-present)*, 9(11):3172–3187, 1997.

[144] M Seki, H Kawamura, and K Sanokawa. Transient temperature profile of a hot wall due to an impinging liquid droplet. *Journal of Heat Transfer*, 100(1):167–169, 1978.

[145] AW Sisko. The flow of lubricating greases. *Industrial & Engineering Chemistry*, 50(12):1789–1792, 1958.

[146] Irina Smagin, Manabendra Pathak, Olga M Lavrenteva, and Avinoam Nir. Motion and shape of an axisymmetric viscoplastic drop slowly falling through a viscous fluid. *Rheologica acta*, 50(4):361–374, 2011.

[147] Robert W Style and Eric R Dufresne. Static wetting on deformable substrates, from liquids to soft solids. *Soft Matter*, 8(27):7177–7184, 2012.

[148] Hariprasad J Subramani, Talal Al-Housseiny, Alvin U Chen, Mingfeng Li, and Osman A Basaran. Dynamics of drop impact on a rectangular slot. *Industrial & Engineering Chemistry Research*, 46(19):6105–6112, 2007.

[149] JJ Thomson and HF Newall. On the formation of vortex rings by drops falling into liquids, and some allied phenomena. *Proceedings of the royal society of London*, 39(239-241):417–436, 1885.

[150] Thomas Vasileiou, Julia Gerber, Jana Prautzsch, Thomas M Schutzius, and Dimos Poulikakos. Superhydrophobicity enhancement through substrate flexibility. *Proceedings of the National Academy of Sciences*, page 201611631, 2016.

[151] LHJ Wachters and NAJ Westerling. The heat transfer from a hot wall to impinging water drops in the spheroidal state. *Chemical Engineering Science*, 21(11):1047–1056, 1966.

[152] An-Bang Wang, Chih-Hung Lin, and Chi-Chang Chen. The critical temperature of dry impact for tiny droplet impinging on a heated surface. *Physics of Fluids (1994-present)*, 12(6):1622–1625, 2000.

[153] Zhixin Wang, Alex A Volinsky, and Nathan D Gallant. Crosslinking effect on polydimethylsiloxane elastic modulus measured by custom-built compression instrument. *Journal of Applied Polymer Science*, 131(22), 2014.

[154] Patricia B Weisensee, Junjiao Tian, Nenad Miljkovic, and William P King. Water droplet impact on elastic superhydrophobic surfaces. *Scientific Reports*, 6:30328, 2016.

[155] Elizabeth A Wilder, Shu Guo, Sheng Lin-Gibson, Michael J Fasolka, and Christopher M Stafford. Measuring the modulus of soft polymer networks via a buckling-based metrology. *Macromolecules*, 39(12):4138–4143, 2006.

[156] AM Worthington. On the forms assumed by drops of liquids falling vertically on a horizontal plate. *Proceedings of the royal society of London*, 25(171-178):261–272, 1876.

[157] Chiyu Xie, Jianying Zhang, Volfango Bertola, and Moran Wang. Lattice boltzmann modeling for multiphase viscoplastic fluid flow. *Journal of Non-Newtonian Fluid Mechanics*, 234:118–128, 2016.

[158] Shi-Chune Yao and Kang Yuan Cai. The dynamics and leidenfrost temperature of drops impacting on a hot surface at small angles. *Experimental Thermal and Fluid Science*, 1(4):363–371, 1988.

[159] AL Yarin. Drop impact dynamics: splashing, spreading, receding, bouncing. *Annu. Rev. Fluid Mech.*, 38:159–192, 2006.

[160] AL Yarin and DA Weiss. Impact of drops on solid surfaces: self-similar capillary waves, and splashing as a new type of kinematic discontinuity. *Journal of Fluid Mechanics*, 283:141–173, 1995.

[161] KY Yasuda, RC Armstrong, and RE Cohen. Shear flow properties of concentrated solutions of linear and star branched polystyrenes. *Rheologica Acta*, 20(2):163–178, 1981.

[162] Duo Zhang, K Papadikis, and Sai Gu. Investigations on the droplet impact onto a spherical surface with a high density ratio multi-relaxation time lattice-boltzmann model. *Communications in Computational Physics*, 16(04):892–912, 2014.

[163] Duo Zhang, Konstantinos Papadikis, and Sai Gu. Application of a high density ratio lattice-boltzmann model for the droplet impingement on flat and spherical surfaces. *International Journal of Thermal Sciences*, 84:75–85, 2014.

Appendix A

Image-processing Code

The present Matlab® code has been developed by the author to process the recorded images from high-speed cameras.

A.1 Code for capturing the contours of both crater and drop fluid

(See Figure 3.14 for reference.)

```
fprintf('image_No  drop_depth  cavity_depth
drop_diameter  cavity_diameter \n')
for n = 8:200
% Define interface
interface = 290;
% Deepen upper part
bright = 20; %deepening height
min_r = 400; %degree of deepening
%Image thresholding
threshold = 0;
%Dilate time
time = 3;
%Dilate time cavity
time2 = 2;
```

```
%%%
```

```
k_cavity_t = interface;
geldrop_uniform = geldrop;
drop_height = bright;
unit = 1/bright;
for i = interface:interface+bright
for j = 1:c_total
if  geldrop_uniform(i,j)<=245
geldrop_uniform(i,j) = geldrop(i,j)-
fix(1*(1-(i-k_cavity_t)*unit)*min_r);
end
end
end
%%%%%%%%%%%%%%%%%%%%%%%%%%%%%%%%%%%%%%%%%%%%%%%%%%%%%%%%%%%%%%%%%%%%%%%%%%%%%%%
%imtool(geldrop_uniform)
%%%%%%%%%%%%%%%%%%%%%%%%%%%%%%%%%%%%%%%%%%%%%%%%%%%%%%%%%%%%%%%%%%%%%%%%%%%%%%%
%Correction
%vertical
%geldrop_uniform(:,1:125) = 255*ones(r_total,125);
%geldrop_uniform(:,555:c_total) =
255*ones(r_total,c_total-554 );
%imtool(geldrop_edge_cut)
geldrop_edge_cut = edge(imfilter(geldrop_uniform, h1),
'canny');
%%%%%%%%%%%%%%%%%%%%%%%%%%%%%%%%%%%%%%%%%%%%%%%%%%%%%%%%%%%%%%%%%%%%%%%%%%%%%%%
%imtool(geldrop_edge_cut)
%%%%%%%%%%%%%%%%%%%%%%%%%%%%%%%%%%%%%%%%%%%%%%%%%%%%%%%%%%%%%%%%%%%%%%%%%%%%%%%
%Correction
%horizontal
```

```
%geldrop_edge_cut(330:430,:)= zeros(430-330+1,c_total);
%geldrop_edge_cut(335:430,505:550)= zeros(430-335+1,
550-505+1);
%vertical
geldrop_edge_cut(:,1:162)= zeros(r_total,162);
geldrop_edge_cut(:,394:c_total)= zeros(r_total,c_total-393);
%imtool(geldrop_edge_cut)
%%%%%%%%%%%%%%%%%%%%%%%%%%%%%%%%%%%%%%%%%%%%%%%%%%%%%%%%%%%%
%Get rid of the 'frame'
cut = 5;  %(pixels)
geldrop2 = geldrop_uniform(cut:(r_total-cut+1),
cut:(c_total-cut+1));
geldrop_edge2 = geldrop_edge_cut(cut:(r_total-cut+1),
cut:(c_total-cut+1));
[r_total, c_total]=size(geldrop_edge2);
white_row = 255*ones(1,c_total);
black_row = zeros(1,c_total);
%Capture the drop fluid and the cavity
se = [1 1 1];
se2 = [0 1 0;1 1 1;0 1 0];
geldrop_edge2_expd = zeros(r_total+50,c_total+100);
geldrop_edge2_expd(1:r_total,50:(c_total+49)) =
geldrop_edge2;
geldrop_edge2_expd(interface-cut+1,:) = ones(1,c_total+100);
for i=1:time
geldrop_edge2_expd = imdilate(geldrop_edge2_expd,
strel('disk',10));
end
```

```
imtool(geldrop_edge2)
geldrop_edge2_expd = imfill(geldrop_edge2_expd,'holes');
for i=1:time
geldrop_edge2_expd = imerode(geldrop_edge2_expd,
strel('disk',10));
end
geldrop_edge2_expd(interface-cut+1,:) = zeros(1,c_total+100);
geldrop_edge2 = geldrop_edge2_expd(1:r_total,50:(c_total+49));
%imtool(geldrop_edge2)
geldrop_cavity2 = imcomplement(im2bw(geldrop2, threshold));
geldrop_cavity2_temp = geldrop_cavity2;
%imtool(geldrop_cavity2_temp)
for i=1:1
geldrop_cavity2_temp = imerode(geldrop_cavity2_temp,
strel('disk',1));
end
for i=1:1
geldrop_cavity2_temp = imdilate(geldrop_cavity2_temp,
strel('disk',1));
end
geldrop_cavity2_expd = zeros(r_total+50,c_total+100);
geldrop_cavity2_expd(1:r_total,50:(c_total+49)) =
geldrop_cavity2_temp;
geldrop_cavity2_expd(interface-cut+1,:) = ones(1,c_total+100);
for i=1:time2
geldrop_cavity2_expd = imdilate(geldrop_cavity2_expd,
strel('disk',8));
end
```

```
geldrop_cavity2_expd = imfill(geldrop_cavity2_expd,'holes');
for i=1:time2
geldrop_cavity2_expd = imerode(geldrop_cavity2_expd,
strel('disk',8));
end
geldrop_cavity2_expd(interface-cut+1,:) = zeros(1,c_total+100);
geldrop_cavity2_temp = geldrop_cavity2_expd(1:r_total,
50:(c_total+49));
geldrop_cavity2 = geldrop_cavity2_temp;
geldrop_cavity2 = imfill(geldrop_cavity2,'holes');
%imtool(geldrop_cavity2)
%Generate RGB components
air = uint8(zeros(r_total, c_total, 3));
substrate = uint8(zeros(r_total, c_total, 3));
drop_fluid = uint8(zeros(r_total, c_total, 3));
cavity = uint8(zeros(r_total, c_total, 3));
all_white = 255*ones(r_total, c_total);
for i=1:interface
air(i,:,1) = white_row;
air(i,:,2) = white_row;
air(i,:,3) = white_row;
end
drop_fluid_b = and(geldrop_edge2,
imcomplement(geldrop_cavity2));
time_extra = 1;
for i=1:time_extra
drop_fluid_b = imerode(drop_fluid_b,se2);
end
```

```
for i=1:time_extra
drop_fluid_b = imdilate(drop_fluid_b,se2);
end
substrate_b = imcomplement(or(drop_fluid_b,geldrop_cavity2));
substrate_b = imcomplement(imfill(imcomplement(substrate_b),
'holes'));
drop_fluid_b = and(imcomplement(substrate_b),
imcomplement(geldrop_cavity2));
interface = 0;
for i = 1: r_total
if min(substrate_b(i,:)) == 0;
break
else
interface = interface+1;
end
end
for i=1:interface
substrate_b(i,:) = black_row;
end
substrate(:,:,2) = substrate_b.*all_white;
substrate(:,:,3) = substrate_b.*all_white;
drop_fluid(:,:,3) = drop_fluid_b.*all_white;
cavity(:,:,1) = geldrop_cavity2.*all_white;
whole = substrate+air+drop_fluid+cavity;
%imtool(substrate)
%imtool(air)
%imtool(drop_fluid)
%imtool(cavity)
```

```
%Measurement
%Depth
drop_bot = r_total;
cavity_bot = r_total;
for i=r_total:-1:1
s = sum(drop_fluid_b(i,:));
if s > 0
break
else
drop_bot = drop_bot - 1;
end
end
for i=r_total:-1:1
s = sum(geldrop_cavity2(i,:));
if s > 0
break
else
cavity_bot = cavity_bot - 1;
end
end
drop_depth   =  abs(interface-drop_bot);
cavity_depth =  abs(interface-cavity_bot);
%Diameter
drop_le = 1;
drop_ri = c_total;
cavity_le = 1;
cavity_ri = c_total;
%imtool(drop_fluid_b)
```

```
for i=1:c_total
s = sum(drop_fluid_b(:,i));
if s > 0
break
else
drop_le = drop_le + 1;
end
end
for i=1:c_total
s = sum(geldrop_cavity2(:,i));
if s > 0
break
else
cavity_le = cavity_le + 1;
end
end
for i=c_total:-1:1
s = sum(drop_fluid_b(:,i));
if s > 0
break
else
drop_ri = drop_ri - 1;
end
end
for i=c_total:-1:1
s = sum(geldrop_cavity2(:,i));
if s > 0
break
```

```
else
cavity_ri = cavity_ri - 1;
end
end
drop_diameter   =  abs(drop_ri-drop_le);
cavity_diameter =  abs(cavity_ri-cavity_le);
%if drop_diameter < cavity_diameter
%   drop_diameter = cavity_diameter;
%end
fprintf('%g %g %g %g %g \n',n,
drop_depth,cavity_depth,drop_diameter,cavity_diameter)
imtool(whole)
if n<100
filename2 = ['Processed00' num2str(n) '.bmp'];
else
filename2 = ['Processed0' num2str(n) '.bmp'];
end
imwrite(whole,filename2,'bmp')
end
```

A.2 Code for isolating drop morphology from spherical substrate and quantitative measurements

(See Figures 3.15 & 3.16 for reference.)

```
clear all;
clc;
close all force;
%%%%%%%%%%%%%%%%%%%%%%%%%%%%%%%%%%%%%%%%%%%%%%%%%%%%%%%%%%%%
```

```
input_path = 'C:\Users\csm13\Desktop\Temp\Frames\';
output_path = 'C:\Users\csm13\Desktop\Temp\Processed\';
convex_original = imread([input_path 'Frame0020.bmp']);
start = 9;
finish = 200;
smooth = 3;
extradialte = 0;
%%%%%%%%%%%%%%%%%%%%%%%%%%%%%%%%%%%%%%%%%%%%%%%%%%%%%%%%%%%%
R_hemisphere = 9/2; %/mm
r1 = 100;
r2 = 150;
%%%%%%%%%%%%%%%%%%%%%%%%%%%%%%%%%%%%%%%%%%%%%%%%%%%%%%%%%%%%
D_water = 3.09;   %/mm
threshold = 0.4;
cut = 3;
%h1 = fspecial('gaussian',[3 2], 1);
h1 = fspecial('gaussian',[6 4], 2);
convex_background = imread([input_path 'Frame0000.bmp']);
%%%%%%%%%%%%%%%%%%%%%%%%%%%%%%%%%%%%%%%%%%%%%%%%%%%%%%%%%%%%
convex_original = rgb2gray(imfilter(convex_original, h1));
convex_background = rgb2gray(imfilter(convex_background,
h1));
convex_binary = im2bw(convex_original,threshold);
convex_background_binary = im2bw(convex_background,
threshold);
[r_total, c_total]=size(convex_binary);
convex_bi = convex_binary(cut:(r_total-cut+1),
cut:(c_total-cut+1));
```

```
convex_background_bi = convex_background_binary(cut:
(r_total-cut+1), cut:(c_total-cut+1));
[r_total, c_total]=size(convex_bi);
convex_bi_reverse = imcomplement(convex_bi);
convex_background_bi_reverse =
imcomplement(convex_background_bi);
convex_bi_reverse_fill = imfill(convex_bi_reverse,'holes');
s = regionprops(convex_bi_reverse_fill, 'Area', 'PixelList');
[~,ind] = max([s.Area]);
pix = sub2ind(size(convex_bi_reverse), s(ind).PixelList(:,2),
 s(ind).PixelList(:,1));
convex_bi_reverse_fill_biggest =
zeros(size(convex_bi_reverse));
convex_bi_reverse_fill_biggest(pix) =
convex_bi_reverse_fill(pix);
convex_background_bi_reverse_fill =
imfill(convex_background_bi_reverse,'holes');
s = regionprops(convex_background_bi_reverse_fill, 'Area',
'PixelList');
[~,ind] = max([s.Area]);
pix = sub2ind(size(convex_bi_reverse), s(ind).PixelList(:,2),
 s(ind).PixelList(:,1));
convex_background_bi_reverse_fill_biggest =
 zeros(size(convex_background_bi_reverse));
convex_background_bi_reverse_fill_biggest(pix) =
 convex_background_bi_reverse_fill(pix);
convex_background_bi_reverse_fill_biggest =
imerode(convex_background_bi_reverse_fill_biggest,
```

```
strel('disk',smooth));
convex_background_bi_reverse_fill_biggest =
imdilate(convex_background_bi_reverse_fill_biggest,
strel('disk',smooth));
%%%% not necessary %%%%
convex_background_bi_reverse_fill_biggest =
imdilate(convex_background_bi_reverse_fill_biggest,
strel('disk',extradialte));
%%%% not necessary %%%%
drop_bi_reverse =
xor(convex_bi_reverse_fill_biggest,
convex_background_bi_reverse_fill_biggest);
s = regionprops(drop_bi_reverse, 'Area', 'PixelList');
[~,ind] = max([s.Area]);
pix = sub2ind(size(drop_bi_reverse), s(ind).PixelList(:,2),
s(ind).PixelList(:,1));
drop_bi_reverse_biggest = zeros(size(drop_bi_reverse));
drop_bi_reverse_biggest(pix) = drop_bi_reverse(pix);
contact_line_temp =
imdilate(convex_background_bi_reverse_fill_biggest,
strel('disk',1)) & drop_bi_reverse_biggest;
drop_bi_reverse_biggest_temp =
(drop_bi_reverse_biggest - contact_line_temp) |
convex_background_bi_reverse_fill_biggest;
drop_bi_reverse_biggest_temp =
imdilate(drop_bi_reverse_biggest_temp,strel('disk',1));
drop_bi_reverse_biggest_temp =
imerode(drop_bi_reverse_biggest_temp,strel('disk',1));
```

```
drop_bi_reverse_biggest = xor(drop_bi_reverse_biggest_temp,
convex_background_bi_reverse_fill_biggest);
s = regionprops(drop_bi_reverse_biggest, 'Area',
'PixelList');
[~,ind] = max([s.Area]);
pix = sub2ind(size(drop_bi_reverse_biggest),
 s(ind).PixelList(:,2), s(ind).PixelList(:,1));
drop_bi_reverse_biggest_temp =
zeros(size(drop_bi_reverse_biggest));
drop_bi_reverse_biggest_temp(pix) =
drop_bi_reverse_biggest(pix);
drop_bi_reverse_biggest = drop_bi_reverse_biggest_temp;
convex_background_bi_reverse_fill_biggest_dilate =
imdilate(convex_background_bi_reverse_fill_biggest,
strel('disk',1));
contact_line =
convex_background_bi_reverse_fill_biggest_dilate
 & drop_bi_reverse_biggest;
[~,hemi_left] =
max(convex_background_bi_reverse_fill_biggest(r_total,:));
[~,hemi_right] =
max(fliplr(convex_background_bi_reverse_fill_biggest
(r_total,:)));
hemi_right = c_total - hemi_right;
convex_background_bi_reverse_fill_biggest(r_total,
(hemi_left:hemi_right)) = 1.;
convex_background_bi_reverse_fill_biggest =
imfill(convex_background_bi_reverse_fill_biggest,'holes');
```

```
convex_bi_reverse_fill_biggest(r_total,
(hemi_left:hemi_right))=1.;
convex_bi_reverse_fill_biggest =
imfill(convex_bi_reverse_fill_biggest,'holes');
s_bottom =
sum(convex_background_bi_reverse_fill_biggest(r_total,:));
imtool(convex_background_bi_reverse_fill_biggest)
hemi_middle = round(hemi_left+0.5*s_bottom);
[~,hemi_top] =max(convex_background_bi_reverse_fill_biggest
(:,hemi_middle));
%%%%%%%%%%%%%%%%%%%%%%%%%%%%%%%%%%%%%%%%%%%%%%%%%%%%%%%%%%%%%%%%%%%%
%find the centre
[~,hemi_lefttop] =
max(convex_background_bi_reverse_fill_biggest
(:,hemi_middle-r1));
[~,hemi_righttop] =
max(convex_background_bi_reverse_fill_biggest
(:,hemi_middle+r1));
p1 = [hemi_middle -hemi_top];
p2 = [hemi_middle-r1 -hemi_lefttop];
p3 = [hemi_middle+r1 -hemi_righttop];
m_r = (p2(2)-p1(2))/(p2(1)-p1(1));
m_t = (p3(2)-p2(2))/(p3(1)-p2(1));
c1x = (m_r*m_t*(p3(2)-p1(2))+m_r*(p2(1)+p3(1))-
m_t*(p1(1)+p2(1)))/(2*(m_r-m_t));
c1y = (-1)/m_r*(c1x-(p1(1)+p2(1))/2)+(p1(2)+p2(2))/2;
c1 = [round(c1x) round(-c1y)]
[~,hemi_lefttop] =
```

```
max(convex_background_bi_reverse_fill_biggest
(:,hemi_middle-r2));
[~,hemi_righttop] =
max(convex_background_bi_reverse_fill_biggest
(:,hemi_middle+r2));
p1 = [hemi_middle -hemi_top];
p2 = [hemi_middle-r2 -hemi_lefttop];
p3 = [hemi_middle+r2 -hemi_righttop];
m_r = (p2(2)-p1(2))/(p2(1)-p1(1));
m_t = (p3(2)-p2(2))/(p3(1)-p2(1));
c2x = (m_r*m_t*(p3(2)-p1(2))+m_r*(p2(1)+p3(1))-
m_t*(p1(1)+p2(1)))/(2*(m_r-m_t));
c2y = (-1)/m_r*(c2x-(p1(1)+p2(1))/2)+(p1(2)+p2(2))/2;
c2 = [round(c2x) round(-c2y)]
center = [round((c1x+c2x)/2) round((-c1y-c2y)/2)]
radius =
round(sqrt((center(1)-hemi_middle)^2+(center(2)-hemi_top)^2))
[~,contact_line_left_border] = max(max(contact_line));
contact_line_mid_x = center(1);
%contact_line_mid_x = contact_line_left_border
+round(sum(max(contact_line))*0.5);
left_contact_line = contact_line(:,1:contact_line_mid_x);
right_contact_line =
contact_line(:,contact_line_mid_x+1:c_total);
[~,contact_line_lepoint_y] =
max(flipud(max(left_contact_line,[],2)));
contact_line_lepoint_y = r_total-contact_line_lepoint_y+1;
[~,contact_line_lepoint_x] =
```

```
max(left_contact_line(contact_line_lepoint_y,:));
[~,contact_line_ripoint_y] =
max(flipud(max(right_contact_line,[],2)));
contact_line_ripoint_y = r_total-contact_line_ripoint_y+1;
[~,contact_line_ripoint_x] =
max(fliplr(right_contact_line(contact_line_ripoint_y,:)));
contact_line_ripoint_x = c_total - contact_line_ripoint_x+1;
mid =
[round((contact_line_lepoint_x+contact_line_ripoint_x)/2),
round((contact_line_lepoint_y+contact_line_ripoint_y)/2)];
tip = zeros(1,2);
if mid(1) == center(1)
tip = [center(1) hemi_top];
else
l = sqrt((center(1)-mid(1))^2+(center(2)-mid(2))^2);
tip(1) = round(center(1)+(mid(1)-center(1))*radius/l);
[~,tip(2)] =
max(convex_background_bi_reverse_fill_biggest(:,tip(1)));
end
tip
line = zeros(r_total,c_total);
if mid(1) ~= center(1)
x1 = center (1);
y1 = -center (2);
x2 = tip(1);
y2 = -tip(2);
k=(y2-y1)/(x2-x1);
b=y1-k*x1;
```

```
if abs(k) >= 1
for j = min(center(2),r_total):-1:1
x_temp = round((-j-b)/k);
if (x_temp >= c_total) || (x_temp <= 1)
break
end
line(j,x_temp)=1;
end
else if k > 0 && k < 1
for i = max(center(1),round((-(r_total-1)-b)/k)):c_total
y_temp = round(-(k*i+b));
if (y_temp >= r_total) || (y_temp <= 1)
break
end
line(y_temp,i)=1;
end
else
for i = min(center(1),round((-(r_total-1)-b)/k)):-1:1
y_temp = round(-(k*i+b));
if (y_temp >= r_total) || (y_temp <= 1)
break
end
line(y_temp,i)=1;
end
end
end
else
line(:,center(1)) = 1. ;
```

```
end
film_north = line &  drop_bi_reverse_biggest;
film_thickness_north =
round(sqrt(sum(max(film_north))^2+
sum(max(film_north,[],2))^2));
film_thickness_north =
film_thickness_north/radius*R_hemisphere/D_water;
if contact_line_lepoint_y >= center(2)
theta_le =
90 + asind(abs(contact_line_lepoint_y-center(2))/radius);
else
theta_le = asind((center(1)-contact_line_lepoint_x)/radius);
end
if contact_line_ripoint_y >= center(2)
theta_ri =
90 + asind(abs(contact_line_ripoint_y-center(2))/radius);
else
theta_ri = asind((contact_line_ripoint_x-center(1))/radius);
end
theta = theta_le+theta_ri;
imtool(convex_bi_reverse_fill_biggest)
imtool(drop_bi_reverse_biggest)
imtool(contact_line)
imtool(line)
imtool(film_north)
%%%%%%%%%%%%%%%%%%%%%%%%%%%%%%%
%           Loop              %
%%%%%%%%%%%%%%%%%%%%%%%%%%%%%%%
```

```
film_thickness_north_seq = zeros(finish-start+1, 1);
theta_seq = zeros(finish-start+1, 1);
contact_angle_left_seq = zeros(finish-start+1, 1);
contact_angle_right_seq = zeros(finish-start+1, 1);
for n = start:finish
if n<100 && n>=10
filename=[input_path 'Frame00' num2str(n) '.bmp'];
elseif n<10
filename=[input_path 'Frame000' num2str(n) '.bmp'];
else
filename=[input_path 'Frame0' num2str(n) '.bmp'];
end
convex_original = imread(filename);
convex_original = rgb2gray(imfilter(convex_original, h1));
convex_binary = im2bw(convex_original,threshold);
[r_total, c_total]=size(convex_binary);
convex_bi = convex_binary(cut:(r_total-cut+1),
cut:(c_total-cut+1));
[r_total, c_total]=size(convex_bi);
convex_bi_reverse = imcomplement(convex_bi);
convex_bi_reverse_fill = imfill(convex_bi_reverse,'holes');
s = regionprops(convex_bi_reverse_fill, 'Area',
'PixelList');
[~,ind] = max([s.Area]);
pix = sub2ind(size(convex_bi_reverse),
s(ind).PixelList(:,2), s(ind).PixelList(:,1));
convex_bi_reverse_fill_biggest =
zeros(size(convex_bi_reverse));
```

```
convex_bi_reverse_fill_biggest(pix) =
convex_bi_reverse_fill(pix);
convex_bi_reverse_fill_biggest(r_total,
(hemi_left:(hemi_left+s_bottom-1)))=1.;
convex_bi_reverse_fill_biggest =
imfill(convex_bi_reverse_fill_biggest,'holes');
drop_bi_reverse =
xor(convex_bi_reverse_fill_biggest,
convex_background_bi_reverse_fill_biggest);
s = regionprops(drop_bi_reverse, 'Area', 'PixelList');
[~,ind] = max([s.Area]);
pix = sub2ind(size(drop_bi_reverse),
s(ind).PixelList(:,2), s(ind).PixelList(:,1));
drop_bi_reverse_biggest = zeros(size(drop_bi_reverse));
drop_bi_reverse_biggest(pix) = drop_bi_reverse(pix);
contact_line_temp =
imdilate(convex_background_bi_reverse_fill_biggest
,strel('disk',1))
& drop_bi_reverse_biggest;
drop_bi_reverse_biggest_temp =
(drop_bi_reverse_biggest - contact_line_temp) |
convex_background_bi_reverse_fill_biggest;
drop_bi_reverse_biggest_temp =
imdilate(drop_bi_reverse_biggest_temp,strel('disk',1));
drop_bi_reverse_biggest_temp =
imerode(drop_bi_reverse_biggest_temp,strel('disk',1));
drop_bi_reverse_biggest = xor(drop_bi_reverse_biggest_temp,
convex_background_bi_reverse_fill_biggest);
```

```
%%%% not necessary %%%%
%drop_bi_reverse_biggest =
imdilate(drop_bi_reverse_biggest,strel('disk',4));
%%%% not necessary %%%%
s = regionprops(drop_bi_reverse_biggest, 'Area',
'PixelList');
[~,ind] = max([s.Area]);
pix = sub2ind(size(drop_bi_reverse_biggest),
s(ind).PixelList(:,2), s(ind).PixelList(:,1));
drop_bi_reverse_biggest_temp =
zeros(size(drop_bi_reverse_biggest));
drop_bi_reverse_biggest_temp(pix) =
drop_bi_reverse_biggest(pix);
drop_bi_reverse_biggest = drop_bi_reverse_biggest_temp;
%
%%%% not necessary %%%%
%drop_bi_reverse_biggest =
imerode(drop_bi_reverse_biggest,strel('disk',4));
%%%% not necessary %%%%
contact_line =
convex_background_bi_reverse_fill_biggest_dilate
& drop_bi_reverse_biggest;
line = zeros(r_total,c_total);
if mid(1) ~= center(1)
x1 = center (1);
y1 = -center (2);
x2 = tip(1);
y2 = -tip(2);
```

```
k=(y2-y1)/(x2-x1);
b=y1-k*x1;
if abs(k) >= 1
for j = min(center(2),r_total):-1:1
x_temp = round((-j-b)/k);
if (x_temp >= c_total) || (x_temp <= 1)
break
end
line(j,x_temp)=1;
end
else if k > 0 && k < 1
for i = max(center(1),round((-(r_total-1)-b)/k)):c_total
y_temp = round(-(k*i+b));
if (y_temp >= r_total) || (y_temp <= 1)
break
end
line(y_temp,i)=1;
end
else
for i = min(center(1),round((-(r_total-1)-b)/k)):-1:1
y_temp = round(-(k*i+b));
if (y_temp >= r_total) || (y_temp <= 1)
break
end
line(y_temp,i)=1;
end
end
end
```

```
else
line(:,center(1)) = 1. ;
end
film_north = line &  drop_bi_reverse_biggest;
film_thickness_north =
round(sqrt(sum(max(film_north))^2+sum(max(film_north,
[],2))^2));
film_thickness_north =
film_thickness_north/radius*R_hemisphere/D_water;
[~,contact_line_left_border] = max(max(contact_line));
contact_line_mid_x = center(1);
%contact_line_mid_x =
contact_line_left_border+
round(sum(max(contact_line))*0.5);
left_contact_line = contact_line(:,1:contact_line_mid_x);
right_contact_line =
contact_line(:,contact_line_mid_x+1:c_total);
[~,contact_line_lepoint_y] =
max(flipud(max(left_contact_line,[],2)));
contact_line_lepoint_y = r_total-
contact_line_lepoint_y+1;
[~,contact_line_lepoint_x] =
max(left_contact_line(contact_line_lepoint_y,:));
[~,contact_line_ripoint_y] =
max(flipud(max(right_contact_line,[],2)));
contact_line_ripoint_y = r_total-
contact_line_ripoint_y+1;
[~,contact_line_ripoint_x] =
```

```
max(fliplr(right_contact_line
(contact_line_ripoint_y,:)));
contact_line_ripoint_x = c_total -
contact_line_ripoint_x+1;
if contact_line_lepoint_y >= center(2)
theta_le =
90 + asind(abs(contact_line_lepoint_y-center(2))/radius);
else
theta_le = asind((center(1)-
contact_line_lepoint_x)/radius);
end
if contact_line_ripoint_y >= center(2)
theta_ri =
90 + asind(abs(contact_line_ripoint_y-center(2))/radius);
else
theta_ri = asind((contact_line_ripoint_x-center(1))
/radius);
end
left_point = [contact_line_lepoint_x
contact_line_lepoint_y];
right_point = [contact_line_ripoint_x
contact_line_ripoint_y];
%%%%%%%%%%%%%%%%%%%%%%%%%%%%%%%%%%%%%%%%%%%%%%%%%%%%
n_mask = 12;
mask_size = 2*n_mask+1;
goniometric_mask = zeros((n_mask+1) , mask_size);
for i= 1:(n_mask+1)
goniometric_mask(i, (n_mask+1-(i-1)):(n_mask+1+(i-1)))
```

```
 = 1.;
end
mask_area = (n_mask+1)^2;
whole_bi =
convex_background_bi_reverse_fill_biggest+
drop_bi_reverse_biggest;
left_measure_region =
whole_bi((left_point(2)-n_mask):left_point(2),
(left_point(1)-n_mask):(left_point(1)+n_mask));
right_measure_region =
whole_bi((right_point(2)-n_mask):right_point(2),
(right_point(1)-n_mask):(right_point(1)+n_mask));
left_area = sum(sum(left_measure_region.*
goniometric_mask));
right_area = sum(sum(right_measure_region.*
goniometric_mask));
if  left_area < mask_area/2
lambda = 1;
left_angle =
90*(1-lambda) +atand(lambda*(mask_area*(1-lambda)
-2*left_area)/(2*left_area-mask_area));
elseif left_area > mask_area/2
lambda = -1;
left_angle =
90*(1-lambda) +atand(lambda*(mask_area*(1-lambda)
-2*left_area)/(2*left_area-mask_area));
else
left_angle = 90;
```

```
end
if  right_area < mask_area/2
lambda = 1;
right_angle =
90*(1-lambda)+atand(lambda*(mask_area*(1-lambda)-
2*right_area)
/(2*right_area-mask_area));
elseif right_area > mask_area/2
lambda = -1;
right_angle =
90*(1-lambda)+atand(lambda*(mask_area*(1-lambda)-
2*right_area)
/(2*right_area-mask_area));
else
right_angle = 90;
end
left_angle = left_angle-theta_le;
right_angle = right_angle-theta_ri;
%%%%%%%%%%%%%%%%%%%%%%%%%%%%%%%%%%%%%%%%%%%%%%%%%%%
theta = theta_le+theta_ri;
film_thickness_north_seq(n-start+1) = film_thickness_north;
theta_seq(n-start+1) = theta;
contact_angle_left_seq(n-start+1) = left_angle;
contact_angle_right_seq(n-start+1) = right_angle;
%imtool(contact_line)
%imtool(film_north)
RGB_hemisphere = uint8(zeros(r_total, c_total, 3));
RGB_drop = uint8(zeros(r_total, c_total, 3));
```

```
RGB_background = uint8(255*ones(r_total, c_total, 3));
all_white = uint8(255*ones(r_total, c_total));
RGB = uint8(255*ones(r_total, c_total, 3));
RGB_hemisphere(:,:,1) =
all_white.*uint8
(convex_background_bi_reverse_fill_biggest);
RGB_drop(:,:,3) = all_white.*uint8(drop_bi_reverse_biggest);
for i=1:3
RGB_background(:,:,i) = RGB_background(:,:,i).
*uint8(imcomplement
(xor(convex_background_bi_reverse_fill_biggest
,drop_bi_reverse_biggest)));
end
RGB_whole = RGB_hemisphere+RGB_drop+RGB_background;
%imtool(RGB_whole)
%path(output_path);
if n<100 && n>=10
filename2 = [output_path 'Processed00' num2str(n) '.bmp'];
elseif n<10
filename2 = [output_path 'Processed000' num2str(n) '.bmp'];
else
filename2 = [output_path 'Processed0' num2str(n) '.bmp'];
end
imwrite(RGB_whole,filename2,'bmp')
% if n==20
%  RGB_drop_temp = uint8(zeros(r_total, c_total, 3));
%  for i=1:3
%   RGB_drop_temp(:,:,i) =
```

```
% all_white.*uint8(drop_bi_reverse_biggest);
%  end
% imwrite(RGB_hemisphere+RGB_drop_temp+RGB_background,
% 'RGB_hemisphere.bmp')
%  for i=1:3
%   RGB_hemisphere(:,:,i) =
% all_white.*uint8
% (convex_background_bi_reverse_fill_biggest);
%  end
% imwrite(RGB_hemisphere+RGB_drop+RGB_background,'drop.bmp')
% imwrite(convex_background_bi_reverse_fill_biggest,'1.bmp')
% imwrite(drop_bi_reverse_biggest,'2.bmp')
% imwrite(xor(convex_background_bi_reverse_fill_biggest,
% drop_bi_reverse_biggest),'3.bmp')
% end
end
[film_thickness_north_min, loc_film_thickness_north_min] =
min(film_thickness_north_seq);
[film_thickness_north_max, loc_film_thickness_north_max] =
max(film_thickness_north_seq(loc_film_thickness_north_min
:length(film_thickness_north_seq)));
loc_film_thickness_north_max =
loc_film_thickness_north_min +
loc_film_thickness_north_max - 1 + start -1;
loc_film_thickness_north_min =
loc_film_thickness_north_min + start -1;
[theta_max, loc_theta_max] = max(theta_seq);
[theta_min, loc_theta_min] =
```

```
min(theta_seq(loc_theta_max:length(theta_seq)));
loc_theta_min = loc_theta_max + loc_theta_min - 1 + start -1;
loc_theta_max = loc_theta_max + start -1;
[contact_angle_left_max, loc_contact_angle_left_max] =
max(contact_angle_left_seq(3:
length(contact_angle_left_seq)));
[contact_angle_left_min, loc_contact_angle_left_min] =
min(contact_angle_left_seq(3:
length(contact_angle_left_seq)));
loc_contact_angle_left_min =
loc_contact_angle_left_min + 3 - 1 + start -1;
loc_contact_angle_left_max =
loc_contact_angle_left_max + 3 - 1 + start -1;
[contact_angle_right_max, loc_contact_angle_right_max] =
max(contact_angle_right_seq(3:
length(contact_angle_right_seq)));
[contact_angle_right_min, loc_contact_angle_right_min] =
min(contact_angle_right_seq(3:
length(contact_angle_right_seq)));
loc_contact_angle_right_min =
loc_contact_angle_right_min + 3 - 1 + start -1;
loc_contact_angle_right_max =
loc_contact_angle_right_max + 3 - 1 + start -1;
fid=fopen([output_path 'Measurement.txt'],'a+');
fprintf(fid,'Mask_size Min_film_north
Max_film_north Max_theta Min_theta Max_CA_left
Min_CA_left Max_CA_right Min_CA_right\r\n');
fprintf(fid,'%3d  %8.6f  %8.6f  %8.4f
```

```
%8.4f  %8.4f  %8.4f  %8.4f  %8.4f\r\n',mask_size,
film_thickness_north_min,film_thickness_north_max,
theta_max,theta_min,contact_angle_left_max,
contact_angle_left_min,contact_angle_right_max,
contact_angle_right_min);
fprintf(fid,'loc  %8d  %8d  %8d  %8d  %8d  %8d  %8d
  %8d\r\n',loc_film_thickness_north_min,
  loc_film_thickness_north_max,loc_theta_max,
  loc_theta_min,loc_contact_angle_left_max,
  loc_contact_angle_left_min,
  loc_contact_angle_right_max,
  loc_contact_angle_right_min);
fprintf(fid,'\r\n');
fprintf(fid,'Image_no. t_/ms film_thickness_north
theta CA_left CA_right\r\n');
for n = start : finish
fprintf(fid,'%3d   %5.1f   %8.6f   %8.4f   %8.4f
%8.4f\r\n',n,0.5*(n-start),
film_thickness_north_seq(n-start+1),
theta_seq(n-start+1),
contact_angle_left_seq(n-start+1),
contact_angle_right_seq(n-start+1));
end
fclose(fid);
```

Appendix B

Technical Data Sheet

A technical data sheet for Carbopol neutralisation from Lubrizol® is presented below.

Lubrizol

noveon
Consumer Specialties

TECHNICAL DATA SHEET

TDS-237
Edition: September 16, 2009
Previous Editions: January, 2002 / July 10, 2008

Neutralizing Carbopol®* and Pemulen™* Polymers in Aqueous and Hydroalcoholic Systems

Effect of pH on Viscosity

Carbopol® and Pemulen™ polymers must be neutralized in order to achieve maximum viscosity. Unneutralized dispersions have an approximate pH range of 2.5-3.5 depending on the polymer concentration. The unneutralized dispersions have very low viscosities, especially Carbopol® ETD and Carbopol® Ultrez polymers. Once a neutralizer is added to the dispersion, thickening gradually occurs as shown in Figure 1. Optimum viscosity is typically achieved at a pH of 6.5-7.5. As demonstrated by the graph, high viscosities can be achieved in pH ranges of 5.0-9.0.

A frequently asked question is "What pH is correct for my finished product?" The answer is that the best pH of the system should be determined by the performance desired for the particular application. The final pH should be consistent with desired functional attributes of the targeted application.

The viscosity of Carbopol® and Pemulen™ polymers will begin to decrease at pH of 9.0 and higher. This is caused by the dampening of the electrostatic repulsion caused by the presence of excess electrolytes. It is possible to achieve high viscosity systems at pH values below 5 and above 9, but the use level of the Carbopol® and Pemulen™ polymer must be increased to obtain these higher viscosity levels.

Figure 1
Carbopol® Polymers Viscosity vs. pH
(0.5 wt% TS Concentration)

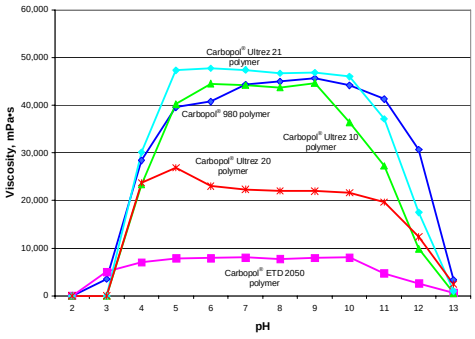

Viscosity Results: Brookfield RVT, 20 rpm @ 25°C

Figure 2

Schematic Depicting Molecule of Carbopol® Polymer in Coiled State

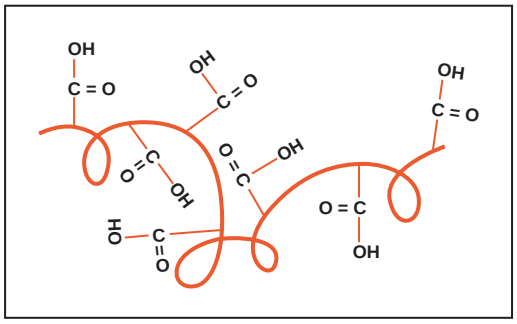

Figure 3

Diagram Depicting Molecule of Carbopol® Polymer in Uncoiled Neutralized State

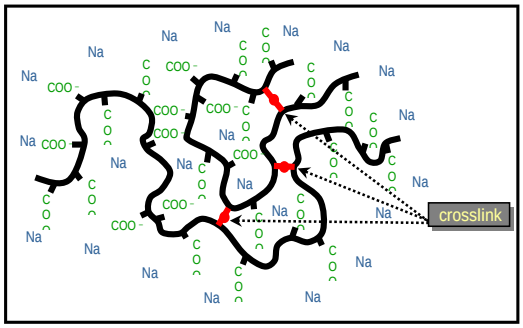

Thickening Mechanism

Carbopol® and Pemulen™ polymers as supplied are dry, tightly coiled acidic molecules. Once dispersed in water, the molecules begin to hydrate and partially uncoil. The most common way to achieve maximum thickening from Carbopol® and Pemulen™ polymers is by converting the acidic Carbopol® or Pemulen™ polymer to a salt. This is easily achieved by neutralizing the Carbopol® or Pemulen™ polymer with a common base such as sodium hydroxide (NaOH) or triethanolamine (TEA).

Figure 4

Neutralization Ratio Chart

Trade Name	CTFA Name	Manufacturer	Neutralization Ratio Base/ Carbopol® Polymer
NaOH (18%)	Sodium Hydroxide		2.3/1.0
Ammonia (28%)	Ammonium Hydroxide		0.7/1.0
KOH (18%)	Potassium Hydroxide		2.7/1.0
L-Arginine	Arginine	Ajinomoto	4.5/1.0
AMP® Ultra PC2000	Aminomethyl Propanol	Dow	0.9/1.0
Neutrol® TE	Tetrahydro-xypropyl Ethylenediamine	BASF	2.3/1.0
TEA (99%)	Triethanolamine		1.5/1.0
Tris Amino® (40%)*	Tromethamine	Dow	3.3/1.0
Ethomeen® C-25	PEG-15 Cocamine	Akzo	6.2/1.0
Diisopropanol-amine	Diisopropanol-amine	Dow	1.2/1.0
Triisopropanol-amine	Triisopropanol-amine	Dow	1.5/1.0

*NOTE: The 40% solution should be made from Tris Amino crystals from the manufacturer. Do not use the pre-dispersed solution from the manufacturer as it contains many impurities.

Common Neutralizers

Figure 4 lists the most common neutralizers used, the manufacturers of these neutralizers, and the appropriate ratio to use (as compared to one part of Carbopol® or Pemulen™ polymers) to achieve exact neutralization at a pH of 7.0. The chart is based on Carbopol® Ultrez 10 polymer, but is applicable to all Carbopol® and Pemulen™ polymers because they all have the same equivalent weight of 76 ± 4.